ADVANCES IN DESIGN AND IMPLEMENTATION OF CEMENTITIOUS BACKFILLS (ADICB)

EDITED BY: Erol Yilmaz, Shuai Cao and Di Wu
PUBLISHED IN: Frontiers in Materials

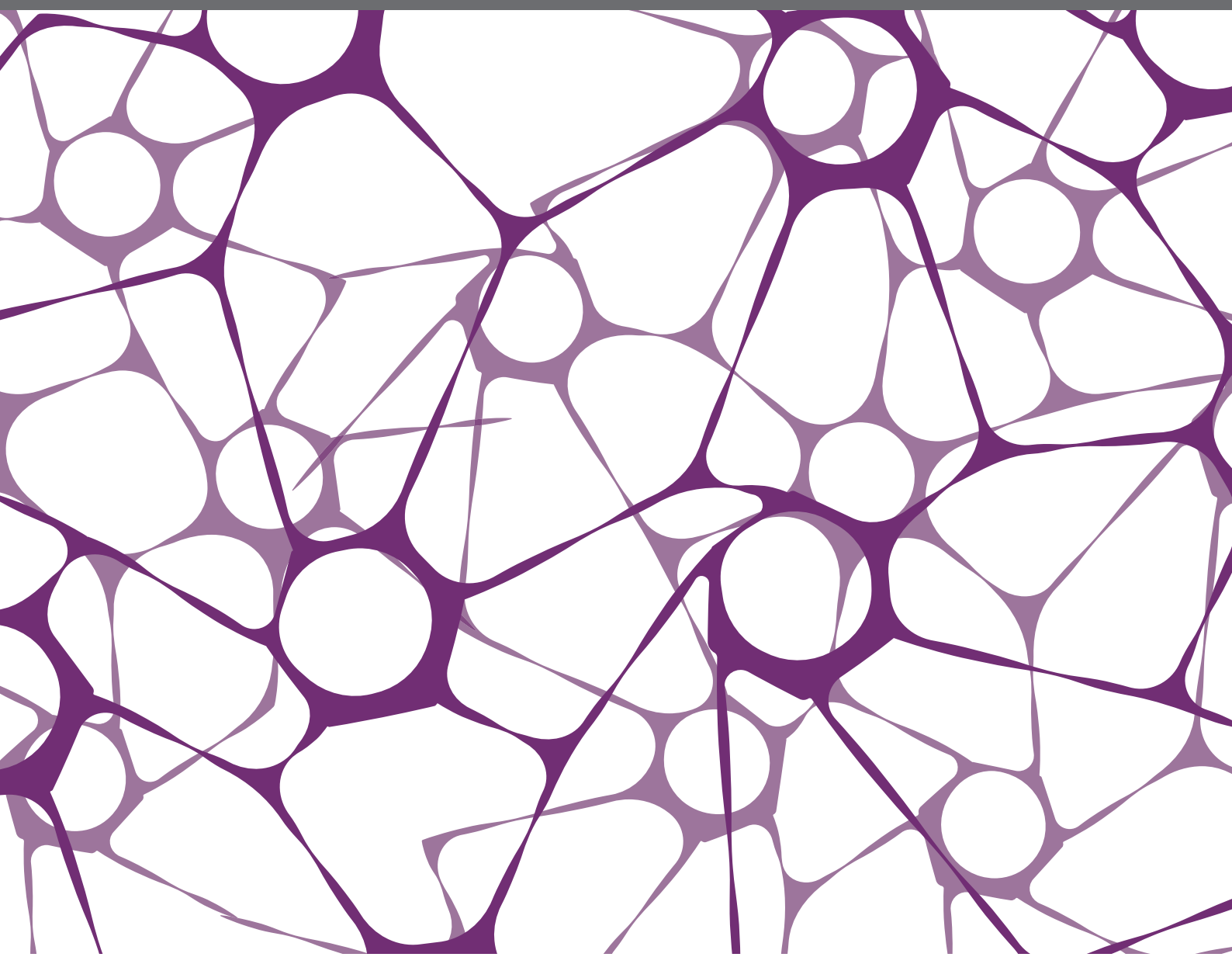

frontiers Research Topics

frontiers

ISSN 1664-8714
ISBN 978-2-83250-146-7
DOI 10.3389/978-2-83250-146-7

About Frontiers

Frontiers is more than just an open-access publisher of scholarly articles: it is a pioneering approach to the world of academia, radically improving the way scholarly research is managed. The grand vision of Frontiers is a world where all people have an equal opportunity to seek, share and generate knowledge. Frontiers provides immediate and permanent online open access to all its publications, but this alone is not enough to realize our grand goals.

Frontiers Journal Series

The Frontiers Journal Series is a multi-tier and interdisciplinary set of open-access, online journals, promising a paradigm shift from the current review, selection and dissemination processes in academic publishing. All Frontiers journals are driven by researchers for researchers; therefore, they constitute a service to the scholarly community. At the same time, the Frontiers Journal Series operates on a revolutionary invention, the tiered publishing system, initially addressing specific communities of scholars, and gradually climbing up to broader public understanding, thus serving the interests of the lay society, too.

Dedication to Quality

Each Frontiers article is a landmark of the highest quality, thanks to genuinely collaborative interactions between authors and review editors, who include some of the world's best academicians. Research must be certified by peers before entering a stream of knowledge that may eventually reach the public - and shape society; therefore, Frontiers only applies the most rigorous and unbiased reviews.
Frontiers revolutionizes research publishing by freely delivering the most outstanding research, evaluated with no bias from both the academic and social point of view. By applying the most advanced information technologies, Frontiers is catapulting scholarly publishing into a new generation.

What are Frontiers Research Topics?

Frontiers Research Topics are very popular trademarks of the Frontiers Journals Series: they are collections of at least ten articles, all centered on a particular subject. With their unique mix of varied contributions from Original Research to Review Articles, Frontiers Research Topics unify the most influential researchers, the latest key findings and historical advances in a hot research area! Find out more on how to host your own Frontiers Research Topic or contribute to one as an author by contacting the Frontiers Editorial Office: frontiersin.org/about/contact

ADVANCES IN DESIGN AND IMPLEMENTATION OF CEMENTITIOUS BACKFILLS (ADICB)

Topic Editors:
Erol Yilmaz, Recep Tayyip Erdoğan University, Turkey
Shuai Cao, University of Science and Technology Beijing, China
Di Wu, University of Science and Technology Beijing, China

Citation: Yilmaz, E., Cao, S., Wu, D., eds. (2022). Advances in Design and Implementation of Cementitious Backfills (ADICB). Lausanne: Frontiers Media SA. doi: 10.3389/978-2-83250-146-7

Table of Contents

04 ***Editorial: Advances in the Design and Implementation of Cementitious Backfills***
Erol Yilmaz, Shuai Cao and Di Wu

07 ***Characterization of Strength and Quality of Cemented Mine Backfill Made up of Lead-Zinc Processing Tailings***
Ufuk Gokhan Akkaya, Kenan Cinku and Erol Yilmaz

18 ***Multiscale Geomechanical Behavior of Fiber-Reinforced Cementitious Composites Under Cyclic Loading Conditions—A Review***
Javaugh McLean and Liang Cui

31 ***Study on the Optimization of Filling Ratio and Strength Variation Characteristics of Cemented Backfills Containing Fly Ash***
Baomeng Chang, Cuifeng Du, Xiaofeng Chu and Long Zhang

41 ***Quantitative Test and Engineering Application of Wear Resistance of a Kind of Mine-Filled Composite Pipeline***
Yong Wang, Gang-feng Yang, Cheng-liang Ma, Quan-li Jia and Qin-guo Jin

47 ***Mechanical Properties and Microstructure Evolution of Cemented Tailings Backfill Under Seepage Pressure***
Yuxian Ke, Yang Shen, Chen Qing, Kaijian Hu, Shi Wang, Qiusong Chen and Huadong Guan

58 ***Strength Analysis and Optimization of Alkali Activated Slag Backfills Through Response Surface Methodology***
Xinghang Dai, Lei Ren, Xiaozhong Gu, Erol Yilmaz, Kun Fang and Haiqiang Jiang

69 ***Temperature Effect on Mohr–Coulomb's Effective Strength Parameters of Paste Backfill***
Alsidqi Hasan and Wee Kiet Ting

82 ***Experimental Study on Sulfate Wetting–Drying Cycle of Metal Tailings Powder Concrete***
Ruidong Wu, Min Zou, Juanhong Liu, Guangtian Zhang and Yueyue Zhang

91 ***Experimental Study on Direct Tensile Properties of Cemented Paste Backfill***
Lijie Guo, Xiaopeng Peng, Yue Zhao, Guangsheng Liu, Guoxing Tang and Andrew Pan

frontiers | Frontiers in Materials

EDITORIAL
published: 24 August 2022
doi: 10.3389/fmats.2022.964111

Editorial: Advances in the Design and Implementation of Cementitious Backfills

Erol Yilmaz[1]*, *Shuai Cao*[2,3]* and *Di Wu*[2,3]*

[1]Department of Civil Engineering, Geotechnical Division, Recep Tayyip Erdogan University, Rize, Turkey, [2]State Key Laboratory of High-Efficient Mining and Safety of Metal Mines of Ministry of Education, University of Science and Technology Beijing, Beijing, China, [3]School of Civil and Resource Engineering, University of Science and Technology Beijing, Beijing, China

Keywords: cementitious backfill, recipe design, geomechanics, in-situ performance, emerging systems

Editorial on the Research Topic

Advances in Design and Implementation of Cementitious Backfills

Backfill plays an essential role in the most modern mining industries worldwide. It is usually applied in the cementitious form to fill underground mined-out openings (stopes and/or voids). Consisting usually of an engineered blend of tailings, binders, and water, cementitious backfills provide numerous benefits ranging from the rapidity of their delivery and mechanical strength to environmental advantages from placing high voluminous processing tailings underground and reducing the size of surface tailing storage facilities like dams. Without hesitation, it expressively improves the safety and productivity of mines and is employed in a more unique role to form advanced mining methods. The design and operation of the backfill are multi-dimensional, covering metallurgical, rheological, hydraulic, mechanical, and geotechnical engineering disciplines. Since any backfill system comprises up to 35% of the mine's operating budget, it is vital for diverse disciplines to work in harmony with each other to create a system that is functional, optimized, and cost-effective for sustainable/green mining. Therefore, there is a need to develop innovative backfill materials and techniques for the negative impact of mining activities on the environment. Recent papers have highlighted improvements in the design and application of cementitious backfills, focusing on their preparation, design, placement, monitoring, performance, and optimization stages. This Research Topic consists of nine research contributions, delivering a broad range of knowledge on mining with a backfill that enhances underground mining efficiency via reduced stope cycle time and the increased recovery of ore. These contributions highlight several examples of cost-effective backfill types and materials, backfill recipe optimization, backfill preparation and delivery to stopes, field placement/curing conditions, stress, and temperature measurements during the pour of cementitious backfills, and monitoring.

The first contribution discusses the strength/quality characteristics of cementitious backfill produced with Pb-Zn mine tailings (Akkaya et al.). Sulfide-rich processing tailings (Pb-Zn ore) were employed to form structural cementitious backfill mixtures. It is estimated that sulfide-rich tailings backfill cured under the influence of air and water cannot resist the chemical reactions that occur, especially in the long term. The mobility of sulfur ions present in Pb-Zn tailings was explored and their effects on backfill strength/durability performance were investigated by some lab experiments (i.e., SEM, XRD, pH, ion chromatography/zeta potential/combustion experiments, and chemical analysis. To eliminate the deleterious effect of sulfurous components, type II and type IV cement (at dosages varying from 3wt% to 7wt%) were used in the backfill. It was suggested that the sort and quantity of the cement experimented on were unsatisfactory owing to the spread-out components and inner sulfate-attack present within these tailings. Cementitious backfills caused the

OPEN ACCESS

Edited and reviewed by:
John L. Provis,
The University of Sheffield,
United Kingdom

***Correspondence:**
Erol Yilmaz
erol.yilmaz@erdogan.edu.tr
Shuai Cao
sandy_cao@ustb.edu.cn
Di Wu
DiWu1218@ustb.edu.cn

Specialty section:
This article was submitted to Structural Materials, a section of the journal Frontiers in Materials

Received: *08 June 2022*
Accepted: *20 June 2022*
Published: *24 August 2022*

Citation:
Yilmaz E, Cao S and Wu D (2022) Editorial: Advances in the Design and Implementation of Cementitious Backfills. Front. Mater. 9:964111. doi: 10.3389/fmats.2022.964111

gypsum problem, as revealed clearly by SEM observations. Nevertheless, the study noticeably showed that elemental analysis conducted by the combustion test system could offer fast/consistent outcomes in the examination of sulfur in Pb-Zn tailings. Hence, important information could be gained about the long-term backfill performance.

The second contribution evaluated the mechanical behavior of fly ash-based cementitious backfill considering the filling rate, cement dosage, and solid content (Chang et al.). In this study, to enhance the mechanical strength of underground filling, and to reduce the cement-related costs leading to social/economic benefits, gold mine tailings and fly ash (industrial solid waste) were effectively utilized. The strength of the 28–56-days cured backfill was greatly affected by the dose of fly ash in the mixture. The addition of too much fly ash caused many fine grains in the backfills and delayed the cement hydration, meaning it did not gain strength in a timely manner. The backfill with a solid content of 74%, a cement dosage of 5%, a tailings-waste rock-fly ash fraction of 2-6-3, and a calcium oxide of 3% provided better mechanical strengths than the backfill recipe implemented in the tested mining site. The backfill's strength is closely related to its pore structure, suggesting that there is a proper ratio of backfilling for cement hydration. If fly ash was being activated first and then contained in the backfill, the corresponding backfill's strength becomes higher because of the improved gel structure created by the hydration of cement. Good integration of fly ash and aggregate will lessen the fill's porosity and ensure a high-quality fill material. As a result, the paper highlighted the significance of the use of fly-ash within filling for its further promotion and application in mines.

The third contribution examines the mechanical strength characteristics of cementitious paste backfills containing alkali activated slag (AAS-CPB) via response surface modeling (Dai et al.). In this paper, the effects of factors such as slag powder SP, silicate modulus SM, and activator content AC on the strength acquisition of 3-/28-days cured AAS-CPB samples were explored. ANOVA was used to explore the status of liberated factors and their connections. It was statistically shown that a robust connection between curing age and strength variation properties exists. The major variables were silicate modulus and activator content. Increasing slag fineness and pH surge backfill strength at early curing ages (3 days), but unreacted slag limits its hydration and strength performance at longer cures. The optimum response values for the backfill were respectively, 0.3, 12,630, and 0.5 for SM, SP, and AC. This contribution highlighted that there was a robust connection among AAS-CPB's test variables, which are necessary to achieve a resilient, lucrative, and viable mine fill for most modern mines worldwide.

The fourth contribution discussed the mechanical/microstructural properties of cementitious backfill exposed to seepage conditions (Ke et al.). The backfill materials placed into underground openings unavoidably endure seepage fields, which negatively affect their ultimate strength behavior. An evolution of strength and pore structure behavior of cemented tailings backfills subjected to diverse seepage water pressures was explored in the present study. It was interpreted that the backfill's strength reduces with augmenting seepage water pressures, which leads to the backfill's microstructure being looser and more porous. The strength of the backfill exposed to seepage also drops with increasing porosity. The initiation/propagation of micro-cracks/pores in the backfill is accelerated by seepage. This eventually results in serious damage to the pore structure of the backfill and a deterioration in its strength properties. This paper also provides information on the strength/microstructure characteristics of the backfill when subjected to seepage and a technical reference for durability analysis of the backfill in water-rich underground mines.

The fifth contribution examines the Mohr-Coulomb strength factor of cementitious tailings backfill, considering temperature influence (Hasan and Ting). Field backfill monitoring indicated inconsistent escalations in total stress during curing, which could be clarified by volumetric expansion, led by a temperature rise in the backfill. Temperature, which is one of the most important curing conditions (i.e., stress and time), actually has a very serious effect on the fresh/hardened characteristics and performance of the backfill. This study explores the effect of temperature (25, 50, and 70°C) under five diverse shearing situations and three effective-stress ranks (16-32–48 kPa) on the shear-strength property of internal/interfacial-friction between non-cemented backfill and cemented backfill containing 5% cement. It suggests that the interfacial friction angle increases with rising temperature, based on the sort of product and the shearing state. The fill's cohesion does not alter with temperature variations occurring in the placed mine backfills over curing time. As a result, the paper highlights the connotation of exact plan limits (i.e., cohesion, friction angle, and shear-strength at diverse temperature-settings) for an accurate and secure stress regime in the placed cementitious backfill materials.

The sixth contribution focuses on the direct tensile properties of cemented paste backfill (Guo et al., 2022). Although many studies have been carried out on the compressive strength of cementitious backfill, the number of studies on its tensile strength is limited due to both the absence of a proper experimental technique and the fill's low tensile strength. Therefore, as an alternative to the traditional indirect tensile strength testing technique, there is a need for new alternative experimental test setups that will provide the direct tensile strength of filling. In this study, a specially designed compression-tensile load transducer (CTLT) was developed and a direct tensile test (DTS) using filling samples was prepared in the shape of a dog bone. Using this newly developed experimental setup, both direct tensile and compressive strength tests were carried out on a total of 47 filling samples and the results were evaluated. The experimental results indicated that the DTS value of the backfill rises with increasing cement content (the most sensitive parameter), solid contents, and curing age. From experimental results, it was observed that a strong link between the fill's direct tensile and compressive strengths exists. The principal contribution of this study is to disclose an innovative experimental test setup that determines the tensile strength of backfill samples. The DTS value determined from filling samples manufactured in the shape of a dog bone and placed in the newly developed CTLT device are critical to efficiently mining backfill designs for most modern mines around the world.

The seventh contribution reviews the geomechanical characteristics of fiber-containing cementitious backfills subjected to cyclic loading conditions (McLean and Cui). During their service life, cementitious fills are exposed to impact/blasting/seismic loads. To enhance the strength performance of backfills subjected to these

loads, there are diverse techniques such as fiber reinforcement in the mining or construction industries. In this review paper, a new perspective is given for fiber reinforced cementitious composites (FRCC), considering the geomechanical processes of embankments subjected to cyclic tensile-shear-compression loading conditions. In terms of macro-scale strength property, it contains state-of-the-art research on pre-/post-peak response and hysteretic behavior. Besides, the pore-pressure effect on the dynamic behavior of non-matured FRCC is thoroughly discussed. A link between microscale crack propagation and damage accumulation for FRCC is also provided, offering future perspectives on fiber reinforcement. The review provides guidance and reference on the multiscale behavior of FRCC subjected to repeated loads. Additionally, it also provides updated information on innovative techniques such as using fibers within cementitious backfills.

The eighth contribution thoroughly examines the engineering design and quantitative experiments of the wear resistance of pipeline transporting backfill mixtures (Wang et al.). Being considered one of the most vital performance signs of backfilling pipelines, wear resistance is really important to better estimate the pipeline's service life. Since it is very difficult to carry out an experimental study on pipelines in underground conditions, there is a need for laboratory devices that measure the pipeline's wear resistance via pipeline material wear. In this article, a new experimental setup and application technique are offered for depicting the wear resistance of newly-established liner complex, conventional, and normal carbon-structural-steel pipelines. Using experimental tests, it determined that the newly developed composite pipeline is respectively, 12.35 and 7.32 times better than the wear resistance of conventional and ordinary carbon structural steel pipelines that are currently used in the industry. Depending on the nature of the materials used in the manufacture of the composite lining, the wear resistance mechanism of the pipeline transporting cementitious backfills to underground mine voids has been well studied. The main contribution of this paper is that composite pipelines provide a good wear resistance during the transport of fill into underground mined-out stopes. Wear resistance, especially in the elbow part of the pipeline, has been an important parameter to evaluate the best way to apply the cementitious backfill.

The last contribution to this Research Topic focuses on the wetting/drying sequence of concrete containing metal tailings (Wu et al.). The tailings can be successfully used together with slag in the production of concrete to utilize large amounts of tailings and to address the shortage of the mineral admixtures used in concrete. In this paper, concrete containing diverse contents of tailings was prepared and subjected to a wetting/drying series experiment for investigating concrete's corrosion resistance. Moreover, the degradation mechanism of the tailings-added concrete material abraded with sulfate is explained by SEM, XRD, and NMR experiments. It has been determined from experimental studies that sulfate corrosion resistance will increase if the tailings are added to the C50 concrete in appropriate amounts. If the tailings/slag ratio used in concrete is 3:7 and 5:5, the resistance to sulfate corrosion could achieve KS180. It has also been determined that a strong link between ultrasonic velocities and the mechanic strengths of concrete samples containing tailings exists. The failure of concrete that has tailings is usually due to the formation of corrosion materials (i.e., ettringite, gypsum). In conclusion, the principal contribution of this study could be considered the addition of tailings powder into conventional concrete, which can significantly reduce its alkalinity, thereby significantly changing its pore structure, and increasing the sulfate corrosion resistance of concrete.

This Research Topic selects and collects eight original research papers and one review paper that have undertaken studies on cementitious materials, undertaken in the lab and via field performance tests. It introduces recent developments in these areas. This Research Topic sheds new light on critical aspects of the backfilling process, with important implications for the mining industry, providing important scientific information that will benefit future research.

AUTHOR CONTRIBUTIONS

This Editorial was cooperatively prepared by EY, SC, and DW. The authors approved the final submitted version.

ACKNOWLEDGMENTS

As the editors, we would like to sincerely thank all the referees and article authors who are experts in their fields for their invaluable suggestions, evaluations, and comments. Moreover, we would like to thank and extend our respect to the journal's internal responsible editors and publishing team, who have made significant contributions to the execution of the long and critical refereeing processes, providing invaluable technical support. This Research Topic would not have been so effective without the continuous support and contributions of these generous people.

REFERENCES

Guo, L., Peng, X., Zhao, Y., Liu, G., Tang, G., and Pan, A. (2022). Experimental study on direct tensile properties of cemented paste backfill. *Front. Mat.* 9, 864264. doi:10.3389/fmats.2022.864264

Conflict of Interest: The authors declare that the research was conducted in the absence of any commercial or financial relationships that could be construed as a potential conflict of interest.

frontiers in Materials

ORIGINAL RESEARCH
published: 14 September 2021
doi: 10.3389/fmats.2021.740116

Characterization of Strength and Quality of Cemented Mine Backfill Made up of Lead-Zinc Processing Tailings

Ufuk Gokhan Akkaya[1]*, *Kenan Cinku*[1] and *Erol Yilmaz*[2]

[1]Department of Mining Engineering, Faculty of Engineering, Istanbul University-Cerrahpasa, Istanbul, Turkey, [2]Department of Civil Engineering, Geotechnical Division, Recep Tayyip Erdogan University, Rize, Turkey

Predicting the reactions of the backfill materials exposed to the effects of air and groundwater will eventually ensure an efficient and accurate mine fill system for sustainable mining operations. This paper reveals the effect of the mobility of sulfur ions within lead-zinc processing tailings on strength and quality of cemented mine backfills. Some laboratory tests such as X-ray diffraction, ion chromatography, scanning electron microscopy, combustion tests, chemical analysis, pH and zeta potential measurements were performed to better characterize the backfill's mechanical and microstructural properties. Moreover, CEM II/A-P Portland pozzolan and CEM IV/A pozzolanic cements as ready-to-use cement products were used for cemented mine backfill preparation. To ensure the carrier of the lead-zinc tailings and to prevent the mobility of the sulfurous components, a binder content ranging from 3 to 7 wt % were employed in mine backfills. The experimental findings demonstrate that the used cement type and proportions were insufficient and some fractures are occurred in the samples due to the sulfur ion mobility. Accordingly, one can state clearly that the elemental analysis through the combustion test method can provide fast and reliable results in the determination of sulfur within lead-zinc processing tailings.

Keywords: sulphurous tailing, sulphate attack, mine backfill, hydraulic binder, mechanical strength

OPEN ACCESS

Edited by:
Antonio Caggiano,
Darmstadt University of Technology, Germany

Reviewed by:
Mamadou Fall,
University of Ottawa, Canada
Jie Xin,
Institute of Rock and Soil Mechanics (CAS), China
Wei-Ting Lin,
National Ilan University, Taiwan

***Correspondence:**
Ufuk Gokhan Akkaya
ufukhan@iuc.edu.tr

Specialty section:
This article was submitted to Structural Materials, a section of the journal Frontiers in Materials

Received: *12 July 2021*
Accepted: *27 August 2021*
Published: *14 September 2021*

Citation:
Akkaya UG, Cinku K and Yilmaz E (2021) Characterization of Strength and Quality of Cemented Mine Backfill Made up of Lead-Zinc Processing Tailings. Front. Mater. 8:740116. doi: 10.3389/fmats.2021.740116

INTRODUCTION

Environmentally sensible mining requires finding different solutions for mineral processing tailings (Qi and Fourie, 2019). Conventional methods such as tailings impoundments are not safe, and they are insufficient to store large amounts of the generated tailings by conservative environmental regulations (Chen et al., 2019; Cao et al., 2021). However, a huge amount of processing tailings can be stored in large gaps or by using filling techniques environmentally friendly (Jiang et al., 2020; Liu et al., 2020). Cemented paste backfill (CPB) is a commonly-employed technique, especially in Canada, China and Australia, in which underground openings called stopes are supported by being filled with high voluminous tailings (Lu et al., 2018; Cao et al., 2021). In addition, ensuring the harmlessness and environmental compatibility of the processing tailings, the durability plays a key role on the overall performance of CPB samples (Libos and Cui, 2020). Typically, CPB is prepared in a surface paste plant by dewatering fine tailings to form a filter cake, then a sufficient amount of mixing water and binder agents is added to create the mixture pumpable to underground stopes (Kou et al., 2020). Since CPB offers several significant environmental, technical, and economic benefits, it is

considered as one of the best available techniques in Europe for the management of tailings (Chen et al., 2021). However, the physical and chemical properties of CPB should be explored exactly before delivering a cost-effective and high-performance backfill to mines (Yang et al., 2020; Cavusoglu et al., 2021). Hence, interactions between the adjacent environment and processing tailings must be considered for surface/underground mining operations.

The tailings stored underground, especially in metal mining, can cause harmful ion mobility and acid mine drainage (AMD) when they interact with oxygen and underground and/or rain waters (Koohestani et al., 2020). The risk of AMD is related to the presence of sulfidic minerals such as pyrite (FeS_2) (Zhao, 2021). The presence of sulfides within cemented composites has a deleterious effect on paste backfill strength due to sulfate attack (Koohestani et al., 2021). Sulfate attack plays a main role in the mechanical strength and service life of concrete (Liu et al., 2020). However, the mechanisms of sulfate attack on CPB are not quite similar to those on concrete. The sulfate attack on CPB is internal, whereas that on concrete is predominantly external. Moreover, in CPB, sulfate can be adsorbed on the surface of C-S-H, thereby weakening the strength of CPB, since C-S-H is largely responsible for the strength development of any cementitious material (Wang et al., 2020; Alainachi & Fall 2020; Koohestani et al., 2018). Conventional sulfate attack in mortar and concrete leads to the formation of expansive ettringite and gypsum (**Eq. 1**) (Jiang et al., 2020).

$$2\left(3CaO.Al_2O_3.12H_2O\right) + 3\left(Na_2SO_4.10H_2O\right) \rightarrow 3CaO.Al_2O_3.3CaSO_4.31H_2O + 2Al\left(OH\right)_3 + 6NaOH + 17H_2O \quad (1)$$

Ettringite minerals cause expanding during sulfate attack in concrete, leading cracking, spalling, and spillage (Baquerizo et al., 2016). The very low solubility of brucite shifts the above reaction to the right side and favors the consumption of calcium hydroxide (Park et al., 2019). This leads to a reduction in pH and, as a result, calcium silicate hydrate (C–S–H) becomes more susceptible to sulfate attack (Mafra et al., 2020). Sulfate attack is directly related to pH of the tailings and its surroundings (Belebchouche et al., 2016). CPB includes iron, silicon, and aluminum hydroxides as well as gypsum at pH values under 9 (Xiapeng et al., 2019). The risks of contaminated neutral drainage within rocks that contain carbonate compounds and AMD occur at moderate (6–8) and low (<5) pH values, respectively (Myagkaya et al., 2020). AMD is eventually formed by the oxidation of pyrite (**Eqs 2**, **3**, **4**).

$$FeS_2 + 3.5O_2 + H_2O \rightarrow Fe^{2+} + 2\left(SO_4^{2-}\right) + 2H^+ \quad (2)$$

$$Fe^{2+} + 0.25O_2 + H^+ \rightarrow Fe^{3+} + 0.5H_2O \quad (3)$$

$$Fe^{3+} + 3H_2O \rightarrow Fe\left(OH\right)_2\left(s\right) + 3H^+ \quad (4)$$

Sulfide-bearing minerals can jeopardize paste structures by lowering pH and degrading the hydrate, resulting in rapid reactivity depending on the saturation and presence of O_2 (Nordstrom et al., 2015). The oxidation process plays an essential role in the conversion of ferrous iron to ferric iron. Each pH value above 4 contributes to this process (Jiménez & Prieto, 2015). When pH is less than 4, AMD occurs through the contribution of iron-oxidizing ferrooxidant bacteria (Levio-Raiman et al., 2021). The bacterium thiobacillus ferrooxidans increases the initial acidification when the pH is above 4.5. Below pH 4.5, thiobacillus ferrooxidans allows acidification to continue by oxidizing Fe^{2+} from pyritic materials (Shirin et al., 2021). Compounds of calcium (CaCO, $CaMg(CO_3)_2$), iron ($FeCO_3$, $Fe(OH)_3$), and magnesium ($MgCO_3$) are key factors for neutralizing AMD from mine tailings (Elghali et al., 2021). In near-neutral mine waters, along with SO_4^2, bicarbonate (HCO_3^-) is a significant anion. In addition, the concentrations of dissolved calcium (Ca^{2+}) and magnesium (Mg^{2+}) ions are generally elevated relative to dissolved iron (Fe^{3+}) and aluminum (Al^{3+}), which precipitate as the pH increases to above 4–5. Hydrolysis reactions cause many metal ions to form the hydroxides with low solubility. Even dissolved gases can undergo hydration. The hydration reactions of dissolved carbon dioxide (CO_2) and sulfur dioxide (SO_2) form carbonic acid (H_2CO_3) and sulfuric acid (H_2SO_3), respectively (Othmani et al., 2015).

Tricalcium aluminate (C_3A) and tetra calcium aluminoferrite (C_4AF) are the most critical compounds to be considered in sulfate-rich processing tailings (Zheng et al., 2017). According to the ASTM C150-07 standard, the C_3A content should not exceed 5% in sulfate resisting cement, while the combined C_3A+ C_4AF amount should be much lower than 25%. Both Portland and Portland-based cements have great importance in the immobilization and storage of hazardous wastes (Zheng et al., 2018). Ettringite is an important structure for immobilizing contaminants. While the creation of ettringite at early stages is linked with the use of added sulfates to avoid flash sets, its formation at later stages due to external sulfate attack or delayed ettringite formation can cause degradation of concrete structures (Gu et al., 2019). In mine backfill applications, the cement is often used to prevent the AMD formation, and also to offer the mechanical strength, which is critical for the stability of CPB (Hefni and Ali, 2021). To reduce/eliminate the negative effects of AMD which is harmful to vegetation, aquatic life, wildlife, groundwater, and strength of mine backfill (Li et al., 2020; Wang et al., 2021), many researchers have studied to reduce the amount of the cement needed by using different types of cement and additives (Xue et al., 2020; Yan et al., 2020; Huan et al., 2021).

This paper presents an experimental investigation of sulfide-bearing tailings and their possibility of utilization in CPB with two different cement types (CEM II and CEM IV) and amounts (3 and 7 wt%). The originality of this research paper lies in addressing the study of ion chromatography and combustion test conducted on CPB samples containing sulfide-rich minerals. To reveal the interaction with sulfurous compounds such as SO_3 and SO_4, the zeta potential values in CPB were also measured.

MATERIALS AND METHODS

Characterization of Lead-Zinc Processing Tailings

In this study, sulfide-rich tailings sampled from a lead-zinc mineral processing plant in Turkey were employed for the preparation of CPB samples. Several analyses on X-ray

TABLE 1 | Chemical analysis of binders types used during the experiments.

Compounds	CEM II/A-P Portland Pozzolan	CEM IV/A Pozzolanic
SiO_2 (%)	17.84	30.82
Al_2O_3 (%)	4.32	6.53
Fe_2O_3 (%)	2.99	4.00
CaO (%)	61.64	49.64
MgO (%)	2.06	2.01
SO_3 (%)	2.93	2.33
Cl (%)	0.01	0.04
Na_2O/K_2O (%)	—	0.68/0.93
CaO-free lime (%)	1.68	0.70
Insoluble residue (%)	0.78	14.13
Undefined (%)	2.45	0.10
Loss of ignition (%)	5.76	2.92
Mineralogical composition (%)	—	7.58 (C_3A)

diffraction (XRD), inductively coupled plasma mass spectrometry (ICP-MS) and ion chromatography were performed for determining the mineralogical and chemical composition of dry and wet tailings samples. To authenticate the state of the mineral phases visually, scanning electron microscopy (SEM) analyses were done. Since the particle size distribution may affect greatly the dissolution rate of the tailings, the particle size distribution analysis was also conducted according to the TS 1,500 standard (equivalent to the ASTM D2487 standard) using the Malvern MS3000 particle size analyzer which measures particles from 10 nm up to 3.5 mm.

Characterization of Binder and Mixing Water

pH measurements were done to reveal interactions between CPB and its storage environment (with the groundwater adjacent rocks and soils). Indeed, the zeta potential of particles is an important indicator of the interaction between them at different pH values (Jiang et al., 2020; Xu et al., 2021). An increase in the zeta potential increases the water retention ability of pastes that are prepared in the particulate environment. The Zeta potential measurements of each dry paste backfill materials were made by concerning pH using a Brookhaven NanoBrook Zeta Plus zeta potential analyzer.

In order to investigate the interaction between the tailings material (1 wt%) and its surroundings, the change in the pH of the medium was determined with respect to time in pH profile experiments. In these experiments, the HCl and NaOH solutions were used to adjust the ambient pH (2, 3, 5.7, 10, and 11).

In this study, two types of Portland Pozzolan (CEM II/A-P) and Puzzolanic (CEM IV/A) type cement produced by Akcansa Co. (Turkey) were used as hydraulic binders. Note that both of them are suitable to employ in cementitious works conducted in aggressive areas where the sulfate and chloride ions are relatively high. The specifications of these two cement types are presented in **Table 1**.

Preparation of Mine Backfills

After the characterization tests, the unconfined compressive strength (UCS) tests were conducted for determining the mechanical behavior of CPB materials containing two types of different commercial and ready-to-use cement products (CEM II and CEM IV). For the UCS tests, 36 cylindrical samples were prepared in a length/diameter ratio of 2/1. These were formed with every 3 samples from both types of cement (CEM II and CEM IV), at two cement ratios (3 and 7 wt%), and three different curing times (7, 14, and 28 days). The slump values ranging from 6 to 10 inches (15.24–25.40 cm) were used for the pumpability of the CPB material in a pipeline. The CPB slump recipes are given in **Table 2**.

Chemical and Microstructural Measurements

The elemental analysis by combustion (LECO 628 S), ion chromatography tests (ICS 1100), and SEM analysis (Jeol JSM 5600) was performed for investigating sulfide-rich compounds, ion release, and their effects on ettringite occurrence. To determine the amount of sulfur in ettringite, the elemental analysis by combustion and ion chromatography was carried out. Meanwhile, to determine the total sulfur in concrete that causes the SO_3 and SO_4 movement, the combustion tests was carried out.

RESULTS AND DISCUSSION

Particle Size Distribution, XRD, Conductivity, pH and Zeta Potential Results of Tailings

From the particle size distribution tests, the tailings were found to have 42 wt% particles finer than 20 μm, classifying the tailings as medium size grained particles which seem to have lower strengths. It also provides the relatively high specific surface of the grains to ensure sufficient surface tension which enables the solids to hold water and offer a thin permanent lubricating film creating the paste. Note that the grain size distribution of the tailings was classified as a homogeneous distribution according to the TS EN ISO14688-2 standard. The specific gravity of the tailings measured by using a helium pycnometer was found to have 3.2.

TABLE 2 | A summary of slump recipes of cemented mine backfills.

Cement type	Amount of solids + cement + water (g)	Cement content (3 wt%)	Cement content (7 wt%)
CEM II/A-P Portland puzzolan	Solids	10,000	10,000
	Cement	300	700
	Water	2,850	2,650
	Slump value (cm)	18.8	18.8
CEM IV/A puzzolanic cement	Solids	10,000	10,000
	Cement	300	700
	Water	2,800	2,700
	Slump value (cm)	18.8	18.8

TABLE 3 | ICP MS results of the tailings.

Oxides (%)		Base and precious metal elements (ppm)				Rare earth elements (ppm)				Radioactive elements (ppm) and others (%)			
SiO_2	36.19	Mo	5.7	Ba	404	La	30.4	Tm	0.27	Th	9	TOT/C	3.16
Al_2O	8.08	Cu	217.2	Co	15.7	Ce	57.2	Yb	1.58	U	6.4	TOT/S	7.49
Fe_2O	13.58	Pb	1,500	Rb	76.4	Pr	6	Lu	0.23			LOI	12.4
MgO	2.54	Zn	1,548	Sn	11	Nd	20.9	Yb	17.2			Sum	99.48
CaO	23.26	Ni	29.4	Sr	191.3	Sm	3.86	Sc	7				
Na_2O	0.2	As	601.8	V	62	Eu	0.99						
K_2O	2.45	Cd	8.2	W	44.6	Gd	3.37						
TiO_2	0.29	Sb	23.6	Zr	76.8	Tb	0.54						
P_2O_5	0.08	Bi	26.5	Hg	0.37	Dy	2.87						
MnO	0.38	Ag	3.7			Ho	0.55						
Cr_2O_3	0.01	Au	0.055			Er	1.62						

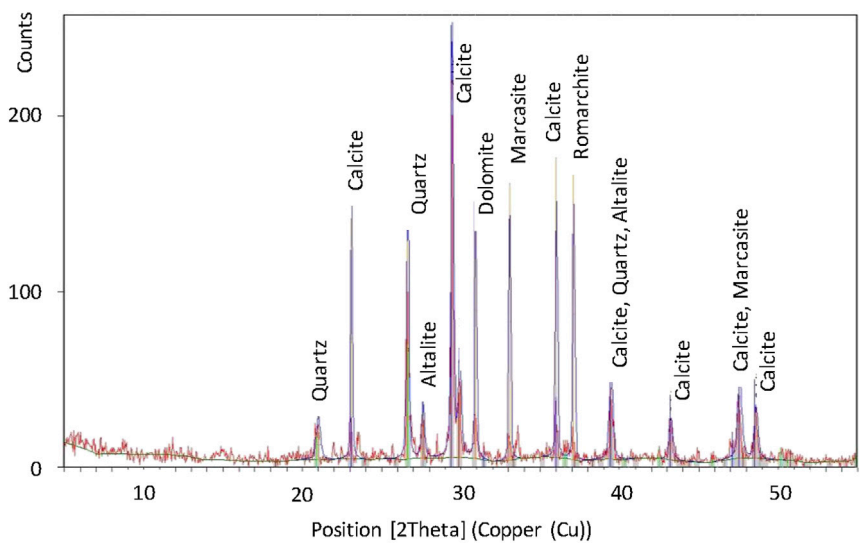

FIGURE 1 | XRD profile result of the tailings sample.

Table 3 lists the results of the ICP-MS analysis in the solids and process water of the tailings materials. Samples includes relatively high quantities of CaO, Fe_2O_3, Zn, Pb, and K. The XRD results (**Figure 1**) are the good agreement with these findings. In addition, the sulfurous contents were high in both dry materials and tailings water according to the ICP-MS test. Earlier studies have shown that a chemical reaction occurs in the presence of sulfate and acid production and that as a consequence, the mechanical strength of the backfill material decreases (Hamberg et al., 2017; Cao et al., 2019; Li et al., 2019).

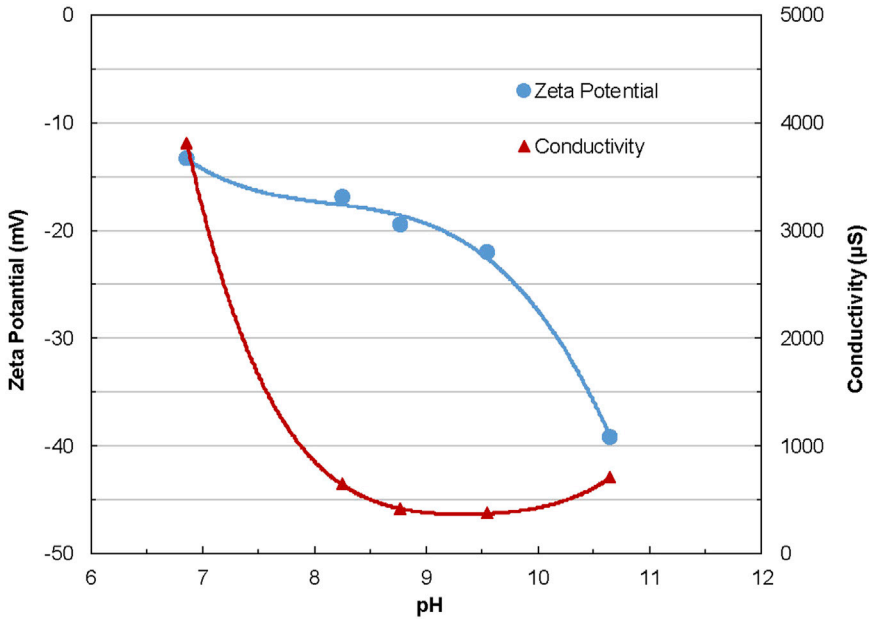

FIGURE 2 | Conductivity and the zeta potential profile of the tailings sample.

Consequently, it can be expected that the sulfate ions affect the cement applications negatively.

The binding of water molecules to fine particles at high zeta potential values provides high retention of paste backfill in a slump. The dry paste's zeta potential was negative. The negative character of dry paste was influenced by the relative abundance of Si^{4+}, Al^{3+}, Ca^{2+}, K^{+}, and Mg^{2+} ions dissolved from the tailings. The zeta potential results of the tailings sample as a function of pH are given in **Figure 2**. It is clear from **Figure 2** that the zeta potential became more negative with the increasing pH. As the zeta potential of the particles becomes more negative with the increasing pH, the electrostatic repulsion forces increase.

Thus, the particles repel each other. OH^{-} ion increase resulting from the pH rise caused zeta potential increase negatively. This proves that OH^{-} is the potential determining ion and will assist in the uniform distribution of particles in the CPB matrix. This refers that the tailings are electro-kinetically stable, and the particles will be easily dispersed in the tailings. These results clearly show that the zeta potential-pH relationship plays a critical role in the stability and homogeneous distribution of paste backfill.

Considering the favorable pH range (pH 6–9) in the relevant regulation (Turkish Official Gazette: No. 25687) to discharge, it can be stated that the tested tailings-based material is in the stable zone (above 25 mV) at pH values above 9. The increase in the pH of the material with the addition of cement contributes to the backfill's stability in the stable zone, and therefore to the homogeneous distribution of the particles in the paste backfill matrix. In addition, the zeta potential results can be utilized to identify the type of anionic or cationic chemicals present for further studies. There are two main reasons why the conductivity (**Figure 2**) values were high at low pH levels. First, high concentrations of NaOH were used to increase the pH of the medium and the second reason is the excessive Ca^{2+}, K^{+}, and Mg^{2+} ions. It can also infer from the zeta potential and conductivity results (**Figure 2**) that since pH became more negative with increasing pH, OH^{-} ions are the potential determining ions.

The pH profile results are seen in **Figure 3**. As seen in **Figure 3**, buffering tended to bring the environmental pH to around 8.5–9 within the first 10 min. It was observed that this tendency occurs faster in the acidic medium and more slowly in the basic medium. Consequently, one can understand that the material possesses a buffering feature and tended to remain stable in this range. This means that the tailings will remain within the allowable pH limits (pH 6–9) of the wastewater discharge range for the mining industry specified in the regulations (Turkish Official Gazette No: 25,687), even when exposed to the effects of rainwater and groundwater. It can be inferred from the zeta potential and pH profile results that ion movement occurs in the material. The use of lime to suppress the acidity of the tailings is one of the reasons for the excessive Ca^{2+} and OH^{-} ions.

UCS Test Results of Cemented Backfill Samples

Figure 4 indicates the results of the UCS test results. It is clear that the UCS test samples became brittle and dispersions occurred as a result of the decreased cement content (3 wt%). The maximum UCS values (700 kPa) were obtained with 7 wt% CEMIV cement ratio at 28 curing days while the UCS values are varying between 0.05 and 4.35 MPa in previous studies (Jiang et al., 2020; Liu et al., 2020). Besides, the lowest UCS values (250 kPa after 28 days) were obtained with 3 wt% CEM IV cement. The results showed

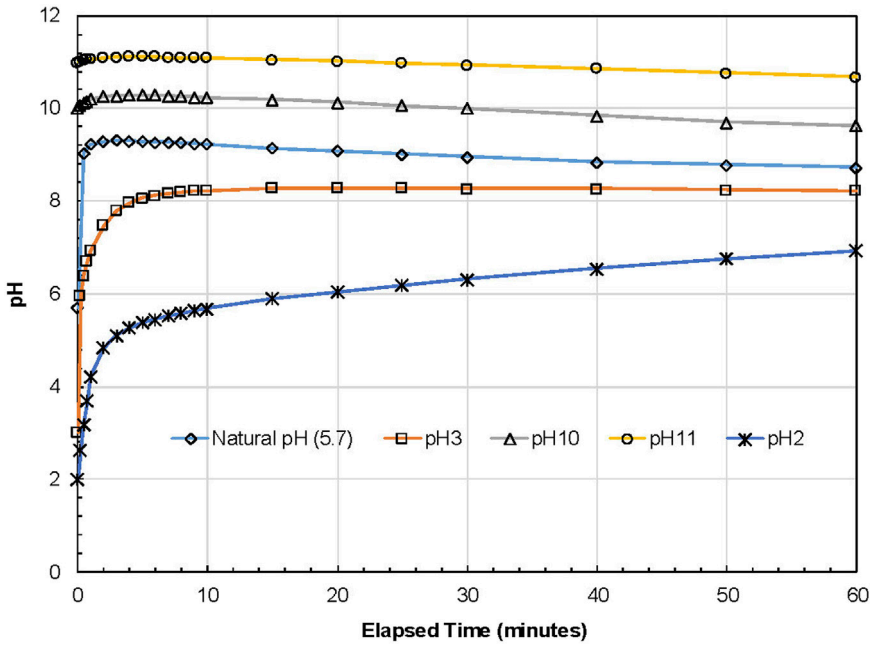

FIGURE 3 | pH profile results for the tested mine tailings.

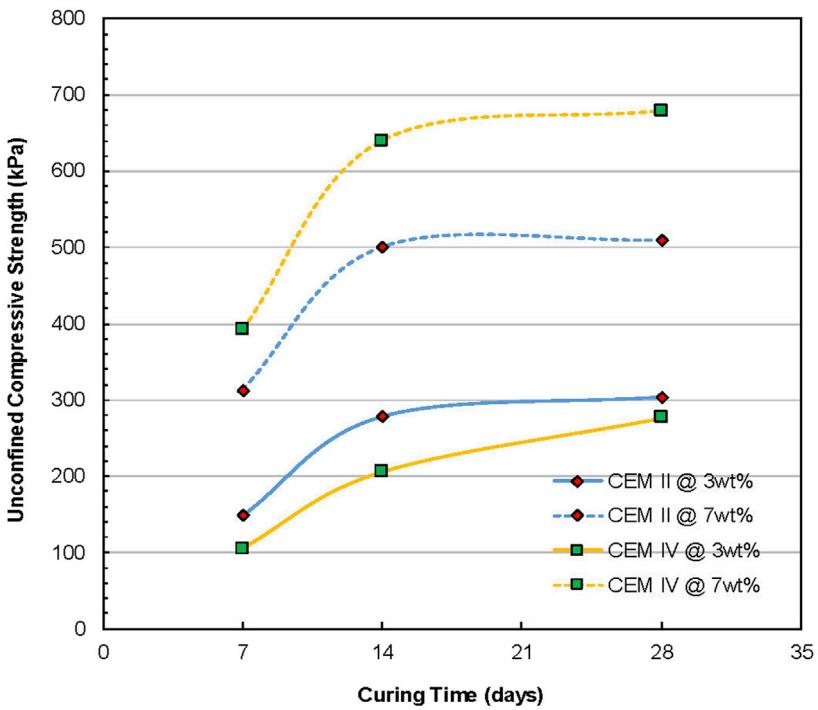

FIGURE 4 | UCS test results of different CPB samples as a function of curing time.

that there was no major difference between OPC and blended cement in the sulfur-rich CPB, in line with the reference (Li & Fall 2016).

The elemental analysis by combustion, ion chromatography, and SEM were performed to investigate the sulfurous compounds, ion release, and their effects on ettringite

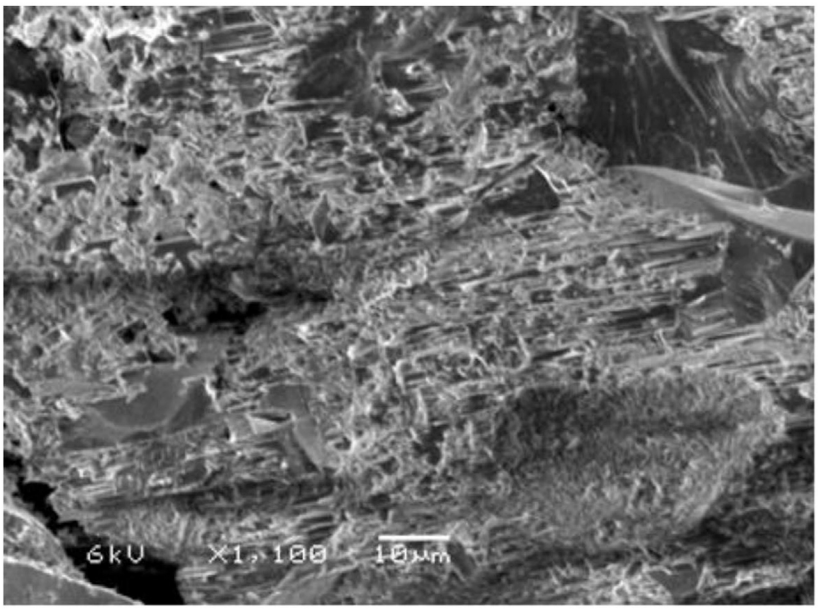

FIGURE 5 | The SEM micrograph of the tested CPB sample.

occurrence. The elemental analysis by combustion and ion chromatography were carried out to define the amount of sulfur in the ettringite. Meanwhile, the use of combustion tests was investigated to determine the total sulfur in the concrete that causes the SO_3 and SO_4 movement. It is important to identify the combustion temperature is vital to obtaining the maximum sulfur ratio. Jiménez and Prieto (Jiménez & Prieto, 2015) investigated the dehydration of ettringite in natural and synthetic samples and showed that the total weight loss in the thermo-gravimetric analysis at 1,000°C was 45.5 and 40.5% for natural and synthetic samples, respectively. It was also stated that for synthetic samples, total weight losses of 32.6 and 35.6% were obtained at the temperatures of 190–300 and 650–800°C, respectively due to the decomposition of calcite at calcination temperature. Moreover, the temperatures of 300, 600, 800, 1,000, and 1,350°C were tested with 0.5 and 1.0 g samples. As a result, it was observed that the backfill sample melted at 1,350°C, and the highest sulfur amount was achieved at 1,000 °C with an amount of 0.5 g.

Analysis of Relationship Between UCS and Total Sulfur by Combustion Tests and SEM

Figure 5 demonstrates the SEM micrograph of CPB samples. Meanwhile, the results of the elemental analysis by combustion tests in **Figure 6** and the ion analysis in **Figure 7** indicated that the reason for the low UCS values (<1 MPa); It is due to sulfur ion mobility over the formation of ettringite within the cemented tailings. These consequences are compatible with the findings of Wang et al. (Wang et al., 2020).

It is clear from **Figure 6** that the expected benefit from cement is realized as the curing time of concrete in two cement types and at different rates increases. The amount of sulfur in CPB samples decreased and the corresponding mechanical strength increased. The fact that the CaO content in CEM II cement type is higher than CEM IV cement type suggests that secondary gypsum ($CaSO_4\_2H_2O$) minerals may occur more within the cemented backfills.

Analysis of Relationship Between UCS and Sulfate by Ion Analysis

When the results of the total sulfur and sulfate tests are compared, it can be seen that increasing the cement content from 3 to 7 wt% diminished the total sulfur amounts due to the residual stiffness. Similarly, the sulfate dispersion in the concrete was reduced due to the stiff structure when the cement amount was increased. The relationship between the obtained results and UCS is given in **Figure 7**.

It is apparent from **Figure 7** that 3 wt% CPB samples containing CEM IV cement type provides the low mechanical strengths. This is mainly due to the high amount of Al in this cement at high sulfate content and the high formation of ettringite ($3CaSO_4\_3CaO\_Al_2O_3\_32H_2O$) with high expansion potential. In high cement quantities, as the curing time increases, the mobility of sulfate within the CPB sample and its conversion to ettringite will slow down.

Analysis of Time-dependent Sulfate and Sulfur Concentrates

Figure 8 demonstrates the relationship of the change in the sulfur and sulfate contents of CPB samples as a function of curing time. It is clear from **Figure 8** that sulfur tends to decrease continuously due to the effect of added cement and slaked lime within CPB samples. On the other hand, the sulfate content tends to increase

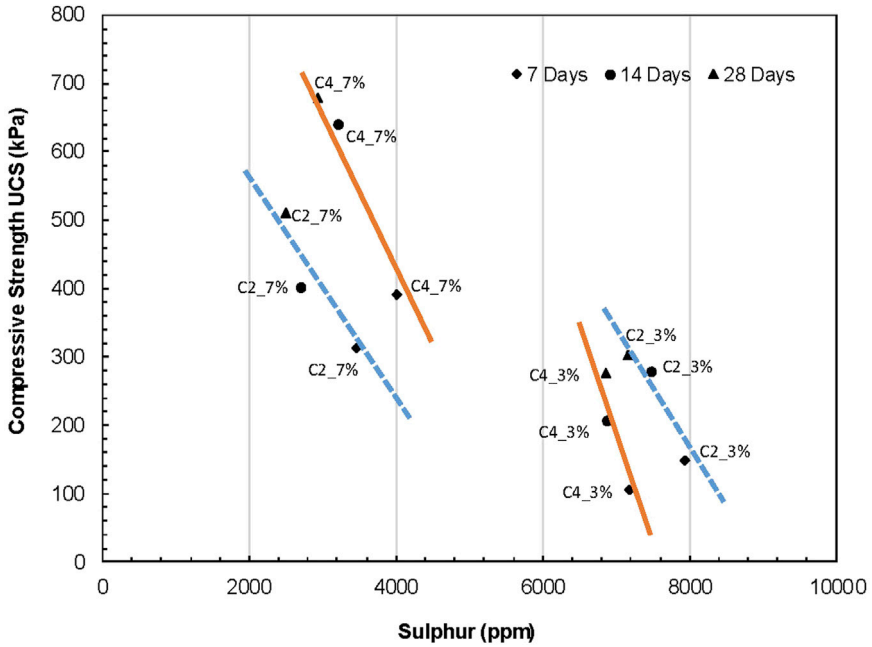

FIGURE 6 | The relationship between the UCS and total sulfur results (by combustion).

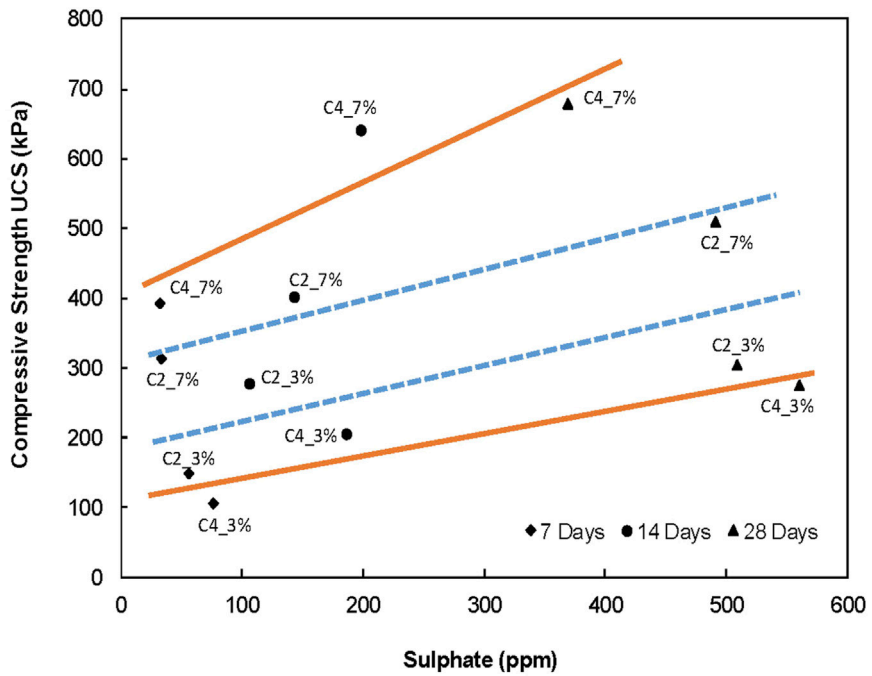

FIGURE 7 | The relationship between UCS and sulfate results (by ion analysis).

continuously, especially from the 7th day. Both findings are compatible with Li et al. (Li et al., 2019).

In the cementitious matrices subjected to sulfate attack, the amount of sulfate ions decreases as the reaction and curing time continues and thus the rate of sulfate attack is inclined to decelerate. The mineral phases (ettringite and gypsum) resulting from the reactions of sulfates with hydration products play a vital role on strength and quality of CPB samples (Gu et al., 2019). The formation of ettringite could generate expansive pressure that tangibly harms CPB samples.

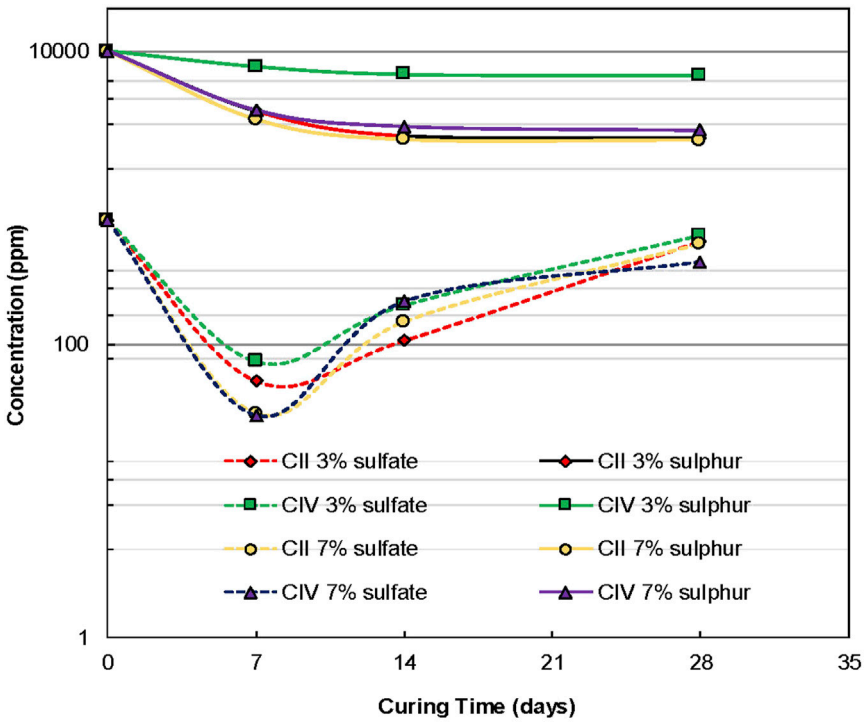

FIGURE 8 | Time-dependent sulfate (by ion analysis) and sulfur (by combustion) concentrations.

In the presence of sulfates, calcium hydroxide created during the cement hydration can lead to the making of gypsum (a source of strength degradation) in CPB.

CONCLUSION

In this study, the usability of Pb-Zn processing tailings in the paste backfill form was investigated experimentally. Several laboratory experiments such as unconfined compressive strength, particle size distribution, pH measurements, elemental analysis by combustion, ion chromatography, SEM, and the zeta potential were undertaken on CPB samples. From the performed experimental tests, the following main findings could be drawn:

✓ Although the tailings were mixed with blended cement, the mechanical strengths of paste backfill were relatively low due to expansive components and internal sulfate attack.
✓ The gypsum problem also occurred in the samples, as discovered by the SEM analysis.
✓ As the amount of sulfur within the paste backfill material decreased and the sulfate contents and mechanical strengths increased.
✓ The CEM IV type cement with a dosage of 7 wt% yielded higher UCS values than the CEM II type cement with a dosage of 3 wt%.
✓ From the SEM images, one can conclude that the increase in the sulfate content was due to the formation of ettringite, which caused the strengths to remain at relatively low values.

As a result of this study, it is suggested that the combustion test will give fast and accurate results for future CPB applications. In today's CPB applications, especially in high sulfur mines, it is predicted that the use of cement at high dosages (greater than a cement dosage of 7 wt%) and fast setting time can prevent the formation of secondary gypsum mineral and ettringite.

DATA AVAILABILITY STATEMENT

The raw data supporting the conclusion of this article will be made available by the authors, without undue reservation.

AUTHOR CONTRIBUTIONS

UA and KC conceived and designed the experiments and samples; UA prepared samples and performed the tests; UA, KC, and EY analyzed the data, UA and KC wrote the manuscript, UA and EY revised the manuscript. All authors read and approved the final manuscript.

FUNDING

This research was supported by The Scientific Research Projects Coordination Unit of Istanbul University–Cerrahpasa (Grant number: 40,888). Special acknowledgements are extended to Prof. Dr. Nuray Tokgoz for her precious contributions.

REFERENCES

Alainachi, I., and Fall, M. (2020). Chemically Induced Changes in the Geotechnical Response of Cementing Paste Backfill in Shaking Table Test. *J. Rock Mech. Geotechnical Eng.* 13 (3), 513–528. doi:10.1016/j.jrmge.2020.11.002

Baquerizo, L. G., Matschei, T., and Scrivener, K. L. (2016). Impact of Water Activity on the Stability of Ettringite. *Cement Concrete Res.* 79, 31–44. doi:10.1016/j.cemconres.2015.07.008

Belebchouche, C., Moussaceb, K., and Aït-Mokhtar, A. (2016). Evaluation of the Encapsulation of Nickel, Chromium and Lead-Rich Wastes in Cement Matrices by TCLP Test. *Eur. J. Environ. Civil Eng.* 20 (7), 711–724. doi:10.1080/19648189.2015.1061458

Cao, S., Xue, G., Yilmaz, E., and Yin, Z. (2021). Assessment of Rheological and Sedimentation Characteristics of Fresh Cemented Tailings Backfill Slurry. *Int. J. Mining, Reclamation Environ.* 35, 319–335. doi:10.1080/17480930.2020.1826092

Cao, S., Xue, G., Yilmaz, E., Yin, Z., and Yang, F. (2021). Utilizing Concrete Pillars as an Environmental Mining Practice in Underground Mines. *J. Clean. Prod.* 278, 123433. doi:10.1016/j.jclepro.2020.123433

Cao, S., Yilmaz, E., Song, W., and Xue, G. (2019). Assessment of Acoustic Emission and Triaxial Mechanical Properties of Rock-Cemented Tailings Matrix Composites. *Adv. Mater. Sci. Eng.* 2019, 1–12. doi:10.1155/2019/6742392

Cavusoglu, I., Yilmaz, E., and Yilmaz, A. O. (2021). Additivity Effect on Properties of Cemented Coal Fly Ash Backfill Containing Water-Reducing Admixtures. *Construction Building Mater.* 267, 121021. doi:10.1016/j.conbuildmat.2020.121021

Chen, Q., Tao, Y., Feng, Y., Zhang, Q., and Liu, Y. (2021). Utilization of Modified Copper Slag Activated by Na2SO4 and CaO for Unclassified Lead/Zinc Mine Tailings Based Cemented Paste Backfill. *J. Environ. Manage.* 290, 112608. doi:10.1016/j.jenvman.2021.112608

Chen, X., Shi, X., Zhou, J., Du, X., Chen, Q., and Qiu, X. (2019). Effect of Overflow Tailings Properties on Cemented Paste Backfill. *J. Environ. Manage.* 235, 133–144. doi:10.1016/j.jenvman.2019.01.040

Elghali, A., Benzaazoua, M., Bouzahzah, H., Abdelmoula, M., Dynes, J. J., and Jamieson, H. E. (2021). Role of Secondary Minerals in the Acid Generating Potential of Weathered Mine Tailings: Crystal-Chemistry Characterization and Closed Mine Site Management Involvement. *Sci. Total Environ.* 784, 147105. doi:10.1016/j.scitotenv.2021.147105

Gu, Y., Martin, R.-P., Omikrine Metalssi, O., Fen-Chong, T., and Dangla, P. (2019). Pore Size Analyses of Cement Paste Exposed to External Sulfate Attack and Delayed Ettringite Formation. *Cement Concrete Res.* 123, 105766. doi:10.1016/j.cemconres.2019.05.011

Hamberg, R., Maurice, C., and Alakangas, L. (2017). Lowering the Water Saturation Level in Cemented Paste Backfill Mixtures - Effect on the Release of Arsenic. *Minerals Eng.* 112, 84–91. doi:10.1016/j.mineng.2017.05.005

Hefni, M., and Ali, M. A. (2021). The Potential to Replace Cement with Nano-Calcium Carbonate and Natural Pozzolans in Cemented Mine Backfill. *Adv. Civil Eng.* 2021, 1–10. doi:10.1155/2021/5574761

Huan, C., Zhu, C., Liu, L., Wang, M., Zhao, Y., Zhang, B., et al. (2021). Pore Structure Characteristics and its Effect on Mechanical Performance of Cemented Paste Backfill. *Front. Mater.* 8, 700917. doi:10.3389/fmats.2021.700917

Jiang, D., Li, X., Jiang, W., Li, C., Lv, Y., and Zhou, Y. (2020). Effect of Tricalcium Aluminate and Sodium Aluminate on Thaumasite Formation in Cement Paste. *Construction Building Mater.* 259, 119842. doi:10.1016/j.conbuildmat.2020.119842

Jiang, H., Fall, M., Yilmaz, E., Li, Y., and Yang, L. (2020). Effect of Mineral Admixtures on Flow Properties of Fresh Cemented Paste Backfill: Assessment of Time Dependency and Thixotropy. *Powder Technol.* 372, 258–266. doi:10.1016/j.powtec.2020.06.009

Jiang, H., Han, J., Li, Y., Yilmaz, E., Sun, Q., and Liu, J. (2020). Relationship between Ultrasonic Pulse Velocity and Uniaxial Compressive Strength for Cemented Paste Backfill with Alkali-Activated Slag. *Nondestructive Test. Eval.* 35 (4), 359–377. doi:10.1080/10589759.2019.1679140

Jiménez, A., and Prieto, M. (2015). Thermal Stability of Ettringite Exposed to Atmosphere: Implications for the Uptake of Harmful Ions by Cement. *Environ. Sci. Technol.* 49 (13), 7957–7964. doi:10.1021/acs.est.5b00536

Koohestani, B., Darban, A. K., Darezereshki, E., Mokhtari, P., Yilmaz, E., and Yilmaz, E. (2018). The Influence of Sodium and Sulfate Ions on Total Solidification and Encapsulation Potential of Iron-Rich Acid Mine Drainage in Silica Gel. *J. Environ. Chem. Eng.* 6 (2), 3520–3527. doi:10.1016/j.jece.2018.05.037

Koohestani, B., Darban, A. K., Mokhtari, P., Darezereshki, E., Yilmaz, E., and Yilmaz, E. (2020). Influence of Hydrofluoric Acid Leaching and Roasting on Mineralogical Phase Transformation of Pyrite in Sulfidic Mine Tailings. *Minerals* 10 (6), 513. doi:10.3390/min10060513

Koohestani, B., Mokhtari, P., Yilmaz, E., Mahdipour, F., and Darban, A. K. (2021). Geopolymerization Mechanism of Binder-free Mine Tailings by Sodium Silicate. *Construction Building Mater.* 268, 121217. doi:10.1016/j.conbuildmat.2020.121217

Kou, Y., Jiang, H., Ren, L., Yilmaz, E., and Li, Y. (2020). Rheological Properties of Cemented Paste Backfill with Alkali-Activated Slag. *Minerals* 10 (3), 288. doi:10.3390/min10030288

Levio-Raiman, M., Briceño, G., Schalchli, H., Bornhardt, C., and Diez, M. C. (2021). Alternative Treatment for Metal Ions Removal from Acid Mine Drainage Using an Organic Biomixture as a Low Cost Adsorbent. *Environ. Technol. Innovation* 24, 101853. doi:10.1016/j.eti.2021.101853

Li, J., Yilmaz, E., and Cao, S. (2020). Influence of Solid Content, Cement/Tailings Ratio, and Curing Time on Rheology and Strength of Cemented Tailings Backfill. *Minerals* 10 (10), 922. doi:10.3390/min10100922

Li, W., and Fall, M. (2016). Sulphate Effect on the Early Age Strength and Self-Desiccation of Cemented Paste Backfill. *Construction Building Mater.* 106, 296–304. doi:10.1016/j.conbuildmat.2015.12.124

Li, Y., Min, X., Ke, Y., Fei, J., Liu, D., and Tang, C. (2019). Immobilization Potential and Immobilization Mechanism of Arsenic in Cemented Paste Backfill. *Minerals Eng.* 138, 101–107. doi:10.1016/j.mineng.2019.04.041

Libos, I. L. S., and Cui, L. (2020). Effects of Curing Time, Cement Content, and Saturation State on Mode-I Fracture Toughness of Cemented Paste Backfill. *Eng. Fracture Mech.* 235, 107174. doi:10.1016/j.engfracmech.2020.107174

Liu, L., Xin, J., Huan, C., Qi, C., Zhou, W., and Song, K.-I. (2020). Pore and Strength Characteristics of Cemented Paste Backfill Using Sulphide Tailings: Effect of Sulphur Content. *Construction Building Mater.* 237, 117452. doi:10.1016/j.conbuildmat.2019.117452

Liu, L., Xin, J., Qi, C., Jia, H., and Song, K.-I. (2020). Experimental Investigation of Mechanical, Hydration, Microstructure and Electrical Properties of Cemented Paste Backfill. *Construction Building Mater.* 263, 120137. doi:10.1016/j.conbuildmat.2020.120137

Lu, H., Qi, C., Chen, Q., Gan, D., Xue, Z., and Hu, Y. (2018). A New Procedure for Recycling Waste Tailings as Cemented Paste Backfill to Underground Stopes and Open Pits. *J. Clean. Prod.* 188, 601–612. doi:10.1016/j.jclepro.2018.04.041

Mafra, C., Bouzahzah, H., Stamenov, L., and Gaydardzhiev, S. (2020). Insights on the Effect of Pyrite Liberation Degree upon the Acid Mine Drainage Potential of Sulfide Flotation Tailings. *Appl. Geochem.* 123, 104774. doi:10.1016/j.apgeochem.2020.104774

Myagkaya, I. N., Lazareva, E. V., Zaikovskii, V. I., and Zhmodik, S. M. (2020). Interaction of Natural Organic Matter with Acid Mine Drainage: Authigenic Mineralization (Case Study of Ursk Sulfide Tailings, Kemerovo Region, Russia). *J. Geochemical Exploration* 211, 106456. doi:10.1016/j.gexplo.2019.106456

Nordstrom, D. K., Blowes, D. W., and Ptacek, C. J. (2015). Hydrogeochemistry and Microbiology of Mine Drainage: An Update. *Appl. Geochem.* 57, 3–16. doi:10.1016/j.apgeochem.2015.02.008

Othmani, M. A., Souissi, F., Bouzahzah, H., Bussière, B., da Silva, E. F., and Benzaazoua, M. (2015). The Flotation Tailings of the Former Pb-Zn Mine of Touiref (NW Tunisia): Mineralogy, Mine Drainage Prediction, Base-Metal Speciation Assessment and Geochemical Modeling. *Environ. Sci. Pollut. Res.* 22, 2877–2890. doi:10.1007/s11356-014-3569-1

Park, I., Tabelin, C. B., Jeon, S., Li, X., Seno, K., Ito, M., et al. (2019). A Review of Recent Strategies for Acid Mine Drainage Prevention and Mine Tailings Recycling. *Chemosphere* 219, 588–606. doi:10.1016/j.chemosphere.2018.11.053

Qi, C., and Fourie, A. (2019). Cemented Paste Backfill for Mineral Tailings Management: Review and Future Perspectives. *Minerals Eng.* 144, 106025. doi:10.1016/j.mineng.2019.106025

Shirin, S., Jamal, A., Emmanouil, C., and Yadav, A. K. (2021). Assessment of Characteristics of Acid Mine Drainage Treated with Fly Ash. *Appl. Sci.* 11, 3910. doi:10.3390/app11093910

Wang, S., Song, X., Wei, M., Liu, W., Wang, X. X., Ke, Y., et al. (2021). Experimental Study on the Effect of Alkalized Rice Straw Content on Mechanical Properties of Cemented Tailings Backfill. *Front. Mater.* (In-press). doi:10.3389/fmats.2021.727925

Wang, Y., Cao, Y., Cui, L., Si, Z., and Wang, H. (2020). Effect of External Sulfate Attack on the Mechanical Behavior of Cemented Paste Backfill. *Construction Building Mater.* 263, 120968. doi:10.1016/j.conbuildmat.2020.120968

Xiapeng, P., Fall, M., and Haruna, S. (2019). Sulphate Induced Changes of Rheological Properties of Cemented Paste Backfill. *Minerals Eng.* 141, 105849. doi:10.1016/j.mineng.2019.105849

Xu, W., Chen, W., Tian, M., and Guo, L. (2021). Effect of Temperature on Time-dependent Rheological and Compressive Strength of Fresh Cemented Paste Backfill Containing Flocculants. *Construction Building Mater.* 267, 121038. doi:10.1016/j.conbuildmat.2020.121038

Xue, G., Yilmaz, E., Song, W., and Cao, S. (2020). Fiber Length Effect on Strength Properties of Polypropylene Fiber Reinforced Cemented Tailings Backfill Specimens with Different Sizes. *Construction Building Mater.* 241, 118113. doi:10.1016/j.conbuildmat.2020.118113

Yan, B., Zhu, W., Hou, C., Yilmaz, E., and Saadat, M. (2020). Characterization of Early Age Behavior of Cemented Paste Backfill through the Magnitude and Frequency Spectrum of Ultrasonic P-Wave. *Construction Building Mater.* 249, 118733. doi:10.1016/j.conbuildmat.2020.118733

Yang, L., Xu, W., Yilmaz, E., Wang, Q., and Qiu, J. (2020). A Combined Experimental and Numerical Study on the Triaxial and Dynamic Compression Behavior of Cemented Tailings Backfill. *Eng. Structures* 219, 110957. doi:10.1016/j.engstruct.2020.110957

Zhao, D. (2021). Reactive MgO-Modified Slag-Based Binders for Cemented Paste Backfill and Potential Heavy-Metal Leaching Behavior. *Construction Building Mater.* 298, 123894. doi:10.1016/j.conbuildmat.2021.123894

Zheng, J., Guo, L., SunLi, X. W., Li, W., and Jia, Q. (2018). Study on the Strength Development of Cemented Backfill Body from Lead-Zinc Mine Tailings with Sulphide. *Adv. Mater. Sci. Eng.* 2018, 1–8. doi:10.1155/2018/7278014

Zheng, J., Guo, L., and Zhao, Z. (2017). Effect of Calcined Hard Kaolin Dosage on the Strength Development of CPB of Fine Tailings with Sulphide. *Adv. Mater. Sci. Eng.* 2017, 1–7. doi:10.1155/2017/8631074

Conflict of Interest: The authors declare that the research was conducted in the absence of any commercial or financial relationships that could be construed as a potential conflict of interest.

Publisher's Note: All claims expressed in this article are solely those of the authors and do not necessarily represent those of their affiliated organizations, or those of the publisher, the editors and the reviewers. Any product that may be evaluated in this article, or claim that may be made by its manufacturer, is not guaranteed or endorsed by the publisher.

frontiers in Materials

REVIEW
published: 28 September 2021
doi: 10.3389/fmats.2021.759126

Multiscale Geomechanical Behavior of Fiber-Reinforced Cementitious Composites Under Cyclic Loading Conditions—A Review

Javaugh McLean[1,2] *and Liang Cui*[1,2]*

[1]Department of Civil Engineering, Lakehead University, Thunder Bay, ON, Canada, [2]State Key Laboratory of Geohazard Prevention and Geoenvironment Protection, Chendu, China

As construction materials, cementitious composites such as cemented paste backfill (CPB), cemented soil, and concrete may be subjected to extreme dynamic loadings including impact, blast, and/or seismic loads during their service life. To improve mechanical performance under dynamic loadings, fiber reinforcement technique has been considered a promising approach and extensively used in practice. In this manuscript, a new perspective on the multiscale geomechanical behavior of fiber-reinforced cementitious composites (FRCC) is provided through a comprehensive review on the macroscale constitutive behavior and the associated mechanical properties, and microscale failure processes under cyclic tensile, shear, and compressive loading conditions. For the macroscale mechanical response, this review includes a detailed analysis of the state-of-the-art research in stress-strain behaviors including pre- and post-peak response and hysteretic behaviors. Moreover, the effects of pore water pressure on the dynamic response of soft FRCCs such as CPB are discussed. Furthermore, the link between microscale crack propagation (including the formation of the interfacial transition zone and fracture process zone) and damage accumulation is established for each type of cyclic loading condition. In addition, a critical discussion on the future development of fiber reinforcement is conducted as well. Therefore, this review not only offers guidance and references to the experimental investigation on the multiscale behavior of FRCCs under cyclic loadings, but also promotes the further development of fiber reinforcement techniques.

Keywords: multiscale, fiber reinforcement, cyclic loading, cementitious materials, crack propagation

OPEN ACCESS

Edited by:
Erol Yilmaz,
Recep Tayyip Erdoğan University, Turkey

Reviewed by:
Lijie Guo,
Beijing General Research Institute of Mining and Metallurgy, China
Hasan Eker,
Karabük University, Turkey
Jingping Qiu,
School of Resources and Civil Engineering, Northeastern University, China

***Correspondence:**
Liang Cui
liang.cui@lakeheadu.ca

Specialty section:
This article was submitted to Structural Materials, a section of the journal Frontiers in Materials

Received: *15 August 2021*
Accepted: *06 September 2021*
Published: *28 September 2021*

Citation:
McLean J and Cui L (2021) Multiscale Geomechanical Behavior of Fiber-Reinforced Cementitious Composites Under Cyclic Loading Conditions—A Review. Front. Mater. 8:759126. doi: 10.3389/fmats.2021.759126

INTRODUCTION

As a type of construction material, cementitious composites are commonly subjected to complex field loading conditions during their service life (Cui and Fall, 2015; Wu et al., 2016; Lin et al., 2020; Xu et al., 2020). As a result, the external loadings may cause the development of compressive, tensile and/or shear stresses in the porous mixture and thus dominate the failure processes at the macroscale (Xu et al., 2019; Libos and Cui, 2020; Liu et al., 2020). However, irrespective of the external loading conditions, the crack initiation is commonly associated with the local stress concentration near defects at the microscale (Wang et al., 2021b). Since mechanical stability is one of the most critical design criteria, cementitious composites are required to offer adequate stress resistance and sufficient

tolerance for permanent deformation in engineering applications. However, as a type of brittle material, cementitious composites such as cemented paste backfill (CPB), cemented soil, and concrete are commonly featured by the limited strain-hardening behavior and weak post-peak performance (Cui and Fall, 2016b; Li et al., 2018b). To improve the mechanical behavior and properties of cementitious composites, it has been found that reinforcement through the addition of short fibers is a promising technique (Dönmez et al., 2020; Cao et al., 2021; Huang et al., 2021b; Külekçi, 2021; Xue et al., 2021). This is because fibers in cementitious materials are able to produce the bridging forces across cracks in the porous matrix (Cao et al., 2019; Xue et al., 2019; Cao et al., 2020; Huang et al., 2021b), thus, acting as crack arresters at the microscale. Correspondingly, the fiber-reinforced cementitious composites (FRCC) can withstand larger plastic deformation and improve material ductility (Li et al., 2018b; Cao et al., 2020). Subsequently, the macroscale stress-strain behavior, especially post-peak behavior, can be considerably improved and becomes more favorable for engineering applications. Therefore, understanding of multiscale geomechanical behaviors of FRCC plays a key role in the safe and optimum design of FRCC.

However, the performance of FRCC is dependent on the in-service and environmental loading conditions. Previous studies show that FRCC can demonstrate distinct mechanical behaviors under monotonic and cyclic loadings (Boulekbache et al., 2016; Dönmez et al., 2020). For example, cyclic loading can cause a progressively decrease in load-carrying capacity of FRCC. Such degradation of load-carrying capacity can be partially attributed to cyclic loading-induced damage accumulation in the porous matrix (Hu et al., 2018). Therefore, the resultant material degradation causes a poor engineering performance of FRCC relative to that under quasi-static loading conditions. Furthermore, the fibers embedded into the matrix can suffer severe extrusion or even rupture during the cyclic loading process, which causes a reduction in the crack bridging capacity (Guo et al., 2020; Zhou et al., 2020). Consequently, FRCC could show different failure patterns, material properties, and constitutive behaviors under cyclic loading conditions. Accordingly, the obtained findings about the quasi-static behavior may be invalid for FRCC under cyclic loading conditions.

Additionally, FRCC may be subjected to various types of dynamic loadings in the field and thus cause different stresses inside the FRCC. For example, as one of the most critical components of a building structure, fiber-reinforced concrete columns such as bridge piers are designed to withstand large axial and shear forces, especially in seismic regions (Wang et al., 2019). Correspondingly, the resultant dynamic compressive and shear stresses govern the stability of FRCC. Furthermore, fiber-reinforced shotcrete (FRS) linings have been widely used in underground mines and civil tunnels to prevent the occurrence of many disasters such as caving, slabbing, and rockburst as a result of complex field loadings (Bernard, 2015; Qiu et al., 2020). As a result, FRS is commonly exposed to high tensile and compressive stresses due to vibrations from blasting operations, which may cause various dynamic failures such as the cracking of the shotcrete lining, failure along the shotcrete-rock interface, and flexural failure of the shotcrete (Sjölander et al., 2020). In addition, fiber reinforcement technique has attracted increasing attention in the optimal design of CPB used in the underground mines (Ma et al., 2016). Once placed into the underground excavations, the hardened backfilling materials are required to provide adequate secondary ground support and thus to maintain the stability of surrounding rock mass (Cui and Fall, 2017b; Cui and Fall, 2018; Wang et al., 2020). Consequently, multiaxial and complex stress states can arise in the backfilling materials (Yilmaz, 2018; Chen et al., 2019; Cui and Fall, 2019). Therefore, to improve the understanding of the multiscale geomechanical behaviors of FRCC under dynamic loadings, this study aims to provide a critical review of 1) the cyclic compressive, tensile, and shear behaviors, 2) the failure patterns, and 3) the mechanical properties of FRCC under cyclic loadings, which can benefit the safe and optimal design of FRCC under cyclic loading conditions (Rena et al., 2016). Future work related to the multiscale fiber reinforcement technique is also suggested through the identification of the research gap in this field of knowledge.

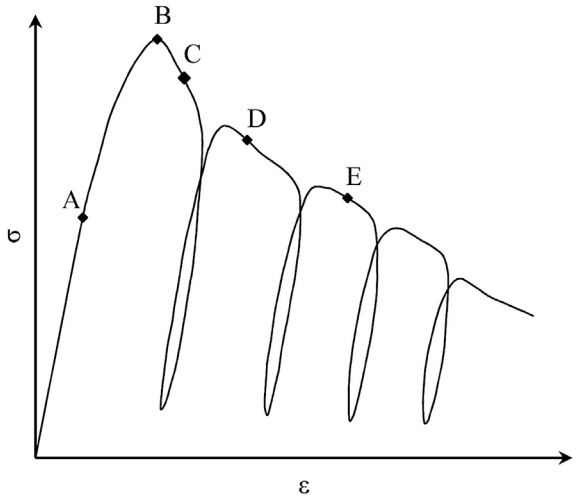

FIGURE 1 | Typical stress-strain curve of FRCC under cyclic tensile loading.

MULTISCALE GEOMECHANICAL BEHAVIOR OF FIBER-REINFORCED CEMENTITIOUS COMPOSITES UNDER CYCLIC LOADINGS

The constitutive behavior of FRCC is commonly evaluated by the stress-strain curves obtained from the conventional cyclic loading-unloading tests. This is because assessing the cyclic stress-strain curves could not only provide insight into the pre- and post-peak behavior of FRCC but also its mechanical properties. The obtained stress-strain behavior and mechanical properties can be directly used in the quantitative analysis such as

stability assessment and strength-based design of FRCC at field scale. In addition, the failure patterns can be identified by macroscale non-destructive evaluation methods such as ultrasound and digital image correlation (DIC) technique and microstructure observation analysis such as scanning electron microscopy (SEM) and X-ray computed tomography (CT) (Li et al., 2018a; Wu et al., 2019; Cao et al., 2021). To further understand the multiscale geomechanical behaviors of FRCC under dynamic loading conditions, a critical review is presented in the following subsections to provide deep insights into the cyclic tensile, shear, and compressive response of FRCC. More specifically, this paper focuses mainly on three aspects: the constitutive behavior, failure patterns, and the mechanical properties of FRCC under cyclic loading conditions.

Cyclic Tensile Behavior of Fiber-reinforced Cementitious Materials

Due to the effects of fiber reinforcement, the constitutive tensile behavior of FRCC under cyclic loading is featured by an ascending branch akin to the plain cementitious material and an enhanced post-peak branch (Liu et al., 2019). **Figure 1** represents a typical stress-strain curve that can be used to explain the damage process of FRCC under cyclic loading conditions. For the pre-peak behavior (path 0B), the material exhibits high elasticity making it difficult to spot the hysteretic loops (Li et al., 2018a). This is because the crack-bridging capacity of the fibers is not activated until the first crack appears; at first-crack stress, the cracks start to propagate in the porous matrix. However, the capacity of fibers bridging such cracks promotes the local stress concentration and causes the further propagation of microcracks. Moreover, point A (**Figure 1**) signals a transition point on the stress-strain curve from linear to non-linear regimes due to the multi-cracking characteristic afforded by the fibers. When the fibers in the weakest crack have failed, the crack localizes, and the material exhibits a softening behavior (Jun and Mechtcherine, 2010). Correspondingly, the peak point B (**Figure 1**) is followed by a noticeable stress drop with distinguished unloading and reloading paths that highlight the hysteretic behavior of FRCC under cyclic tensile loading (Boulekbache et al., 2016). However, in the post-peak region (paths CD and DE in **Figure 1**), fiber sliding, and pull-out mechanisms are the main contributors to the energy dissipation capacity of FRCC, which causes more defined hysteretic loops with increasing load cycles (Xu et al., 2018a). Conversely, the sudden drop after the peak stress is associated with the fracturing of the cementitious matrix. The cracks begin to propagate and coalesce into the main crack causing severe deformation of fibers, fracturing of fibers, and debonding of fibers with the continuously increasing displacement and loading cycles. Therefore, it has been widely accepted that fiber reinforcement in cementitious composites mainly affects the post-peak performance, specifically to transform the brittle nature of cementitious matrix to a more ductile one with improved mechanical properties (Pakravan and Ozbakkaloglu, 2019). In Particular, previous studies (Caverzan et al., 2012; Khlef et al., 2019) have successfully demonstrated the benefits of incorporating fibers into the cementitious matrix to improve the cyclic tensile behavior of FRCC. The results confirmed that the integration of fibers into cementitious matrix significantly improves peak stress, peak strain, ductility, and material toughness. Furthermore, the degradation rate of material properties such as stiffness is significantly alleviated by the inclusion of fibers with increasing volume fraction or aspect ratio (Chung et al., 2021).

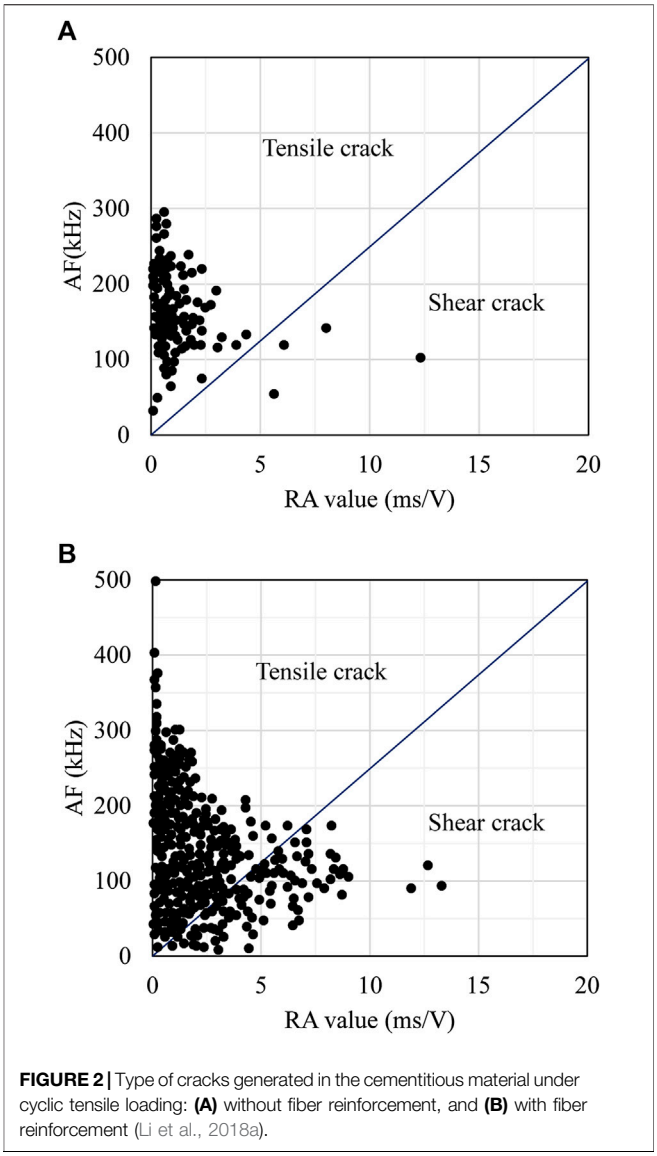

FIGURE 2 | Type of cracks generated in the cementitious material under cyclic tensile loading: **(A)** without fiber reinforcement, and **(B)** with fiber reinforcement (Li et al., 2018a).

In addition to the constitutive behavior of FRCC, understanding the bridging behavior and any synergy between these bridging mechanisms in FRCC is vital to determining its crack-restraining capabilities. The acoustic emission (AE) technique, as a non-destructive testing approach, has been widely adopted for the investigation of local damage in

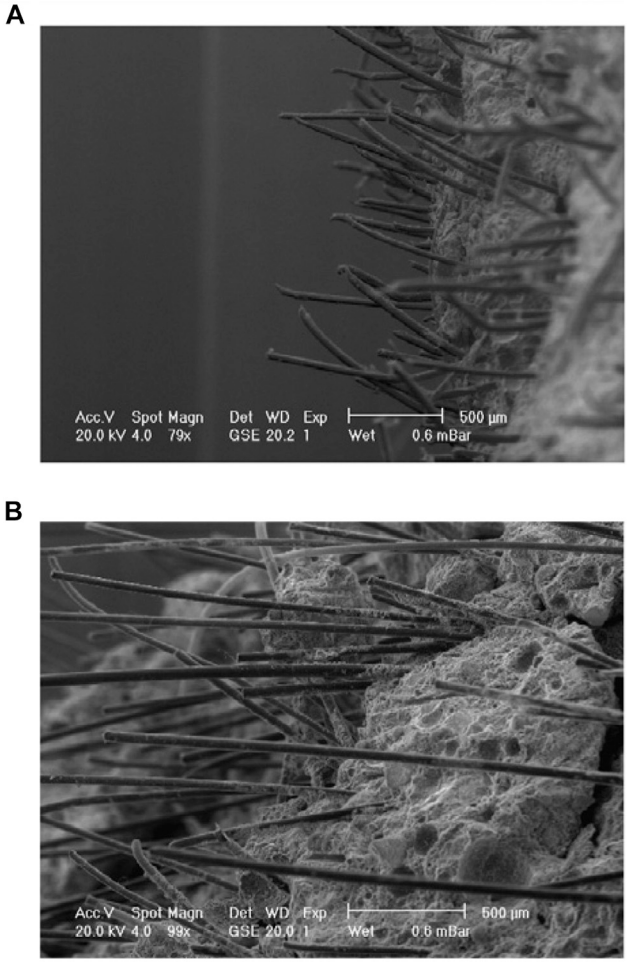

FIGURE 3 | Comparison of pullout lengths of fibers embedded in the cementitious materials under **(A)** monotonic loading, and **(B)** cyclic loading (Mechtcherine et al., 2011).

cementitious materials. This is because AE indices such as the average frequency and rise angle can be used to characterize the mode of cracking and quantify the damage level in FRCC (Aggelis et al., 2011). For example, Li et al. (2018a) and Aggelis (2011) utilized AE technique to investigate cracking modes of FRCC under cyclic tensile loadings. As shown in **Figure 2**, it has been found that compared with plain concrete FRCCs produce far more AE events and show clear signs of crack propagation due to the fiber reinforcement. Moreover, it has also been found that a cementitious composite subjected to complex loadings experiences tensile cracks in the initial stage of the damage process while shear cracks dominate in the later stages (Yuyama et al., 1999). In addition, Soulioti et al. (2009) described each fiber pull-out incident as a potential AE event, and these events increase with the fiber volume content, which clearly indicates the development of multiple cracking in the FRCCs. Furthermore, the failure patterns of FRCCs under cyclic tensile loading can be qualitatively analyzed by examining the pull-out length of fibers (**Figure 3**) and the crack surfaces (**Figure 4**) through SEM observation. In comparison to quasi-static experiments, fibers that pulled-out due to dynamic loading are approximately 91.6% longer with distinct wave-shaped textures in the axial direction, indicative of pronounced plastic deformation (Mechtcherine et al., 2011). This pronounced plastic deformation is a result of higher strain rates and higher crack opening velocities resulting in fiber-matrix debonding, destroyed fibers, and ultimately loosening of the microstructure due to pronounced micro-crack development (Müller and Mechtcherine, 2017). Moreover, several factors such as the bond strength between the fiber and the cementitious matrix, fiber aspect ratio, and matrix strength can contribute to the multiscale behavior of FRCC (Yu et al., 2018). Further investigations are necessary to fully understand the multiscale mechanical behavior of FRCC under cyclic tensile loading.

Cyclic Shear Behavior of Fiber-reinforced Cementitious Materials

Due to the incompatible material properties and the interfacial transition zone (ITZ) between fibers and cementitious matrix, the reinforcing effect mainly occurs in the post-cracking stages indicating that the pre-cracking response of FRCC is dominated by the cementitious matrix (Xu et al., 2018b). Therefore, to identify the characteristics of the cyclic shear behavior of FRCC, the focus of this review is placed on its post-cracking response. In the post-cracking stags, the cyclic shear response is highlighted by distinct constitutive behaviors: pinched hysteresis loops and accumulated volumetric plastic strain. The pinching of the strain curve (see **Figure 5**) is attributed to the combined effects of frictional resistance and stiffness degradation, respectively (Hung et al., 2013; Carnovale and Vecchio, 2014). This is because the inclusion of fibers not only increases the shear resistance through their dowel action and axial fiber stress (Claus, 2009) but also causes the multi-cracking behavior of the FRCC matrix. Although the multi-cracked matrix implies a stronger energy-dissipation ability and thus a higher load-carrying capacity, the generated multiple cracks inevitably cause a considerable reduction in the stiffness during the unloading process. Therefore, the stiffness degradation under cyclic shear loading contributes to a more pinched hysteresis loop (Pekoz and Pincheira, 2004; Festugato et al., 2013). However, the multiple cracks can offer a higher friction resistance for a given shear displacement, which indicates a higher energy dissipation capacity. In other words, the improved friction resistance by multiple cracks intends to increase the area of hysteresis loops and thus results in a more complex unloading/reloading behavior. It should be noted that the effectiveness of friction resistance along crack surfaces depends on the degree of crack closeness during the unloading/reloading process. For example, when stiff fibers such as steel fibers are adopted, the reinforcing fibers may prevent the cracks from closing and weakens the interface shear resistance (Toé Casagrande et al., 2006).

Another important characteristic of the cyclic shear response is the accumulation of volumetric plastic strain. For soft cementitious materials such as CPB, shear deformation causes volume changes (especially volume contraction) and increases

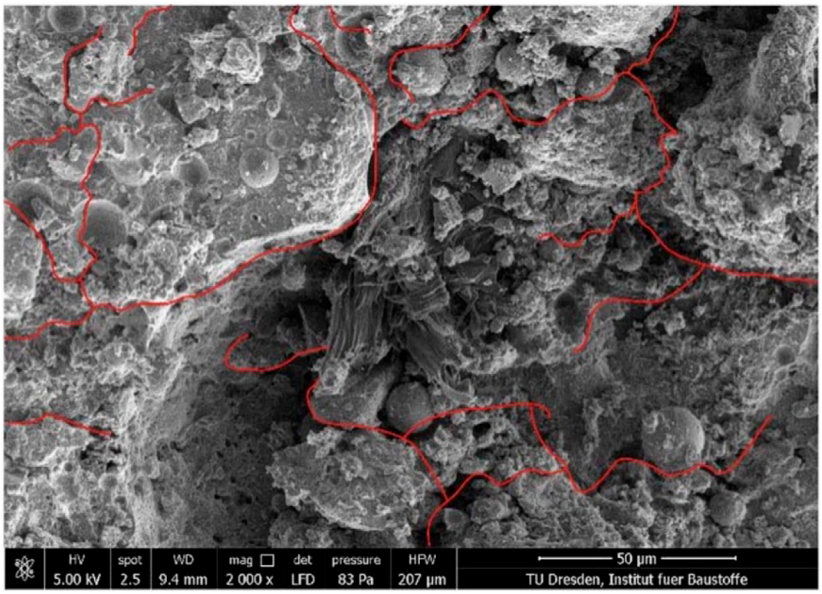

FIGURE 4 | Typical crack surfaces of FRCC under cyclic tensile loading (Müller and Mechtcherine, 2017).

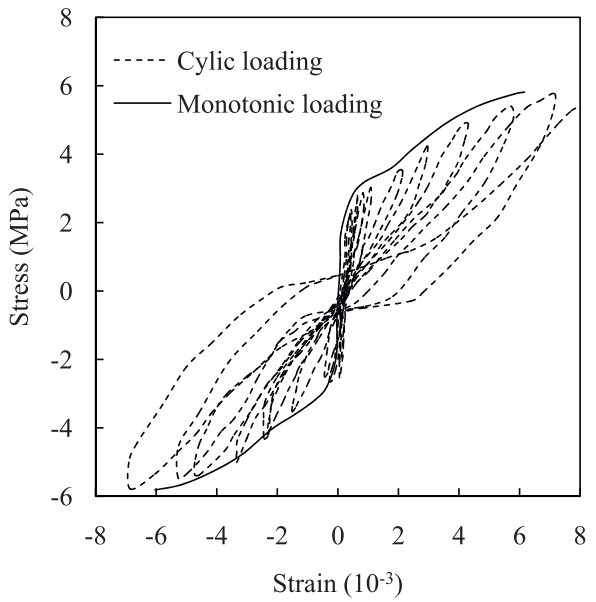

FIGURE 5 | Pinched hysteresis loops of FRCC under cyclic loading (Carnovale and Vecchio, 2014).

pore water pressure, which may contribute to material liquefaction (Cui and Fall, 2017a; Cui and Fall, 2020). Under cyclic shear loading, the accumulation of volumetric plastic strain occurs in the matrix. Due to the irrecoverable nature of this deformation, the matrix retains this volume change during the unloading process. Correspondingly, the accumulation of plastic strain under cyclic loading will result in the continuous development of excess PWP (Lu et al., 2017). This excess PWP causes a reduction in effective stress and material strength. In engineering applications, it is imperative to have a material with rapid dissipation of excess PWP. In this regard, it has been found that the incorporation of fibers into cementitious materials can accelerate PWP dissipation (Festugato et al., 2013). This is because 1) the inclusion of fibers induces multiple cracking responses. The resultant macro- and micro-cracks directly form the preferential seepage channels inside the matrix and thus increases the nominal hydraulic conductivity, and 2) the ITZ formed between fibers and matrix possess a larger pore size compared to those inside the matrix (Chakilam and Cui, 2020). Such larger pores can further enhance the hydraulic conductivity of FRCCs. As a result, rapid dissipation of excess PWP can be expected in soft FRCC under cyclic shear loadings, especially during the post-cracking stages. Festugato et al. (2013) studied the cyclic shear response of fiber-reinforced CPB (FR-CPB). Cyclic shear tests were performed on FR-CPB specimens under 50 kPa of initial effective vertical stress and +/−2.5% of controlled shear strain. After 1,500 cycles, the FR-CPB specimens (see **Figure 6A**) had an excess pore water pressure of approximately 40 kPa and shown a 27% reduction in excess pore water pressure compared to that (approximately 55 kPa) of the non-reinforced specimens (see **Figure 6B**). Moreover, the confirmed rapid dissipation of excess PWP by the inclusion of fibers directly increases the effective stress.

For the failure patterns under cyclic shear loading, cementitious materials can exhibit significant quasi-ductile behavior when compared to the behavior of their individual components (Scrivener et al., 2004). Such macro-scale mechanical behavior can be attributed to the development of multiple micro-cracks primarily in the ITZ between cement paste and aggregate, which is often considered the weak link in cementitious materials. When fibers are introduced into the

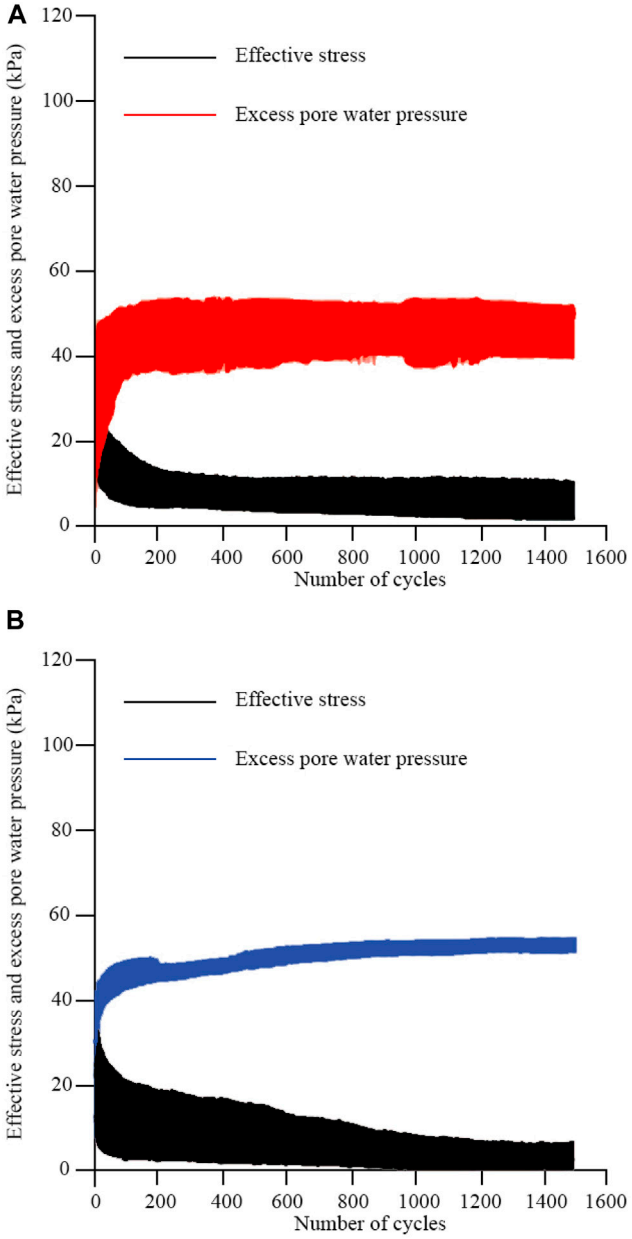

FIGURE 6 | Evolution of excess pore water pressure and effective stress in cemented paste backfill under cyclic shear loading: **(A)** with fiber reinforcement, and **(B)** without fiber reinforcement (Festugato et al., 2013).

porous matrix, a series of new ITZ between fibers and solid particles in the cementitious matrix can be generated (see **Figure 7A**). Similarly, the ITZ associated with the inclusion of fibers possesses strong heterogeneity and weaker fracture toughness compared with the cementitious matrix (Prokopski and Halbiniak, 2000). Consequently, when micro-cracks propagate into the new ITZ, the composite may experience crack deflection and/or branching parallel to the fibers. Furthermore, as shown in **Figure 7B**, fibers can serve as a crack isolator in conjunction with the ITZ and prevent the coalescence of micro-cracks (Pupurs, 2012; Chasioti and Vecchio, 2017). Together with the stress transfer mechanism of fiber reinforcement, this crack isolator role played by the ITZ can further contribute to 1) the improvement of post-cracking stiffness and maintenance of matrix integrity (Dinh et al., 2021) and 2) multiple cracking behaviors of FRCC (Huang et al., 2021a; Li et al., 2021). Under shear loading conditions, the resultant multiple cracks cause more crack surfaces to exist in the cementitious matrix, and subsequently, more energy can be dissipated. Moreover, the inherent crack deflection and branching indicate that shear cracks can transform into tensile cracks (Pereira et al., 2011). As the cracks propagate further into the cementitious matrix, a relatively larger-scale fracture process zone (FPZ) can be formed ahead of the crack front and results in the complex nature of the cracking process in cementitious materials. More precisely, the FPZ is defined as a damage region between the intact material and the fully developed macro-crack (Otsuka and Date, 2000). Previous studies

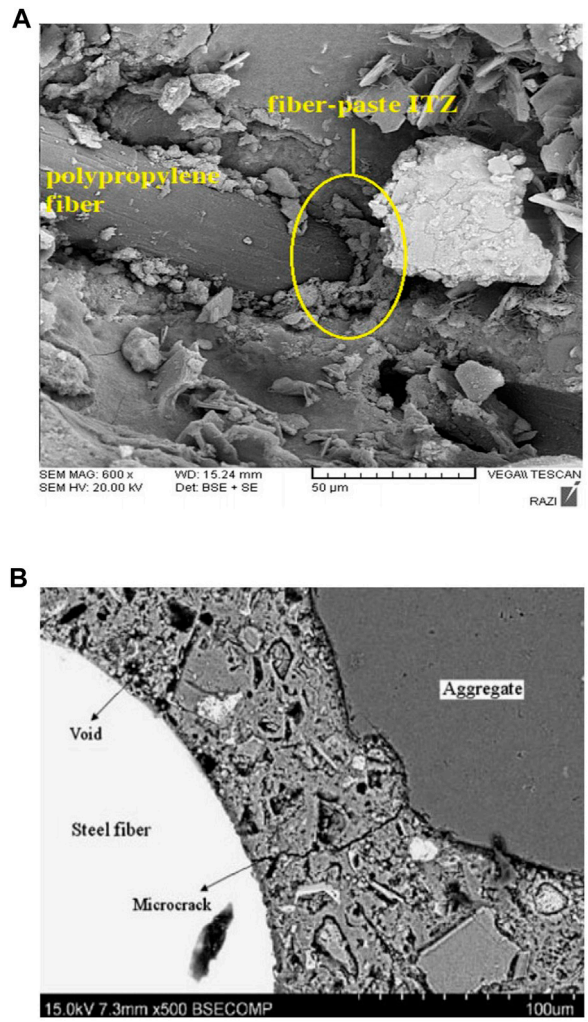

FIGURE 7 | SEM images of **(A)** ITZ between fiber and matrix (Behforouz et al., 2020), and **(B)** crack isolator role played by fiber (Wang et al., 2020).

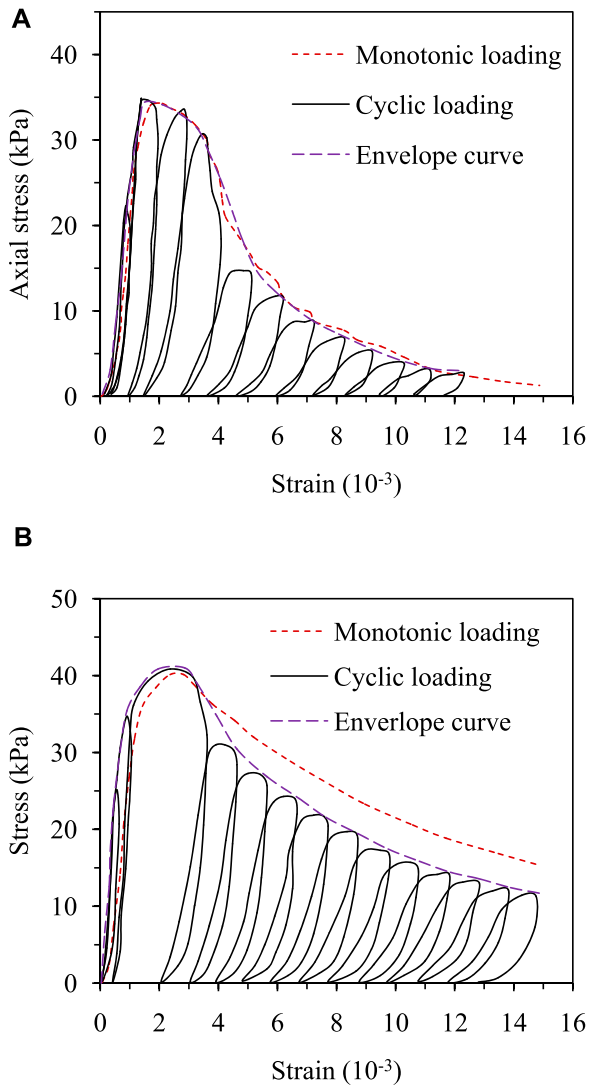

FIGURE 8 | Typical stress-strain curves of cementitious material under cyclic compressive loading: **(A)** without fiber reinforcement, **(B)** with fiber reinforcement (Li et al., 2017).

(Jankowski and Styś, 1990; Brooks, 2013) confirm that the formation of FPZ has the ability to delay crack growth and results in non-linear fracture behaviors. The FPZ of cementitious materials without fibers consists of two zones 1) zone of micro-cracks and 2) aggregate bridging zone. When fibers are introduced to the matrix, the fibers can form the additional fiber bridging zone (Park et al., 2010), which not only extends the net bridging zone but also enlarges the zone of micro-cracks through fiber-induced multiple cracking processes. As a result, the reinforced FPZ improves the fracture toughness of the FRCC. Then, under cyclic shear loading, more energy can be dissipated by this enhanced FPZ, which also confirms the role of fiber reinforcement in the post-cracking stages. In addition, the FPZ will become a crushed zone under cyclic shear loading (Erarslan, 2016). This crushed zone with loose particles and dust has two interesting implications: 1) the separation of solid particles from its original matrix requires more energy dissipation and 2) the existence of particles and dust in the crack space prevents the closure of cracks, thus, affecting the macro-scale volume change. Hence, the crack propagation in the ITZ and FPZ eventually affects the crack coalescence and thus the failure patterns at the macroscale. More specifically, the low tensile strength of plain cementitious materials implies that flexural failure plays a crucial role in the failure patterns (Liu et al., 2019). However, when fibers are introduced, the stress transfer mechanism causes a more important role played by the combined flexural and shear failure patterns. For instance, Li et al. (2019) found that the hybrid-fiber reinforced shear keys experienced concrete crushing and spalling from the specimens during tests and was accompanied by shear tension failure mode under cyclic loading. This is because the opening of flexural cracks was delayed by fiber bridging effect which leads to crack inclination and the subsequent flexure-shear failure. Similar findings were also obtained in recent publications (Choun and Park, 2015; Ying and Jin-Xin, 2018), which further highlights the effect of fiber reinforcement on the failure patterns of cementitious materials under cyclic shear loading.

Cyclic Compressive Behavior of Fiber-Reinforced Cementitious Materials

The envelope curve, usually referenced as the upper boundary of the cyclic response, can be used to analyze the constitutive behavior of FRCC under cyclic compressive loading (Xu et al., 2018a). Specifically, the deviation of the envelope stress-strain curve from the monotonic envelope could be an important mechanical characteristic of FRCC's post-peak behavior. For instance, through an experimental study on the axial cyclic compression behavior of FRCC, Li et al. (2017) found that the envelope curve consists of the ascending and the descending branches. As shown in **Figure 8**, the ascending branch prior to the peak stress closely traces the monotonic envelope curve. The minimal pre-peak deviation between cyclic and monotonic envelope curves was also observed from the synthetic FRCCs (Xu et al., 2018b), which further confirms the weak effect of fiber reinforcement on the pre-peak behavior under compressive loading conditions. Contrastingly, the post-peak discrepancy between cyclic and monotonic envelope curves appears when the fibers are introduced into the cementitious materials (see **Figures 8A,B**). The inconsistent cyclic and monotonic envelop curves in the post-peak stage can be attributed to the strengthened multiple-cracking characteristic of FRCC under cyclic compressive loading (Nataraja et al., 1999; Krahl et al., 2019). Specifically, this multiple cracking process results in significant microscale damage accumulation and macroscale stress deterioration (Li et al., 2017; Xu et al., 2018a). Consequently, fiber reinforcement is able to yield different damage and post-peak (softening or hardening) mechanisms responsible for the macroscale mechanical response under monotonic and/or cyclic loadings (Krahl et al., 2019). Secondly, it has also been found that the increased loading cycles result in a more defined hysteresis loop in FRCC, which indicates an improved hysteretic energy dissipation capability. In

contrast, plain cementitious composites are featured with narrow hysteresis loops under cyclic compressive loading (Deng and Zhang, 2017) and several major cracks from the beginning of loading till specimen failure (Yu et al., 2020). This is because the formation of fiber bridging zone in the vicinity of crack front extends FPZ and the resultant stress transfer causes multiple cracking in the matrix (Li et al., 2017; Yu et al., 2020). More precisely, the prerequisite for the effectiveness of fiber reinforcement is the development of locally matched stress levels between fibers and adjacent cementitious matrix (Abbas and Iqbal Khan, 2016; Mohonee and Goh, 2016). However, distinct mechanical properties between fiber and granular materials may cause the unmatched stress levels when the deformation of fiber drops to a certain value and thus fade the local fiber reinforcement effect (Libos and Cui, 2021). In other words, the cyclic loading and unloading processes will repeatedly reactivate and deactivate the fiber reinforcement at the cost of damage accumulation in the cementitious matrix. Consequently, strengthened stress transfer through combined fiber and aggregate bridging zones into the cementitious matrix is able to endow the materials with significantly improved mechanical performance including the higher hysteretic energy dissipation capacity.

In addition to the stress-strain response, the macroscale volume change of FRCC can also demonstrate different characteristics when subjected to cyclic compressive loading. The macroscale volume change is intimately related to the crack opening and closing during the loading and unloading processes (Alkan et al., 2007). As previously discussed, fibers embedded into the matrix may act as crack arresters and cause crack branching and deflection. Consequently, both tensile and shear cracks are able to propagate inside the cementitious composite and promote multiple cracking behaviors. The effect of tensile crack on volume change is straightforward, i.e., the opening and closing of tensile cracks can directly cause the local volume expansion and contraction. However, the volume change associated with shear cracks is dependent on cementation extent (Amini et al., 2014). To maintain the shear crack growth, the debonding process accompanied by the particle sliding and rotation along the rough crack surfaces are required (Wang et al., 2021a). Therefore, similar to the overconsolidated soils, a larger local volume expansion can be expected along the shear cracks when FRCCs are prepared with higher cement content (Jiang et al., 2011). Conversely, soft cementitious materials with lower cement content such as FR-CPB possess weak bond strength. As a result, the shearing process along crack surfaces can cause the debonding processes to a larger regime in the vicinity of crack surfaces and promote particle re-packing to a higher extent, which in turn weakens the sliding and rotation of particles along the crack surfaces. Consequently, the locally depressed volume expansion can be expected in soft cementitious materials (Cui and Fall, 2016a). Additionally, the introduction of fibers indirectly contributes to the confinement of the cementitious composite (Ramesh et al., 2003). This is because fiber bridging capacity is able to provide passive confinement to the damaged matrix (Zhou et al., 2015) and thus further limit the volume change at a given stress level.

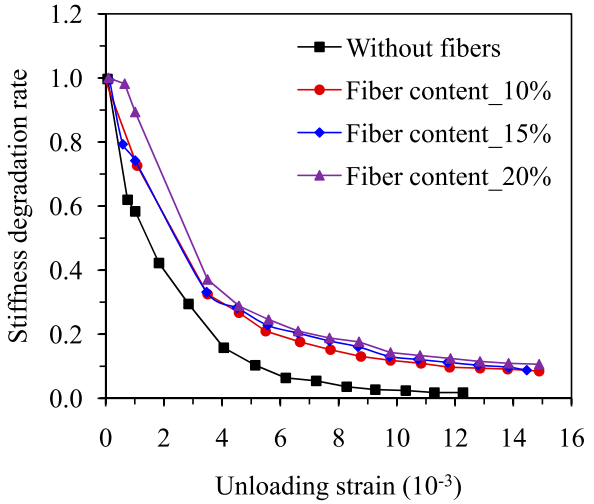

FIGURE 9 | Effect of fiber volume fraction on stiffness degradation (Li et al., 2017).

In terms of mechanical properties of FRCCs under cyclic compressive loading, the elastic modulus, compressive strength, the energy dissipation capacity and Poisson's ratio can be extracted from the macroscale stress-strain behaviors and used to evaluate the engineering performance of FRCCs. Specifically, the evolution of elastic modulus can be used as a valuable indicator for the damage accumulation inside cementitious materials. When materials are cyclically loaded, the material stiffness degrades due to crack propagation. However, it has been confirmed that the addition of fibers into the cementitious matrix is able to effectively alleviate the degradation rate of elastic stiffness (see **Figure 9**) (Yu et al., 2020) and improve the ductile response of cementitious material at the macroscale (Siva and Pankaj, 2019). With regards to composite strength, the effect of fibers is less significant, and some studies (Banthia and Gupta, 2004; Tahenni et al., 2016) even found a negative effect of fibers on the compressive strength of FRCCs. As previously discussed, fibers are most effective when their tensile strength is mobilized through their bridging capacity across tensile cracks. However, under compressive loading fibers may initiate matrix crushing through local stress concentration and induce defects in the cementitious matrix as a result of inadequate compactness (Boulekbache et al., 2010; Boulekbache et al., 2012), which may adversely affect the compressive strength of FRCC. However, the fiber reinforcement technique is able to act as a positive contributor to the compressive strength when a multiscale reinforcement approach is adopted. The critical discussion on the potential usage of the multiscale reinforcement technique will be presented in *Discussion on the Multiscale Reinforcement Technique*. Furthermore, the hysteresis loops in **Figure 8** suggest the inclusion of fibers significantly improves the hysteretic energy dissipation in FRCCs (Li et al., 2017; Xu et al., 2018a). When FRCCs are cyclically loaded, the reinforcement mechanisms including fiber bridging, fiber sliding, fiber pull-out, and fiber-matrix debonding are responsible for the

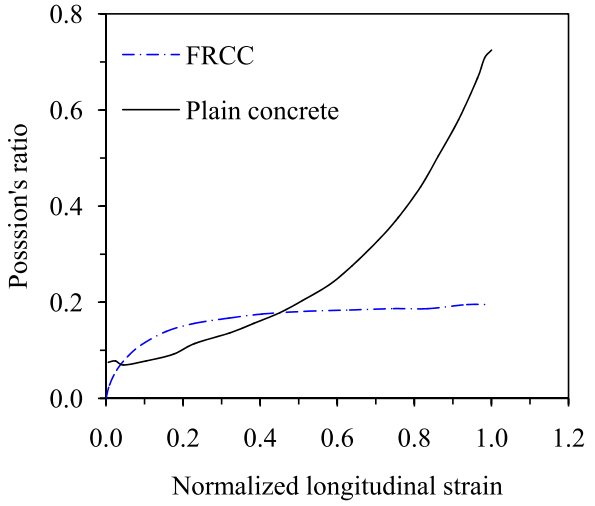

FIGURE 10 | Effect of fiber volume fraction on stiffness degradation (Zhou et al., 2015).

formation of energy dissipation capacity (Trainor et al., 2013). Correspondingly, the absence of these mechanisms in plain cementitious materials inevitably results in smaller hysteretic loops and subsequent low energy dissipation capacity, because the coalescence of microcracks into macrocracks is the only avenue for energy dissipation in plain cementitious materials. Lastly, Zhou et al. (2015) have identified that the cracking process significantly influences the evolution of Poisson's ratio. As illustrated in **Figure 10**, Poisson's ratio of plain cementitious materials increases exponentially with axial strain due to progressive micro-cracking in the cementitious matrix. However, when the fiber reinforcement is introduced into the cementitious materials, the Poisson's ratio shows a logarithmic relationship to the axial strain and such observation clearly confirms the fiber's crack-bridging capacity is also able to restrict further crack opening in the lateral direction and thus affects the macroscale volume change.

For the failure patterns of FRCCs under compressive loading, the plain cementitious composites are dominated by tensile cracks parallel to the loading direction (Xu et al., 2018a). With the introduction of fibers into the matrix, the failure mode is transformed into a more ductile shear failure (Yu et al., 2020). For instance, through CT scan technology, Mínguez et al. (2019) reconstruct crack propagation inside the cementitious matrix under cyclic compressive loadings. The obtained CT images (**Figure 11**) clearly show the crack branching and deflection inside the FRCCs. Such cracking process inside the matrix can be attributed to multiple mechanisms including 1) exceedance of the tensile strength of the matrix, 2) debonding between fibers and matrix, and 3) debonding between aggregates and matrix (Li et al., 2017). More specifically, due to the relatively weak tensile strength, the tensile microcracks can be developed in the matrix under cyclic compressive loadings. However, due to the development of FPZ in the vicinity of crack surfaces, the initial tensile microcracks are restrained and/or deflected by the fibers, limiting crack growth and thus restricting volume changes in the cementitious matrix (Li et al., 2017; Xu et al., 2018a; Siva and Pankaj, 2019). In other words, these fibers act as crack barriers, resulting in a more curved and inclined cracking path as the load increases (Yun et al., 2007; Li et al., 2017). The microscale crack deflection and possible branching in the vulnerable regions such as ITZ can further complicate the local stress state including shear stress concentration and associated shear crack propagation (Huang et al., 2018). Consequently, FRCCs may exhibit both macroscale tensile and shear cracks under cyclic compressive loadings.

DISCUSSION ON THE MULTISCALE REINFORCEMENT TECHNIQUE

Based on the comprehensive review on constitutive behavior, mechanical properties, and failure patterns of FRCC, it can be found the effect of fiber reinforcement mainly appears in the post-peak stage. However, the role played by fibers in the pre-peak region is not well understood. For instance, the present studies on the fiber reinforcement technique indicate the usage of only one type of fiber has a very limited effect on the pre-peak behavior of

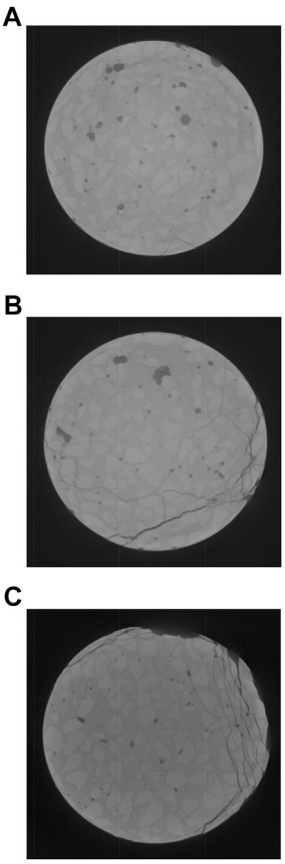

FIGURE 11 | CT images of cracking process in FRCC under cyclic compressive loading: **(A)** 0 cycles, **(B)** 20,000 cycles, and **(C)** 2,000,000 cycles (Mínguez et al., 2019).

FRCC. Since the effectiveness of fiber reinforcement at the pre-peak stage is closely associated with the improvement of peak stress (i.e., material strength), more studies are required to explore the mechanisms behind the pre-peak reinforcement techniques. In this regard, it has been confirmed that cracks within cementitious composites exist in multiscale dimensions. Therefore, the synergistic use of fibers with different geometrical and mechanical properties in cementitious composites is often motivated by the multiscale nature of the cracking processes in FRCC. For example, recent studies (Masud and Chorzepa, 2016; Alshaghel et al., 2018; Pan et al., 2018) suggests that a multiscale reinforcement approach is able to form a hierarchically reinforced cementitious matrix and effectively improve the dynamic response of FRCC, especially its pre-peak behavior. This is because crack initiation is abated at the nanoscale level by employing nanofibers, and crack growth is delayed at micro and macro levels respectively by incorporating micro and macro fibers (Pereira et al., 2012). Therefore, the multiscale reinforcement techniques have the potentials to significantly improve the integrity and stability of FRCC at the field scale. However, due to the discrete nature of artificial fibers (including nanoparticles and micro- and macro-fibers), the multiscale reinforcement approach cannot form a continuous reinforcement network in the porous matrix. Consequently, the locally unreinforced zones always exist in FRCC and thus create the preferential regimes for crack propagation. Therefore, more studies are urgently required to overcome such structural and functional defects associated with fiber reinforcement technique, especially for soft cementitious materials under extreme loading conditions.

CONCLUSION

This literature review presents a comprehensive overview of start-of-the-art research on the FRCC under cyclic loading conditions. The macroscale constitutive behavior and the associated mechanical properties, and microscale cracking processes under cyclic tensile, shear, and compressive loading conditions are summarized in-depth. Based on the study findings in the present literature, the following conclusions can be drawn:

1) For the macroscale constitutive behavior, the fiber reinforcement mainly improves the post-cracking behavior, especially in the post-peak stage. Correspondingly, the enhancement of material stiffness, hysteretic energy dissipation capacity, and ductility has been observed from FRCC under cyclic tensile, shear, and compressive loadings.
2) The crack opening and closing at the microscale govern the macroscale volume change under cyclic tensile loadings. In contrast, the shear-induced volume change is dominated by the particle repackaging along the shear cracks.
3) The inclusion of fibers is able to enlarge the pore size of ITZ and accelerate dissipation of the excess PWP under cyclic loading. Therefore, rapid changes in effective stress and the mechanical properties are expected in the soft cementitious materials such as CPB.
4) For the microscale crack propagation under cyclic loadings, introducing fibers into the cementitious matrix extends the FPZ and causes complex cracking processes such as crack deflection and branching. Consequently, the FRCC commonly demonstrates both tensile and shear cracks under cyclic loadings.
5) Based on the multiscale geomechanical behavior of FRCC, the multiscale reinforcement technique can be considered a promising approach to restrict cracking at different length scales inside the cementitious matrix under cyclic loadings.

AUTHOR CONTRIBUTIONS

LC conceived the original ideas and supervised this study. JM carried out the comprehensive review and wrote this article.

FUNDING

This work was funded by Natural Sciences and Engineering Research Council of Canada (NSERC), and also funded by the State Key Laboratory of Geohazard Prevention and Geoenvironment Protection Open Fund (SKLGP2021K004).

REFERENCES

Abbas, Y. M., and Iqbal Khan, M. (2016). Fiber-Matrix Interactions in Fiber-Reinforced Concrete: A Review. *Arab J Sci Eng* 41, 1183–1198. doi:10.1007/s13369-016-2099-1

Aggelis, D. G. (2011). Classification of Cracking Mode in Concrete by Acoustic Emission Parameters. *Mechanics Research Communications* 38, 153–157. doi:10.1016/j.mechrescom.2011.03.007

Aggelis, D. G., Soulioti, D. V., Sapouridis, N., Barkoula, N. M., Paipetis, A. S., and Matikas, T. E. (2011). Acoustic Emission Characterization of the Fracture Process in Fibre Reinforced Concrete. *Construction and Building Materials* 25, 4126–4131. doi:10.1016/j.conbuildmat.2011.04.049

Alkan, H., Cinar, Y., and Pusch, G. (2007). Rock Salt Dilatancy Boundary from Combined Acoustic Emission and Triaxial Compression Tests. *International Journal of Rock Mechanics and Mining Sciences* 44, 108–119. doi:10.1016/j.ijrmms.2006.05.003

Alshaghel, A., Parveen, S., Rana, S., and Fangueiro, R. (2018). Effect of Multiscale Reinforcement on the Mechanical Properties and Microstructure of Microcrystalline Cellulose-Carbon Nanotube Reinforced Cementitious Composites. *Composites Part B: Engineering* 149, 122–134. doi:10.1016/j.compositesb.2018.05.024

Amini, Y., Hamidi, A., and Asghari, E. (2014). Shear strength-dilation characteristics of cemented sand-gravel mixtures. *International Journal of Geotechnical Engineering* 8, 406–413. doi:10.1179/1939787913y.0000000026

Banthia, N., and Gupta, R. (2004). Hybrid Fiber Reinforced Concrete (Hyfrc): Fiber Synergy in High Strength Matrices. *Mat. Struct.* 37, 707–716. doi:10.1007/bf02480516

Bernard, E. S. (2015). Age-Dependent Changes in Post-Crack Performance of Fibre Reinforced Shotcrete Linings. *Tunnelling and Underground Space Technology* 49, 241–248. doi:10.1016/j.tust.2015.05.006

Boulekbache, B., Hamrat, M., Chemrouk, M., and Amziane, S. (2010). Flowability of Fibre-Reinforced Concrete and Its Effect on the Mechanical Properties of the

Material. *Construction and Building Materials* 24, 1664–1671. doi:10.1016/j.conbuildmat.2010.02.025

Boulekbache, B., Hamrat, M., Chemrouk, M., and Amziane, S. (2012). Influence of Yield Stress and Compressive Strength on Direct Shear Behaviour of Steel Fibre-Reinforced Concrete. *Construction and Building Materials* 27, 6–14. doi:10.1016/j.conbuildmat.2011.07.015

Boulekbache, B., Hamrat, M., Chemrouk, M., and Amziane, S. (2016). Flexural Behaviour of Steel Fibre-Reinforced Concrete under Cyclic Loading. *Construction and Building Materials* 126, 253–262. doi:10.1016/j.conbuildmat.2016.09.035

Brooks, Z (2013). *Fracture Process Zone: Microstructure and Nanomechanics in Quasi-Brittle Materials PhD thesis*. Massachusetts Institute of Technology.

Cao, S., Yilmaz, E., and Song, W. (2019). Fiber Type Effect on Strength, Toughness and Microstructure of Early Age Cemented Tailings Backfill. *Construction and Building Materials* 223, 44–54. doi:10.1016/j.conbuildmat.2019.06.221

Cao, S., Yilmaz, E., Yin, Z., Xue, G., Song, W., and Sun, L. (2021). Ct Scanning of Internal Crack Mechanism and Strength Behavior of Cement-Fiber-Tailings Matrix Composites. *Cement and Concrete Composites* 116, 103865. doi:10.1016/j.cemconcomp.2020.103865

Cao, S., Zheng, D., Yilmaz, E., Yin, Z., Xue, G., and Yang, F. (2020). Strength Development and Microstructure Characteristics of Artificial Concrete Pillar Considering Fiber Type and Content Effects. *Construction and Building Materials* 256, 119408. doi:10.1016/j.conbuildmat.2020.119408

Carnovale, D., and Vecchio, F.J. (2014). Effect of Fiber Material and Loading History on Shear Behavior of Fiber-Reinforced Concrete. *ACI Structural Journal* 111, 1235–1244.

Caverzan, A., Cadoni, E., and Di Prisco, M. (2012). Tensile Behaviour of High Performance Fibre-Reinforced Cementitious Composites at High Strain Rates. *International Journal of Impact Engineering* 45, 28–38. doi:10.1016/j.ijimpeng.2012.01.006

Chakilam, S., and Cui, L. (2020). Effect of Polypropylene Fiber Content and Fiber Length on the Saturated Hydraulic Conductivity of Hydrating Cemented Paste Backfill. *Construction and Building Materials* 262, 120854. doi:10.1016/j.conbuildmat.2020.120854

Chasioti, S.G., and Vecchio, F.J. (2017). Shear Behavior and Crack Control Characteristics of Hybrid Steel Fiber-Reinforced Concrete Panels. *ACI Structural Journal* 114, 209. doi:10.14359/51689164

Chen, X., Shi, X., Zhou, J., and Yu, Z. (2019). Influence of Polypropylene Fiber Reinforcement on Tensile Behavior and Failure Mode of Tailings Cemented Paste Backfill. *IEEE Access* 7, 69015–69026. doi:10.1109/access.2019.2919480

Choun, Y.-S., and Park, J. (2015). Evaluation of Seismic Shear Capacity of Prestressed Concrete Containment Vessels with Fiber Reinforcement. *Nuclear Engineering and Technology* 47, 756–765. doi:10.1016/j.net.2015.06.006

Chung, J.-H., Son, D.-H., Kim, S.-Y., Bae, B.-I., and Choi, C.-S. (2021). Hysteretic Behavior of Reinforced Concrete Coupling Beams According to Volume Fraction of Steel Fiber. *Sustainability* 13, 182. doi:10.3390/su13010182

Claus, T (2009). *Non-Linear Finite Element Analysis of Shear Critical Reinforced Concrete BeamsMaster's degree*. Delft University of Technology.

Cui, L., and Fall, M. (2015). A coupled thermo-hydro-mechanical-chemical model for underground cemented tailings backfill. *Tunnelling and Underground Space Technology* 50, 396–414. doi:10.1016/j.tust.2015.08.014

Cui, L., and Fall, M. (2016a). An Evolutive Elasto-Plastic Model for Cemented Paste Backfill. *Computers and Geotechnics* 71, 19–29. doi:10.1016/j.compgeo.2015.08.013

Cui, L., and Fall, M. (2016b). Multiphysics Model for Consolidation Behavior of Cemented Paste Backfill. *International Journal of Geomechanics* 17, 04016077.

Cui, L., and Fall, M. (2017a). Modeling of Pressure on Retaining Structures for Underground Fill Mass. *Tunnelling and Underground Space Technology* 69, 94–107. doi:10.1016/j.tust.2017.06.010

Cui, L., and Fall, M. (2017b). Multiphysics Modeling of Arching Effects in Fill Mass. *Computers and Geotechnics* 83, 114–131. doi:10.1016/j.compgeo.2016.10.021

Cui, L., and Fall, M. (2018). Multiphysics Modeling and Simulation of Strength Development and Distribution in Cemented Tailings Backfill Structures. *Int J Concr Struct Mater* 12, 25. doi:10.1186/s40069-018-0250-y

Cui, L., and Fall, M. (2019). Mathematical Modelling of Cemented Tailings Backfill: A Review. *International Journal of Mining, Reclamation and Environment* 33, 389–408. doi:10.1080/17480930.2018.1453320

Cui, L., and Fall, M. (2020). Numerical Simulation of Consolidation Behavior of Large Hydrating Fill Mass. *International Journal of Concrete Structures and Materials* 14, 1–16. doi:10.1186/s40069-020-0398-0

Deng, M., and Zhang, Y. (2017). Cyclic Loading Tests of Rc Columns Strengthened with High Ductile Fiber Reinforced Concrete Jacket. *Construction and Building Materials* 153, 986–995. doi:10.1016/j.conbuildmat.2017.07.175

Dinh, N. H., Park, S.-H., and Choi, K.-K. (2021). Effect of Dispersed Micro-Fibers on Tensile Behavior of Uncoated Carbon Textile-Reinforced Cementitious Mortar after High-Temperature Exposure. *Cement and Concrete Composites* 118, 103949. doi:10.1016/j.cemconcomp.2021.103949

Dönmez, D., Dönmez, A. A., and Gençoğlu, M. (2020). Mechanical Response of Textile Reinforced Cementitious Composite Tubes under Monotonic and Cyclic Loadings. *Construction and Building Materials* 251, 118963. doi:10.1016/j.conbuildmat.2020.118963

Erarslan, N. (2016). Microstructural Investigation of Subcritical Crack Propagation and Fracture Process Zone (Fpz) by the Reduction of Rock Fracture Toughness under Cyclic Loading. *Engineering Geology* 208, 181–190. doi:10.1016/j.enggeo.2016.04.035

Festugato, L., Fourie, A., and Consoli, N. C. (2013). Cyclic Shear Response of Fibre-Reinforced Cemented Paste Backfill. *Géotechnique Letters* 3, 5–12. doi:10.1680/geolett.12.00042

Guo, M., Zhong, Q., Zhou, Y., Hu, B., Huang, Z., and Yue, Y. (2020). Influence of Flexural Loading and Chloride Exposure on the Fatigue Behavior of High-Performance Lightweight Engineered Cementitious Composites. *Construction and Building Materials* 249, 118512. doi:10.1016/j.conbuildmat.2020.118512

Hu, J.-H., Sun, M.-Q., Li, J., and Wang, Y.-J. (2018). Mechanical Performances and Evolution of Stiffness of Thin-Walled Strain Hardening Cement-Based Composites Pipes During Cyclic Loading. *Construction and Building Materials* 184, 400–407. doi:10.1016/j.conbuildmat.2018.07.001

Huang, B.-T., Li, Q.-H., Xu, S.-L., Liu, W., and Wang, H.-T. (2018). Fatigue Deformation Behavior and Fiber Failure Mechanism of Ultra-High Toughness Cementitious Composites in Compression. *Materials & Design* 157, 457–468. doi:10.1016/j.matdes.2018.08.002

Huang, B.-T., Weng, K.-F., Zhu, J.-X., Xiang, Y., Dai, J.-G., and Li, V. C. (2021a). Engineered/Strain-Hardening Cementitious Composites (Ecc/Shcc) with an Ultra-High Compressive Strength over 210 mpa. *Composites Communications* 26, 100775. doi:10.1016/j.coco.2021.100775

Huang, Z., Cao, S., and Yilmaz, E. (2021b). Investigation on the Flexural Strength, Failure Pattern and Microstructural Characteristics of Combined Fibers Reinforced Cemented Tailings Backfill. *Construction and Building Materials* 300, 124005. doi:10.1016/j.conbuildmat.2021.124005

Hung, C.-C., Su, Y.-F., and Yu, K.-H. (2013). Modeling the Shear Hysteretic Response for High Performance Fiber Reinforced Cementitious Composites. *Construction and Building Materials* 41, 37–48. doi:10.1016/j.conbuildmat.2012.12.010

Jankowski, L. J., and Styś, D. J. (1990). Formation of the Fracture Process Zone in Concrete. *Engineering Fracture Mechanics* 36, 245–253. doi:10.1016/0013-7944(90)90005-2

Jiang, M. J., Yan, H. B., Zhu, H. H., and Utili, S. (2011). Modeling Shear Behavior and Strain Localization in Cemented Sands by Two-Dimensional Distinct Element Method Analyses. *Computers and Geotechnics* 38, 14–29. doi:10.1016/j.compgeo.2010.09.001

Jun, P., and Mechtcherine, V. (2010). Behaviour of Strain-hardening Cement-based Composites (SHCC) under monotonic and cyclic tensile loading. *Cement and Concrete Composites* 32, 801–809. doi:10.1016/j.cemconcomp.2010.07.019

Khlef, F. L., Barbosa, A. R., and Ideker, J. H. (2019). Tension and Cyclic Behavior of High-Performance Fiber-Reinforced Cementitious Composites. *J. Mater. Civ. Eng.* 31, 04019220. doi:10.1061/(asce)mt.1943-5533.0002844

Krahl, P. A., Gidrão, G. d. M. S., and Carrazedo, R. (2019). Cyclic Behavior of Uhpfrc under Compression. *Cement and Concrete Composites* 104, 103363. doi:10.1016/j.cemconcomp.2019.103363

Külekçi, G. (2021). Comparison of Field and Laboratory Result of Fiber Reinforced Shotcrete Application. *Periodica Polytechnica Civil Engineering* 65, 463–473. doi:10.3311/ppci.17033

Li, B., Chi, Y., Xu, L., Li, C., and Shi, Y. (2018a). Cyclic Tensile Behavior of Sfrc: Experimental Research and Analytical Model. *Construction and Building Materials* 190, 1236–1250. doi:10.1016/j.conbuildmat.2018.09.140

Li, B., Chi, Y., Xu, L., Shi, Y., and Li, C. (2018b). Experimental Investigation on the Flexural Behavior of Steel-Polypropylene Hybrid Fiber Reinforced Concrete. *Construction and Building Materials* 191, 80–94. doi:10.1016/j.conbuildmat.2018.09.202

Li, B., Xu, L., Chi, Y., Huang, B., and Li, C. (2017). Experimental Investigation on the Stress-Strain Behavior of Steel Fiber Reinforced Concrete Subjected to Uniaxial Cyclic Compression. *Construction and Building Materials* 140, 109–118. doi:10.1016/j.conbuildmat.2017.02.094

Li, Q.-H., Yin, X., Huang, B.-T., Luo, A.-M., Lyu, Y., Sun, C.-J., and Xu, S.-L. (2021). Shear Interfacial Fracture of Strain-Hardening Fiber-Reinforced Cementitious Composites and Concrete: A Novel Approach. *Engineering Fracture Mechanics* 253, 107849. doi:10.1016/j.engfracmech.2021.107849

Li, Z.-X., Li, C.-H., and Yan, J.-B. (2019). Seismic Behaviour of Hybrid-Fibre Reinforced Concrete Shear Keys in Immersed Tunnels. *Tunnelling and Underground Space Technology* 88, 16–28. doi:10.1016/j.tust.2019.02.022

Libos, I.L.S., and Cui, L. (2020). "Mechanical Properties and Behavior of Early-Age Fiber-Reinforced Cemented Paste Backfill," in Proceedings of the 5rd International Conference on Civil Structural and Transportation Engineering (Virtual Conference: Avestia).

Libos, I.L.S., and Cui, L. (2021). "Time- and Temperature-Dependence of Compressive and Tensile Behaviors of Polypropylene Fiber-Reinforced Cemented Paste Backfill," in *Frontiers of Structural and Civil Engineering*. (in presss).

Lin, J.-X., Song, Y., Xie, Z.-H., Guo, Y.-C., Yuan, B., Zeng, J.-J., and Wei, X. (2020). Static and Dynamic Mechanical Behavior of Engineered Cementitious Composites with Pp and Pva Fibers. *Journal of Building Engineering* 29, 101097. doi:10.1016/j.jobe.2019.101097

Liu, N., Cui, L., and Wang, Y. (2020). Analytical Assessment of Internal Stress in Cemented Paste Backfill. *Advances in Materials Science and Engineering* 2020, 6666548. doi:10.1155/2020/6666548

Liu, X., Wu, T., and Liu, Y. (2019). Stress-Strain Relationship for Plain and Fibre-Reinforced Lightweight Aggregate Concrete. *Construction and Building Materials* 225, 256–272. doi:10.1016/j.conbuildmat.2019.07.135

Lu, G., Fall, M., and Cui, L. (2017). A Multiphysics-Viscoplastic Cap Model for Simulating Blast Response of Cemented Tailings Backfill. *Journal of Rock Mechanics and Geotechnical Engineering* 9, 551–564. doi:10.1016/j.jrmge.2017.03.005

Ma, G., Li, Z., Yi, X., and Guo, L. (2016). Macro-Meso Experiment of Fiber-Reinforced Cement Paste Filling Material. *Journal of Beijing University of Technology* 42, 406–412.

Masud, M., and Chorzepa, M. G. (2016). Impact Resilience of Multiscale Fibre Reinforced Composites. *Magazine of Concrete Research* 68, 379–390. doi:10.1680/jmacr.15.00184

Mechtcherine, V., Millon, O., Butler, M., and Thoma, K. (2011). Mechanical Behaviour of Strain Hardening Cement-Based Composites under Impact Loading. *Cement and Concrete Composites* 33, 1–11. doi:10.1016/j.cemconcomp.2010.09.018

Mínguez, J., Gutiérrez, L., González, D. C., and Vicente, M. A. (2019). Plain and Fiber-Reinforced Concrete Subjected to Cyclic Compressive Loading: Study of the Mechanical Response and Correlations with Microstructure Using Ct Scanning. *Applied Sciences* 9, 3030. doi:10.3390/app9153030

Mohonee, V. K., and Goh, K. L. (2016). Effects of fibre-fibre interaction on stress uptake in discontinuous fibre reinforced composites. *Composites Part B: Engineering* 86, 221–228. doi:10.1016/j.compositesb.2015.10.015

Müller, S., and Mechtcherine, V. (2017). Fatigue Behaviour of Strain-Hardening Cement-Based Composites (Shcc). *Cement and Concrete Research* 92, 75–83. doi:10.1016/j.cemconres.2016.11.003

Nataraja, M. C., Dhang, N., and Gupta, A. P. (1999). Stress-strain curves for steel-fiber reinforced concrete under compression. *Cement and Concrete Composites* 21, 383–390. doi:10.1016/s0958-9465(99)00021-9

Otsuka, K., and Date, H. (2000). Fracture Process Zone in Concrete Tension Specimen. *Engineering Fracture Mechanics* 65, 111–131. doi:10.1016/s0013-7944(99)00111-3

Pakravan, H. R., and Ozbakkaloglu, T. (2019). Synthetic Fibers for Cementitious Composites: A Critical and in-Depth Review of Recent Advances. *Construction and Building Materials* 207, 491–518. doi:10.1016/j.conbuildmat.2019.02.078

Pan, J., Cai, J., Ma, H., and Leung, C. K. Y. (2018). Development of Multiscale Fiber-Reinforced Engineered Cementitious Composites with PVA Fiber and CaCO3 Whisker. *J. Mater. Civ. Eng.* 30, 04018106. doi:10.1061/(asce)mt.1943-5533.0002305

Park, K., Paulino, G. H., and Roesler, J. (2010). Cohesive Fracture Model for Functionally Graded Fiber Reinforced Concrete. *Cement and Concrete Research* 40, 956–965. doi:10.1016/j.cemconres.2010.02.004

Pekoz, H.A., and Pincheira, J.A. (2004). "Seismic Response of Strength and Stiffness Degrading Single Degree of Freedom Systems," in 13th World Conference on Earthqauke Engineering, Canada (Vancouver, B.C.).

Pereira, E., Fischer, G., and Barros, J.A. (2011). "Image-Based Detection and Analysis of Crack Propagation in Cementitious Composites," in International RILEM Conference On Advances In Construction Materials Through Science and Engineering, China (Hong Kong).

Pereira, E. B., Fischer, G., and Barros, J. A. O. (2012). Effect of Hybrid Fiber Reinforcement on the Cracking Process in Fiber Reinforced Cementitious Composites. *Cement and Concrete Composites* 34, 1114–1123. doi:10.1016/j.cemconcomp.2012.08.004

Prokopski, G., and Halbiniak, J. (2000). Interfacial Transition Zone in Cementitious Materials. *Cement and Concrete Research* 30, 579–583. doi:10.1016/s0008-8846(00)00210-6

Pupurs, A. (2012). *Micro-Crack Initiation and Propagation in Fiber Reinforced Composites*. Luleå tekniska universitet: PhD Degree PhD thesis.

Qiu, J., Luo, L., Li, X., Li, D., Chen, Y., and Luo, Y. (2020). Numerical Investigation on the Tensile Fracturing Behavior of Rock-Shotcrete Interface Based on Discrete Element Method. *International Journal of Mining Science and Technology* 30, 293–301. doi:10.1016/j.ijmst.2020.03.007

Ramesh, K., Seshu, D. R., and Prabhakar, M. (2003). Constitutive Behaviour of Confined Fibre Reinforced Concrete under Axial Compression. *Cement and Concrete Composites* 25, 343–350. doi:10.1016/s0958-9465(02)00051-3

Rena, C.Y., Cifuentes, H., Rivero, I., Ruiz, G., and Zhang, X. (2016). Dynamic Fracture Behaviour in Fibre-Reinforced Cementitious Composites. *Journal of the Mechanics and Physics of Solids* 93, 135–152.

Scrivener, K. L., Crumbie, A. K., and Laugesen, P. (2004). The Interfacial Transition Zone (Itz) between Cement Paste and Aggregate in Concrete. *Interface Science* 12, 411–421. doi:10.1023/b:ints.0000042339.92990.4c

Siva, C. R., and Pankaj, A. (2019). Flexural Behavior of Reinforced Concrete Beams with High Performance Fiber Reinforced Cementitious Composites. *J. Cent. South Univ.* 26, 2609–2622. doi:10.1007/s11771-019-4198-0

Sjölander, A., Hellgren, R., Malm, R., and Ansell, A. (2020). Verification of Failure Mechanisms and Design Philosophy for a Bolt-Anchored and Fibre-Reinforced Shotcrete Lining. *Engineering Failure Analysis* 116, 104741. doi:10.1016/j.engfailanal.2020.104741

Soulioti, D., Barkoula, N. M., Paipetis, A., Matikas, T. E., Shiotani, T., and Aggelis, D. G. (2009). Acoustic Emission Behavior of Steel Fibre Reinforced Concrete under Bending. *Construction and Building Materials* 23, 3532–3536. doi:10.1016/j.conbuildmat.2009.06.042

Tahenni, T., Chemrouk, M., and Lecompte, T. (2016). Effect of Steel Fibers on the Shear Behavior of High Strength Concrete Beams. *Construction and Building Materials* 105, 14–28. doi:10.1016/j.conbuildmat.2015.12.010

Toé Casagrande, M. D., Coop, M. R., and Consoli, N. C. (2006). Behavior of a Fiber-Reinforced Bentonite at Large Shear Displacements. *J. Geotech. Geoenviron. Eng.* 132, 1505–1508. doi:10.1061/(asce)1090-0241(2006)132:11(1505)

Trainor, K. J., Foust, B. W., and Landis, E. N. (2013). Measurement of Energy Dissipation Mechanisms in Fracture of Fiber-Reinforced Ultrahigh-Strength Cement-Based Composites. *J. Eng. Mech.* 139, 771–779. doi:10.1061/(asce)em.1943-7889.0000545

Wang, P., Zhao, M., Du, X., and Liu, J. (2019). Dynamic Response of Bridge Pier under Combined Earthquake and Wave-Current Action. *J. Bridge Eng.* 24, 04019095. doi:10.1061/(asce)be.1943-5592.0001471

Wang, S., Xu, L., Yin, C., Chen, Z., and Chi, Y. (2021a). Experimental Investigation on the Damage Behavior of Ultra-High Performance Concrete Subjected to Cyclic Compression. *Composite Structures* 267, 113855. doi:10.1016/j.compstruct.2021.113855

Wang, Y., Cao, Y., Cui, L., Si, Z., and Wang, H. (2020). Effect of External Sulfate Attack on the Mechanical Behavior of Cemented Paste Backfill. *Construction and Building Materials* 263, 120968. doi:10.1016/j.conbuildmat.2020.120968

Wang, Z.-C., Duan, D.-Y., Wang, S.-H., Mo, Y., and Yin, Y.-G. (2021b). Mechanical Behavior of the Novel Gradient Concrete Tower of a Cable-Stayed Bridge. *Frontiers in Materials* 8. doi:10.3389/fmats.2021.676440

Wu, D., Liu, Y.-C., Zheng, Z.-X., and Wang, S. (2016). Impact Energy Absorption Behavior of Cemented Coal Gangue-Fly Ash Backfill. *Geotech Geol Eng* 34, 471–480. doi:10.1007/s10706-015-9958-5

Wu, D., Zhao, R., and Qu, C. (2019). Effect of Curing Temperature on Mechanical Performance and Acoustic Emission Properties of Cemented Coal Gangue-Fly Ash Backfill. *Geotech Geol Eng* 37, 3241–3253. doi:10.1007/s10706-019-00839-8

Xu, L., Li, B., Chi, Y., Li, C., Huang, B., and Shi, Y. (2018a). Stress-Strain Relation of Steel-Polypropylene-Blended Fiber-Reinforced Concrete under Uniaxial Cyclic Compression. *Advances in Materials Science and Engineering* 2018, 9174943. doi:10.1155/2018/9174943

Xu, L., Li, B., Ding, X., Chi, Y., Li, C., Huang, B., and Shi, Y. (2018b). Experimental Investigation on Damage Behavior of Polypropylene Fiber Reinforced Concrete under Compression. *Int J Concr Struct Mater* 12, 68. doi:10.1186/s40069-018-0302-3

Xu, W.-B., Liu, B., and Wu, W.-L. (2020). Strength and Deformation Behaviors of Cemented Tailings Backfill under Triaxial Compression. *J. Cent. South Univ.* 27, 3531–3543. doi:10.1007/s11771-020-4568-7

Xu, W., Li, Q., and Zhang, Y. (2019). Influence of Temperature on Compressive Strength, Microstructure Properties and Failure Pattern of Fiber-Reinforced Cemented Tailings Backfill. *Construction and Building Materials* 222, 776–785. doi:10.1016/j.conbuildmat.2019.06.203

Xue, G., Yilmaz, E., Feng, G., Cao, S., and Sun, L. (2021). Reinforcement Effect of Polypropylene Fiber on Dynamic Properties of Cemented Tailings Backfill under Shpb Impact Loading. *Construction and Building Materials* 279, 122417. doi:10.1016/j.conbuildmat.2021.122417

Xue, G., Yilmaz, E., Song, W., and Cao, S. (2019). Mechanical, Flexural and Microstructural Properties of Cement-Tailings Matrix Composites: Effects of Fiber Type and Dosage. *Composites Part B: Engineering* 172, 131–142. doi:10.1016/j.compositesb.2019.05.039

Yilmaz, E. (2018). Stope Depth Effect on Field Behaviour and Performance of Cemented Paste Backfills. *International Journal of Mining, Reclamation and Environment* 32, 273–296. doi:10.1080/17480930.2017.1285858

Ying, M., and Jin-Xin, G. (2018). Seismic Failure Modes and Deformation Capacity of Reinforced Concrete Columns under Cyclic Loads. *Periodica Polytechnica Civil Engineering* 62, 80–91. doi:10.3311/ppci.9893

Yu, K.-Q., Yu, J.-T., Dai, J.-G., Lu, Z.-D., and Shah, S. P. (2018). Development of Ultra-High Performance Engineered Cementitious Composites Using Polyethylene (Pe) Fibers. *Construction and Building Materials* 158, 217–227. doi:10.1016/j.conbuildmat.2017.10.040

Yu, K., Ding, Y., Liu, J., and Bai, Y. (2020). Energy Dissipation Characteristics of All-Grade Polyethylene Fiber-Reinforced Engineered Cementitious Composites (Pe-Ecc). *Cement and Concrete Composites* 106, 103459. doi:10.1016/j.cemconcomp.2019.103459

Yun, H.-D., Yang, I.-S., Kim, S.-W., Jeon, E., Choi, C.-S., and Fukuyama, H. (2007). Mechanical Properties of High-Performance Hybrid-Fibre-Reinforced Cementitious Composites (Hphfrccs). *Magazine of Concrete Research* 59, 257–271. doi:10.1680/macr.2007.59.4.257

Yuyama, S., Li, Z.-W., Ito, Y., and Arazoe, M. (1999). Quantitative Analysis of Fracture Process in Rc Column Foundation by Moment Tensor Analysis of Acoustic Emission. *Construction and Building Materials* 13, 87–97. doi:10.1016/s0950-0618(99)00011-2

Zhou, J., Pan, J., and Leung, C. K. Y. (2015). Mechanical Behavior of Fiber-Reinforced Engineered Cementitious Composites in Uniaxial Compression. *J. Mater. Civ. Eng.* 27, 04014111. doi:10.1061/(asce)mt.1943-5533.0001034

Zhou, Y., Zhong, Q., Xing, F., Sui, L., Huang, Z., and Guo, M. (2020). Influence of Cyclic Loading on the Tensile Fracture Characteristics of Ultra-High Performance Engineered Cementitious Composites. *Construction and Building Materials* 240, 117937. doi:10.1016/j.conbuildmat.2019.117937

Conflict of Interest: The authors declare that the research was conducted in the absence of any commercial or financial relationships that could be construed as a potential conflict of interest.

Publisher's Note: All claims expressed in this article are solely those of the authors and do not necessarily represent those of their affiliated organizations, or those of the publisher, the editors, and the reviewers. Any product that may be evaluated in this article, or claim that may be made by its manufacturer, is not guaranteed or endorsed by the publisher.

frontiers in Materials

ORIGINAL RESEARCH
published: 02 November 2021
doi: 10.3389/fmats.2021.764410

Study on the Optimization of Filling Ratio and Strength Variation Characteristics of Cemented Backfills Containing Fly Ash

Baomeng Chang[1,2]*, *Cuifeng Du*[1,2]*, *Xiaofeng Chu*[3] and *Long Zhang*[3]

[1]School of Civil and Resources Engineering, University of Science and Technology Beijing, Beijing, China, [2]State Key Laboratory of High-Efficient Mining and Safety of Metal Mines of Ministry of Education, University of Science and Technology Beijing, Beijing, China, [3]Jiaojia Gold Mine, Shandong Gold Mining (Laizhou) Co., Ltd., Yantai, China

The fly ash for underground filling can effectively utilize solid waste, improve the strength of the backfill, and reduce the cost, thus creating good social and economic benefits. Relying on the filling requirements of a gold mine in Jilin, this paper carried out the filling ratio experiments containing fly ash and analyzed the reasons for the variation of the backfill strength based on the hydration characteristics of cement and fly ash and scanning electron microscope. The results show that fly ash has an overall effect on the strength of the backfill, and the strength development is mainly concentrated in the period of 28–56 d; when the filling slurry contains tailings, the excessive amount of fly ash is likely to cause a large number of fine particles to obstruct the hydration of cementitious materials; when the concentration of the filling slurry is 74%, the cement content is 5%, the mass ratio of waste rock-tailings-fly ash is 6:2:3, and the CaO content is 6:3, the strength of the backfill is significantly higher than the current strength of the backfill of the mine, and the cost can be saved by RMB 0.56 per cubic meter; the strength characteristics of the backfill mainly depend on the pore structure; when the filling slurry is better matched, the cement and fly ash hydration generates a large number of C-S-H gel particles, which wraps the aggregate to form a dense structure with less pore structure, and the strength of the backfill increases; the strength variation process of backfill containing cement and fly ash is divided into cement hydration period, fly ash infiltration period, and slurry hardening period. To enhance the strength of the backfill, it is necessary to determine the appropriate cementitious material ratio to maximize the excitation of fly ash hydration during the fly ash infiltration period, and the hydration produces a gel structure with an excellent aggregate ratio. In addition, the slurry hardening reduces the porosity of the backfill. The results can provide basic data and theoretical guidance for further promotion and application of fly ash in mine filling.

Keywords: fly ash, cementitious filling, hydration, filling ratio, scanning electron microscope

OPEN ACCESS

Edited by:
Erol Yilmaz,
Recep Tayyip Erdoğan University, Turkey

Reviewed by:
Jiangyu Wu,
China University of Mining and Technology, China
Chongchong Qi,
Central South University, China

***Correspondence:**
Baomeng Chang
changbaomeng@163.com
Cuifeng Du
1367724455@qq.com

Specialty section:
This article was submitted to Structural Materials, a section of the journal Frontiers in Materials

Received: *25 August 2021*
Accepted: *23 September 2021*
Published: *02 November 2021*

Citation:
Chang B, Du C, Chu X and Zhang L (2021) Study on the Optimization of Filling Ratio and Strength Variation Characteristics of Cemented Backfills Containing Fly Ash. Front. Mater. 8:764410. doi: 10.3389/fmats.2021.764410

INTRODUCTION

The cemented filling method is increasingly used in metal mines because of its effective ground pressure control, as well as its good environmental and economic benefits (Chen et al., 2021; Li et al., 2021). However, as mineral resources enter the deep mining stage, the ground pressure control and filling costs are increasing. There is an urgent need to find low-cost alternative cementitious materials that can increase the strength of the backfill (Yin et al., 2018; Qi and Fourie, 2019).

Fly ash is a powdered solid waste discharged from coal-fired thermal power plants after burning pulverized coal, whose reserves are huge and inexpensive (Nath and Sarker, 2015; Fang et al., 2018; Fu et al., 2018; Fan et al., 2019). As a substitute for filling cementing material, fly ash can reduce the cost of filling, improve the strength of the backfill, and create good economic and social benefits (Azmee and Shafiq, 2019; Ardahanli et al., 2021; Zafar and Alqahtani, 2021). Some scholars have studied the application of fly ash in the field of mine filling (Capasso et al., 2019; Chen et al., 2020; Yang, 2020): Behera et al. analyzed the chemical composition, morphology, and mineral composition of fly ash to explore its application prospects in mine filling (Behera et al., 2019); Liang et al. optimized the best filling ratio of fly ash, quicklime, gypsum, and cement by orthogonal experiments (Liang et al., 2019); Wang et al. used fly ash as cementitious material and coal gangue as aggregate to determine the best ratio of filling slurry by integrated equilibrium method (Wang et al., 2019); Yang et al. predicted the effect of fly ash content on backfill strength based on backfill strength and BP neural network model (Yang et al., 2019); Wang studied the properties of compressive strength of fly ash-doped filling slurry (Wang, 2020); Liu et al. analyzed the effect of different excitants on the strength properties of fly ash-containing backfill (Liu et al., 2021); Cui et al. studied the effect of excitants on the strength of fly ash-containing backfill by controlling variables and mechanical analysis (Cui et al., 2018). Current research on backfill containing fly ash has focused more on macroscopic strength variation, while research on the influence of microstructure on the strength of backfill and the determination of the stages of strength variation of backfill needs to be further developed. Therefore, based on the filling demand of a gold mine in Jilin and from the perspectives of macroscopic strength and microstructural changes, this paper carried out experiments of fly ash on the effect of backfill strength and the optimization of the filling ratio containing fly ash, analyzed the effect of fly ash on the strength of the backfill, selected the optimal filling ratio for the mine, and determined the causes of the strength variation, the strength variation stage, and the influence of each stage on the strength development of the backfill containing fly ash based on the hydration characteristics of cement and fly ash and the scanning electron microscope. The research provides basic data and theoretical guidance for the further promotion and application of fly ash in mine filling.

ENGINEERING BACKGROUND

The gold mine in Jilin adopts the sublevel open stopping with delayed filling, which is divided into two phases according to the sequence of mining. The first phase of the stope after filling needs to support the surrounding rock to ensure the safety of the second phase of mining. For the mining requirement, the 28 d strength of the backfill of the first phase stope should reach 0.8 MPa. The filling aggregate is tailings and crushed waste rock, cement is used as cementing material, and the slurry concentration reaches 70–75%, which is transported to the stope by gravity. However, since the mine's tailings contain cyanide, it cannot be used for underground filling. Therefore, all the filling tailings are purchased. Moreover, the filling times line is increasing with the mining, so the slurry concentration needs to be reduced to achieve gravity transportation. To achieve the expected backfill strength, it is necessary to increase the cement consumption, which further increases the filling cost. According to monitoring the existing backfill quality of the mine, the backfill strength can only reach 0.67 MPa at 28 d and 1.05 MPa at 56 d when the cement content is 10% and the waste rock-tailings ratio is 3:1. The insufficient backfill strength has led to many collapses (**Figure 1** shows the collapsed backfill of the stope), which seriously threatens the second phase of the stope. Based on this background, it is proposed to add fly ash to the filling material of the mine and carry out proportional experiments of cemented filling with fly ash to increase the strength of the backfill and reduce the filling cost.

FIGURE 1 | The collapsed backfill of the stope.

EXPERIMENT MATERIALS AND SCHEME

Experiment Materials

1) The moisture content of the waste rock used for filling is 3.63%, and the gradation is measured by manual screening, as shown in **Figure 2**. The particle size of the waste rock ranges

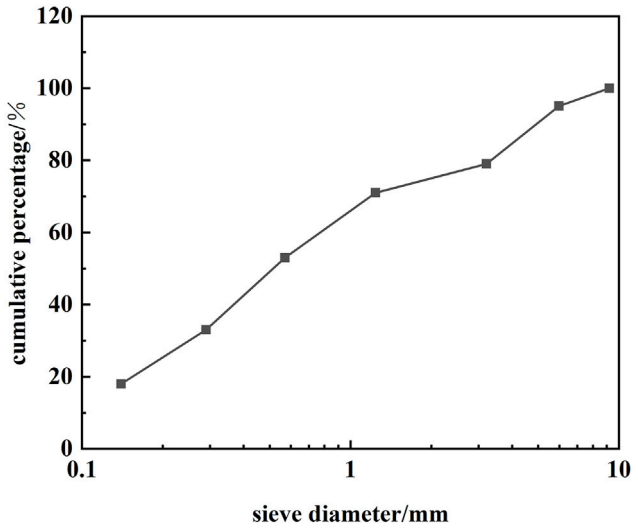

FIGURE 2 | Gradation of filling waste rock.

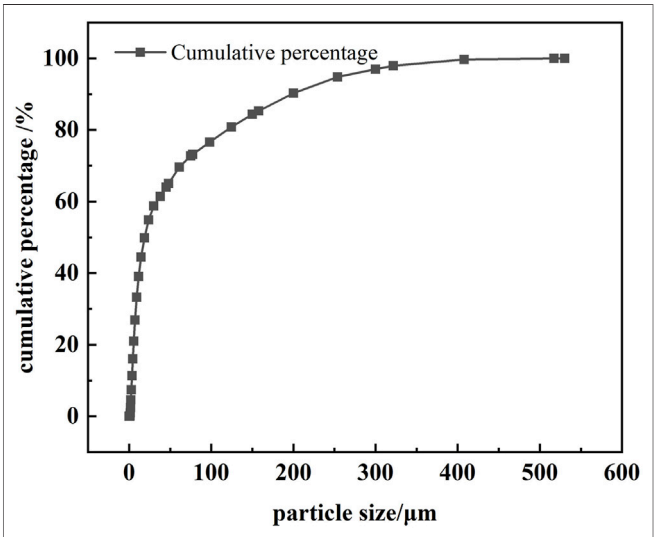

FIGURE 3 | Cumulative percentage of tailings particle size.

from 0.1 to 10 mm, and the range of –2 mm is relatively high, nearly 70%.

2) The moisture content of tailings is 12.36%. Particle size distribution is tested by the laser particle size analyzer, and the result is shown in **Figure 3**. The particle size distribution range is 0.243–521.6 μm, of which 0 ~ 1 μm accounted for 1.45%, 1–10 μm accounted for 14.21%, 10–100 μm accounted for 57.34%, and 100–530 μm accounted for 27%. The mineral composition of tailings tested by XRD is shown in **Figure 4** and is mainly quartz, albite, and dolomite, and the main chemical composition tested by XRF is SiO_2 and Al_2O_3, accounting for 83.51%.
3) The cement is 32.5 ordinary Portland cement, the main mineral composition and chemical composition of which

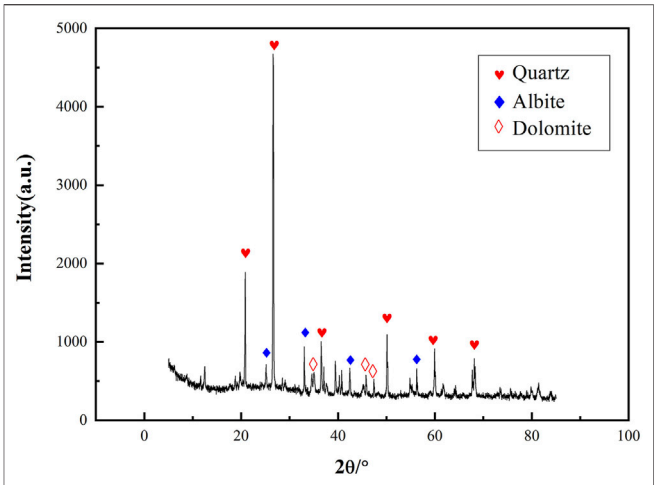

FIGURE 4 | Mineral composition of tailings.

TABLE 1 | Chemical composition of cement.

Chemical composition	CaO	SiO_2	Al_2O_3	Fe_2O_3	MgO
Content/%	52.89	27.72	7.56	2.89	3.86
Chemical composition	Na_2O	K_2O	P_2O_5	MnO	TiO_2
Content/%	0.79	1.34	0.27	1.87	0.81

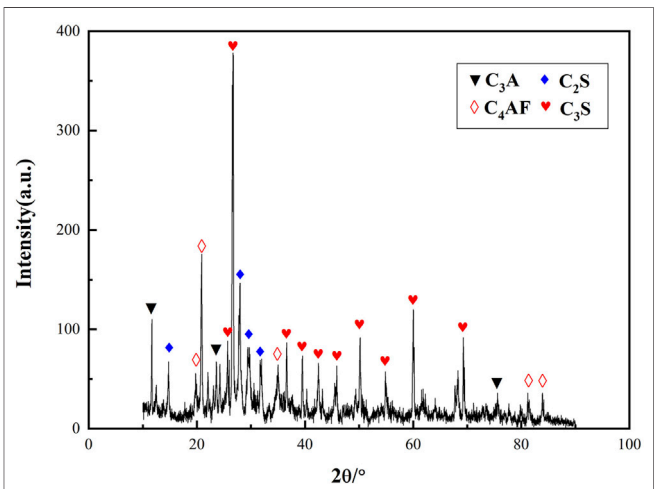

FIGURE 5 | Mineral composition of cement.

were determined by XRD and XRF, respectively. The chemical composition is shown in **Table 1**, and the mineral composition is shown in **Figure 5**. The main chemical composition of the cement is CaO and SiO_2, accounting for 80.61% of the total cement. The main mineral composition is tricalcium silicate ($3CaO•SiO_2$, abbreviated as C_3S), dicalcium silicate ($2CaO•SiO_2$, abbreviated as C_2S), tricalcium aluminate ($3CaO•Al_2O_3$, abbreviated as C_3A), and tetra-calcium ferroaluminate

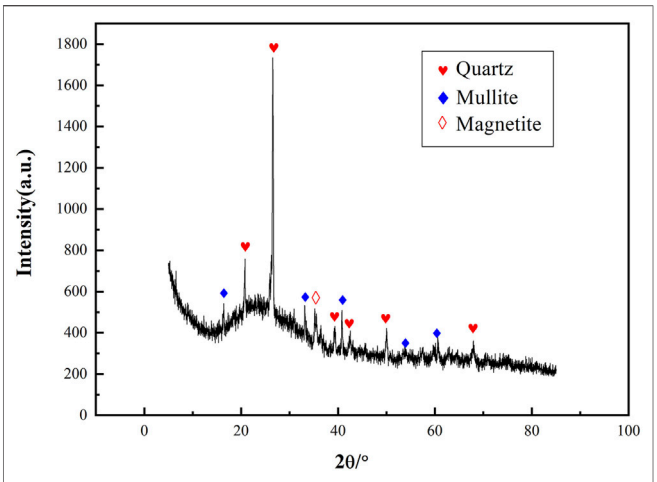

FIGURE 6 | Mineral composition of fly ash.

($4CaO•Al_2O_3•Fe_2O_3$, abbreviated C_4AF), with contents of 49.18, 16.08, 8.56, and 7.02%, respectively.

4) The moisture content of fly ash is 8.69% and the chemical composition is SiO_2 content 54.1%, Al_2O_3 content 23.2%, Fe_2O_3 content 4.3%, and CaO content 2.9%. The mineral composition is shown in **Figure 6** and is mainly quartz, mullite, and magnetite. According to ASTM C 618 standard, the fly ash has low CaO content and poor activity, and it belongs to class F (Dai et al., 2021).

Experiment Scheme

It was determined in the field that the filling slurry concentration realizes gravity transportation at about 74%, when the slurry diffusivity was more than 80 cm, with good workability and no segregation and precipitation (Xiao et al., 2019; Huang et al., 2021). Therefore, this value was taken as the standard of filling slurry concentration. According to the filling materials in the mine, experiments of fly ash on the effect of the backfill strength and the optimization of the backfill ratio were carried out. The experiment scheme of fly ash on the effect of the backfill strength is shown in **Table 2**, and the optimization experiments of the backfill ratio are carried out based on the results of the experiments in **Table 2**.

The materials of each experiment scheme placed in the mixing bucket were weighted. The mixer was used to mix the slurry evenly. Then, the slurry was loaded into the mold of φ80 × 200 mm. Because of the low initial strength of the backfill, it was easy to be damaged after demoulding. Therefore, it was demoulded after 24 h and moved to the constant temperature and humidity box for maintenance, with the temperature set at 20 ± 1°C and humidity at 95%. After curing to the predetermined age, the uniaxial compressive strength was measured by WES-100 hydraulic universal testing machine, and representative backfill blocks were selected and made into standard specimens. The microstructure characteristics were observed by scanning electron microscope after gold spraying (Hu et al., 2019; Xie, et al., 2020) to analyze the variation mechanism of backfill strength. The flow chart of experiments is shown in **Figure 7**.

ANALYSIS OF EXPERIMENT RESULTS

Study on the Effect of Fly Ash on the Strength of Backfill

To analyze the effect of fly ash on the strength of backfill, group A and group B experiments were conducted, respectively. The results of 28, 56, and 90 d uniaxial compressive strength of backfill are shown in **Figure 8**.

When the cement content was 9%, the 28 d uniaxial compressive strength of the backfill without fly ash was 0.57 MPa and the 56 d uniaxial compressive strength was 0.97 MPa. As can be seen from **Figure 8**, the strength of the backfill in both groups A and B is significantly improved under the condition of adding fly ash. The 28 d uniaxial compressive strength is greater than 1.65 MPa. The 56 d uniaxial compressive strength is greater than 2.24 MPa. That is, the addition of fly ash in the slurry has an overall promoting effect on the strength of the backfill.

As shown in **Figure 8A**, when the filling aggregate was all waste rock, the strength of the backfill gradually increased with the increase of fly ash to cement mass ratio, and both of them increased approximately linearly. The 56 d strength was 2.24 times the 28 d strength (mean value), while the strength grew less from 56 to 90 d during the maintenance period. The strength development of backfill containing fly ash was mainly concentrated in the maintenance period from 28 to

TABLE 2 | Experiments of the fly ash on the effect of backfill strength.

Number	Concentration/%	Cement content/%	The mass ratio of fly ash-cement	The mass ratio of waste rock-tailings
A-1	74	9	2	All waste rock
A-2	74	9	3	All waste rock
A-3	74	9	4	All waste rock
A-4	74	9	5	All waste rock
B-1	74	9	2	3:1
B-2	74	9	3	3:1
B-3	74	9	4	3:1
B-4	74	9	5	3:1

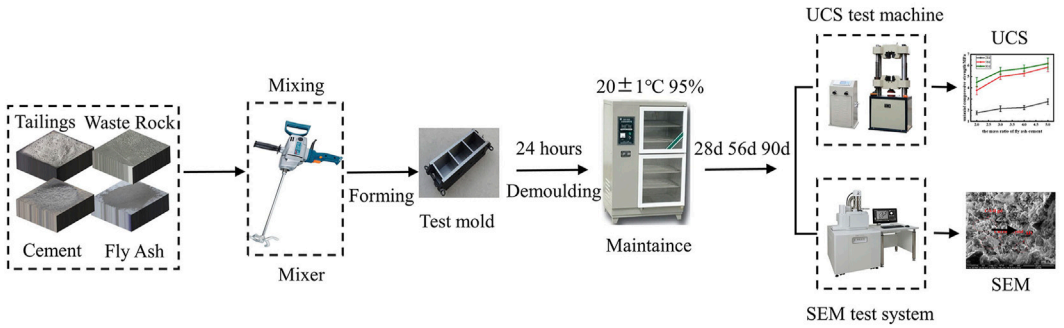

FIGURE 7 | Experiments flow chart.

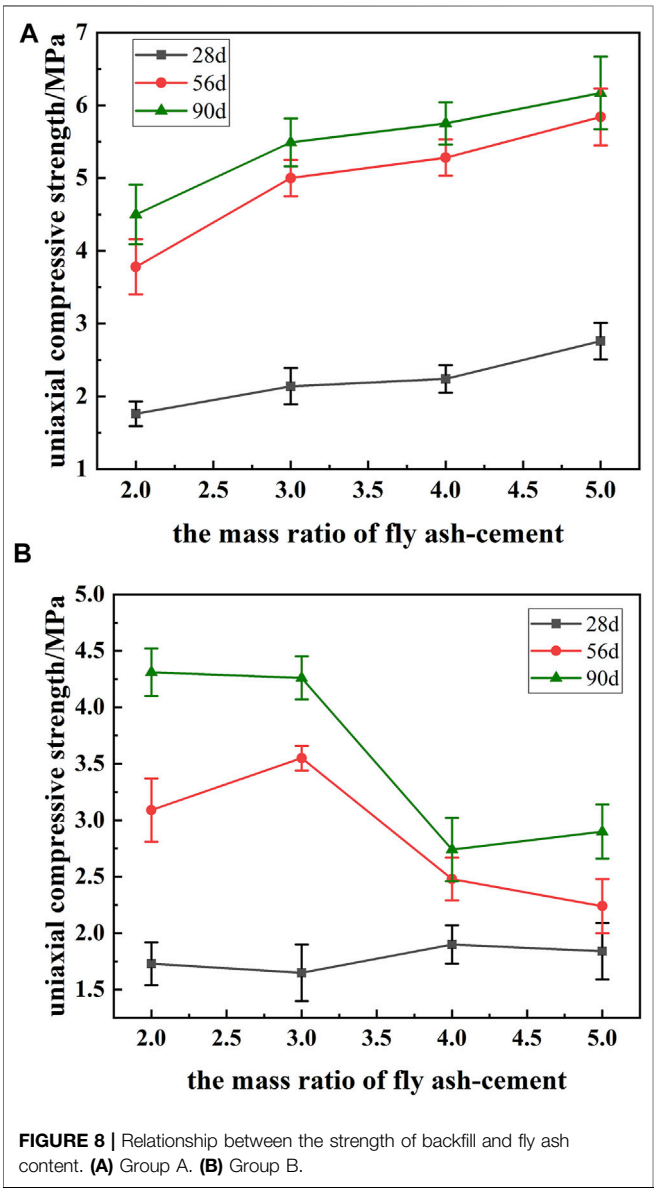

FIGURE 8 | Relationship between the strength of backfill and fly ash content. **(A)** Group A. **(B)** Group B.

56 d, after which the growth trend slowed down. As shown in **Figure 8B**, when the filling aggregate was waste rock and tailings with the ratio of 3:1, after the fly ash-cement mass ratio exceeded 3 (the fly ash-tailings mass ratio was about 3:2 at this time), the strength of the backfill suddenly decreased, and fly ash had a great negative effect on the strength at this time, which is different from the study of Dong et al., 2018. Generally, the increase of fly ash content promotes the strength of backfill in the middle and late stages, and the main reason for fly ash inhibiting the strength of backfill in this experiment is as follows: as the tailing particles were fine, the continuous increase of fly ash content led to more fine particles in the backfill, which hindered the hydration of cementitious materials and affected the growth of the backfill strength. Therefore, fly ash has a two-way effect on the late strength of the backfill under the condition of tailings. It is necessary to determine the appropriate filling ratio of tailings and fly ash.

Study on Optimization of Filling Ratio with Fly Ash

1) From the results of group A, it can be seen that under the condition that the filling aggregate is all waste rock, the strength of the backfill shows an increasing trend with the increase of fly ash content. However, when the amount of filling aggregate is too much, the bonding quality of the interface between slurry and aggregate will be reduced, weakening the integrity of the backfill. Therefore, the group C experiment was conducted to determine the appropriate ratio of filling aggregate to fly ash: the filling slurry concentration was 74%, the cement content was 6.5%, the filling aggregate was all waste rock, and the mass ratios of waste rock-fly ash were 1:1, 2:1, 3:1, and 4:1, respectively. In addition, due to the poor activity of the fly ash, 3% content CaO was added to the slurry

As shown in **Figure 9**, the 28 d uniaxial compressive strength of the backfill gradually decreased with the increase of waste rock

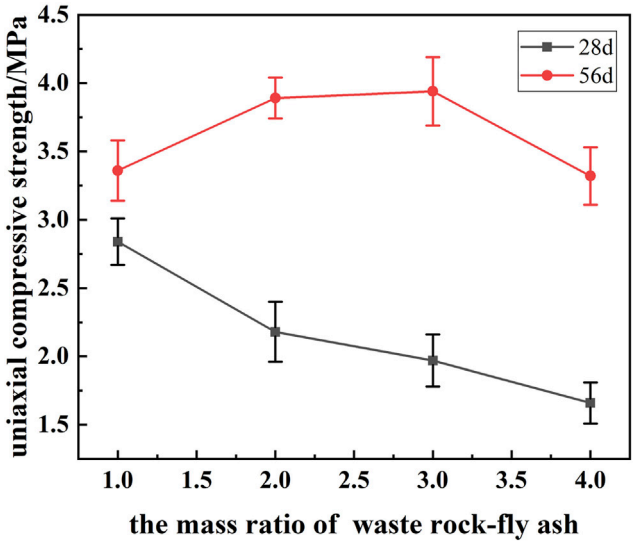

FIGURE 9 | The relationship between backfill strength and mass ratio of waste rock to fly ash (group C).

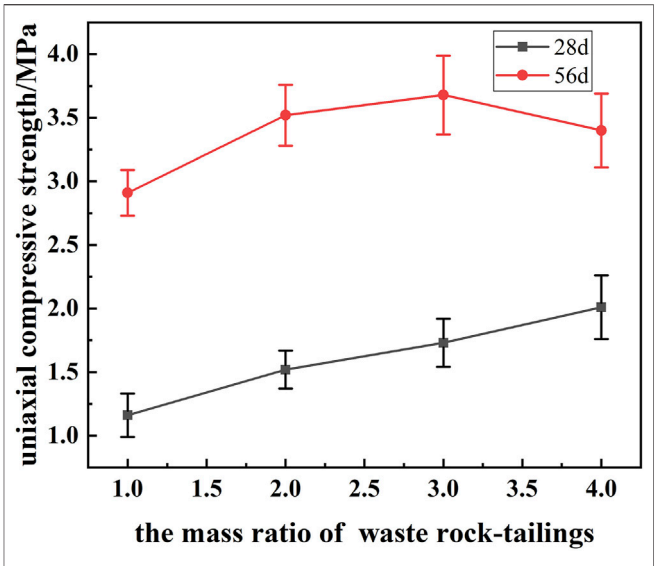

FIGURE 10 | The relationship between backfill strength and waste rock to tailings ratio (group D).

content, while the 56 d uniaxial compressive strength showed a trend of increasing and then decreasing. As fly ash mainly affected the strength of the backfill in the middle and late stages, the fly ash was not heavily hydrated at 28 d. The waste rock was not completely wrapped by the gel and the integrity was poor; therefore, the strength at 28 d decreased with the increase of waste rock; while at 56 d, the fly ash was hydrated to produce a large amount of gel and wrapped waste rock, which showed that the strength of the backfill was higher than that at 28 d, and increased first with the increase of waste rock content. When the waste rock-fly ash mass ratio exceeded 2:1, too much waste rock was not wrapped. The 56 d strength of the backfill started to decrease, which was the optimal value of the waste rock to fly ash, that is, the early strength of the backfill met the demand and had no inhibitory effect on the middle and late strength.

2) Group D experiment was carried out based on the waste rock-fly ash mass ratio of 2:1, and tailings were added to the filling aggregate to determine the optimum tailings content. Group D experiment scheme: the cement content was 6.5%, the mass ratio of waste rock-fly ash was 2:1, the mass ratios of waste rock-tailings were 1:1, 2:1, 3:1, and 4:1, respectively, and CaO content was 3%

As can be seen from **Figure 10**, with the increase of waste rock to tailings mass ratio, i.e., with the decrease of tailings content, the 28 d uniaxial compressive strength of the backfill increased linearly. The 56 d uniaxial compressive strength showed a trend of first increase and then decrease. The minimum strength of the backfill was 1.16 MPa when the mass ratio of waste rock-tailings was 1:1, which was better than that of the backfill without fly ash; the 56 d uniaxial compressive strength reached the maximum when the waste rock-tailings mass ratio

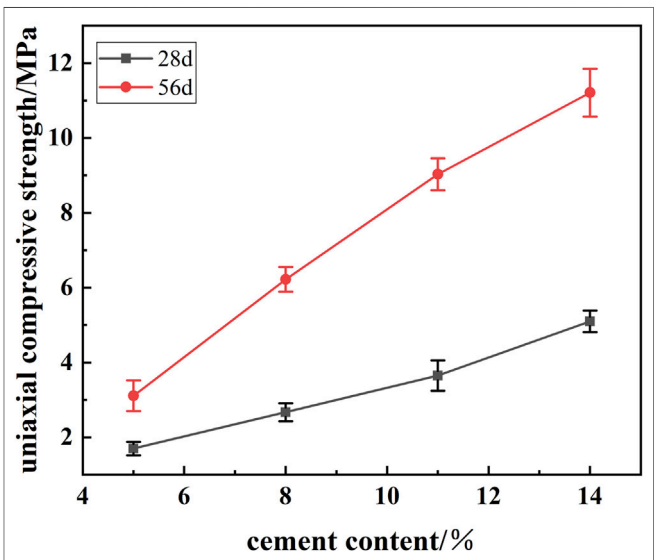

FIGURE 11 | The relationship between the strength of backfill and cement content (group E).

was 3:1. At this time, the number of tailings had no inhibiting effect on both 28 d and 56 d uniaxial compressive strength.

3) Based on the results of group C and group D, the optimal mass ratio of waste rock-tailings-fly ash was determined to be 6:2:3. On this basis, group E experiments were conducted to determine the optimal cement content to meet the filling demand of the mine: the mass ratio of waste rock-tailings-fly ash was 6:2:3, CaO content was 3%, and the cement content was 5, 8, 11, and 14%, respectively.

From **Figure 11**, it can be seen that the uniaxial compressive strength of the backfill at 28 and 56 d increases linearly with the increase of cement content, and the fitting equations are as follows:

$$28\text{d}: \cdot y = 0.373x - 0.26\left(R^2 = 0.989\right), \quad (1)$$

$$56d: \cdot y = 0.904x - 1.19\left(R^2 = 0.994\right). \quad (2)$$

where y is the uniaxial compressive strength of the backfill, MPa; x is cement content. The slope of the 56 d fitting equation was significantly greater than that of 28 d, i.e., its strength development was significantly higher than that of 28 d. The increase of cement content had a more obvious effect on the 56 d strength of the backfill. This was mainly since 28–56 d was the main hydration stage of fly ash, and the increase of cement content led to the increase of generated OH^-, which promoted the hydration of a large amount of fly ash during 28–56 d.

4) When the filling slurry concentration was 74%, the mass ratio of waste rock-tailings-fly ash was 6:2:3, CaO content was 3%, and cement content was 5%; the uniaxial compressive strength of the backfill at 28 and 56 d was 1.70 and 3.11 Mpa, respectively, which met the demand of filling of the mine. Based on the market price of building materials at the mine site, the filling cost was calculated as follows: the price of 32.5 ordinary Portland cement bought from local cement plant was RMB 340 per ton; the waste rock was produced from underground mining, and the transportation and crushing cost was RMB 20 per ton; all tailings were purchased from other mines at a cost of RMB 18 per ton; fly ash was taken from nearby thermal power generation at a price of RMB 70 per ton; CaO was purchased from local enterprises at a price of RMB 240 per ton. After calculation, with the filling slurry concentration of 74%, the mass ratio of waste rock-tailings-fly ash of 6:2:3, CaO content of 3%, and cement content of 5%, the cost of filling slurry was RMB 80.32 per cubic meter. Compared with the current filling ratio under the condition of 74% concentration of filling slurry, 10% cement content, and 3:1 mass ratio of waste rock-tailings, it can save RMB 0.56 per cubic meter. In addition, the strength of the backfill can be increased by about 1 MPa at 28 d and 2 MPa at 56 d. It not only makes a large amount of use of fly ash and reduces the cost of filling but also improves the strength of the backfill significantly, which improves the safety factor and economic benefits of mining.

Analysis of Microstructure and Strength Variation Characteristics of the Backfill

To analyze the reasons for the strength variation of the backfill, the backfill of the stope, group A3, and group B3 were selected, respectively. Their images were magnified to 2000 times to observe the microstructure by scanning electron microscope. The images of the backfill are shown in **Figure 12**.

The backfill is a porous structure composed of cementitious material hydrated colloid, $Ca(OH)_2$ crystals, solid particles, and pores, etc. The relationship between its strength and porosity is as follows:

$$S = S_0 \exp\left(-bp\right), \quad (3)$$

where S is the ideal state strength of the backfill, MPa; S_0 is the strength of the backfill when the porosity is 0, MPa; b is a constant related to the cementitious material and maintenance age; p is the internal porosity of the backfill. It can be seen that the strength decreases exponentially as the porosity of the backfill increases, which can be analyzed visually by the structural characteristics of the backfill pores (Cao and Song, 2018; Nakata et al., 2018; Wang and Qiao, 2019). The reaction process of cement and fly ash hydration in the backfill: C_3S, C_2S, C_3A, and C_4AF in cement react with water to generate $Ca(OH)_2$ and C-S-H, calcium aluminate, and other gel materials, in which $Ca(OH)_2$ is the intermediate product to promote the mutual reaction of ions in the solution and then reacts with a large amount of SiO_2 and Al_2O_3 in fly ash to promote the generation of gel materials. The gel material can bind to the aggregate and fill the pore structure after hardening and is the key component affecting the strength of the backfill (Yu et al., 2018).

From **Figure 12A**, the 28 d scanning electron microscope of the backfill can be seen that the cement was hydrated to generate part of the flocculent C-S-H gel, accompanied by a small amount of fibrous AFt and plate-like $Ca(OH)_2$ crystals. There were still some inert particles around the gel that have not been wrapped. The overall structure was relatively loose, with a more developed pore structure (Zhang et al., 2021). The strength of the backfill was low at 0.67 MPa, which did not meet the demand of the mine; **Figure 12B** shows the structure of the backfill at 28 d under the condition of adding fly ash and waste rock. The hydration of cement and fly ash was obvious, generating a large number of flocculent C-S-H gel, and the hydration products were staggered and well wrapped around the aggregate. Compared with Figure 12A, the structural integrity and connectivity were enhanced. The pores were filled with C-S-H gels. The strength was well developed, reaching 2.24 MPa. **Figure 12C** shows the structure of the 28 d backfill under the condition of adding fly ash, waste rock, and tailings. Due to the increase of fine particles in the slurry caused by the addition of fly ash and tailings, and the poor hydration condition of fly ash, the amount of C-S-H gel was reduced compared with **Figure 12B**. A large number of fine particles of tailings were not connected and the distribution was more dispersed, which led to the increase in the porosity of the backfill and the inability to form a dense structure (Liu et al., 2018; Fu et al., 2020). The macroscopic performance of the backfill strength is reduced to 1.90 MPa. Comparing **Figure 9D** and **Figure 9A**, it can be seen that during 28–56 d, the flocculent gel further developed and closely connects with the aggregate. Besides, the tightness of the backfill increased significantly and the porosity decreased, i.e., a large amount of hydration reaction of fly ash occurs during 28–56 d.

Based on the results of scanning electron microscope analysis and the hydration characteristics of cement and fly ash, the strength variation process of the backfill containing fly ash can be divided into three stages: cement hydration period, fly ash

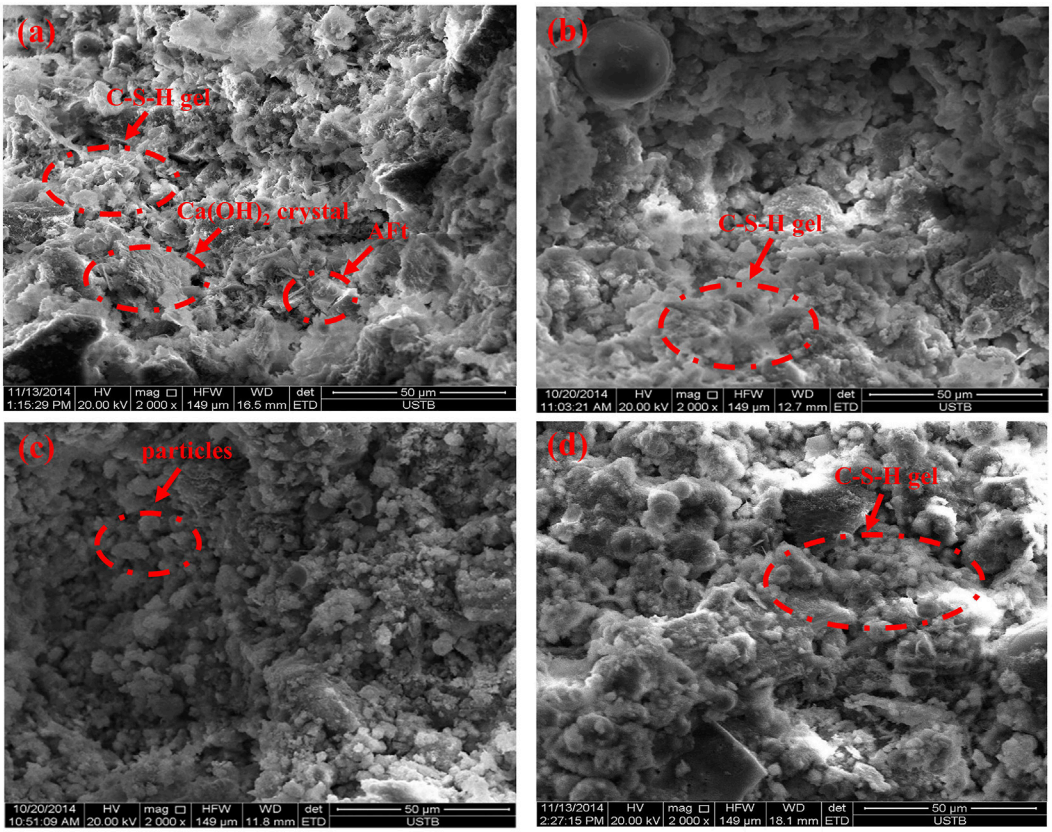

FIGURE 12 | Scanning electron microscope comparison of the backfill. **(A)** 28 d backfill of stope. **(B)** 28 d backfill of group A3. **(C)** 28 d backfill of group B3. **(D)** 56 d backfill of group A3.

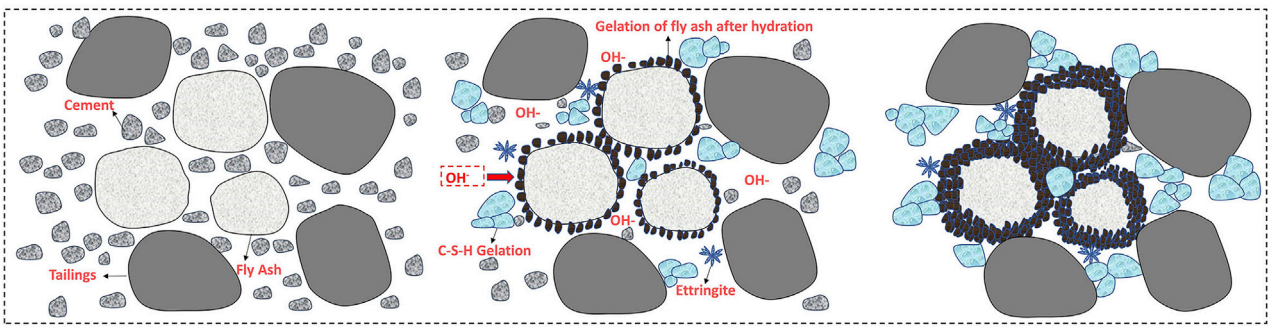

FIGURE 13 | The strength variation process of backfill.

infiltration period, and slurry hardening period, as shown in **Figure 13**.

During the hydration period of cement, C_3S, C_2S, C_3A, and C_4AF in cement were hydrated to generate $Ca(OH)_2$, C-S-H, and other gel materials. The slurry is in a strong alkali state, and the surface of fly ash was wrapped by gel particles after hydration, which led to slow OH^- infiltration, thus reducing its hydration rate and less participation in the early stage of hydration. During the fly ash infiltration period, although the gels were gathered on the surface of fly ash particles, their structure was not stable and was continuously destroyed and reorganized under the osmotic pressure of the slurry solution to promote OH^- infiltration (Zhang et al., 2020; He et al., 2021). In addition, the pores between the cementitious particles also provided channels for OH^- immersion. The OH^- reacted with a large amount of SiO_2 and Al_2O_3 in fly ash to accelerate the hydration of fly ash in the middle and late stages, which continuously generated C-S-H and calcium aluminate gels, and it was the main stage of hydration

reaction occurring in fly ash. However, when tailings were added to the slurry, the hydration conditions of fly ash deteriorated due to its finer particles and larger specific surface, which could be uniformly distributed around the fly ash and reduced the contact area between fly ash and $Ca(OH)_2$ (Lee and Kim, 2017; Liu et al., 2018). The fly ash itself had no strength, thus presenting the results of group B: when the fly ash-cement mass ratio exceeded 3, the late strength of the backfill decreased instead. During the hardening period of the slurry, the gel particles generated by the hydration reaction of cement and fly ash combined and continuously formed a structurally stable gel and wrapped coarse and fine aggregates to form a dense structure with reduced porosity, which macroscopically showed an increase in the strength of the filled body. Therefore, to play the role of fly ash in the backfill, firstly, it was necessary to determine the appropriate cementitious material ratio to generate the right amount of OH^- during the hydration period of cement to maximize the activation of fly ash and increase its hydration; secondly, the gel structure produced by hydration needed to be in excellent ratio with the aggregate in the stage of slurry hardening period, with good connection performance to reduce the porosity and ensure the quality of the backfill.

CONCLUSION

In this paper, the effect of fly ash on the backfill strength was analyzed based on the experiments of the filling ratio containing fly ash, and the variation process of backfill strength was analyzed. The specific conclusions are as follows:

1) Fly ash had a promoting effect on the strength of the backfill, and the strength development was mainly concentrated on 28–56 d; When the filling material contains tailings, adding too much fly ash will lead to a large number of fine particles in the backfill, hindering the hydration of cementitious material and affecting the development of backfill strength.
2) When the filling slurry concentration was 74%, the cement content was 5%, the mass ratio of waste rock-tailings-fly ash was 6:2:3, and the CaO content was 3%, the strength of the backfill was significantly higher than that of the current backfill of the mine, and the filling cost could be saved by RMB 0.56 per cubic meter.
3) The pore structure of the backfill determined its strength characteristics. To play the role of fly ash in the backfill, it is first necessary to determine the appropriate ratio of cementitious materials to generate the OH^- during the cement hydration period and activate the fly ash; secondly, the gel structure generated by hydration needs to be well proportioned with the aggregate during the slurry hardening period to reduce the porosity and ensure the quality of the backfill.

DATA AVAILABILITY STATEMENT

The original contributions presented in the study are included in the article/Supplementary Material; further inquiries can be directed to the corresponding authors.

AUTHOR CONTRIBUTIONS

BC: conceptualization, investigation, and writing—review and editing. CD: supervision. XC: writing—original draft. LZ: methodology and data curation.

FUNDING

This study was supported by the Funds of National Key Research and Development Program of China (2018YFC0604605) and Fundamental Research Fund for the Central Universities (FRF-TP-19-039A1).

REFERENCES

Ardahanli, M., Oltulu, M., and Alameri, I. (2021). The Effect of Preheating on the Properties of the Fly Ash Self-Compacting Concrete. *Black Sea J. Eng. Sci.* 4, 81–88. doi:10.34248/bsengineering.858520

Behera, S. K., Mishra, D. P., Ghosh, C. N., Prashant, Mandal, P. K., Singh, K. M. P., et al. (2019). Characterization of lead-zinc Mill Tailings, Fly Ash and Their Mixtures for Paste Backfilling in Underground Metalliferous Mines. *Environ. Earth Sci.* 78, 394. doi:10.1007/s12665-019-8395-9

Cao, S., and Song, W. (2018). Medium-Term Strength and Electromagnetic Radiation Characteristics of Cemented Tailings Backfill under Uniaxial Compression. *Geotech. Geol. Eng.* 36, 3979–3986. doi:10.1007/s10706-018-0542-7

Capasso, I., Lirer, S., Flora, A., Ferone, C., Cioffi, R., Caputo, D., et al. (2019). Reuse of Mining Waste as Aggregates in Fly Ash-Based Geopolymers. *J. Clean. Prod.* 220, 65–73. doi:10.1016/j.jclepro.2019.02.164

Chen, Q.-s., Sun, S.-y., Liu, Y.-k., Qi, C.-c., Zhou, H.-b., and Zhang, Q.-l. (2021). Immobilization and Leaching Characteristics of Fluoride from Phosphogypsum-Based Cemented Paste Backfill. *Int. J. Miner. Metall. Mater.* 28, 1440, 1452. doi:10.1007/s12613-021-2274-6

Chen, Y.-g., Guan, L.-l., Zhu, S.-y., and Chen, W.-j. (2021). Foamed concrete Containing Fly Ash: Properties and Application to Backfilling. *Construction Building Mater.* 273, 121685. doi:10.1016/j.conbuildmat.2020.121685

Cui, B., Liu, Y., Li, H., Guo, H., and Lu, Yao. (2018). Experimental Study of the Chemical Excitation on Gelation of Cement and Fly Ash Filling Paste. *Min. Res. Dev.* 38, 127–131. doi:10.13827/j.cnki.kyyk.2018.03.028

Dai, X., Ren, Q., Aydın, S., Yardımcı, M. Y., Lesage, K., and De Schutter, G. (2021). Enhancing Thixotropy and Structural Build-Up of Alkali-Activated Slag/fly Ash Pastes with Nano clay. *Mater. Struct.* 54, 163. doi:10.1617/s11527-021-01760-4

Dong, Y., Yang, Z., Gao, Q., and Yang, X. (2018). Effect of Fly Ash Content on Properties of Backfilling Materials Prepared with Iron Tailings. *J. Guangxi Univ.* 43, 219–225. doi:10.13624/j.cnki.issn.1001-7445.2018.0219

Fan, W.-D., Liu, B., Luo, X., Yang, J., Guo, B., and Zhang, S.-G. (2019). Production of Glass-Ceramics Using Municipal Solid Waste Incineration Fly Ash. *Rare Met.* 38, 245–251. doi:10.1007/s12598-017-0976-8

Fang, G., Ho, W. K., Tu, W., and Zhang, M. (2018). Workability and Mechanical Properties of Alkali-Activated Fly Ash-Slag concrete Cured at Ambient Temperature. *Construction Building Mater.* 172, 476–487. doi:10.1016/j.conbuildmat.2018.04.008

Fangfang, L., Xiyang, F., and Li, C. (2021). Effect of Different Activators on Rheological and Strength Properties of Fly Ash-Based Filling Cementitious Materials. *Adv. Civil Eng.* 2021, 1–9. doi:10.1155/2021/5538695

Fu, B., Cheng, Z., and Han, J. (2018). Experimental Study on Impermeability of Alkali Activated Fly Ash-Slag Concrete. *Bull. Chin. Ceram. Soc.* 37, 2255–2259. doi:10.16552/j.cnki.issn1001-1625.2018.07.031

Fu, J., Wang, J., and Song, W. (2020). Damage Constitutive Model and Strength Criterion of Cemented Paste Backfill Based on Layered Effect Considerations. *J. Mater. Res. Tech.* 9, 6073–6084. doi:10.1016/j.jmrt.2020.04.011

He, J., Long, G., Ma, K., Xie, Y., and Cheng, Z. (2021). Improvement of the Hydration of a Fly Ash-Cement System by the Synergic Action of Triethanolamine and C-S-H Seeding. *ACS Sust. Chem. Eng.* 9, 2804–2815. doi:10.1021/acssuschemeng.0c08618

Hu, J., Zhao, F., Ren, Q., Kuang, Y., Zhou, T., and Luo, Z. (2019). Microscopic Characterization and Strength Characteristics of Cemented Backfill under Different Humidity Curing Conditions. *R. Soc. Open Sci.* 6, 191227. doi:10.1098/rsos.191227

Huang, S., Yan, E., Fang, K., and Li, X. (2021). Effects of Binder Type and Dosage on the Mode I Fracture Toughness of Cemented Paste Backfill-Related Structures. *Construction Building Mater.* 270, 121854. doi:10.1016/j.conbuildmat.2020.121854

Lee, S.-H., and Kim, G.-S. (2017). Self-cementitious Hydration of Circulating Fluidized Bed Combustion Fly Ash. *J. Korean Ceram. Soc.* 54, 128–136. doi:10.4191/kcers.2017.54.2.07

Li, G., Sun, Y., and Qi, C. (2021). Machine Learning-Based Constitutive Models for Cement-Grouted Coal Specimens under Shearing. *Int. J. Mining Sci. Tech.* doi:10.1016/j.ijmst.2021.08.005

Liang, Y., Kong, H., Wang, C., Sun, Q., and Wang, D. (2019). Study on the Strength of Fly Ash Paste Filling Replacing Strip Pillar. *Min. Res. Dev.* 39, 84–87. doi:10.13827/j.cnki.kyyk.2019.07.018

Liu, S., Li, Z., Li, Y., and Cao, W. (2018). Strength Properties of Bayer Red Mud Stabilized by Lime-Fly Ash Using Orthogonal Experiments. *Construction Building Mater.* 166, 554–563. doi:10.1016/j.conbuildmat.2018.01.186

Liu, X., Zhao, X., Yin, H., Chen, J., and Zhang, N. (2018). Intermediate-calcium Based Cementitious Materials Prepared by MSWI Fly Ash and Other Solid Wastes: Hydration Characteristics and Heavy Metals Solidification Behavior. *J. Hazard. Mater.* 349, 262–271. doi:10.1016/j.jhazmat.2017.12.072

M. Azmee, N., and Shafiq, N. (2019). Investigating the Impacts of Ultra-Fine Calcium Carbonate in High-Volume Fly Ash Concrete for Structural Rehabilitation for Sustainable Development. *Sustainability* 11, 4671–4716. doi:10.3390/su11174671

Nakata, Y., Saito, T., Kajita, H., Otsuka, S., and Haruyama, N. (2018). Influence on Properties of High-Strength concrete by the Change of Sand-Total Aggregate Ratio in Identical Water-Cement Ratio. *Nihon Kenchiku Gakkai Kozokei Ronbunshu* 83, 751–761. doi:10.3130/aijs.83.751

Nath, P., and Sarker, P. K. (2015). Use of OPC to Improve Setting and Early Strength Properties of Low Calcium Fly Ash Geopolymer concrete Cured at Room Temperature. *Cement and Concrete Composites* 55, 205–214. doi:10.1016/j.cemconcomp.2014.08.008

Qi, C., and Fourie, A. (2019). Cemented Paste Backfill for mineral Tailings Management: Review and Future Perspectives. *Minerals Eng.* 144, 106025. doi:10.1016/j.mineng.2019.106025

Wang, C., Liu, Y., Hu, H., Li, Y., and Lu, Y. (2019). Study on Filling Material Ratio and Filling Effect: Taking Coarse Fly Ash and Coal Gangue as the Main Filling Component. *Adv. Civil Eng.* 2019, 1–11. doi:10.1155/2019/2898019

Wang, H., and Qiao, L. (2019). Coupled Effect of Cement-To-Tailings Ratio and Solid Content on the Early Age Strength of Cemented Coarse Tailings Backfill. *Geotech Geol. Eng.* 37, 2425–2435. doi:10.1007/s10706-018-00766-0

Wang, X. (2020). Experimental Study on the Performance of Goaf Filling Materials with High Content of Fly Ash. *IOP Conf. Ser. Earth Environ. Sci.* 569, 012014. doi:10.1088/1755-1315/569/1/012014

Xiao, B., Wen, Z., Wu, F., Li, L., Yang, Z., and Gao, Q. (2019). A Simple L-Shape Pipe Flow Test for Practical Rheological Properties of Backfill Slurry: A Case Study. *Powder Tech.* 356, 1008–1015. doi:10.1016/j.powtec.2019.09.012

Xie, S., Sun, Y., Wang, E., Chen, D., Wu, X., and Qi, P. (2020). Experimental and Mechanistic Research on Modifying the Mechanic Properties of the High Water Backfill Material by Electrochemical Treatment. *Sci. Rep.* 10, 17027. doi:10.1038/s41598-020-74115-8

Yang, J. (2020). Rheological Study on Cemented Coal Gangue Fly-Ash Backfill Slurry Associated with Fly Ash Impacts. *Kem* 831, 100–104. doi:10.4028/www.scientific.net/kem.831.100

Yang, X., Li, L., and Gao, Q. (2019). Study on Test and Ratio Optimization of Waste Rock-Fly Ash Aggregate Filling Slurry. *IOP Conf. Ser. Earth Environ. Sci.* 330, 042032. doi:10.1088/1755-1315/330/4/042032

Yin, B., Kang, T., Kang, J., Chen, Y., Wu, L., and Du, M. (2018). Investigation of the Hydration Kinetics and Microstructure Formation Mechanism of Fresh Fly Ash Cemented Filling Materials Based on Hydration Heat and Volume Resistivity Characteristics. *Appl. Clay Sci.* 166, 146–158. doi:10.1016/j.clay.2018.09.019

Yu, J., Li, G., and Leung, C. K. Y. (2018). Hydration and Physical Characteristics of Ultrahigh-Volume Fly Ash-Cement Systems with Low Water/binder Ratio. *Construction Building Mater.* 161, 509–518. doi:10.1016/j.conbuildmat.2017.11.104

Zafar, I., and Alqahtani, F. K. (2021). Effectiveness of Extended Curing for Fly Ash concrete against Corrosion Propagation under Severe Chloride Exposure. *Struct. Concrete*, 1–16. doi:10.1002/suco.202000614

Zhang, C., Fu, J., Song, W., Du, C., and Fu, H. (2021). High-volume Ultrafine Fly Ash-Cement Slurry Mechanical Properties and Strength Development Model Establishment. *Construction Building Mater.* 277, 122350. doi:10.1016/j.conbuildmat.2021.122350

Zhang, W., Wu, F., and Zhang, Y. (2020). Early Hydration and Setting Process of Fly Ash-Blended Cement Paste under Different Curing Temperatures. *J. Wuhan Univ. Technol.* 35, 87–96. doi:10.1007/s11595-020-2292-7

Conflict of Interest: Authors XC and LZ were employed by the company Jiaojia Gold Mine, Shandong Gold Mining (Laizhou) Co., Ltd.

The remaining authors declare that the research was conducted in the absence of any commercial or financial relationships that could be construed as a potential conflict of interest.

frontiers in Materials

ORIGINAL RESEARCH
published: 05 January 2022
doi: 10.3389/fmats.2021.744944

Quantitative Test and Engineering Application of Wear Resistance of a Kind of Mine-Filled Composite Pipeline

*Yong Wang[1], Gang-feng Yang[1], Cheng-liang Ma[2], Quan-li Jia[2] and Qin-guo Jin[3]**

[1]School of Civil and Resource Engineering, University of Science and Technology Beijing, Beijing, China, [2]School of Materials Science and Engineering, Zhengzhou University, Zhengzhou, China, [3]Zhengzhou Special Flux Materials Co., Ltd., Zhengzhou, China

Wear resistance is one of the most important performance indicators of filling pipelines, but there are few studies on its quantitative test and life prediction. In this paper, an experimental device and its application method for testing the wear resistance of the pipeline are proposed, and the device is used to test the wear resistance of the self-developed lining composite pipeline, the traditional 16 Mn steel pipeline and the ordinary carbon structural steel pipeline. The results show that the wear resistance of the composite lining material is 12.35 times of that of 16 Mn steel and 7.32 times of that of ordinary carbon structural steel. The wear resistance mechanism is analyzed from the perspective of the material composition of the composite liner, mainly because the composite liner material uses fused alumina grain sand, silicon carbide and other extremely wear-resistant materials with high hardness as aggregate, and the aggregates are spherical or nearly spherical particles, with smooth surface and small friction resistance. Finally, through a comparison engineering application of a certain iron ore concentrate transportation. Compared with the traditional 16 Mn steel pipeline, the composite lined pipeline has been used for more than 5 years without any problems, while the traditional 16 Mn steel pipeline is worn through within 1 year. Engineering application shows that the composite lined pipeline has good wear resistance, and it also confirms the reliability of the detection method proposed in this paper.

Keywords: pipeline, wear resistance, quantitative test, mechanism, engineering application

OPEN ACCESS

Edited by:
Erol Yilmaz,
Recep Tayyip Erdoğan University, Turkey

Reviewed by:
Lijie Guo,
Beijing General Research Institute of Mining and Metallurgy, China
Liang Cui,
Lakehead University, Canada

****Correspondence:***
Qin-guo Jin
jinqinguo.zz@163.com

Specialty section:
This article was submitted to Structural Materials, a section of the journal Frontiers in Materials

Received: *21 July 2021*
Accepted: *22 October 2021*
Published: *05 January 2022*

Citation:
Wang Y, Yang G-f, Ma C-l, Jia Q-l and Jin Q-g (2022) Quantitative Test and Engineering Application of Wear Resistance of a Kind of Mine-Filled Composite Pipeline. Front. Mater. 8:744944. doi: 10.3389/fmats.2021.744944

INTRODUCTION

The technology of full tailings filling mining can use the surface tailings to the maximum extent and is widely used in mines at home and abroad (Ghirian and Fall 2013; Wu et al., 2016; Wu et al., 2018). Pipeline transportation is considered as the "throat" project of filling mining technology, which plays a very important role in filling technology. However, in actual filling, it often encounter that the filling pipe wears through, resulting in the construction of the drilled hole having to be discarded in a shorter time (Mao et al., 2018; Shi et al., 2020). Therefore, serious wear and short service life of the filling pipeline is one of the main problems faced by the mine filling, causing serious economic losses and affecting production efficiency. There are two main reasons for this phenomenon: one is that it is difficult to predict the wear resistance of the

filling pipe before it is used; on the other hand, the wear resistance of the pipe material itself is poor.

At present, much research has been carried out on pipeline wear at home and abroad. A variety of wear-resistant pipes have been researched in China (FU et al., 2017), including single material pipes and composite pipes. Among them, surfacing composite pipes (Deng et al., 2013; Wang et al., 2016) and bimetallic composite pipes (Li et al., 2011; Wang et al., 2013; Cao et al., 2014; Wang et al., 2015) have good comprehensive performance and long service life, and are increasingly used in domestic mines. For the research of pipeline wear, there are mainly two methods: experimental analysis and numerical simulation. The main methods of pipe wear test in China are rotary motion test and loop pipe simulation test (Zou et al., 2004). Rotary motion test is to put the test grinding block in the slurry for circular motion, and its wear resistance is characterized by the amount of metal loss of the grinding block. Loop pipe simulation test is to test the pipeline wear resistance by simulating the actual situation of pipeline transportation. The above two methods have long test cycles, less wear in a short time, and it is difficult to quickly define the wear resistance of the pipeline. Numerical simulation is mainly based on the theory of solid-liquid two-phase flow, through CFD, FLUENT fluid mechanics and fluid dynamics module of Ansys software, the discrete particle model (DPM) (Guo and Zhang, 2015), Mixture mixed model (Wu et al., 2019) and dense discrete phase model (DDPM) (Liu et al., 2015) on the simulation analysis under different conditions of pipeline wear. The wear of different parts of the pipeline, the influence of different flow rate and particle size on the wear of the pipeline can be obtained. The numerical simulation is focusing more on the identification of the easy-wearing pipe section, and there is less research on the wear resistance of the pipeline itself.

According to the definition of the American Material Test, foreign scholars have found that elastomer materials can absorb the elastic deformation caused by the wear medium and make their plastic deformation small, but their use has certain limitations (Xie et al., 2015). For many years, foreign countries have tested pipeline wear by jet impact tester (SimonLi et al., 1981), Coriolis wear tester (Chandel, 2010) and tank wear tester (Tsai et al., 1981), which are used to evaluate the properties of pipe materials under different conditions and discuss the dependence of wear on relative velocity, impact angle and solid concentration (Rawat et al., 2017). Using the ASTM G65-04 wear tester (Hewitt et al., 2009) for wear resistance testing can quickly determine the on-site pipeline wear performance.

In conclusion, foreign countries have established relevant standards for pipeline wear resistance testing, but China's research in this field is relatively backward, leading to engineering analogy for pipeline product selection and life evaluation, with certain limitations and blindness. If the wear resistance can be quantitatively evaluated before filling pipeline is selected, it will reduce the risk of selection of mine pipeline, save the cost of pipe and prolong the service life of borehole. To this end, this paper proposes a rapid testing device for pipeline wear performance, and compares the wear resistance of a self-developed pipeline material with commonly used 16 Mn steel and ordinary carbon steel. And through the iron ore concentrate transportation pipeline with higher wear resistance requirements for engineering verification, the wear resistance of the new composite pipeline and the reliability of the wear resistance test method were verified.

DEVICE AND METHOD

Experimental Device

For the measurement of the wear resistance of pipeline materials, we have independently developed a wear resistance test device. The main body of the device is composed of the base cabinet, supporting table, protective cover, rotating iron disc, waterproof gauze, waterproof gauze fixing device, fixed shaft, motor, pipe material fixing bracket, pipe material, adding water pipe and counterweight material, as shown in **Figure 1**. The base cabinet is located at the bottom of the whole device, the supporting table is fixed on the upper surface of the base cabinet, the protective cover is fixed on the top of the supporting table, and the rotating iron disc is placed inside the protective cover. Waterproof gauze is paved on the surface of the rotating iron disc, waterproof gauze fixing device is located on the surface of the side wall of the rotating iron disc, the fixed shaft is fixed on the base cabinet, through the support table, connected to the rotating iron disc, the motor is placed in the base cabinet. The pipe material fixing bracket is fixed on the supporting table wall, the pipe material is fixed on the side of the pipe material fixing bracket, the water-adding pipe is located above the boundary between the waterproof gauze and the pipe material, and the counterweight material is above the pipe material.

The device is small in size and flexible in movement, and can be tested in the laboratory or in the field. Abrasion resistance testing can be performed on various pipelines before on-site pipeline selection, which provides a basis for later on-site pipeline selection and has strong practical value.

Testing Method

In this study, three pipeline materials were selected, including commonly used 16 Mn steel materials, ordinary carbon structural steel materials, and self-developed composite wear-resistant materials. The performance of the self-developed wear-resistant materials is shown in **Table 1**.

Firstly, the measured pipeline material is fixed in the middle of the disk radius on the side of the pipeline material fixation bracket, and is closely attached to the surface of the waterproof gauze. The counterweight material is placed above the tested wear-resisting pipeline material, and the rotating shaft speed is set at 1,000 r/min, with a certain pressure. Turn on the motor, the waterproof gauze is rotated by rotating the iron disc to wear down the lower surface of the pipeline material. Wear the test material for 1 h, and smooth its surface. At this time, the mass of the pipeline material after drying ism_0; Then wear the wear-resistant material for 1 h, and the mass of the drying test material is m_1, areas, and density ρ. Then the wear thickness of the tested pipeline material is calculated as formula **(1)**, where the wear thickness h is the specific quantitative indicators of pipeline wear resistance.

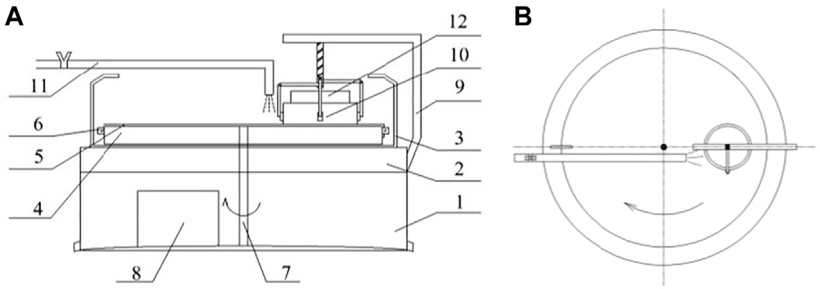

FIGURE 1 | Front view **(A)** and top view **(B)** of the wear resistance test device for filled pipes (In the picture, 1- Base cabinet; 2- Support table; 3- Protective cover; 4- Rotating iron disc; 5- Waterproof gauze; 6- Waterproof gauze fixing device; 7- Fixed shaft; 8- Motor; 9- Pipe material fixing bracket; 10- Pipe material; 11- Add water pipe; 12- Counterweight material).

TABLE 1 | Performance indicators of self-developed wear-resistant materials.

Indicator name	Compressive strength (MPa)	Flexural strength (MPa)	Crush strength (MPa)	Apparent porosity (%)	Bulk density (m^3)
Industry standard value	>30.00	>10.00	>280.00	<16.00	>2.65
Actual measured value	37.38	13.73	291	11.79	3.1

TABLE 2 | Test results of wear resistance.

Material under test	After 1 h wear/g	After 2 h wear/g	Wear mass/g	Material area/cm^2	Weight pressure during test/kPa	Material density g/cm^3	Wear thickness/mm
New wear-resistant material ZX	1719	1715	4	119.13	5.54	3.10	0.1083 0.1314
New wear-resistant material ZXZ	1826	1820	6	125.24	5.55	3.10	0.1545
16 Mn steel	345	315	30	23.16	5.59	7.98	1.6232
Ordinary carbon structural steel	1808	1749	59	78.70	5.54	7.80	0.9612

$$h = \frac{(m_0 - m_1)/\rho}{s} \quad (1)$$

In the formula, h- wear thickness of pipeline material under test, mm; m_0- mass of dried material after 1 h wear of test material, g; m_1- mass of dried material after 2 h wear of test material, g; ρ- density of test material, g/cm^2; s- area of worn surface of test material, cm^2.

Using the above method, the wear thickness of the self-developed wear-resistant material is h_1, the wear thickness of the 16 Mn steel material is h_2, and the wear thickness of the ordinary carbon structural steel material is h_3. The wear thickness of the new wear-resistant pipe in this study is $\frac{h_1}{h_2}$ times that of 16 Mn steel pipe and $\frac{h_1}{h_3}$ times that of ordinary carbon structural steel.

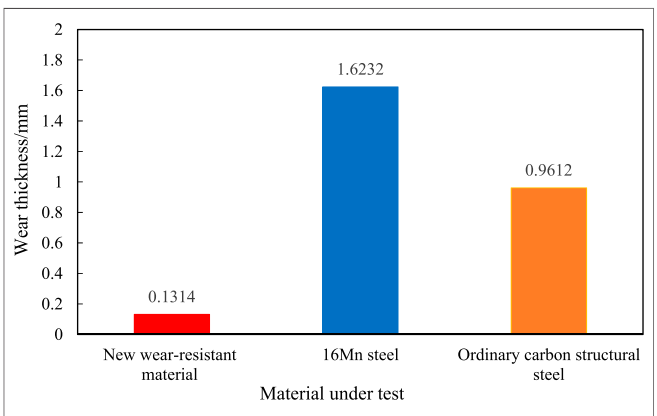

FIGURE 2 | The comparison of wear thickness of different materials.

RESULTS AND ANALYSIS

In order to ensure the reliability of the experiment, two tests are performed on the new composite material wear-resistant pipeline, and the average value is taken. The wear thickness is compared with the wear of 16 Mn steel and ordinary carbon structural steel materials. In order to ensure the comparability of the test results, although the area of the tested materials is

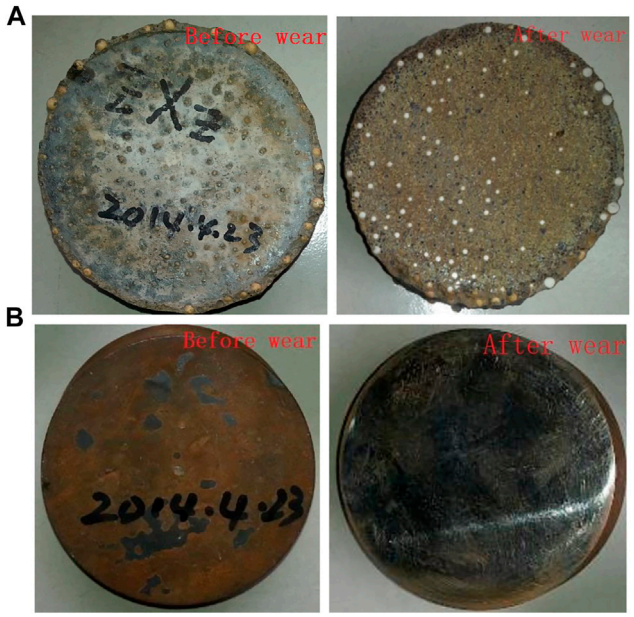

FIGURE 3 | Comparison of before and after wear of pipe samples [**(A)**: new wear-resistant materials; **(B)**: 16 Mn steel materials].

different, the pressure of the counterweight remains basically the same during the test. The test uses sandpaper model BYZ62-P40. The test results are shown in **Table 2**, and the comparison of wear thickness of different materials is shown in **Figure 2**. It can be seen from **Table 2** and **Figure 2** that the average value of the two wear thicknesses of the new wear-resistant material is 0.1314 mm. The wear thicknesses of 16 Mn steel and ordinary carbon structural steel are 1.6232 and 0.9612 mm, respectively. The wear thickness of 16 Mn steel is 12.35 times that of wear-resistant lining materials, and the wear thickness of ordinary carbon structural steel is 7.32 times that of wear-resistant lining materials. It can be seen that the wear resistance of the new wear-resistant pipeline lining material is significantly better than that of 16 Mn steel and ordinary carbon steel materials. **Figure 3** shows the comparison between a wear-resistant lining material and 16 Mn steel before and after the test. As can be seen from **Figure 3**, under the same pressure and time wear conditions, the wear degree of 16 Mn steel sample is more serious, and the sample morphology changes significantly with that before wear, while the sample morphology of the new wear-resistant material shows little difference with that before wear.

It can be seen from **Table 2** that the wear resistance of the new wear-resistant materials is significantly better than that of 16 Mn steel and ordinary carbon structural steel materials. For this reason, it is necessary to analyze the wear resistance of the new wear-resistant material. There are two main reasons why the composite material has good wear resistance:

1) The main body material of the lining has high hardness. The pipeline material uses corundum grain sand, silicon carbide and other extremely wear-resistant materials as aggregates. Corundum has a Mohs hardness of 9, and silicon carbide has a Mohs hardness of 9.5, second only to diamond, and both have great hardness. As a comparison, the Mohs hardness of 16 Mn steel and ordinary structural carbon steel aggregate is between 4 and 6, far less than that of corundum and silicon carbide. It should be noted that the Mohs hardness represents a standard of mineral hardness, which is defined as the use of a notch method to scratch the surface of the tested mineral with a pyramidal diamond needle and measure the depth of the scratch. The depth of the scratch is the Mohs hardness. The difference between it and the Protodyakonov coefficient is that the Mohs hardness can only represent the order of hardness from largest to smallest, not the degree of softness and hardness, while the Protodyakonov coefficient represents the degree of hardness of minerals.
2) The pipeline material has a smooth surface. As shown in **Figure 4**, the selected aggregates are spherical or nearly spherical particles to make the surface of the pipeline material smooth. When the delivered material comes into contact with it, the small friction coefficient can pass smoothly, reducing the wear between the material and the pipeline, and enhancing the wear resistance of the pipeline.

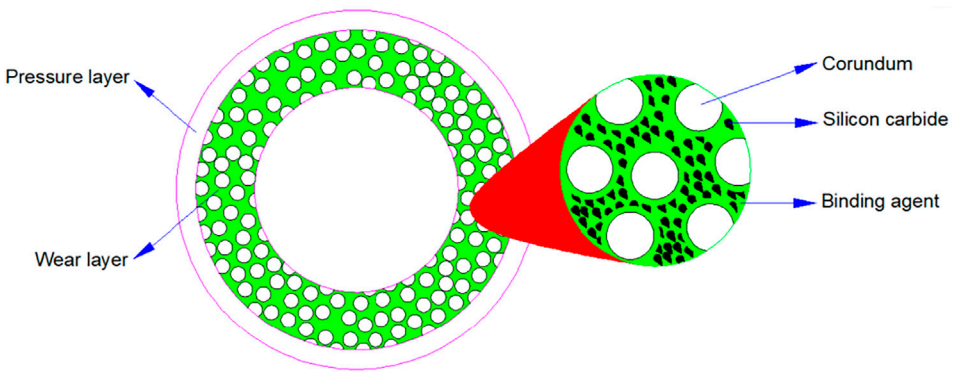

FIGURE 4 | Internal structure diagram of composite pipe.

FIGURE 5 | The traditional 16 Mn steel pipeline was worn out and repaired in less than a year.

FIGURE 6 | Engineering application of new wear-resistant pipeline.

ENGINEERING APPLICATION VERIFICATION

In order to quickly and clearly verify the wear of the pipeline, a certain iron ore concentrate transportation pipeline is selected for engineering verification. The iron ore originally uses traditional 16 Mn steel pipeline, which are severely worn and often need to be shut down for repairs. The pipeline need to be replaced every 6 months to a year, as shown in **Figure 5**.

Since August 2014, one of the delivery pipelines was replaced with a new composite wear-resistant pipeline, and the other delivery pipeline still uses 16 Mn steel pipelines for comparison, as shown in **Figure 6**. The new composite wear-resistant pipeline has been used until now, and there have been no problems such as pipeline wear through. Through the actual engineering application of the new wear-resistant pipeline, its wear resistance is verified, and the reliability of the pipeline wear resistance test method used in the study is also verified. It should be noted that the wear through of the traditional 16 Mn steel pipeline mainly occurs in the elbow part (**Figure 5**). In the application of this project, the elbow part of the new composite wear-resistant pipeline has not been worn through for more than 5 years. For mine filling, the severely worn parts of the pipeline also mainly occur in the elbow part. Therefore, the new wear-resistant pipeline has good engineering application value in the field of mine filling.

CONCLUSION

1) In this paper, an experimental device and its application method for testing the wear resistance of the pipeline are proposed. The device can quickly and quantitatively obtain the wear resistance of the pipeline through the wear of the pipeline material, and then predict the service life of the pipeline.
2) This method is used to test the wear resistance of self-developed pipeline lining composite materials, traditional 16 Mn steel and ordinary carbon structural steel. The results show that the wear resistance of the new wear-resistant pipeline lining material is significantly better than that of 16 Mn steel and carbon structural steel. The internal reasons for the good wear resistance of the new lining material are analyzed from the two aspects of aggregate composition and structure.
3) Through a comparison engineering application of a certain iron ore concentrate transportation. The composite lined pipeline has been used for more than 5 years without any problems, while the traditional 16 Mn steel pipeline is worn through within 1 year. The practical application has verified the wear resistance of the composite lined pipeline and the reliability of the proposed test method. Especially, the good wear resistance in elbow part lays a good practical foundation for mine filling application.

DATA AVAILABILITY STATEMENT

The original contributions presented in the study are included in the article/Supplementary Material, further inquiries can be directed to the corresponding author.

AUTHOR CONTRIBUTIONS

YW: Investigation, Writing- original draft, Funding acquisition. G-fY: Investigation, Writing - original draft. C-lM: Conceptualization, Methodology, Supervision, Writing - review and editing. Q-lJ: Formal analysis, Writing - original draft. Q-gJ: Supervision, Funding acquisition. All authors read and approved the final manuscript.

FUNDING

This research was funded by the National Natural Science Foundation of China (No. 52042402), the Fundamental Research Funds for the Central Universities (No. FRF-IDRY-20-031).

REFERENCES

Cao, X. Y., Deng, J., and Shang, G. C. H., (2014). Progress Made in Research on Cladding Process for Bimetal Clad Pipe. *Steel Pipe* 43 (02), 11–15.

Chandel, S. (2010). *Studies on the Flow of High Concentration Coal Ash through Pipelines*. PHD dissertation (New Delhi: Indian Institute of Technology Delhi).

Deng, D. W., Chen, R., and Zhang, H. C. (2013). Present Status and Development Tendency of Plasma Transferred Arc Welding. *J. Mech. Eng.* 49 (7), 106–112. doi:10.3901/jme.2013.07.106

Fu, Y. H., Wang, L. L., and Li, N. (2017). Research on Development and Technology of Wear-Resistant Pipeline for Filling in Mine. *Nonferrous Met. Designs* 44 (1), 1–4. doi:10.3969/j.issn.1004-2660.2017.01.001

Ghirian, A., and Fall, M. (2013). Coupled Thermo-Hydro-Mechanical-Chemical Behaviour of Cemented Paste Backfill in Column Experiments. Part I: Physical, Hydraulic and thermal Processes and Characteristics. *Eng. Geology.* 164, 195–207. doi:10.1016/j.enggeo.2013.01.015

Guo, J., and Zhang, B. X. (2015). Numerical Investigation of Impact Erosion in Liquid-Solid Two-phase Flow of the Backfilling Pipe. *Sci. Tech. Rev.* 33 (11), 49–53. doi:10.3981/j.issn.1000-7857.2015.11.008

Hewitt, D., Allard, S., and Radziszewski, P. (2009). Pipe Lining Abrasion Testing for Paste Backfill Operations. *Minerals Eng.* 22, 1088–1090. doi:10.1016/j.mineng.2009.03.010

Li, F. G., Wei, B., and Shao, X. D., (2011). Technical and Economic Analysis on Bimetal Pipeline. *Corrosion Sci. Prot. Tech.* 23 (01), 86–88.

Liu, Y. Y., Chen, Y. H., and Zhu, C. W. (2015). Analysis of Erosive Wear of Backfilling Transportation Pipeline. *Lubrication Eng.* 40 (07), 106–109. doi:10.3969/j.issn.0254-0150.2015.07.022

Mao, M. F., Wang, B. W., and Zhu, J. R. (2018). Study on Wear Mechanism of Gravity Transportation Pipeline for Backfilling Slurry[J]. *Metal Mine* 47 (04), 178–184. doi:10.19614/j.cnki.jsks.201804032

Rawat, A., Singh, S. N., and Seshadri, V. (2017). Erosion Wear Studies on High Concentration Fly Ash Slurries. *Wear* 378-379, 114–125. doi:10.1016/j.wear.2017.02.039

Shi, H. W., Huang, J. R., and Qiao, D. P. (2020). Study on the Abrasion of High Concentration Filling Slurry Self Flowing Pipeline in Deep Mine. *Nonferrous Met. (Mining Section)* 72 (04), 13–18. doi:10.3969/j.issn.1671-4172.2020.04.003

SimonLi, K-K., Humphrey Joseph, A. C., and Levy Alan, V. (1981). Erosive Wear of Ductile Metals by a Particle-Laden High Velocity Liquid Jet. *Wear* 73 (2), 295–309.

Tsai, W. J. A. I., Humphrey, J. A. C., Cornet, I., and Levy, A. V. (1981). Experimental Measurement of Accelerated Erosion in a Slurry Pot Tester. *Wear* 68 (3), 289–303.

Wang, H., Zeng, X. G., and Xiao, Y. G. (2016). Pipe Welding and SHS Ceramic Lined Preparation and Performance Test. *Pipeline Tech. Equipment* (1), 33–36. doi:10.3969/j.issn.1004-9614.2016.01.011

Wang, Y. F., Yuan, J. L., and Zhang, Y. F. (2013). Technology Status and Development Direction of Bimetal Pipe. *Welded Pipe and Tube* 36 (02), 5–9. doi:10.19291/j.cnki.1001-3938.2013.02.001

Wang, Y. F., Zhao, S. D., and Zhang, C. Y. (2015). Research Status and Development of Forming Technology for Bi-metal-lined Pipe *China Metalforming Equipment Manufacturing Tech.* 50 (03), 84–89. doi:10.16316/j.issn.1672-0121.2015.03.024

Wu, A. X., Wang, Y., and Wang, H. J. (2016). Status and Prospects of the Paste Backfill Technology. *Metal Mine* 45 (7), 1–9. doi:10.3969/j.issn.1001-1250.2016.07.001

Wu, A. X., Yang, Y., and Cheng, H. Y. (2018). Status and Prospects of Paste Technology in China. *Chin. J. Eng.* 40 (05), 517–525. doi:10.13374/j.issn2095-9389.2018.05.001

Wu, X. S., Wang, Y. P., and Tang, D. R. (2019). Influence of Solid Particle Concentration on Wear of Horizontal Pipeline. *Education Modernization* 6 (34), 200–201. doi:10.16541/j.cnki.2095-8420.2019.34.079

Xie, Y. s., (Jimmy)Jiang, J., and Tufa, K. Y. (2015). Wear Resistance of Materials Used for Slurry Transport. *Wear* 332-333, 1104–1110. doi:10.1016/j.wear.2015.01.005

Zou, W. S., Wu, G. F., and Huang, J. Z. (2004). The Study on Pipewall Abrasion in Long Distance Slurry Pipeline Transportation. *Mining Metallurgical Eng.* (02), 1–3. doi:10.3969/j.issn.0253-6099.2004.02.001

Conflict of Interest: Author Q-gJ was employed by the company Zhengzhou Special Flux Materials Co., Ltd.

The remaining authors declare that the research was conducted in the absence of any commercial or financial relationships that could be construed as a potential conflict of interest.

Publisher's Note: All claims expressed in this article are solely those of the authors and do not necessarily represent those of their affiliated organizations, or those of the publisher, the editors and the reviewers. Any product that may be evaluated in this article, or claim that may be made by its manufacturer, is not guaranteed or endorsed by the publisher.

frontiers in Materials

ORIGINAL RESEARCH
published: 17 January 2022
doi: 10.3389/fmats.2021.818698

Mechanical Properties and Microstructure Evolution of Cemented Tailings Backfill Under Seepage Pressure

Yuxian Ke[1,2], *Yang Shen*[1,2], *Chen Qing*[3], *Kaijian Hu*[1,2]*, *Shi Wang*[1,2], *Qiusong Chen*[4]* and *Huadong Guan*[1]

[1]Jiangxi Province Key Laboratory of Mining Engineering, Jiangxi University of Science and Technology, Ganzhou, China, [2]School of Resources and Environment Engineering, Jiangxi University of Science and Technology, Ganzhou, China, [3]Periodical Press, Jiangxi University of Science and Technology, Ganzhou, China, [4]School of Resource and Safety Engineering, Central South University, Changsha, China

Cemented tailing backfill (CTB) in underground mine inevitably experiences seepage field, which complicates its mechanical behavior. In this study, the mechanical properties and microstructure characteristics of CTB under different seepage water pressures (SWPs) were investigated. The results show that, with the increase in SWP, the mechanical properties of CTB decrease, but the decreasing trend reduces gradually. Higher SWP leads the microstructure of CTB looser and more porous, and the largest proportion of pores initiated and propagated by SWP is micropores, which means the damage in CTB under seepage is mostly caused by micropores. Besides, the mechanical properties of CTB under seepage decrease exponentially with the increase in porosity and present linearly inverse proportional relation to the pore area fractal dimension. Results above indicate that SWP has a significant deterioration effect on the mechanical properties and microstructure of CTB. The research could not only extend the knowledge of mechanical properties and microstructure characteristics of CTB under seepage but also provide a theoretical reference for mechanical index determination and stability analysis of CTB in water-rich underground mines.

Keywords: cemented tailing backfill, paste backfill, mechanical properties, microstructure, seepage, green mining

OPEN ACCESS

Edited by:
Shuai Cao,
University of Science and Technology Beijing, China

Reviewed by:
Junmeng Li,
China University of Mining and Technology, China
Lang Liu,
Xi'an University of Science and Technology, China

***Correspondence:**
Kaijian Hu
hukaijian@jxust.edu.cn
Qiusong Chen
qiusong.chen@csu.edu.cn

Specialty section:
This article was submitted to Structural Materials, a section of the journal Frontiers in Materials

Received: *19 November 2021*
Accepted: *07 December 2021*
Published: *17 January 2022*

Citation:
Ke Y, Shen Y, Qing C, Hu K, Wang S, Chen Q and Guan H (2022) Mechanical Properties and Microstructure Evolution of Cemented Tailings Backfill Under Seepage Pressure. Front. Mater. 8:818698. doi: 10.3389/fmats.2021.818698

INTRODUCTION

Cemented tailing backfilling is the most effective way to maximize the utilization of tailings and to minimize the amounts of environmental hazards (Ke et al., 2017a; Cao et al., 2018; Li et al., 2021a; Li et al., 2021b; Tana et al., 2021). It has become the preferred mining method for the sustainable development of underground mining industry (Fall and Samb, 2009; Ke et al., 2017b; Yu et al., 2021; Chen et al., 2022). One of the global concerns in this means is the high cost of cemented tailing backfill (CTB) due to the high cement dosage. A decrease in cement dosage can significantly reduce the cost for the binder; cost takes up 60% to 80% of CTB total cost (Ghirian and Fall, 2013; Ghirian and Fall, 2014; Tan et al., 2019; Li et al., 2021d). However, the desired strength of CTB is mainly provided by the hydration of cement. Reducing the cement content will severely restrict the strength of CTB and cause potential security threats to mining operations (Yilmaz et al., 2015; Behera et al., 2021). Usually, the strength index of CTB is bound to be conservatively designed under safety first

situation, resulting in large cement consumption and high cost. The mechanical properties of CTB are the fundamental basis for determining its reasonable strength index (Xu et al., 2019; Qiu et al., 2020; Yin et al., 2020; Qi et al., 2021). Therefore, it is of great theoretical value and practical application significance to clearly understand the mechanical properties of CTB under different conditions.

At present, numerous researches have already been carried out to investigate the effect of various factors on the mechanical properties of CTB. Cao et al. (2018) concluded that uniaxial compressive strength (UCS) of CTB increases with the higher cement-tailings ratio and solid concentration. Xu et al. (2020) and Jiang et al. (2020) studied the influence of curing age on the mechanical properties of CTB, which concluded that the increase in curing age could remarkably improve the UCS of CTB. Fall et al. (2010), Wu et al. (2021), Chen et al. (2021a), Chen et al. (2021b), and Haiqiang et al. (2016) noted that curing temperature had a significant impact on the strength development of CTB, and the appropriate temperature conducive to improving the mechanical performance of CTB is approximately 50°C. Yilmaz et al. (2009) investigated the influence of curing pressure on mechanical properties of CTB by a self-designed test system and observed that the compressive strength development of CTB curing under vertical pressure was higher than that without vertical pressure ones, which could be mainly due to the applied pressure during curing process and improved consolidation process of the CTB material. Xiu et al. (2021) and Cao et al. (2019a) studied the effects of loading rates on the UCS of CTB and found that the increase in loading rate had a strengthening effect on the UCS, and the correlation between the UCS and the loading rates was more consistent with exponential function when the loading rates were between 0.1 and 2 mm/min. Wang et al. (2020a) reported that cyclic loading and unloading had perceptible effect on the mechanical properties of CTB, and the direct reason for the change of UCS is the change of deformation modulus caused by cyclic loading and unloading. In addition, to improve the mechanical properties of CTB, many scholars investigated the influence of alternative binders [fly ash (Behera et al., 2020), lime (Sharma and Kumar, 2021), limestone powder (Zheng et al., 2016), granulated blast furnace slag (Mashifana and Sithole, 2021), copper slag (Chen et al., 2021c), and lithium slag (He et al., 2019)], synthetic fibers [polypropylene fibers (Chakilam and Cui, 2020), polyacrylonitrile fibers (Cao et al., 2019b), and glass fibers (Zhou et al., 2021)], and plant fibers [rice straw (Wang et al., 2020b; Chen et al., 2020) and corn straw (Wang et al., 2021a)] on the mechanical properties of CTB. The above literatures obtained plentiful valuable results and enhanced the understanding of the mechanical properties of CTB. However, there is no relevant research that considered the influence of groundwater seepage on the mechanical properties of CTB. The groundwater is the most common fluid in mining, which is related to more than 60% of mine engineering damage. It is one of the most important factors affecting mine engineering safety, especially in water-rich underground mines. Many researches have been conducted to reveal the influence of water seepage on the mechanical properties of rock materials. Wang et al. (2015) found that there were obvious weakening effects of seepage pressures on the mechanical properties after coarse sandstone damages. Xiao et al. (2020) applied triaxial compressive test on red sandstone under seepage pressure and concluded that seepage pressure reduced the stress eigenvalues of rocks and affected its value of strain stiffness. Kou et al. (2021) reported that seepage pressure promotes tensile crack initiation and propagation of artificial rock-like materials, and its ultimate failure mode transforms from pure shear failure mode to the mixed tensile-shear one with the increase in seepage pressure. The CTB, a kind of artificial functional composite materials, is filled with a large number of micropores and microcracks. Groundwater can easily flow through these micropores form seepage, which would induce the initiation and propagation of defects such as micropores and microcracks in CTB, and result in the change of its mechanical properties.

This article aims to explore the effect of SWP on the mechanical properties and microstructure characteristics of CTB. The seepage experiments were applied to simulate the damage of CTB caused by different SWPs. The mechanical properties of CTB with different SWPs were evaluated by UCS test. Then, microstructure characteristics of CTB were analyzed using nuclear magnetic resonance (NMR) and scanning electron microscopy (SEM). Next, the relationships among mechanical properties (UCS and elastic modulus), microstructure characteristics (pore size distribution, porosity, and fractal dimension), and SWP were established. The research results can provide a theoretical and fundamental basis to determine the UCS and elastic modulus indexes and analyze the stability of CTB in water-rich underground mines.

MATERIALS AND METHODS

Experimental Materials

Tailings

The tailings used for preparing CTB specimens were derived from a copper mine in Jiangxi Province, China. The particle size distribution of the tailings was analyzed using a laser particle size analyzer (Winner 2000), as shown in **Figure 1**. The effective diameter d_{10}, median diameter d_{50}, and constrained diameter d_{60} were 5.62, 68.41, and 90.88 μm, respectively, indicating the particle size of the tailings was medium to fine. The nonuniformity coefficient C_u and curvature coefficient C_c of the particles were 16.17 and 2.15, respectively, indicating a wide size distribution and a well particle gradation continuity of tailings. Furthermore, the main chemical compositions of the tailings were determined via X-ray fluorescence spectroscopy (XRF-1800), and the details of main chemical compositions of the tailings are shown in **Table 1**. The proportions of SiO_2 and CaO in the tailings were 33.02% and 15.68%, respectively, which is benefit to the strength development of CTB.

Binder and Water

The binder used in the preparation of CTB specimens was ordinary Portland cement (P.O32.5), commonly used in the copper mine. The chemical compositions of the P.O32.5 are listed in **Table 2**, and the specific gravity and specific surface

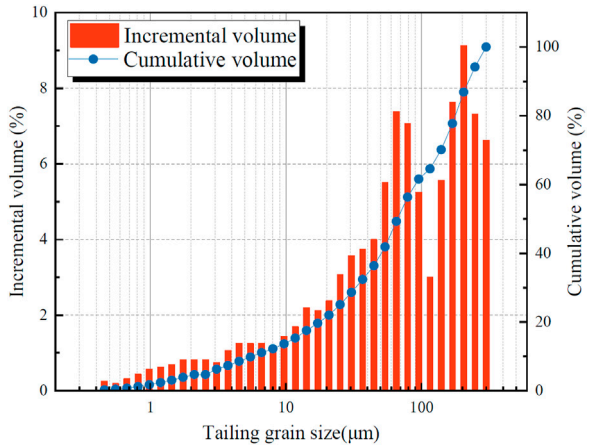

FIGURE 1 | Particle size distribution of tailings.

area of the P.O32.5 are 3.15 and 1.1 m^2/g, respectively. The mixed water was common tap water.

Experimental Methods

The experimental procedure is shown in **Figure 2**, which consisted of CTB specimen preparation, seepage experiment, NMR test, UCS test, and SEM test.

CTB Specimen Preparation

Three CTB specimens were prepared for each experimental condition, and the average results of each experimental condition are shown for further analysis. Cylindrical molds with a diameter of 50 mm and a height of 100 mm were used to make the CTB specimens, and the backfill pulp was mixed with the cement–tailing mass ratio of 1:4 and the solid mass concentration of 76% according to backfilling practice in the copper mine. Then, uniformly stirred pulp was poured into the

TABLE 1 | Chemical composition of the tailings.

Composition	SiO_2	CaO	Fe	S	Al_2O_3	MgO	K	Mn	F	Cu	P	Pb
wt%	33.02	15.68	10.37	4.55	2.56	1.82	0.37	0.085	0.080	0.065	0.049	0.0095

TABLE 2 | The chemical composition of P.O32.5.

Compositions	CaO	SiO_2	Al_2O_3	Fe_2O_3	SO_2	MgO	Na_2O	Other
wt%	63.66	21.26	4.5	2.8	2.58	1.66	0.18	3.36

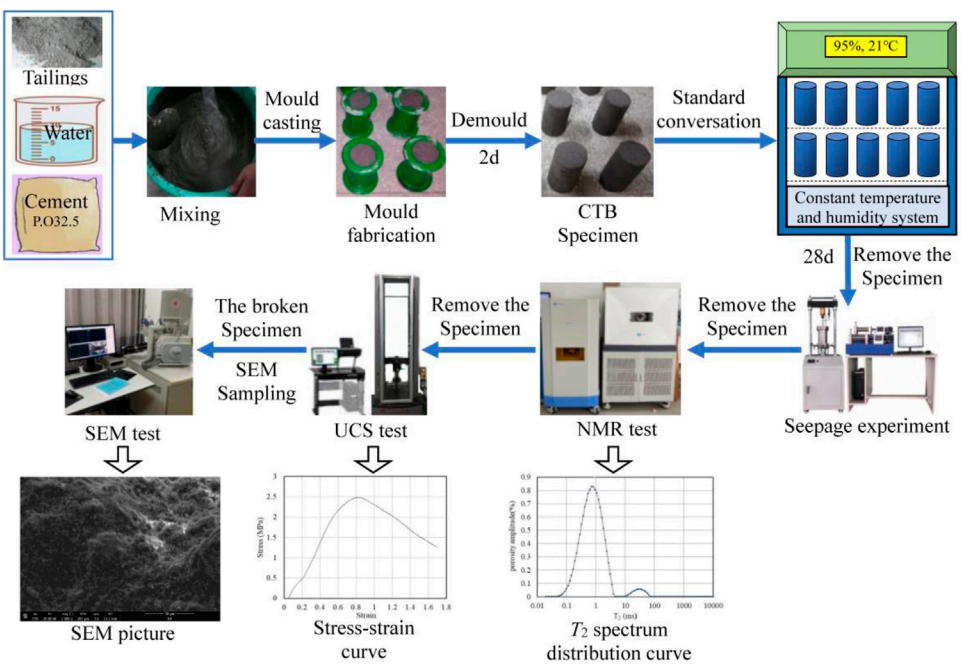

FIGURE 2 | Schematic diagram of experiments routine.

cylindrical molds and gently vibrated the sample holders a few times to eliminate bubbles. The CTB specimens were taken out of the molds after 2 days and cured in a constant temperature and humidity standard curing box (temperature of 20°C ± 1°C, humidity of 90%) for 28 days. Finally, the diameter and height of the cured CTB specimen were measured and recorded before the experiments.

Seepage Experiment

In this study, the seepage experiments were carried out on KSR-100 backfill triaxial creep test system (Jiangsu Yongchang Instrument Corporation, Suzhou, China). The KSR-100 owns three independent control systems for axial pressure, confining pressure, and seepage pressure, with the maximum axial load, confining pressure and seepage pressure being 100 kN, 10 MPa, and 10 MPa, respectively. Usually, the height of mining stope is less than 100 m, and there is a gap between the CTB and roof; the SWP in CTB is less than 1.0 MPa during mining operation. Thus, the SWPs were set to 0, 0.2, 0.5, and 0.8 MPa in the experiment, and the confining pressure kept constant at 1.0 MPa as it should be limited to be greater than the maximum SWP. Besides, the seepage water was tap water and has a pH of 7.0. The specific experimental scheme is shown in **Table 3**.

The stress state of CTB specimen during seepage experiment is presented in **Figure 3**. The seepage experiment steps are as follows: (1) placing porous discs at both ends of CTB specimen and wrap them (except at both ends) with a layer of heat-shrink film and installing them on the base of the KSR-100; (2) simultaneously applying confining pressure and axial pressure to 1.0 MPa at a loading rate of 2 kPa/min; (3) applying seepage pressure to predetermined value at the same loading rate when confining pressure and axial pressure were stable and kept for a period of time (approximately 72 h according to the experiment results) until the water seepage volume-time curve changed steadily; (4) unloading seepage pressure and simultaneously unloading confining pressure and axial pressure at the same unloading rate of 2 kPa/min; and (5) terminating the seepage experiment and taking out the sample for subsequent experiments.

NMR Test

The heat-shrink film was removed from the CTB specimens after seepage experiment, and the excess moisture was wiped off from the surface of CTB specimens. Then, the CTB specimens were fully wrapped with a layer of polytetrafluoroethylene film to avoid moisture loss before the NMR test. An NM-60 NMR instrument (Suzhou Niumag Analytical Instrument Corporation, Suzhou, China) was applied to perform the NMR test on CTB specimens, and the distribution of transverse relaxation time (T2) of CTB specimens can be obtained. The NMR test detail parameters refer to literatures (Gao et al., 2020; Hu et al., 2020; Wang et al., 2021b).

UCS Test

After the NMR test, the CTB specimens were removed to an electronic universal testing machine (WDW-20H; Jinan Huaxing Instrument Corporation, Jinan, China) for UCS test. The loading speed was 0.5 mm/min. Then the stress–strain curve, UCS, and elastic modulus of CTB specimens can be obtained.

SEM Test and Image Preprocessing

Once the UCS test was accomplished, one cubic sample with a side length of approximately 1 cm was cut from the center part of the broken CTB specimen for SEM test. An SEM system (MLA650F, USA) was applied to observe the microstructure of the CTB specimens, and more than 10 SEM images for each CTB

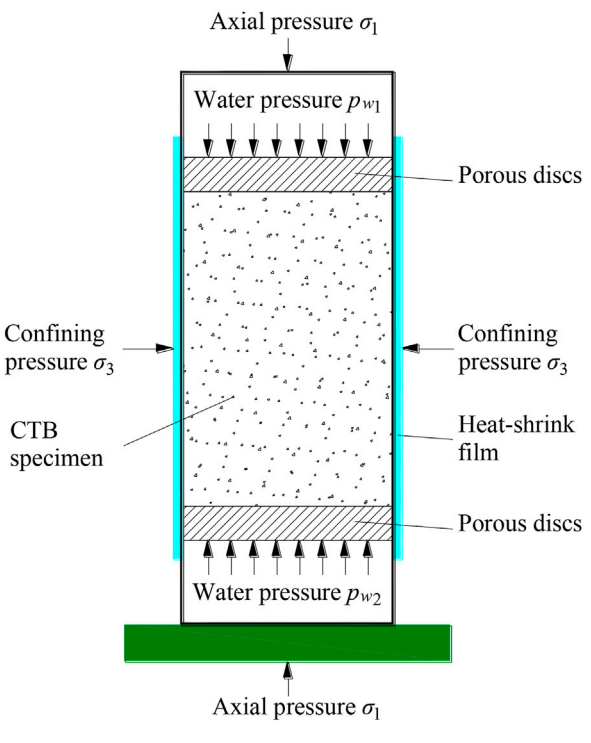

FIGURE 3 | Schematic diagram of stress of CTB specimen during seepage experiment.

TABLE 3 | Seepage experiment scheme.

Specimen number	Cement/tailings	Concentration (wt.%)	SWP (MPa)	Confining pressure (MPa)
ST-1, ST-2, ST-3	1:4	76	0	1.0
ST-4, ST-5, ST-6			0.2	
ST-7, ST-8, ST-9			0.5	
ST-10, ST-11, ST-12			0.8	

specimen were obtained. Prior to the test, the cubic sample was dried at 50°C and sprayed with gold.

It is generally accepted that the SEM micrograph is difficult to be directly used for quantitative analysis, although in this article the SEM micrograph was binary-processed using the MATLAB image processing toolbox and the obtained binary SEM micrograph was a black-and-white bitmap, in which the black and white regions represent the pore and structure, respectively. Correspondingly, for each experimental condition, nine SEM micrographs were preprocessed, and their mean results were used for further quantitative analysis.

RESULTS AND DISCUSSION

Effect of Seepage on Mechanical Properties of CTB

The UCS and elastic modulus are the two most important mechanical property parameters of CTB. Therefore, the UCS and elastic modulus of CTB under different SWPs were obtained for analysis. As shown in **Figure 4**, with an increase in SWP from 0 to 0.8 MPa, the UCS of CTB specimens decreased from 6.11 to 4.08 MPa; the elastic modulus decreased from 7.27×10^2 to 4.14×10^2 MPa. The UCS loss rates of CTB specimens were 17.18%, 28.97%, and 33.22%, and the elastic modulus loss rates of CTB specimens were 24.07%, 37.14%, and 43.05% when the SWP increased from 0 to 0.2 MPa and, 0.5 and 0.8 MPa, respectively. The results suggested that SWP had an obvious weakening effect on the UCS and elastic modulus of CTB, whereas the weakening effect was decreasing overall with the increase in SWP; that is, the higher the SWP, the less apparent the weakening effect on mechanical properties of CTB. The weakening effect of SWP on the UCS and elastic modulus are consistent with the findings reported by Hou et al. (2020). In addition, the mechanical properties of CTB are related to its internal microstructure (Yang et al., 2019; Zhou et al., 2019; Tana et al., 2021); the results indicated that the seepage would cause a certain degree of damage to the internal microstructure of CTB.

Microstructure Characteristics of CTB Under Different SWPs

Effect of SWP on Porosity of CTB

The porosity is a key feature reflecting the variation in microstructure characteristics of CTB. The porosity of CTB specimens under different SWPs was obtained from NMR test results, as shown in **Figure 5**. It can be noted that the porosity increased obviously with the increase in SWP. With an increase in SWP from 0 to 0.8 MPa, the porosity of CTB specimens increased from 4.687% to 15.337%. The porosity of CTB specimens increased by 3.390, 7.699, and 10.650 when the SWP increased from 0 to 0.2 MPa, 0.5 and 0.8 MPa, respectively. The results proved that SWP had a significant promoting effect on the initiation and propagation of pores and microcracks in CTB specimens, which contributed to the porosity and microstructure damage of CTB specimens. Meanwhile, a high SWP corresponded to a higher promoting effect, whereas the influence rate was gradually decreasing.

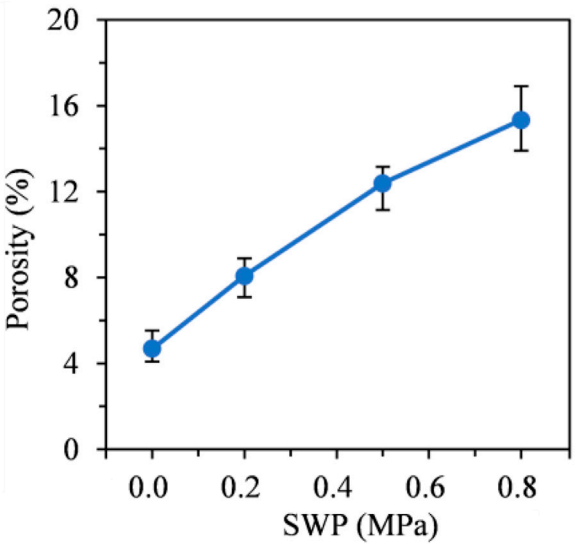

FIGURE 5 | Effect of seepage on porosity of CTB specimens.

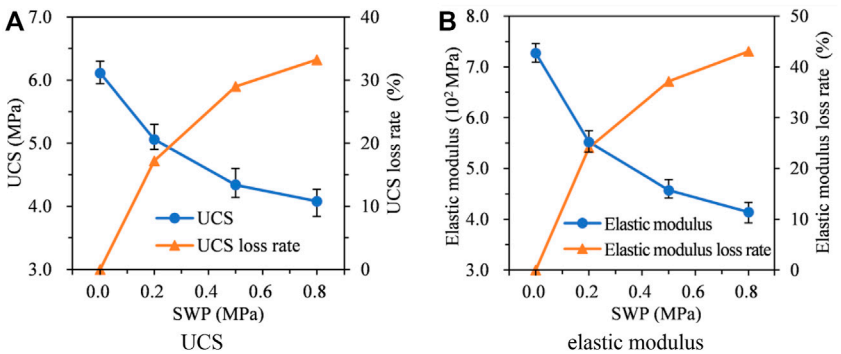

FIGURE 4 | Effect of seepage on **(A)** UCS and **(B)** elastic modulus of CTB specimens.

Effect of Seepage on Pore Size Distribution Characteristics of CTB

According to the NMR measurement principle, a smaller T_2 value represents a smaller pore size, and *vice versa*. **Figure 6** shows the T_2 distribution of CTB specimens after adopting a different SWPs. It can be found that there were three peaks at each T_2 distribution. Peak 1 (leftmost peak) was obviously higher than peak 2 (middle peak), and peak 2 was obviously higher than peak 3 (rightmost peak), indicating that most of the main pores of CTB specimens were micropores, followed by mesopores, and the least were macropores. The three peaks were discontinuous, revealing that there was no direct link channel among the three kinds of pores. **Figure 7** shows the variation law of peak area of CTB specimens with SWP. As can be seen, with the increase in SWP; peaks 1 and 2 areas of CTB specimens showed an obvious increasing trend, whereas peak 3 area hardly changed. With an increase in SWP from 0 to 0.8 MPa, peak 1 area increased from 4.492 to 14.841, and peak 2 area increased from 0.132 to 0.439, and the areas of peaks 1 and 2 accounted for 98.67% to 99.63% of the total peak area. Peak 1 area increased by 3.258, 7.508, and 10.349; and peak 2 area increased by 0.131, 0.202, and 0.307 when the SWP increased from 0 to 0.2 MPa, 0.5 and 0.8 MPa, respectively. The results suggested that the pores in CTB specimens initiated and propagated by seepage were mainly micropores and mesopores, and the macropore volume hardly affected by SWP. To sum up, micropore volume of CTB was the most increasing one as SWP increased, and the damage in CTB under seepage was mostly caused by micropores.

Effect of SWP on Pore Area Fractal Dimension of CTB

Figure 8 shows the SEM micrographs and their binarization results of CTB specimens under different SWPs. With a larger SWP, the microscopic surface of specimen was looser, and the pore area was larger. The fractal dimension is one of the most important basic parameters of microstructure characteristics of CTB. Thus, fractal theory was used to analyze the effect of SWP on the pore area fractal dimension of CTB specimens in this study. The pore area fractal dimension of binarized SEM micrographs was determined via box counting (Zhao et al., 2022; Zhang et al., 2020; Wu et al., 2019; Sun et al., 2019). As shown in **Figure 9**, the changing regularity of SWP on pore area fractal dimension of CTB specimens was similar to SWP on porosity. With an increase in SWP from 0 to 0.8 MPa, the pore area fractal dimension of CTB specimens increased from 1.815 to 1.903. The pore area fractal dimension of CTB specimens increased by 0.036, 0.067, and 0.088 when the SWP increased from 0 to 0.2 MPa, 0.5 and 0.8 MPa, respectively. A large pore area fractal dimension represents a high complexity of pores and a worse uniformity of pores. These findings further indicated that a higher SWP will make the microstructure of CTB looser and more porous, resulting in more microcracks and pores. Microcracks propagated and connected with pores, forming defects, which deteriorated the microstructure and weakened the mechanical properties of CTB (Mower and Long, 2016; Gu et al., 2020).

Relationship Between Mechanical Properties and Microstructure Characteristics

Relationship Among UCS, Elastic Modulus, and Porosity

The porosity of CTB has an important influence on its mechanical properties. **Figure 10** shows the relationship

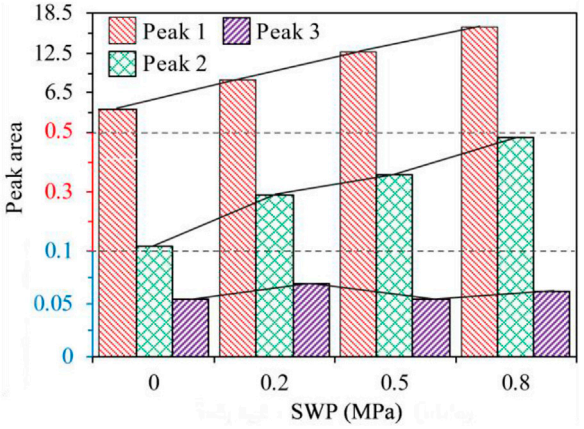

FIGURE 7 | Effect of SWP on peak area of CTB specimens.

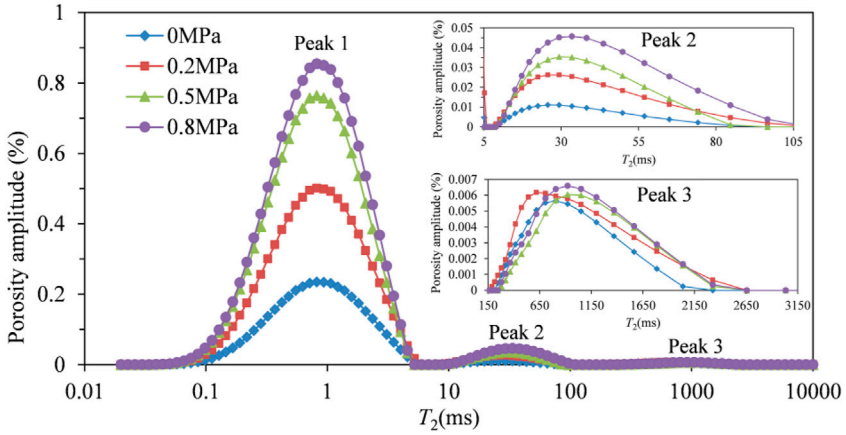

FIGURE 6 | Effect of SWP on T_2 distribution of CTB specimens.

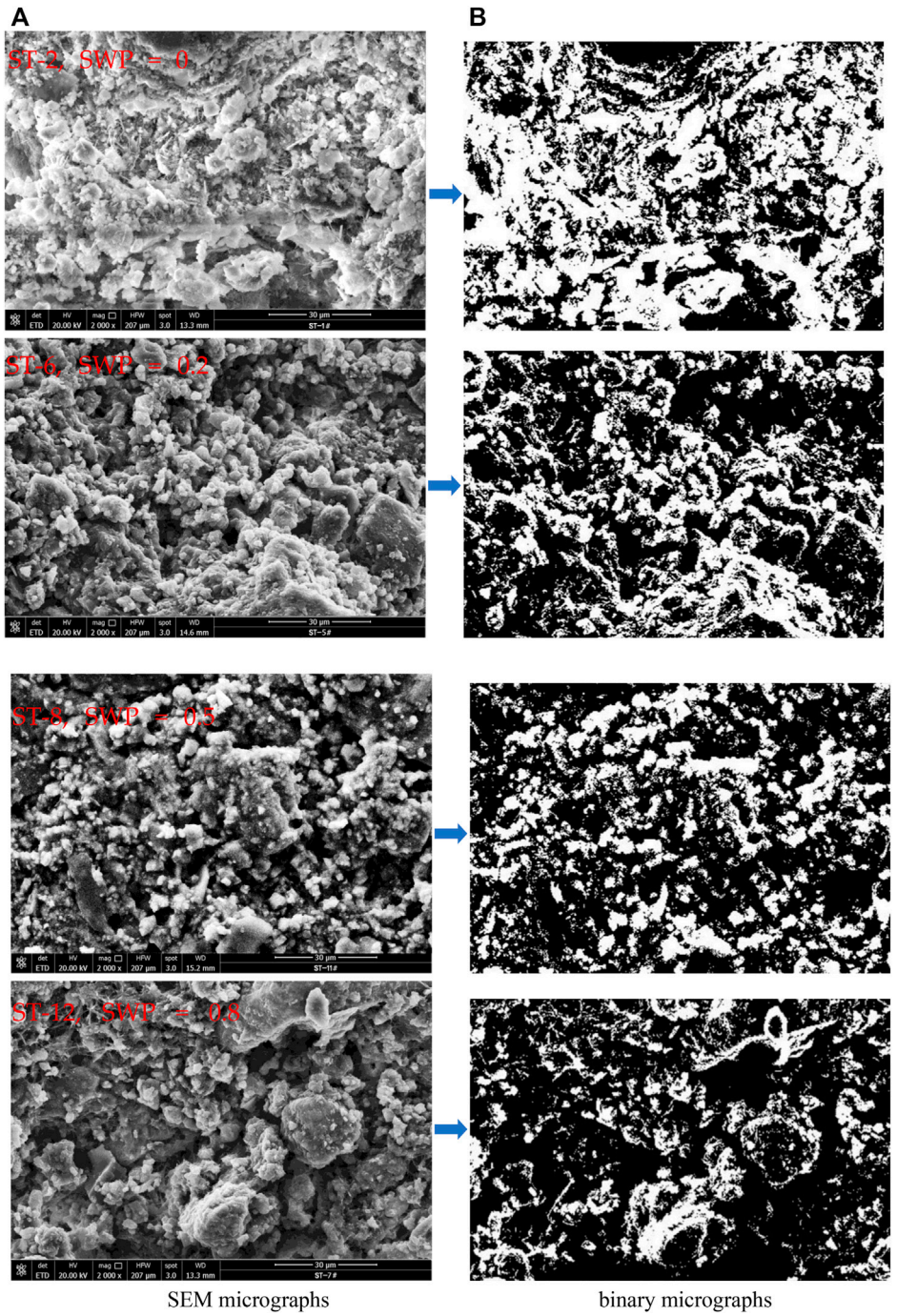

FIGURE 8 | (A) SEM micrographs and **(B)** binary micrographs of CTB specimens.

among UCS, elastic modulus, and porosity. It can be clearly seen that both the UCS and elastic modulus of CTB decreased with the increase in porosity, and both relationships were strongly nonlinear. The relationship among UCS, elastic modulus, and porosity can be fitted as $\sigma_c = 5.012e^{\frac{-n}{7.484}} + 3.393$ ($R^2 = 0.9529$) and $E = 7.896e^{\frac{-n}{6.168}} + 3.475$ ($R^2 = 0.9487$), respectively, where σ_c is the fitted UCS of CTB (MPa), E is the fitted elastic modulus of CTB (10^2 MPa), n is the porosity of CTB, and R is correlation coefficient. Both correlation coefficients were greater than 0.9, which demonstrated that the fitted equations were highly reliable. Thus, the UCS and elastic modulus of CTB under different

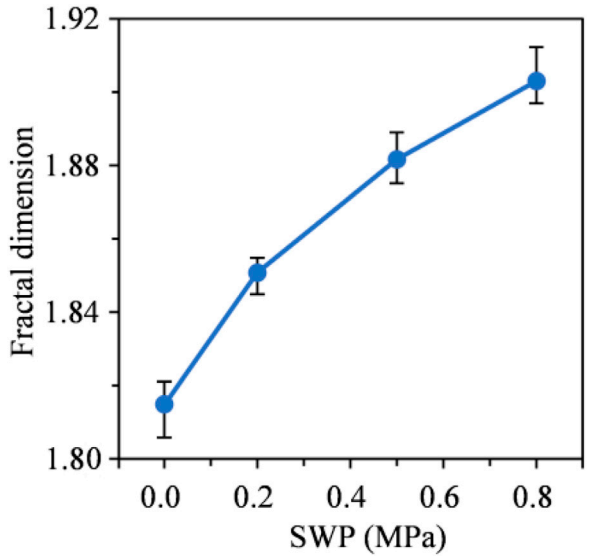

FIGURE 9 | Effect of SWP on pore area fractal dimension of CTB specimens.

SWPs can be evaluated using the above two fitting functions according to the porosity measured by NMR, which provides an effective method for obtaining UCS and elastic modulus of CTB under different SWPs.

Relationship Among UCS, Elastic Modulus, and Pore Area Fractal Dimension

The relationships among UCS, elastic modulus, and pore area fractal dimension for CTB are shown in **Figure 11**. It can be clearly seen that both the UCS and elastic modulus of CTB were negatively correlated with its pore area fractal dimension; that is, the higher the pore area fractal dimension, the lower the UCS and elastic modulus of CTB. The fitted line among UCS, elastic modulus, and pore area fractal dimension for CTB were $\sigma_c = -23.66D + 48.49$ ($R^2 = 0.9414$), $E = -35.35D + 71.22$ ($R^2 = 0.9367$), respectively, where D is the pore area fractal dimension of CTB. The two high correlation coefficients meant significant correlations and reliable fitting lines. These results indicated that the complexity of pores would lead to a lower UCS and elastic modulus of CTB, which was consistent with the findings by Ouellet et al. (2007) and Liu et al. (2020).

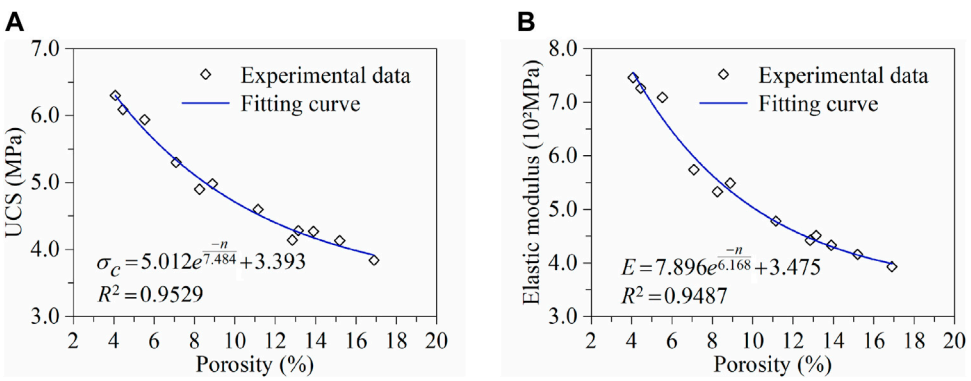

FIGURE 10 | Relationship among **(A)** UCS, **(B)** elastic modulus and porosity.

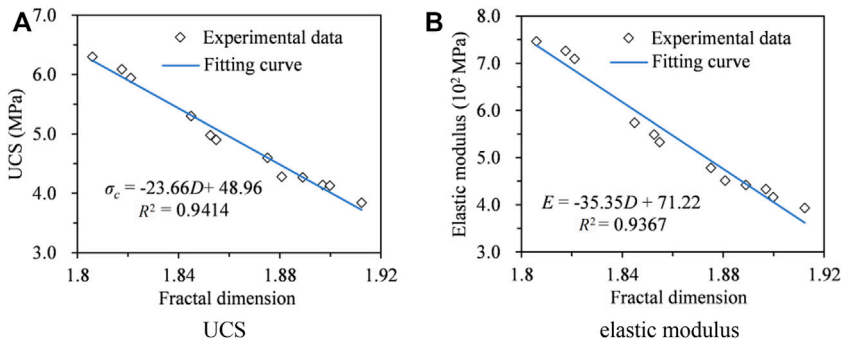

FIGURE 11 | Relationship among **(A)** UCS, **(B)** elastic modulus and pore area fractal dimension.

CONCLUSION

In this study, the effects of SWP on the mechanical properties and microstructure characteristics of CTB were studied through a series of laboratory experiments as follows: seepage experiments were conducted to simulate the damage of CTB caused by seepage; UCS tests were performed to obtain the mechanical properties of CTB. Also, NMR and SEM tests were used to analyze the microstructure characteristics of CTB. Based on the results presented in this article, the following conclusions can be drawn:

(1) Seepage had a significant deterioration effect on the mechanical properties of CTB. The UCS and elastic modulus of CTB decreased with the increase in SWP, whereas the decreasing trend reduced gradually with the increase in SWP.
(2) Seepage promoted the initiation and propagation of microcracks and pores in CTB. Higher SWP initiated and propagated more microcracks and pores in CTB, resulting in a looser and more porous microstructure of CTB, and a higher porosity and pore area fractal dimension, which seriously damaged the microstructure and weakened the mechanical properties of CTB.
(3) The T_2 spectrum showed that the pores in CTB with the largest proportion initiated and propagated by seepage were micropores, which means the damage in CTB under seepage mostly caused by micropores.
(4) The UCS and elastic modulus of CTB under seepage decrease exponentially with the increased porosity and present linearly inverse proportional relation to the pore area fractal dimension.

DATA AVAILABILITY STATEMENT

The original contributions presented in the study are included in the article/supplementary material, further inquiries can be directed to the corresponding authors.

AUTHOR CONTRIBUTIONS

Conceptualization, YK and YS; methodology, YK and KH; software, CQ, QC; validation, YS, CQ, and QC; formal analysis, YK, KH, and YS; investigation, YK, and CQ; resources, YS, and CQ; data curation, YK; writing—original draft preparation, YK and YS; writing—review and editing, KH, YK, YS, SW, QC, and HG; visualization, YK and CQ; supervision, YK, SW, KH, and HG; project administration, YS; funding acquisition, YK, SW, KH, and HG; All authors have read and agreed to the published version of the manuscript.

FUNDING

The research was supported by the National Natural Science Foundation of China (No. 51804135, 51804134), Natural Science Foundation of Jiangxi Province (No. 20192BAB216017), Doctoral Startup Fund of Jiangxi University of Science and Technology (No. jxxjbs17070), Program of Qingjiang Excellent Young Talents, Jiangxi University of Science and Technology (No. jxustqjyx2020007)and Science and technology research project of Jiangxi Provincial Department of Education (GJJ190499).

REFERENCES

Behera, S. K., Mishra, D. P., Singh, P., Mishra, K., Mandal, S. K., Ghosh, C. N., et al. (2021). Utilization of Mill Tailings, Fly Ash and Slag as Mine Paste Backfill Material: Review and Future Perspective. *Construction Building Mater.* 309, 125120. doi:10.1016/j.conbuildmat.2021.125120,

Behera, S. K., Ghosh, C. N., Mishra, D. P., Singh, P., Mishra, K., Buragohain, J., et al. (2020). Strength Development and Microstructural Investigation of lead-zinc Mill Tailings Based Paste Backfill with Fly Ash as Alternative Binder. *Cement Concrete Comp.* 109, 103553. doi:10.1016/j.cemconcomp.2020.103553

Cao, S., Yilmaz, E., and Song, W. D. (2018). Evaluation of Viscosity, Strength and Microstructural Properties of Cemented Tailings Backfill. *Minerals* 8, 352. doi:10.3390/min8080352

Cao, S., Yilmaz, E., and Song, W. (2019). Fiber Type Effect on Strength, Toughness and Microstructure of Early Age Cemented Tailings Backfill. *Construction Building Mater.* 223, 44–54. doi:10.1016/j.conbuildmat.2019.06.221

Cao, S., Yilmaz, E., Song, W., Yilmaz, E., and Xue, G. (2019). Loading Rate Effect on Uniaxial Compressive Strength Behavior and Acoustic Emission Properties of Cemented Tailings Backfill. *Construction Building Mater.* 213, 313–324. doi:10.1016/j.conbuildmat.2019.04.082

Chakilam, S., and Cui, L. (2020). Effect of Polypropylene Fiber Content and Fiber Length on the Saturated Hydraulic Conductivity of Hydrating Cemented Paste Backfill. *Construction Building Mater.* 262, 120854. doi:10.1016/j.conbuildmat.2020.120854

Chen, Q. S., Tao, Y. B., Feng, Y., Zhang, Q. L., and Liu, Y. K. (2021). Utilization of Modified Copper Slag Activated by Na2SO4 and CaO for Unclassified lead/zinc Mine Tailings Based Cemented Paste Backfill. *J. Environ. Manage.* 290, 112608. doi:10.1016/j.jenvman.2021.112608

Chen, Q., Tao, Y., Zhang, Q., and Qi, C. (2022). The Rheological, Mechanical and Heavy Metal Leaching Properties of Cemented Paste Backfill under the Influence of Anionic Polyacrylamide. *Chemosphere* 286, 131630. doi:10.1016/j.chemosphere.2021.131630

Chen, S. M., Wu, A. X., Wang, Y. M., and Wang, W. (2021). Correlation of Coupled Effects of Curing Stress and Curing Temperature on the Mechanical and Physical Properties of Cemented Paste Backfill Based on gray Relational Analysis. *Arab J. Geosci.* 14, 479. doi:10.1007/s12517-021-06659-6

Chen, S. M., Wu, A. X., Wang, Y. M., and Wang, W. (2021). Coupled Effects of Curing Stress and Curing Temperature on Mechanical and Physical Properties of Cemented Paste Backfill. *Construction Building Mater.* 273, 121746. doi:10.1016/j.conbuildmat.2020.121746

Chen, X., Shi, X. Z., Zhou, J., Yu, Z., and Huang, P. S. (2020). Determination of Mechanical, Flowability, and Microstructural Properties of Cemented Tailings Backfill Containing rice Straw. *Construction Building Mater.* 246, 118520. doi:10.1016/j.conbuildmat.2020.118520

Fall, M., Célestin, J. C., Pokharel, M., and Touré, M. (2010). A Contribution to Understanding the Effects of Curing Temperature on the Mechanical Properties of Mine Cemented Tailings Backfill. *Eng. Geology.* 114, 397–413. doi:10.1016/j.enggeo.2010.05.016

Fall, M., and Samb, S. S. (2009). Effect of High Temperature on Strength and Microstructural Properties of Cemented Paste Backfill. *Fire Saf. J.* 44, 642–651. doi:10.1016/j.firesaf.2008.12.004

Gao, R. G., Zhou, K. P., Liu, W., and Ren, Q. F. (2020). Correlation between the Pore Structure and Water Retention of Cemented Paste Backfill Using Centrifugal and Nuclear Magnetic Resonance Methods. *Minerals* 10, 610. doi:10.3390/min10070610

Ghirian, A., and Fall, M. (2014). Coupled Thermo-Hydro-Mechanical-Chemical Behaviour of Cemented Paste Backfill in Column Experiments. *Eng. Geology.* 170, 11–23. doi:10.1016/j.enggeo.2013.12.004

Ghirian, A., and Fall, M. (2013). Coupled Thermo-Hydro-Mechanical-Chemical Behaviour of Cemented Paste Backfill in Column Experiments. Part I: Physical, Hydraulic and thermal Processes and Characteristics. *Eng. Geology.* 164, 195–207. doi:10.1016/j.enggeo.2013.01.015

Gu, J. L., Yang, S. L., Gao, M. J., Bai, J., and Liu, K. (2020). Influence of Deposition Strategy of Structural Interface on Microstructures and Mechanical Properties of Additively Manufactured Al alloy. *Addit Manuf* 34, 101370. doi:10.1016/j.addma.2020.101370

Haiqiang, J., Fall, M., and Cui, L. (2016). Yield Stress of Cemented Paste Backfill in Sub-zero Environments: Experimental Results. *Minerals Eng.* 92, 141–150. doi:10.1016/j.mineng.2016.03.014

He, Y., Chen, Q., Qi, C., Zhang, Q., and Xiao, C. (2019). Lithium Slag and Fly Ash-Based Binder for Cemented fine Tailings Backfill. *J. Environ. Manage.* 248, 109282. doi:10.1016/j.jenvman.2019.109282

Hou, J., Guo, Z., Liu, W., and Zhang, Y. (2020). Mechanical Properties and Meso-Structure Response of Cemented Gangue-Fly Ash Backfill with Cracks under Seepage- Stress Coupling. *Construction Building Mater.* 250, 118863. doi:10.1016/j.conbuildmat.2020.118863

Hu, J.-h., Ren, Q.-f., Yang, D.-j., Ma, S.-w., Shang, J.-l., Ding, X.-t., et al. (2020). Cross-scale Characteristics of Backfill Material Using NMR and Fractal Theory. *Trans. Nonferrous Met. Soc. China* 30, 1347–1363. doi:10.1016/S1003-6326(20)65301-8

Jiang, F.-f., Zhou, H., Sheng, J., Kou, Y.-y., and Li, X.-d. (2020). Effects of Temperature and Age on Physico-Mechanical Properties of Cemented Gravel Sand Backfills. *J. Cent. South. Univ.* 27, 2999–3012. doi:10.1007/s11771-020-4524-6

Ke, Y., Wang, X., and Zhang, Q. (2017). Flocculating Sedimentation Characteristic of Pre-magnetized Crude Tailings Slurry. *Chin. J. Nonferrous Met.* 27, 392–398. doi:10.19476/j.ysxb.1004.0609.2017.02.021

Ke, Y., Wang, X., Zhang, Q., and Liu, E. (2017). Strength Determination of Crude Tailings Backfill in Deep Mine Based on Non-linear Constitutive Mode. *J. Northeast. University(Nat. Science)* 38, 280–283. doi:10.3969/j.issn.1005-3026.2017.02.026

Kou, M. M., Liu, X. R., Wang, Z. Q., and Tang, S. D. (2021). Laboratory Investigations on Failure, Energy and Permeability Evolution of Fissured Rock-like Materials under Seepage Pressures. *Eng. Fract Mech.* 247, 107694. doi:10.1016/j.engfracmech.2021.107694

Li, J., Cao, S., Yilmaz, E., and Liu, Y. P. (2021). Compressive Fatigue Behavior and Failure Evolution of Additive Fiber-Reinforced Cemented Tailings Composites. *Int. J. Miner. Metall. Mater.* 29, 1. doi:10.1007/s12613-021-2351-x

Li, J., Huang, Y., Li, W., Guo, Y., Ouyang, S., and Cao, G. (2021). Study on Dynamic Adsorption Characteristics of Broken Coal Gangue to Heavy Metal Ions under Leaching Condition and its Cleaner Mechanism to Mine Water. *J. Clean. Prod.* 329, 129756. doi:10.1016/j.jclepro.2021.129756

Li, J., Huang, Y., Pu, H., Gao, H., Li, Y., Ouyang, S., et al. (2021). Influence of Block Shape on Macroscopic Deformation Response and Meso-Fabric Evolution of Crushed Gangue under the Triaxial Compression. *Powder Tech.* 384, 112–124. doi:10.1016/j.powtec.2021.02.001

Liu, L., Xin, J., Huan, C., Qi, C., Zhou, W., and Song, K.-I. (2020). Pore and Strength Characteristics of Cemented Paste Backfill Using Sulphide Tailings: Effect of sulphur Content. *Construction Building Mater.* 237, 117452. doi:10.1016/j.conbuildmat.2019.117452

Mashifana, T., and Sithole, T. (2021). Clean Production of Sustainable Backfill Material from Waste Gold Tailings and Slag. *J. Clean. Prod.* 308, 127357. doi:10.1016/j.jclepro.2021.127357

Mower, T. M., and Long, M. J. (2016). Mechanical Behavior of Additive Manufactured, Powder-Bed Laser-Fused Materials. *Mater. Sci. Eng. A* 651, 198–213. doi:10.1016/j.msea.2015.10.068

Ouellet, S., Bussière, B., Aubertin, M., and Benzaazoua, M. (2007). Microstructural Evolution of Cemented Paste Backfill: Mercury Intrusion Porosimetry Test Results. *Cement Concrete Res.* 37, 1654–1665. doi:10.1016/j.cemconres.2007.08.016

Qi, C. C., Ly, H. B., Le, L. M., Yang, X. Y., Guo, L., and Pham, B. T. (2021). Improved Strength Prediction of Cemented Paste Backfill Using a Novel Model Based on Adaptive Neuro Fuzzy Inference System and Artificial Bee colony. *Construction Building Mater.* 284, 122857. doi:10.1016/j.conbuildmat.2021.122857

Qiu, J. P., Guo, Z. B., Yang, L., Jiang, H. Q., and Zhao, Y. L. (2020). Effect of Tailings Fineness on Flow, Strength, Ultrasonic and Microstructure Characteristics of Cemented Paste Backfill. *Construction Building Mater.* 263, 120645. doi:10.1016/j.conbuildmat.2020.120645

Sharma, K., and Kumar, A. (2021). Influence of rice Husk Ash, Lime and Cement on Compaction and Strength Properties of Copper Slag. *Transp Geotech* 27, 100464. doi:10.1016/j.trgeo.2020.100464,

Sun, W., Zuo, Y., Wu, Z., Liu, H., Xi, S., Shui, Y., et al. (2019). Fractal Analysis of Pores and the Pore Structure of the Lower Cambrian Niutitang Shale in Northern Guizhou Province: Investigations Using NMR, SEM and Image Analyses. *Mar. Pet. Geology.* 99, 416–428. doi:10.1016/j.marpetgeo.2018.10.042

Tan, Y.-y., Yu, X., Elmo, D., Xu, L.-h., and Song, W.-d. (2019). Experimental Study on Dynamic Mechanical Property of Cemented Tailings Backfill under SHPB Impact Loading. *Int. J. Miner. Metall. Mater.* 26, 404–416. doi:10.1007/s12613-019-1749-1

Tana, A. E. B., Yin, S. H., and Wang, L. M. (2021). Investigation on Mechanical Characteristics and Microstructure of Cemented Whole Tailings Backfill. *Minerals* 11, 592. doi:10.3390/min11060592

Wang, H. C., Qi, T. Y., Feng, G. R., Wen, X. Z., Wang, Z. H., Shi, X. D., et al. (2021). Effect of Partial Substitution of Corn Straw Fly Ash for Fly Ash as Supplementary Cementitious Material on the Mechanical Properties of Cemented Coal Gangue Backfill. *Construction Building Mater.* 280, 122553. doi:10.1016/j.conbuildmat.2021.122553

Wang, J., Fu, J. X., and Song, W. D. (2020). Mechanical Properties and Microstructure of Layered Cemented Paste Backfill under Triaxial Cyclic Loading and Unloading. *Construction Building Mater.*, 257. 119540. doi:10.1016/j.conbuildmat.2020.119540

Wang, L., Liu, J.-f., Pei, J.-l., Xu, H.-n., and Bian, Y. (2015). Mechanical and Permeability Characteristics of Rock under Hydro-Mechanical Coupling Conditions. *Environ. Earth Sci.* 73, 5987–5996. doi:10.1007/s12665-015-4190-4

Wang, S., Song, X. P., Wei, M. L., Liu, W., Wang, X. J., Ke, Y. X., et al. (2021). Strength Characteristics and Microstructure Evolution of Cemented Tailings Backfill with rice Straw Ash as an Alternative Binder. *Construction Building Mater.* 297, 123780. doi:10.1016/j.conbuildmat.2021.123780

Wang, S., Song, X. P., Chen, Q. S., Wang, X. J., Wei, M. L., Ke, Y. X., et al. (2020). Mechanical Properties of Cemented Tailings Backfill Containing Alkalized rice Straw of Various Lengths. *J. Environ. Manage.* 276, 111124. doi:10.1016/j.jenvman.2020.111124

Wu, D., Sun, W., Liu, S., and Qu, C. L. (2021). Effect of Microwave Heating on Thermo-Mechanical Behavior of Cemented Tailings Backfill. *Construction Building Mater.* 266, 121180. doi:10.1016/j.conbuildmat.2020.121180

Wu, Y., Tahmasebi, P., Lin, C., Zahid, M. A., Dong, C., Golab, A. N., et al. (2019). A Comprehensive Study on Geometric, Topological and Fractal Characterizations of Pore Systems in Low-Permeability Reservoirs Based on SEM, MICP, NMR, and X-ray CT Experiments. *Mar. Pet. Geology.* 103, 12–28. doi:10.1016/j.marpetgeo.2019.02.003

Xiao, W. J., Zhang, D. M., and Wang, X. J. (2020). Experimental Study on Progressive Failure Process and Permeability Characteristics of Red sandstone under Seepage Pressure. *Eng. Geol.* 265, 105406. doi:10.1016/j.enggeo.2019.105406

Xiu, Z. G., Wang, S. H., Ji, Y. C., Wang, F. L., Ren, F. Y., and Nguyen, V. T. (2021). Loading Rate Effect on the Uniaxial Compressive Strength (UCS) Behavior of Cemented Paste Backfill (CPB). *Construction Building Mater.* 271, 121526. doi:10.1016/j.conbuildmat.2020.121526

Xu, W. B., Li, Q. L., and Liu, B. (2020). Coupled Effect of Curing Temperature and Age on Compressive Behavior, Microstructure and Ultrasonic Properties of Cemented Tailings Backfill. *Construction Building Mater.* 237, 117738. doi:10.1016/j.conbuildmat.2019.117738

Xu, W., Cao, Y., and Liu, B. (2019). Strength Efficiency Evaluation of Cemented Tailings Backfill with Different Stratified Structures. *Eng. Structures* 180, 18–28. doi:10.1016/j.engstruct.2018.11.030

Yang, L. H., Wang, H. J., Li, H., and Zhou, X. (2019). Effect of High Mixing Intensity on Rheological Properties of Cemented Paste Backfill. *Minerals* 9, 240. doi:10.3390/min9040240

Yilmaz, E., Belem, T., and Benzaazoua, M. (2015). Specimen Size Effect on Strength Behavior of Cemented Paste Backfills Subjected to Different Placement Conditions. *Eng. Geology.* 185, 52–62. doi:10.1016/j.enggeo.2014.11.015

Yilmaz, E., Benzaazoua, M., Belem, T., and Bussière, B. (2009). Effect of Curing under Pressure on Compressive Strength Development of Cemented Paste Backfill. *Minerals Eng.* 22, 772–785. doi:10.1016/j.mineng.2009.02.002

Yin, S. H., Shao, Y. J., Wu, A. X., Wang, Z. Y., and Yang, L. H. (2020). Assessment of Expansion and Strength Properties of Sulfidic Cemented Paste Backfill Cored from Deep Underground Stopes. *Construction Building Mater.* 230, 116983. doi:10.1016/j.conbuildmat.2019.116983

Yu, S., Ke, Y., Deng, H., Tian, G., and Deng, J. (2021). Experimental Investigation of Porous and Mechanical Characteristics of Single-Crack Rock-like Material under Freeze-Thaw Weathering. *Minerals* 11, 1318. doi:10.3390/min11121318

Zhang, J. Z., Tang, Y. J., He, D. X., Sun, P., and Zou, X. Y. (2020). Full-scale Nanopore System and Fractal Characteristics of clay-rich Lacustrine Shale Combining FE-SEM, nano-CT, Gas Adsorption and Mercury Intrusion Porosimetry. *Appl. Clay Sci.* 196, 105758. doi:10.1016/j.clay.2020.105758

Zhao, Y., Wang, C. L., Ning, L., Zhao, H. F., and Bi, J. (2022). Pore and Fracture Development in Coal under Stress Conditions Based on Nuclear Magnetic Resonance and Fractal Theory. *Fuel* 309, 122112. doi:10.1016/j.fuel.2021.122112

Zheng, J., Zhu, Y., and Zhao, Z. (2016). Utilization of limestone Powder and Water-Reducing Admixture in Cemented Paste Backfill of Coarse Copper Mine Tailings. *Construction Building Mater.* 124, 31–36. doi:10.1016/j.conbuildmat.2016.07.055

Zhou, N., Du, E. B., Zhang, J. X., Zhu, C. L., and Zhou, H. Q. (2021). Mechanical Properties Improvement of Sand-Based Cemented Backfill Body by Adding Glass Fibers of Different Lengths and Ratios. *Construction Building Mater.* 280, 122408. doi:10.1016/j.conbuildmat.2021.122408

Zhou, N., Ma, H. B., Ouyang, S. Y., Germain, D., and Hou, T. (2019). Influential Factors in Transportation and Mechanical Properties of Aeolian Sand-Based Cemented Filling Material. *Minerals* 9, 116. doi:10.3390/min9020116

Conflict of Interest: The authors declare that the research was conducted in the absence of any commercial or financial relationships that could be construed as a potential conflict of interest.

Publisher's Note: All claims expressed in this article are solely those of the authors and do not necessarily represent those of their affiliated organizations, or those of the publisher, the editors and the reviewers. Any product that may be evaluated in this article, or claim that may be made by its manufacturer, is not guaranteed or endorsed by the publisher.

frontiers in Materials

ORIGINAL RESEARCH
published: 21 February 2022
doi: 10.3389/fmats.2022.844608

Strength Analysis and Optimization of Alkali Activated Slag Backfills Through Response Surface Methodology

Xinghang Dai[1], Lei Ren[2], Xiaozhong Gu[2], Erol Yilmaz[3], Kun Fang[2,3] and Haiqiang Jiang[2]**

[1]School of Civil Engineering, Liaoning Petrochemical University, Fushun, China, [2]Key Laboratory of Ministry of Education on Safe Mining of Deep Metal Mines, Northeastern University, Shenyang, China, [3]Department of Civil Engineering, Geotechnical Division, Recep Tayyip Erdogan University, Fener, Turkey, [4]Department of Civil Engineering, Lakehead University, Thunder Bay, ON, Canada

The significant difference in water-to-binder ratio, activator type and concentration between alkali-activated slag (AAS) paste/mortar/concrete and AAS-based cemented paste backfill (AAS-CPB) means that previous results related to the properties and mix optimization of AAS materials cannot be directly translated to AAS-CPB. This study statistically identifies the effect of key influential variables such as silicate modulus, slag fineness and activator concentration on 3- and 28 day unconfined compressive strength (UCS) of AAS-CPB by central composite design (CCD) established in response surface methodology (RSM). In this study, the prominence of independent variables and their relations are investigated by using ANOVA (analysis of variance) having a significant level of 0.05. ANOVA results certify that there is a strong link between the level of variable contribution on UCS performance of AAS-CPB and curing age. Obviously, silicate modulus and activator concentration are the most major variables influencing UCS at 3 and 28 days, respectively. Increased fineness of slag and higher pH of pore solution enhance 3 day UCS, but restrain the further hydration of unreacted slag and subsequent the gain in strength at advanced curing ages. The combination of independent variables of silicate modulus (0.295), slag fineness (12630.2), activator concentration (0.45) gives the optimum responses.

Keywords: tailings, alkali activated slag backfill, strength development, response surface methodology, activator type, slag fineness

OPEN ACCESS

Edited by:
Huisu Chen,
Southeast University, China

Reviewed by:
Lijie Guo,
Beijing General Research Institute of Mining and Metallurgy, China
Xiaojun Zhu,
Anhui University, China

****Correspondence:***
Kun Fang
kfang078@uottawa.ca
Haiqiang Jiang
jianghaiqiang@mail.neu.edu.cn

Specialty section:
This article was submitted to Structural Materials, a section of the journal Frontiers in Materials

Received: *28 December 2021*
Accepted: *04 February 2022*
Published: *21 February 2022*

Citation:
Dai X, Ren L, Gu X, Yilmaz E, Fang K and Jiang H (2022) Strength Analysis and Optimization of Alkali Activated Slag Backfills Through Response Surface Methodology. Front. Mater. 9:844608. doi: 10.3389/fmats.2022.844608

1 INTRODUCTION

Mining activities and ore processing are closely linked by the generation of considerable volumes of underground voids and mine tailings, respectively (Benzaazoua et al., 2004; Hajkowicz et al., 2011). If not managed properly, these voids and tailings can bring about severe and long-term operational (e.g., ground or strata instability) (Jafari et al., 2021), environmental (e.g., heavy metal pollution) (Koohestani et al., 2018) and geotechnical risks (e.g., tailings dam failure and subsidence) (Rana et al., 2021). In recent years, technological progresses coupled with environmental regulation changes, including cemented paste backfill (CPB) system, have also triggered the development in tailings and voids management (Benzaazoua et al., 1999; Fall et al., 2010). Recycling mine tailings into underground mined-out voids, CPB has been well accepted by the mining industry as one of the most effective systems for handling tailings and underground voids (Fall et al., 2008; Ercikdi et al., 2009b; Yilmaz et al., 2011). CPB is mainly a homogeneous material formed by uniformly blending

mine tailings, hydraulic binders and mixing water in a certain mass ratio (Helinski et al., 2007; Simms and Grabinsky, 2009). Mine tailings, the fine-grained and uneconomic residue of ore processing plant, is used at a typical solid concentration of 75-85wt.% for making CPB (Ercikdi et al., 2013; Ouattara et al., 2018) while mixing water, the water recycled from the plant or municipal water, is used at a typical content of 15-25wt.% to reach a desirable CPB slump required for its delivery to underground mined-out stopes (Zhao et al., 2020). The yield stress and mechanical strength of CPB are intensely affected by the type and quality of mine tailings and mixing water employed for preparing CPB materials (Kesimal et al., 2003; Simon and Grabinsky, 2013; Wu et al., 2015; Jiang and Fall 2017). Besides, the general use or ordinary Portland cement (also known as OPC) is most often used as a typical hydraulic binder within CPB's production for its versatility and availability (Ercikdi et al., 2009a; Tariq and Yanful, 2013).

While numerous works have been completed so far on mortar and concrete (Rakhimova and Rakhimov, 2015), relatively little work for the enhanced CPB performance has been done by the use of new lab tool and materials. There are some clear differences between CPB, mortar and concrete (Benzaazoua et al., 2004). Fresh and hardened characteristics of CPB is quite different from those of mortar and concrete (Li et al., 2021). This means that the amount of the water used within CPB is far more than the chemical binding capability of OPC within CPB, thereby leading to slow acquisition in the strength and low strength, especially for early ages. Moreover, mine fill cost as a percentage of the investment of the mining operation accounts for about 20%, and OPC takes up to 75% of the paste backfill costs (Belem and Benzaazoua, 2008). The usage and manufacture of OPC ingests quantities of natural resources while discharging a large amount of carbon dioxide (CD) to air (Turner and Collins, 2013). As stated by statistics, making 1-ton cement consumes 1.5-ton raw resources and produces 0.8-ton CD simultaneously (Ahmari et al., 2012; Jiang et al., 2019). All of these disadvantages have prompted the mining industry to seek for less expensive and environmental-friendly alternative binders (Behera et al., 2021).

In recent years, alkali-activated slag (AAS) materials, a new low-carbon cementitious material, have attracted increasing attention in the concrete industry (Aydin and Baradan, 2012; Bilim et al., 2013; Yuan et al., 2015; Gebregziabiher et al., 2016; Abdollahnejad et al., 2019). AAS is produced by activating slag additive with different types of activator (El-Wafa and Fukuzawa, 2018; Yang J. et al., 2019). Typical activators used for AAS are alkali hydroxide, silicate, carbonate or sulfate (Cihangir et al., 2015; Luukkonen et al., 2018; Korde et al., 2019). Recent research results show that compared with OPC-based CPB (OPC-CPB), AAS-based CPB (AAS-CPB) have excellent properties such as better-quality fluidity (Koohestani et al., 2021; Zaibo et al., 2021; Zhang et al., 2021), higher mechanical strength (Cihangir et al., 2018; Jiang et al., 2020; Cavusoglu et al., 2021), and better sulfate corrosion resistance (Cao et al., 2019b; Zhu et al., 2021b; Zheng et al., 2021). In addition, a recent study showed that usage of AAS in mine backfill fabrication can reduce the cementing cost up to 35% (Saedi et al., 2019). To sum up, AAS materials have great potential to serve as promising alternative to OPC within CPB production (Guo et al., 2021). Formulation and optimization of AAS binder is an important subject in the design of CPB (Sun et al., 2019). Several works suggest that the characteristics of AAS-CPB are significantly influenced by the sort and dosage of activator (Cihangir et al., 2015; Cihangir et al., 2018; Jiang et al., 2019; Rena et al., 2022) as well as slag characteristics (Xue et al., 2020). This means that the mixture proportion design of AAS-CPB is a complex multi-variable optimization system (Fall et al., 2008). Nevertheless, AAS-CPB materials have been classically expressed by trial and error method to obtain the anticipated properties for a given curing time and CPB mix recipe (Zhang and Yue, 2018; Yang et al., 2020). Such methods often require massive workloads, which are often unsatisfactory due to the neglect of interactions between components (Zhou et al., 2020).

There are some methods dealing the effect of several features on laboratory-based target variable (Köken and Lawal, 2021). One of them is to use response surface methodology (RSM) which uses the multivariate nonlinear regression method and strive for the optimal experimental conditions (Oraon et al., 2006; Palanikumar, 2007; Soto-Pérez et al., 2015). Being one of the most entirely used experimental design ways, RSM uses central composite design (CCD) for appraising the link between autonomous factors and responses (Zhu et al., 2021a). Recent work has indicated that the amount of OPC and silica fume to have concrete's desired unconfined compressive strength (UCS) is optimized by using the CCDs with RSM (Anurag et al., 2021). Time-dependent effect on the design of cementitious materials incorporating fly ash and iron oxide as mineral additives has been also optimized by using the RSM analysis (Gao et al., 2016).

Several works (e.g. Dai et al., 2019; Sun et al., 2020; Hefni and Hassani, 2021) have been done on CPB materials through the RSM technique. Nevertheless, none of them mentions the effect of silicate modulus, slag fineness and activator concentration on 3- and 28 day UCS of AAS-CPB. To fill this information gap, an extensive work on AAS-CPB samples by taking into account the most inducing factors leading to high UCS values at 3 and 28 days was carried out using the RSM analysis. A combination of experimental design and analytical modeling was also utilized for offering the best mixture ratios for AAS-CPB samples.

2 MATERIALS AND METHODS

2.1 Materials

2.1.1 Tailings

Silica-based tailings (ST) having a silicon dioxide of 98.6wt.% was employed for making CPB samples. Due to the fact that mine tailings (MT) chemistry is relatively complex and have a profound effect on the testing results, it is critical to use ST as aggregate material within CPB. This will eventually eradicate hesitations in the outcomes of MT-based CPB materials (Cao et al., 2019a). Indeed, it is pertinent to note that the grain size distribution (GSD) of ST consisting mainly of quartz (most prevalent mineral on Earth) is fairly akin to the mean GSD of MT found in most modern hard rock mines worldwide (Jafari et al., 2020). **Figure 1** presents the cumulative GSD curves of ST material which is wet analyzed on Malvern Panalytical Mastersizer laser diffraction test device coupled with a Hydro

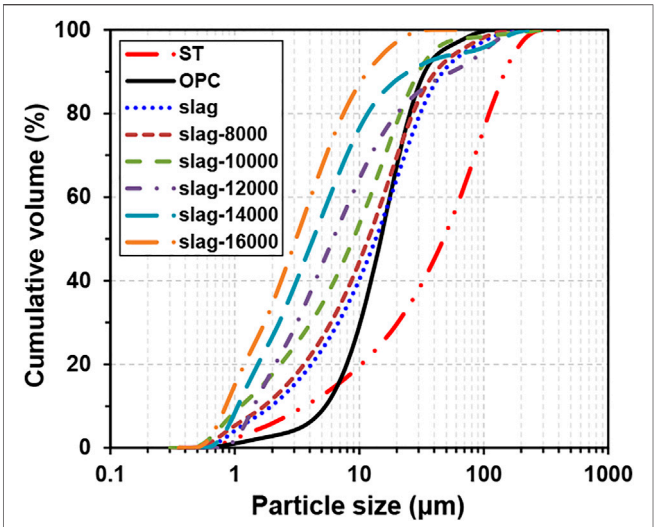

FIGURE 1 | Cumulative GSD curves of the studied materials.

S dispersion unit of a 150 ml capacity). The measurement of GSD points that the tailings sample has contained 28.41% particle size smaller than 20 μm. **Table 1** also lists the fundamental physical characteristics of ST considered as artificial tailings in this study.

2.1.2 Binder Materials

The binder used in this experiment includes an AAS binder and a typical commercial p O 42.5R OPC which is used as a reference. Slag was ensured by an iron-steel plant situated in Hubei province, China, in powder form. **Table 2** points out the main oxide and physical analyses of as-received slag and OPC. It is apparent that specific gravity (SG), specific surface area (SSA) and uniformity coefficient of OPC and as-received slag materials are respectively 3.3, 5,808 cm^2/g, and 3.29, and 2.87, 7,251 cm^2/g, and 9.11. GSD of as-received slag appears to be finer than that of OPC (**Figure 1**). X-ray diffraction (XRD) displays that slag exhibits a wide-peak package between (2θ) 25° and 35°, indicating that slag is almost completely vitreous with an amorphous structure (**Figure 2**). To appraise the influence of slag fineness on UCS performance of AAS-CPB, as-received slag was ground to BET-based SSA values of 8,073, 10,056, 11,934, 14,065 and 15,932 cm^2/g, respectively, using a ball mill. Note that Brunauer, Emmett and Teller (BET) theory is employed for assessing gas adsorption data and creating a SSA result stated in cm^2/g. The obtained slag materials are designated as slag-8,000, slag-10,000, slag-12,000, slag-14,000 and slag-16,000. The GSD curves of these grinded slags are shown in **Figure 1**.

2.1.3 Activators

Alkaline activator used was a mix of water glass (WG) solution (SiO_2 = 29.3%; Na_2O = 12.7%; H_2O = 58.0%) and sodium hydroxide (SH) with >99% purity. SH and WG were mixed in various proportions to obtain alkaline activators with silicate modulus (SiO_2 to Na_2O ratio by mass) in the range of 0.26–0.42. WG's density and pH values are respectively 1,490 kg/m^3 and 12.5. The mixing water considered in this study was de-ionized water. Details on activator's preparation can be found elsewhere 35.

2.2 Specimen Manufacturing and UCS Testing

Total 102 AAS-CPB specimens in triplicate were manufactured by mixing ST, slag, alkali activator and water for about 10 min in a double spiral blender. Prior to mixing, ST and slag were agitated by hand for 1 min. The solid concentration and slag dosage of all mixtures were set to 75% and 6%, respectively. Homogenized AAS-CPB samples were cast into plastic cylindrical molds having *D*×*H*: 50 × 100 mm. Note that there is no perforated hole at the bottom of molds for drainage purposes. The cylindrical molds were then capped with lids and maintained in a cure room holding 20 ± 1°C temperature and 95% moisture until 28 days. Following the desired cure period, the UCS tests of AAS-CPB samples were done by using a full automatic press (i.e., Humboldt HM-5030; 50 kN capacity). UCS test was done at a stress rate of 1 mm per minute until specimen fails under stress application. Before testing, CPB was taken out from the curing chamber and levelled with flat and parallel end surfaces for UCS testing. Note that the final result was calculated by averaging the results of three diverse UCS tests.

2.3 Experimental Design and Statistical Analysis

It has been reported that silicate modulus, slag fineness, activator concentration and curing temperature are the key influencing factors in the hydration of AAS binder. Since the slag nature and curing temperature are uncontrolled variables, silicate modulus, slag fineness and activator concentration (alkali activator/slag by mass) were selected as independent variables and are labeled x_1, x_2 and x_3. UCS at 3 and 28 days were taken as the response variables. Being the most frequently utilized RSM design, CCC was adopted to design the experiment. The effects of each independent variable were assessed at five levels, with the coded values of -alpha, −1, 0, +1, +alpha (**Table 3**), resulting in seventeen different experimental runs with three replicates at the center points. The spatial distribution of these experimental runs is illustrated in **Figure 3**. The levels of the variables were

TABLE 1 | A summary of physical characteristics of the studied ST material.

Type/ element	D_{10} (μm)	D_{30} (μm)	D_{50} (μm)	D_{60} (μm)	Fines (-20 μm, %)	Uniformity coefficient C_u	Curvature coefficient C_c	Specific gravity (–)	Specific surface (cm^2/g)
ST	3.66	20.4	38.8	63.7	29.6	17.4	1.79	2.65	4,238

$C_u = D_{60}/D_{10}$; $C_c = (D_{30})^2/(D_{10}\times D_{60})$.

TABLE 2 | Oxide analysis and physical characteristics of the tested slag and OPC materials.

Oxide analysis	OPC	Slag (as received)	Physical characteristics	OPC	Slag (as received)
CaO	61.75	41.95	Specific gravity (–)	3.3	2.87
Fe_2O_3	4.89	0.59	Specific surface (cm^2/g)	5,808	7,251
SiO_2	20.21	34.02	Fines (<20 μm, %)	66.3	66.6
Al_2O_3	3.98	15.23	C_u (–)	3.29	9.11
MgO	2.57	6.32	C_c (–)	1.25	1.34
SO_3	1.52	0.19	D_{50} (μm)	17.9	16.8

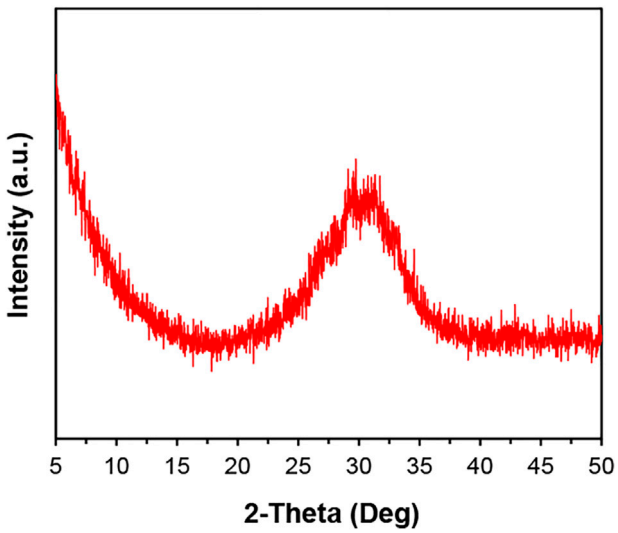

FIGURE 2 | Analysis of XRD profile of the studied slag material.

selected to vary from: 0.26–0.42 for silicate modulus (x_1), 8,000–16000 cm^2/g for slag fineness (x_2) and 0.25–0.45 for activator concentration (x_3), as illustrated in **Table 4**. CCD's experimental results were tailored by using a second order polynomial function, as demonstrated obviously in **Eq. 1**. The mathematical modeling and analysis of variance (ANOVA) were comprehensively carried out by the Design-Expert 11 software.

$$Y = \beta_0 + \sum_{i}^{k} \beta_i X_i + \sum_{i=1}^{k} \beta_{ii} X_i^2 + \sum \sum_{i<j}^{k} \beta_{ij} X_i X_j + \varepsilon \qquad (1)$$

where Y is the anticipated UCS response, X_i and X_j are the points of autonomous factors x_i and x_j, β_0 is the intercept, β_i, β_{ii} and β_{ij} are respectively the linear, quadratic and interaction coefficients, and ε is the associated random error (Pinheiro et al., 2020).

3 RESULTS AND DISCUSSIONS

3.1 Mechanical Assessments

3.1.1 Strength Resistance

3- and 28-day UCS performance of all AAS-CPB mixtures are presented in **Table 3** and **Figure 4**. All AAS-CPB samples, except for 28 day cured E12 sample, exhibit consistently superiority in the strength over CPBs made of OPC, indicating AAS has enormous potential to become an alternative to OPC in the backfill industry. This distinctive disparity in the UCS development can be explained by the difference in cement hydrating products between AAS and OPC. Previous researches (Wang et al., 1994; Wang and Scrivener, 1995; Brough and Atkinson, 2002; Gruskovnjak et al., 2006) have demonstrated that C(N)-A-S-H gel having a high Si/Ca molar ratio is major hydration products for AAS binder.

The strengths of 3 day cured AAS-CPBs range between 0.34 and 1.64, while the strengths of 28 day cured AAS-CPBs are measured in the range of 1.71–3.64 MPa. This significant fluctuation in UCS at both 3- and 28 day curing ages indicates that UCS is significantly affected by the mix composition. At 3 days, E9 with the lowest silicate modulus produces the greatest compressive strength. Meanwhile, the comparison of E9, E10 and E15 which have the same slag fineness and activator concentration indicates that the compressive strength increases with decreasing silicate modulus. The lowest 3 day strength is observed for E11 which has the lowest slag fineness. A comparison of E11and E15 that have the same silicate modulus and activator concentration reveals that an increase in slag fineness from 8,000 cm^2/g to 12000 cm^2/g yields a 197% growth in strength. This finding indicating that increasing slag fineness can improve the mechanical resistance value of AAS-CPB samples at 3 days.

The highest 28 day mechanical resistance is amazingly measured for E13 which has the lowest activator concentration in all the runs. By comparing E13, E14 and E15 which have the same silicate modulus and slag fineness, one can settle that low activator concentration is linked with high strength. It is found, surprisingly, E12 with the highest slag fineness and pretty high 3 day strength shows the lowest strength. This observation shows that the influence of autonomous variables and their connections on UCS is time-dependent.

3.1.2 RSM Modeling

The second order polynomial model (**Eq. 1**) was employed to apt measured UCS results following ANOVA. The ANOVA results for each reliant factor is summarized in **Table 4**. The absence of fit at a major level of 0.05 is employed to certify the aptness of the developed models. The *F*-values for the lack of

TABLE 3 | CCD and determined reliant variables.

Exp no	Autonomous variable blend design						Determined dependent variables	
	Coded			Non-coded			Y_{3d} (MPa)	Y_{28d} (MPa)
	X_1	X_2	X_3	x_1 (–)	x_2 (cm^2/g)	x_3 (–)		
E1	–1	–1	–1	0.30	10,000	0.3	0.84 ± 0.05	2.78 ± 0.11
E2	1	–1	–1	0.38	10,000	0.3	0.56 ± 0.11	3.31 ± 0.14
E3	–1	1	–1	0.30	14,000	0.3	1.29 ± 0.12	2.43 ± 0.08
E4	1	1	–1	0.38	14,000	0.3	0.71 ± 0.08	2.69 ± 0.09
E5	–1	–1	1	0.30	10,000	0.4	0.89 ± 0.07	2.45 ± 0.13
E6	1	–1	1	0.39	10,000	0.4	0.61 ± 0.11	2.64 ± 0.15
E7	–1	1	1	0.30	14,000	0.4	1.58 ± 0.08	2.34 ± 0.23
E8	1	1	1	0.38	14,000	0.4	1.09 ± 0.13	2.01 ± 0.25
E9	–2	0	0	0.26	12,000	0.35	1.64 ± 0.21	2.25 ± 0.21
E10	2	0	0	0.42	12,000	0.35	0.79 ± 0.13	2.51 ± 0.18
E11	0	–2	0	0.34	8,000	0.35	0.34 ± 0.04	2.41 ± 0.07
E12	0	2	0	0.24	16,000	0.35	1.21 ± 0.07	1.71 ± 0.16
E13	0	0	–2	0.34	12,000	0.25	0.67 ± 0.03	3.64 ± 0.07
E14	0	0	2	0.34	12,000	0.45	1.34 ± 0.12	2.44 ± 0.13
E15	0	0	0	0.34	12,000	0.35	1.01 ± 0.16	3.01 ± 0.06
E16	0	0	0	0.21	12,000	0.35	1.06 ± 0.08	2.91 ± 0.05
E17	0	0	0	0.21	12,000	0.35	0.96 ± 0.09	2.94 ± 0.14
E_{OPC}	—	—	—	—	—	—	0.29 ± 0.03	1.95 ± 0.07

[a] x_1: *silicate modulus;* x_2: *slag fineness;* x_3: *activator concentration.*
[b] Y_{3d}: *3 day UCS;* Y_{28d}: *28 day UCS.*
[c] E_{OPC}, *refers to OPC-CPB.*

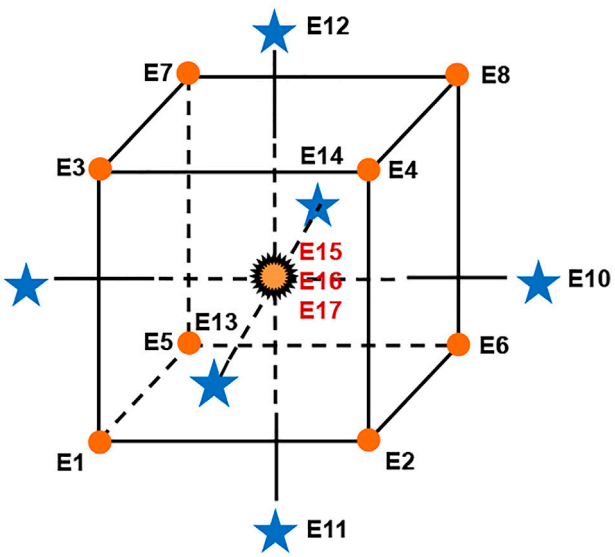

FIGURE 3 | Schematic illustration of CCD (dot in the middle of cube represents three replicates of the center point).

fit were 2.74 for 3 day UCS model and 3.25 for 28 day UCS model, implying that the derived models precisely apt the measured results. The R^2 values of 0.981 and 0.986 for 3-day UCS and 28 day UCS models, respectively, also confirms the good accuracy of the models. Plotting of the predicted values from the models versus the measured results produce perfectly linear curves, as shown clearly in **Figure 5**. All these verify the accuracy and reliability of the response surface models. The significance of all factors including main or quadratic, and their interactions is assessed by using the *p*-value at a significance level of 0.05. The factor is considered statistically substantial if its *p*-value is below 0.05. The predicted models after removing insignificant factors are given by **Eq. 2** for 3 day UCS and **Eq. 3** for 28 day UCS. As shown in **Eqs 2**, **3**, both models are expressed in second order polynomial form and all the linear factors significantly affect the response. For the 3 day UCS model, the slag fineness shows the most significant impact. The higher slag fineness and the lower silicate modulus and activator concentration, the greater the 3 day UCS. Unlike the 3 day UCS model, the most substantial linear variable influencing the 28 day UCS is activator concentration. The 28 day strength is predicted to be positively correlated with all the linear factors. Besides, the quadratic term of activator concentration does not show significant contribution to 3- and 28 day strength.

$$Y_{3d} = 3.71 - 5.6226X_1 + 0.0274X_2 - 0.7679X_3 + 2.1715X_1^2 - 0.0002X_2^2 - 0.0283X_1X_2 + 0.095X_2X_3 \quad (2)$$

$$Y_{28d} = -9.006 + 20.71X_1 + 0.0795X_2 + 4.71X_3 - 6.42X_1^2 - 0.0009X_2^2 - 0.0438X_1X_2 - 15.5X_1X_3 \quad (3)$$

3.1.3 Main and Interactional Effects

3.1.3.1 3 day UCS

To assess the effect of key and interactional variables of autonomous factors on 3 day UCS performance, 3D response-surface schemes are produced, as shown in **Figures 6–8**. These

TABLE 4 | ANOVA of RSM regression analysis.

Term	3 day UCS					28 day UCS				
	Degree-of-freedom	Sum of squares	Average square	*F* Value	*p* Value	Degree-of-freedom	Sum of squares	Average square	*F* Value	*p* Value
Model	9	2.01	0.2233	39.77	<0.0001	9	3.41	0.3785	55.19	<0.0001
X_1	1	0.6931	0.6931	123.42	<0.0001	1	0.0856	0.0856	12.47	0.0096
X_2	1	0.7700	0.7700	137.13	<0.0001	1	0.6045	0.6045	88.14	<0.0001
X_3	1	0.2783	0.2783	49.55	0.0002	1	1.09	1.09	158.46	<0.0001
X_1*X_1	1	0.0462	0.0462	8.23	0.0240	1	0.4045	0.4045	58.97	0.0001
X_2*X_2	1	0.0724	0.0724	12.89	0.0088	1	0.9763	0.9763	142.34	<0.0001
X_3*X_3	1	0.0003	0.0003	0.04	0.8368	1	0.0081	0.0081	1.19	0.3123
X_1*X_2	1	0.0325	0.0325	5.79	0.0470	1	0.078	0.078	11.37	0.0119
X_1*X_3	1	0.0010	0.0010	0.18	0.6839	1	0.1081	0.1081	15.76	0.0054
X_2*X_3	1	0.0406	0.0406	7.23	0.0311	1	0.0066	0.0066	0.96	0.3589
Residual (error)	7	0.0393	0.0056			7	0.0480	0.0069		
Lack of fit	5	0.0343	0.0069	2.74	0.2883	5	0.0427	0.0085	3.25	0.2521
Pure error	2	0.0050	0.0025			2	0.0053	0.0026		
Total	16	2.05				16	3.45			
R^2		0.9808					0.9861			
Adj-R^2		0.9562					0.9682			

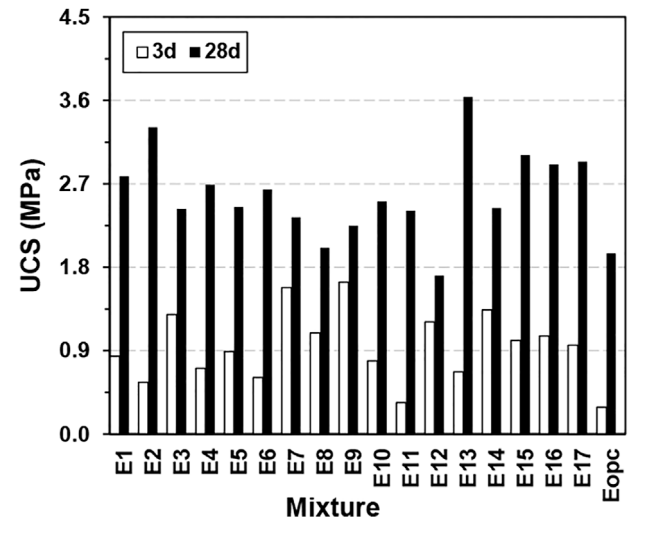

FIGURE 4 | Plots of UCS performance of 3- and 28 day cured CPB samples.

figures also enable us to identify the main trend of UCS development and then predict the optimal direction of UCS.

Figure 6 shows response surface plots of 3 day strength against the slag fineness and silicate modulus at a fixed activator concentration of 0.35. ANOVA shows that the slag fineness is the most significant independent variable influencing the 3 day strength. It is obvious that mixtures with high slag fineness give the greatest strength. Indeed, a higher slag fineness is associated with the increased reactivity and consequently more amount of hydration products (Hallet et al., 2020). The quadratic effect is also significant (**Table 4** and **Figure 6**), but its negative coefficient suggests antagonistic effect on the strength. The effect of slag fineness also depends on the silicate modulus since the interaction between slag fineness and silicate modulus is also significant (**Table 4**). The results presented in **Figure 6** show that the positive effect of MT on 3 day strength become progressively less obvious with increasing silicate modulus suggesting negative contribution of this binary interaction. Therefore, increasing MT while reducing silicate modulus is beneficial to the response.

ANOVA shows that the silicate modulus is the second most significant factor affecting the 3 day strength. As displayed in **Figure 7**, enhanced 3 day strength is observed with the decrease of the silicate modulus and is emphasized by the negative coefficient for the silicate modulus X_1 (**Eq. 2**). This is mainly because a higher pH accelerates the silicon and aluminum dissolved from slag at every-early ages, thereby resulting in more amounts of hydration products. Similar results were also made on other alkali activated materials (Sathonsaowaphak et al., 2009; Ahmari et al., 2012; Sukmak et al., 2013). The quadratic effect is also significant and is expected to increase the 3 day strength with increasing amounts. The outcomes presented in **Figure 8** and **Table 4** suggests that interaction between silicate modulus and activator concentration is negligible.

Figure 8 illustrates the response-surface and contour schemes of 3 day UCS against activator concentration and slag fineness for a silicate modulus of 0.34. Of the linear effects, the activator content is the least weighty (**Table 4**). The highest 3 day strength is achieved when activator content and slag fineness are at high levels while the silicate modulus is held at the level of 0.34. The influence of silicate modulus on the 3 day UCS performance chiefly dependents on level of slag fineness. As slag fineness is high, the increase of activator content enriches the 3 day strength performance, and this positive effect is counteracted with a decrease in slag fineness. This implies that the interaction of activator concentration and slag fineness has a significant effect on the UCS growth.

3.1.3.2 28 day UCS

Response surface and contour plots of 28 day strength were produced against two autonomous factors whereas the third

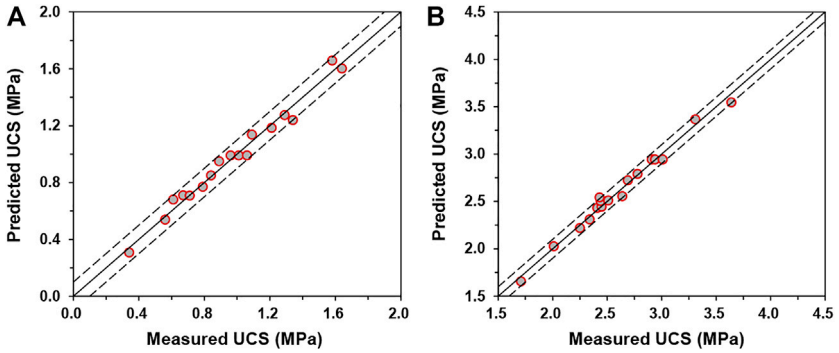

FIGURE 5 | Measured and predicted strengths for 3 day **(A)** and 28 day **(B)** cured AAS-CPB samples.

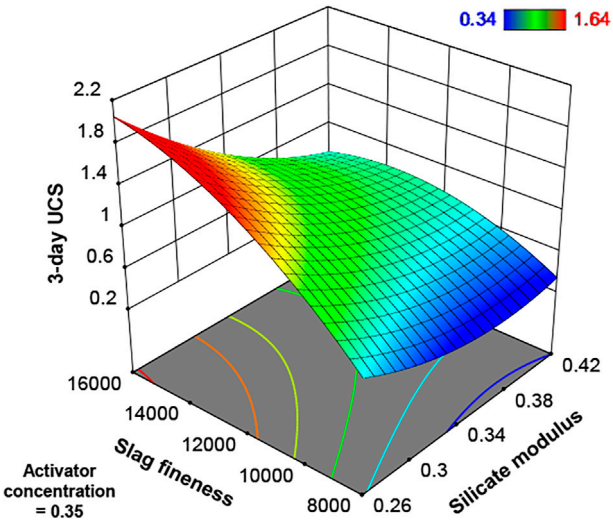

FIGURE 6 | Response-surface of the influence of slag fineness and its interaction with silicate modulus at a fixed activator concentration of 0.35.

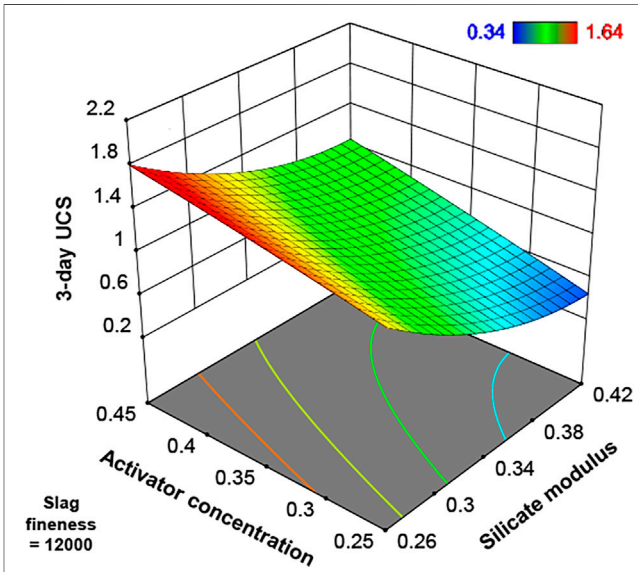

FIGURE 7 | Response-surface of the influence of silicate modulus and its interaction with activator concentration at a fixed slag fineness of 12000 cm^2/g.

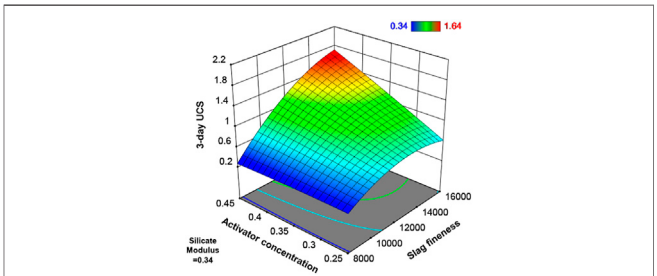

FIGURE 8 | Response-surface of the influence of activator concentration and its interaction with slag fineness for a silicate modulus of 0.34.

one is fixed constantly, as shown in **Figures 9–11**. Comparing the findings of the influence of independent variables on 3 day **6–8** and 28 day UCS (**Figures 9–11**) reveals that the plots for 28 days exhibits patterns different from those for 3 days. This suggests that the level of contribution that the variables on the strength is a function of curing time. ANOVA shows that activator concentration is the most significant independent variable influencing the 28 day UCS. From **Figure 9**, linear effect is observed for the activator concentration in the response surface and counter plots. Contrary to the 3 day strength, the 28 day strength decreases with the increase of activator concentration. Indeed, the increase of alkali promotes the hydration of slag at earlier ages, but excessive alkali will cause the formation of a dense shell surrounding slag particle thereby limiting the late-age hydration of unreacted slag.

In **Table 4** and **Figure 9**, one can observe that there is minor interaction between activator concentration and slag fineness. This indicates that the effect of slag fineness is conditioned by the activator concentration, i.e. the importance of the activator concentration hides the effect of the slag fineness. **Figure 9** shows the plots of the 28-day strength against the slag fineness and silicate modulus for an activator

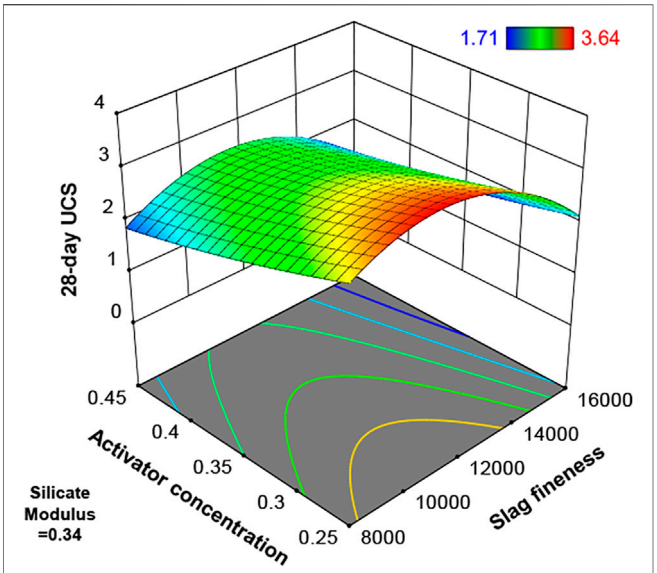

FIGURE 9 | Response-surface of the influence of activator concentration and its interaction with slag fineness for a silicate modulus of 0.34.

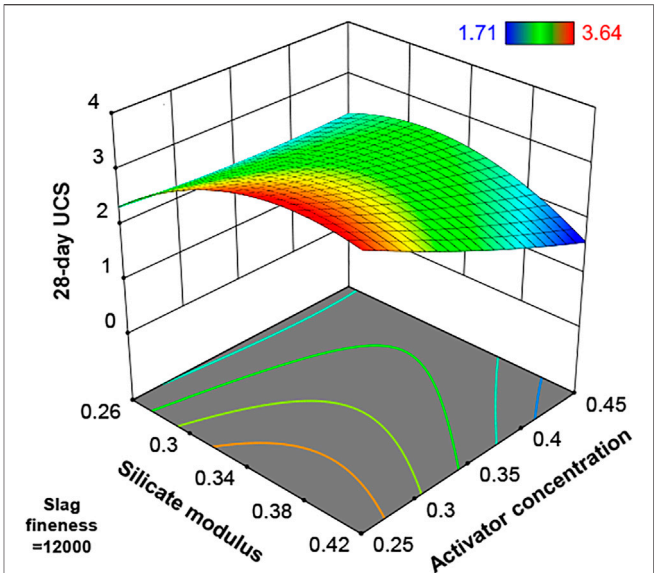

FIGURE 11 | Response-surface of the influence of activator concentration and its interaction with silicate modulus for a slag fineness of 12000 cm^2/g.

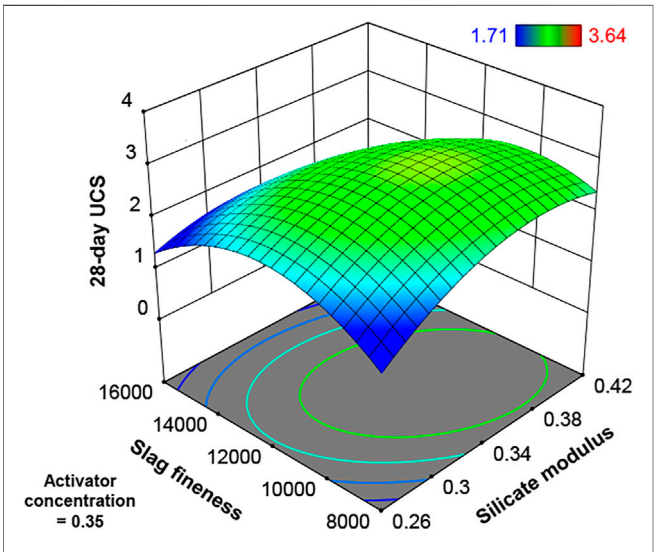

FIGURE 10 | Response-surface of the influence of slag fineness and its interaction with silicate modulus for an activator concentration of 0.35.

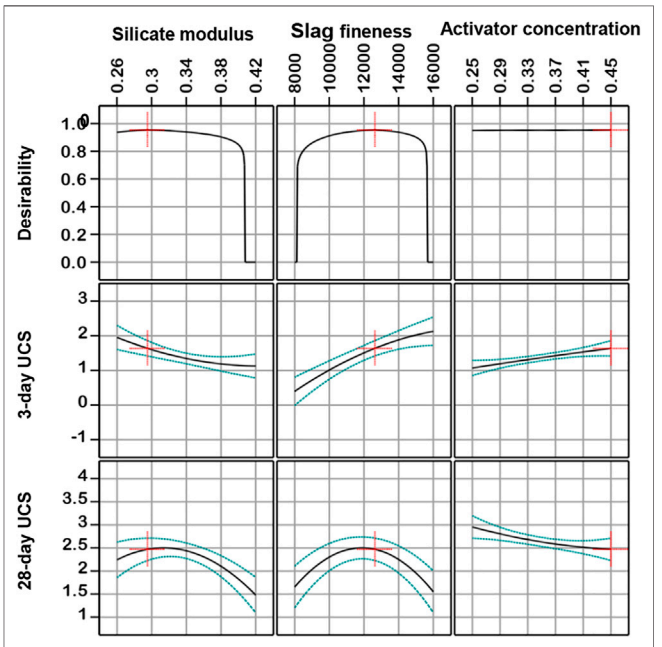

FIGURE 12 | Optimization results of RSM.

concentration = 0.35. As shown in **Table 4**, slag fineness is the second statistically significant factor for the 28 day strength, whereas at 3 days of curing it is of the most significance. This implies that the strength increment with increasing fineness of slag is more pronounced at early age rather than at later ages.

The maximum pattern of 28 day strength as a function of slag fineness and silicate modulus can be clearly seen in **Figure 10**. The 28 day strength is enhanced as the slag fineness increases up to around 10667 cm^2/g; however, the trend reverses with a further increase in the slag fineness. The quadratic effect of the slag fineness appears to be more significant than the corresponding linear effect and the negative coefficient suggests that the favorable effect erodes along with the higher slag fineness. The greatest 28 day strength is obtained around the center of the design from which variations in the slag fineness and/or silicate modulus lead to a reduction in strength. ANOVA also indicates that the binary interaction is statistically significant and has a negative influence on the response.

TABLE 5 | Optimization criteria for AAS-CPB.

Optimize items	Lower limit	Upper limit	Optimization goal
Independent variable			
Silicate modulus	0.26	0.42	—
Slag fineness	8,000	16000	—
Activator concentration	0.25	0.45	—
Response variable			
3 day UCS (MPa)	0.34	1.64	Maximum value
28 day UCS (MPa)	1.71	3.64	Maximum value

ANOVA indicates that the silicate modulus is the factor least statistically relevant. From **Figure 11**, it is obvious that as the silicate modulus increases from 0.26 to 0.42, CPBs experience a gradual increase in the 28 day strength, followed by a decrease. This is because an increase in silica inclines to reduce the hydration rate, causing higher degree of hydration and enriched UCS (Gebregziabiher et al., 2016), and the strength is a result of the competition between the hydration rate and the hydration degree. Moreover, it is found that the level of this transition point depends on activator concentration, i.e. the greater the activator concentration, the lower the transition point level. This funding indicates that there is a strong binary interaction between the silicate modulus and activator concentration.

3.1.4 Response Optimization

The mathematical models between UCS and the independent variables allows finding the optimum combinations that could produce the greatest strength at 3 and 28 days. Equal importance is signed to the optimization goals of 3 day and 28 day UCSs. The optimization criteria are summarized in **Table 5**. The desirability function approach is used for the optimization of the responses. As illustrated in **Figure 12**, the mixture with a combination of independent variables of silicate modulus = 0.295, slag fineness = 12630.2 cm^2/g, activator concentration = 0.45 (denoted as $E_{optimal}$) gives the optimum responses. The 3 day and 28 day strength is predicted as 1.64 and 2.47 MPa respectively with a global desirability of 0.955.

4 CONCLUSION

According to the results obtained from tests and analyses, following conclusions can be drawn:

✓ The magnitude of input that autonomous variables on UCS is a function of time. The most significant variables influencing 3- and 28 day UCS are slag fineness and activator concentration, respectively.

✓ Increasing hydration reaction area and the pH of pore solution favors the strength development at the very early ages. However, it is found that excessive alkali leads to the formation of a dense shell surrounding slag particle, thus reducing the strength acquisition at later ages.

✓ The mix proportion giving the optimal responses is silicate modulus = 0.295, slag fineness = 12630.2 cm^2/g, activator concentration = 0.45 with a forecast 3- and 28 day UCS of 1.64 and 2.47 MPa, respectively.

The CCD-based RSM is proved to be a reliable tool for the optimization of AAS-CPB synthesis. This methodology can be of great use in practice since there are fairly strong interactions among the components of AAS-CPB. In addition, the technical information of this investigation will be beneficial for the design of durable, cost-effective and sustainable AAS-CPB.

DATA AVAILABILITY STATEMENT

The original contributions presented in the study are included in the article/Supplementary Material, further inquiries can be directed to the corresponding authors.

AUTHOR CONTRIBUTIONS

All authors listed have made a substantial, direct and intellectual contribution to the work, and approved it for publication.

FUNDING

The authors would like to acknowledge the funding by the National Natural Science Foundation of China (grant number 51804063) and the Fundamental Research Funds for the Central Universities (grant number N2101043) is sincerely acknowledged by the writers for its generous support this research project.

REFERENCES

Abdollahnejad, Z., Luukkonen, T., Mastali, M., Kinnunen, P., and Illikainen, M. (2019). Development of One-Part Alkali-Activated Ceramic/Slag Binders Containing Recycled Ceramic Aggregates. *J. Mater. Civ. Eng.* 31, 04018386. doi:10.1061/(asce)mt.1943-5533.0002608

Ahmari, S., Zhang, L., and Zhang, J. (2012). Effects of Activator Type/concentration and Curing Temperature on Alkali-Activated Binder Based on Copper Mine Tailings. *J. Mater. Sci.* 47, 5933–5945. doi:10.1007/s10853-012-6497-9

AnuragKumar, R., Goyal, S., and Srivastava, A. (2021). A Comprehensive Study on the Influence of Supplementary Cementitious Materials on Physico-Mechanical, Microstructural and Durability Properties of Low Carbon Cement Composites. *Powder Tech.* 394, 645–668. doi:10.1016/j.powtec.2021.08.081

Aydın, S., and Baradan, B. (2012). Mechanical and Microstructural Properties of Heat Cured Alkali-Activated Slag Mortars. *Mater. Des.* 35, 374–383. doi:10.1016/j.matdes.2011.10.005

Behera, S. K., Mishra, D. P., Singh, P., Mishra, K., Mandal, S. K., Ghosh, C. N., et al. (2021). Utilization of Mill Tailings, Fly Ash and Slag as Mine Paste Backfill Material: Review and Future Perspective. *Construction Building Mater.* 309, 125120. doi:10.1016/j.conbuildmat.2021.125120

Belem, T., and Benzaazoua, M. (2008). Design and Application of Underground Mine Paste Backfill Technology. *Geotech. Geol. Eng.* 26, 147–174. doi:10.1007/s10706-007-9154-3

Benzaazoua, M., Fall, M., and Belem, T. (2004). A Contribution to Understanding the Hardening Process of Cemented Pastefill. *Minerals Eng.* 17, 141–152. doi:10.1016/j.mineng.2003.10.022

Benzaazoua, M., Ouellet, J., Servant, S., Newman, P., and Verburg, R. (1999). Cementitious Backfill with High Sulfur Content Physical, Chemical, and Mineralogical Characterization. *Cement Concrete Res.* 29, 719–725. doi:10.1016/S0008-8846(99)00023-X

Bilim, C., Karahan, O., Atiş, C. D., and İlkentapar, S. (2013). Influence of Admixtures on the Properties of Alkali-Activated Slag Mortars Subjected to Different Curing Conditions. *Mater. Des.* 44, 540–547. doi:10.1016/j.matdes.2012.08.049

Brough, A. R., and Atkinson, A. (2002). Sodium Silicate-Based, Alkali-Activated Slag Mortars - Part I. Strength, Hydration and Microstructure. *Cement Concrete Res.* 32, 865–879. doi:10.1016/S0008-8846(02)00717-2

Cao, S., Xue, G., and Yilmaz, E. (2019a). Flexural Behavior of Fiber Reinforced Cemented Tailings Backfill under Three-Point Bending. *IEEE Access* 7, 139317–139328. doi:10.1109/access.2019.2943479

Cao, S., Yilmaz, E., Song, W., and Xue, G. (2019b). Assessment of Acoustic Emission and Triaxial Mechanical Properties of Rock-Cemented Tailings Matrix Composites. *Adv. Mater. Sci. Eng.* 2019, 1–12. doi:10.1155/2019/6742392

Cavusoglu, I., Yilmaz, E., and Yilmaz, A. O. (2021). Sodium Silicate Effect on Setting Properties, Strength Behavior and Microstructure of Cemented Coal Fly Ash Backfill. *Powder Tech.* 384, 17–28. doi:10.1016/j.powtec.2021.02.013

Cihangir, F., Ercikdi, B., Kesimal, A., Deveci, H., and Erdemir, F. (2015). Paste Backfill of High-Sulphide Mill Tailings Using Alkali-Activated Blast Furnace Slag: Effect of Activator Nature, Concentration and Slag Properties. *Minerals Eng.* 83, 117–127. doi:10.1016/j.mineng.2015.08.022

Cihangir, F., Ercikdi, B., Kesimal, A., Ocak, S., and Akyol, Y. (2018). Effect of Sodium-Silicate Activated Slag at Different Silicate Modulus on the Strength and Microstructural Properties of Full and Coarse Sulphidic Tailings Paste Backfill. *Construction Building Mater.* 185, 555–566. doi:10.1016/j.conbuildmat.2018.07.105

Dai, C., Wu, A., Qi, Y., and Chen, Z. (2019). The Optimization of Mix Proportions for Cement Paste Backfill Materials via Box-Behnken Experimental Method. *J. Inst. Eng. India Ser. D* 100, 307–316. doi:10.1007/s40033-019-00180-7

El-Wafa, M. A., and Fukuzawa, K. (2018). Early-Age Strength of Alkali-Activated Municipal Slag–Fly Ash–Based Geopolymer Mortar. *J. Mater. Civ. Eng.* 30, 04018040. doi:10.1061/(asce)mt.1943-5533.0002234

Ercikdi, B., Baki, H., and İzki, M. (2013). Effect of Desliming of Sulphide-Rich Mill Tailings on the Long-Term Strength of Cemented Paste Backfill. *J. Environ. Manage.* 115, 5–13. doi:10.1016/j.jenvman.2012.11.014

Ercikdi, B., Cihangir, F., Kesimal, A., Deveci, H., and Alp, İ. (2009a). Utilization of Industrial Waste Products as Pozzolanic Material in Cemented Paste Backfill of High Sulphide Mill Tailings. *J. Hazard. Mater.* 168, 848–856. doi:10.1016/j.jhazmat.2009.02.100

Ercikdi, B., Kesimal, A., Cihangir, F., Deveci, H., and Alp, İ. (2009b). Cemented Paste Backfill of Sulphide-Rich Tailings: Importance of Binder Type and Dosage. *Cement and Concrete Composites* 31, 268–274. doi:10.1016/j.cemconcomp.2009.01.008

Fall, M., Benzaazoua, M., and Saa, E. G. (2008). Mix Proportioning of Underground Cemented Tailings Backfill. *Tunnelling Underground Space Tech.* 23, 80–90. doi:10.1016/j.tust.2006.08.005

Fall, M., Célestin, J. C., Pokharel, M., and Touré, M. (2010). A Contribution to Understanding the Effects of Curing Temperature on the Mechanical Properties of Mine Cemented Tailings Backfill. *Eng. Geology.* 114, 397–413. doi:10.1016/j.enggeo.2010.05.016

Gao, Y., Xu, J., Luo, X., Zhu, J., and Nie, L. (2016). Experiment Research on Mix Design and Early Mechanical Performance of Alkali-Activated Slag Using Response Surface Methodology (RSM). *Ceramics Int.* 42, 11666–11673. doi:10.1016/j.ceramint.2016.04.076

Gebregziabiher, B. S., Thomas, R. J., and Peethamparan, S. (2016). Temperature and Activator Effect on Early-Age Reaction Kinetics of Alkali-Activated Slag Binders. *Construction Building Mater.* 113, 783–793. doi:10.1016/j.conbuildmat.2016.03.098

Gruskovnjak, A., Lothenbach, B., Holzer, L., Figi, R., and Winnefeld, F. (2006). Hydration of Alkali-Activated Slag: Comparison with Ordinary Portland Cement. *EMPA Act.* 34, 119–128. doi:10.1680/adcr.2006.18.3.119

Guo, Z., Qiu, J., Jiang, H., Zhang, S., and Ding, H. (2021). Improving the Performance of Superfine-Tailings Cemented Paste Backfill with a New Blended Binder. *Powder Tech.* 394, 149–160. doi:10.1016/j.powtec.2021.08.029

Hajkowicz, S. A., Heyenga, S., and Moffat, K. (2011). The Relationship between Mining and Socio-Economic Well Being in Australia's Regions. *Resour. Pol.* 36, 30–38. doi:10.1016/j.resourpol.2010.08.007

Hallet, V., De Belie, N., and Pontikes, Y. (2020). The Impact of Slag Fineness on the Reactivity of Blended Cements with High-Volume Non-ferrous Metallurgy Slag. *Construction Building Mater.* 257, 119400. doi:10.1016/j.conbuildmat.2020.119400

Hefni, M., and Hassani, F. (2021). Effect of Air Entrainment on Cemented Mine Backfill Properties: Analysis Based on Response Surface Methodology. *Minerals* 11, 81–18. doi:10.3390/min11010081

Helinski, M., Fahey, M., and Fourie, A. (2007). Numerical Modeling of Cemented Mine Backfill Deposition. *J. Geotech. Geoenviron. Eng.* 133, 1308–1319. doi:10.1061/(asce)1090-0241(2007)133:10(1308)

Jafari, M., Shahsavari, M., and Grabinsky, M. (2020). Experimental Study of the Behavior of Cemented Paste Backfill under High Isotropic Compression. *J. Geotech. Geoenvironmental Eng.* 146, 06020019. doi:10.1061/(asce)gt.1943-5606.0002383

Jafari, M., Shahsavari, M., and Grabinsky, M. (2021). Drained Triaxial Compressive Shear Response of Cemented Paste Backfill (CPB). *Rock Mech. Rock Eng.* 54, 3309–3325. doi:10.1007/s00603-021-02464-5

Jiang, H., and Fall, M. (2017). Yield Stress and Strength of saline Cemented Tailings in Sub-zero Environments: Portland Cement Paste Backfill. *Int. J. Mineral Process.* 160, 68–75. doi:10.1016/j.minpro.2017.01.010

Jiang, H., Han, J., Li, Y., Yilmaz, E., Sun, Q., and Liu, J. (2020). Relationship between Ultrasonic Pulse Velocity and unconfined compressive strength for Cemented Paste Backfill with Alkali-Activated Slag. *Nondestructive Test. Eval.* 35, 359–377. doi:10.1080/10589759.2019.1679140

Jiang, H., Qi, Z., Yilmaz, E., Han, J., Qiu, J., and Dong, C. (2019). Effectiveness of Alkali-Activated Slag as Alternative Binder on Workability and Early Age Compressive Strength of Cemented Paste Backfills. *Construction Building Mater.* 218, 689–700. doi:10.1016/j.conbuildmat.2019.05.162

Kesimal, A., Ercikdi, B., and Yilmaz, E. (2003). The Effect of Desliming by Sedimentation on Paste Backfill Performance. *Minerals Eng.* 16, 1009–1011. doi:10.1016/S0892-6875(03)00267-X

Köken, E., and Lawal, A. I. (2021). Investigating the Effects of Feeding Properties on Rock Breakage by Jaw Crusher Using Response Surface Method and Gene Expression Programming. *Adv. Powder Tech.* 32, 1521–1531. doi:10.1016/j.apt.2021.03.007

Koohestani, B., Darban, A. K., Darezereshki, E., Mokhtari, P., Yilmaz, E., and Yilmaz, E. (2018). The Influence of Sodium and Sulfate Ions on Total Solidification and Encapsulation Potential of Iron-Rich Acid Mine Drainage in Silica Gel. *J. Environ. Chem. Eng.* 6, 3520–3527. doi:10.1016/j.jece.2018.05.037

Koohestani, B., Mokhtari, P., Yilmaz, E., Mahdipour, F., and Darban, A. K. (2021). Geopolymerization Mechanism of Binder-free Mine Tailings by Sodium Silicate. *Construction Building Mater.* 268, 121217. doi:10.1016/j.conbuildmat.2020.121217

Korde, C., Cruickshank, M., West, R. P., and Pellegrino, C. (2019). Activated Slag as Partial Replacement of Cement Mortars: Effect of Temperature and a Novel Admixture. *Construction Building Mater.* 216, 506–524. doi:10.1016/j.conbuildmat.2019.04.172

Li, J., Yilmaz, E., and Cao, S. (2021). Influence of Industrial Solid Waste as Filling Material on Mechanical and Microstructural Characteristics of Cementitious Backfills. *Construction Building Mater.* 299, 124288. doi:10.1016/j.conbuildmat.2021.124288

Luukkonen, T., Abdollahnejad, Z., Yliniemi, J., Kinnunen, P., and Illikainen, M. (2018). One-part Alkali-Activated Materials: A Review. *Cement Concrete Res.* 103, 21–34. doi:10.1016/j.cemconres.2017.10.001

Oraon, B., Majumdar, G., and Ghosh, B. (2006). Application of Response Surface Method for Predicting Electroless Nickel Plating. *Mater. Des.* 27, 1035–1045. doi:10.1016/j.matdes.2005.01.025

Ouattara, D., Mbonimpa, M., Yahia, A., and Belem, T. (2018). Assessment of Rheological Parameters of High Density Cemented Paste Backfill Mixtures Incorporating Superplasticizers. *Construction Building Mater.* 190, 294–307. doi:10.1016/j.conbuildmat.2018.09.066

Palanikumar, K. (2007). Modeling and Analysis for Surface Roughness in Machining Glass Fibre Reinforced Plastics Using Response Surface Methodology. *Mater. Des.* 28, 2611–2618. doi:10.1016/j.matdes.2006.10.001

Pinheiro, C., Rios, S., Viana da Fonseca, A., Fernández-Jiménez, A., and Cristelo, N. (2020). Application of the Response Surface Method to Optimize Alkali Activated Cements Based on Low-Reactivity Ladle Furnace Slag.

Construction Building Mater. 264, 120271. doi:10.1016/j.conbuildmat.2020.120271

Rakhimova, N. R., and Rakhimov, R. Z. (2015). Alkali-activated Cements and Mortars Based on Blast Furnace Slag and Red clay brick Waste. *Mater. Des.* 85, 324–331. doi:10.1016/j.matdes.2015.06.182

Rana, N. M., Ghahramani, N., Evans, S. G., McDougall, S., Small, A., and Take, W. A. (2021). Catastrophic Mass Flows Resulting from Tailings Impoundment Failures. *Eng. Geology.* 292, 106262. doi:10.1016/j.enggeo.2021.106262

RenaYadav, S., Yadav, S., Killedar, D. J., Kumar, S., and Kumar, R. (2022). Eco-innovations and Sustainability in Solid Waste Management: An Indian Upfront in Technological, Organizational, Start-Ups and Financial Framework. *J. Environ. Manage.* 302, 113953. doi:10.1016/j.jenvman.2021.113953

Saedi, M., Behfarnia, K., and Soltanian, H. (2019). The Effect of the blaine Fineness on the Mechanical Properties of the Alkali-Activated Slag Cement. *J. Building Eng.* 26, 100897. doi:10.1016/j.jobe.2019.100897

Sathonsaowaphak, A., Chindaprasirt, P., and Pimraksa, K. (2009). Workability and Strength of lignite Bottom Ash Geopolymer Mortar. *J. Hazard. Mater.* 168, 44–50. doi:10.1016/j.jhazmat.2009.01.120

Simms, P., and Grabinsky, M. (2009). Direct Measurement of Matric Suction in Triaxial Tests on Early-Age Cemented Paste Backfill. *Can. Geotech. J.* 46, 93–101. doi:10.1139/T08-098

Simon, D., and Grabinsky, M. (2013). Apparent Yield Stress Measurement in Cemented Paste Backfill. *Int. J. Mining, Reclamation Environ.* 27, 231–256. doi:10.1080/17480930.2012.680754

Soto-Pérez, L., López, V., and Hwang, S. S. (2015). Response Surface Methodology to Optimize the Cement Paste Mix Design: Time-dependent Contribution of Fly Ash and Nano-Iron Oxide as Admixtures. *Mater. Des.* 86, 22–29. doi:10.1016/j.matdes.2015.07.049

Sukmak, P., Horpibulsuk, S., and Shen, S.-L. (2013). Strength Development in clay-fly Ash Geopolymer. *Construction Building Mater.* 40, 566–574. doi:10.1016/j.conbuildmat.2012.11.015

Sun, Q., Tian, S., Sun, Q., Li, B., Cai, C., Xia, Y., et al. (2019). Preparation and Microstructure of Fly Ash Geopolymer Paste Backfill Material. *J. Clean. Prod.* 225, 376–390. doi:10.1016/j.jclepro.2019.03.310

Sun, Q., Wei, X., Li, T., and Zhang, L. (2020). Strengthening Behavior of Cemented Paste Backfill Using Alkali-Activated Slag Binders and Bottom Ash Based on the Response Surface Method. *Materials* 13, 855. doi:10.3390/ma13040855

Tariq, A., and Yanful, E. K. (2013). A Review of Binders Used in Cemented Paste Tailings for Underground and Surface Disposal Practices. *J. Environ. Manage.* 131, 138–149. doi:10.1016/j.jenvman.2013.09.039

Turner, L. K., and Collins, F. G. (2013). Carbon Dioxide Equivalent (CO2-e) Emissions: A Comparison between Geopolymer and OPC Cement concrete. *Construction Building Mater.* 43, 125–130. doi:10.1016/j.conbuildmat.2013.01.023

Wang, S.-D., and Scrivener, K. L. (1995). Hydration Products of Alkali-Activated Slag Cement. *Cement Concrete Res.* 25, 561–571. doi:10.1016/0008-8846(95)00045-E

Wang, S.-D., Scrivener, K. L., and Pratt, P. L. (1994). Factors Affecting the Strength of Alkali-Activated Slag. *Cement Concrete Res.* 24, 1033–1043. doi:10.1016/0008-8846(94)90026-4

Wu, A., Wang, Y., Wang, H., Yin, S., and Miao, X. (2015). Coupled Effects of Cement Type and Water Quality on the Properties of Cemented Paste Backfill. *Int. J. Mineral Process.* 143, 65–71. doi:10.1016/j.minpro.2015.09.004

Xue, G., Yilmaz, E., Song, W., and Cao, S. (2020). Fiber Length Effect on Strength Properties of Polypropylene Fiber Reinforced Cemented Tailings Backfill Specimens with Different Sizes. *Construction Building Mater.* 241, 118113. doi:10.1016/j.conbuildmat.2020.118113

Yang, J., Sun, Z., Li, B., Ji, Y., and Hu, K. (2019). Measuring Volume Change of Alkali-Activated Slag Pastes in Early Stage by Using Helium Pycnometry. *J. Mater. Civ. Eng.* 31, 06019011. doi:10.1061/(asce)mt.1943-5533.0002900

Yang, L., Xu, W., Yilmaz, E., Wang, Q., and Qiu, J. (2020). A Combined Experimental and Numerical Study on the Triaxial and Dynamic Compression Behavior of Cemented Tailings Backfill. *Eng. Structures* 219, 110957. doi:10.1016/j.engstruct.2020.110957

Yilmaz, E., Belem, T., Benzaazoua, M., Kesimal, A., Ercikdi, B., and Cihangir, F. (2011). Use of High-Density Paste Backfill for Safe Disposal of Copper/zinc Mine Tailings. *Gospod. Surowcami Miner./Miner. Resour. Manag.* 27, 81–94.

Yuan, B., Yu, Q. L., and Brouwers, H. J. H. (2015). Reaction Kinetics, Reaction Products and Compressive Strength of Ternary Activators Activated Slag Designed by Taguchi Method. *Mater. Des.* 86, 878–886. doi:10.1016/j.matdes.2015.07.077

Zaibo, Z., Juanhong, L., Aixiang, W., and Hongjiang, W. (2021). Coupled Effects of Superplasticizers and Glazed Hollow Beads on the Fluidy Performance of Cemented Paste Backfill Containing Alkali-Activated Slag and MSWI Fly Ash. *Powder Technol.* 399, 116726. doi:10.1016/j.powtec.2021.08.012

Zhang, L., and Yue, Y. (2018). Influence of Waste Glass Powder Usage on the Properties of Alkali-Activated Slag Mortars Based on Response Surface Methodology. *Construction Building Mater.* 181, 527–534. doi:10.1016/j.conbuildmat.2018.06.040

Zhang, S., Ren, F., Zhao, Y., Qiu, J., and Guo, Z. (2021). The Effect of Stone Waste on the Properties of Cemented Paste Backfill Using Alkali-Activated Slag as Binder. *Construction Building Mater.* 283, 122686. doi:10.1016/j.conbuildmat.2021.122686

Zhao, Y., Taheri, A., Karakus, M., Chen, Z., and Deng, A. (2020). Effects of Water Content, Water Type and Temperature on the Rheological Behaviour of Slag-Cement and Fly Ash-Cement Paste Backfill. *Int. J. Mining Sci. Tech.* 30, 271–278. doi:10.1016/j.ijmst.2020.03.003

Zheng, J., Tang, Y., and Feng, H. (2021). Utilization of Low-Alkalinity Binders in Cemented Paste Backfill from Sulphide-Rich Mine Tailings. *Construction Building Mater.* 290, 123221. doi:10.1016/j.conbuildmat.2021.123221

Zhou, N., Zhang, J., Ouyang, S., Deng, X., Dong, C., and Du, E. (2020). Feasibility Study and Performance Optimization of Sand-Based Cemented Paste Backfill Materials. *J. Clean. Prod.* 259, 120798. doi:10.1016/j.jclepro.2020.120798

Zhu, L., Jin, Z., Zhao, Y., and Duan, Y. (2021a). Rheological Properties of Cemented Coal Gangue Backfill Based on Response Surface Methodology. *Construction Building Mater.* 306, 124836. doi:10.1016/j.conbuildmat.2021.124836

Zhu, Y., Wang, Z., Li, Z., and Yu, H. (2022b). Experimental Research on the Utilization of Gold Mine Tailings in Magnesium Potassium Phosphate Cement. *J. Building Eng.* 45, 103313. doi:10.1016/j.jobe.2021.103313

Conflict of Interest: The authors declare that the research was conducted in the absence of any commercial or financial relationships that could be construed as a potential conflict of interest.

Publisher's Note: All claims expressed in this article are solely those of the authors and do not necessarily represent those of their affiliated organizations, or those of the publisher, the editors and the reviewers. Any product that may be evaluated in this article, or claim that may be made by its manufacturer, is not guaranteed or endorsed by the publisher.

frontiers in Materials

ORIGINAL RESEARCH
published: 04 March 2022
doi: 10.3389/fmats.2021.794089

Temperature Effect on Mohr–Coulomb's Effective Strength Parameters of Paste Backfill

Alsidqi Hasan[1]* *and Wee Kiet Ting*[2]

[1]Senior Lecturer, The Department of Civil Engineering, Universiti Malaysia Sarawak, Kota Samarahan, Malaysia, [2]Graduate Student, The Department of Civil Engineering, Universiti Malaysia Sarawak, Kota Samarahan, Malaysia

In-stope paste backfill monitoring at different mine sites showed anomalous increase in total stress during rest periods. One of the explanations according to a recent laboratory-model experiment was attributed to volumetric expansion caused by temperature increase within the backfill. This paper extends the understanding whether the Mohr–Coulomb's effective strength parameters are affected by such temperature increase. The effects are explained through evaluating the apparent cohesion and the effective internal and interfacial friction angles under different temperature conditions. A series of modified direct shear tests were performed on saturated specimens under three controlled temperature levels: 25°C, 50°C, and 70°C. The specimens consist of cemented paste backfill and uncemented paste backfill. The results show that the effective internal and the interfacial friction angles increase as the temperature increases, depending on the type of material and the shearing condition, whereas the temperature increase does not significantly affect the apparent cohesion. The findings serve as a reference for engineers and academics in explaining the stress anomaly and to better understand the shear behavior of paste backfill under different temperature conditions for mine stope backfill design.

Keywords: cemented paste backfill, effective stress, temperature, mine backfill, arching

OPEN ACCESS

Edited by:
Erol Yilmaz,
Recep Tayyip Erdoğan University, Turkey

Reviewed by:
Chongchong Qi,
Central South University, China
Mamadou Fall,
University of Ottawa, Canada

****Correspondence:***
Alsidqi Hasan
halsidqi@unimas.my

Specialty section:
This article was submitted to Structural Materials, a section of the journal Frontiers in Materials

Received: *13 October 2021*
Accepted: *21 December 2021*
Published: *04 March 2022*

Citation:
Hasan A and Ting WK (2022) Temperature Effect on Mohr–Coulomb's Effective Strength Parameters of Paste Backfill. Front. Mater. 8:794089. doi: 10.3389/fmats.2021.794089

INTRODUCTION

Technological advancement increases the demand on the minerals which could be fulfilled through mining (Yilmaz et al., 2003; Bai et al., 2018). The scarcity of minerals in the shallow ground level necessitates deeper underground level to be explored by the industry to stay profitable (Sheshpari 2015). Underground mining produces mined-out voids (stopes) that could cause underground instability and indirectly give impact to the ore recovery rate and safety issues (Rankine and Sivakugan 2007; Xuan et al., 2013; Adajar and Pabilona 2018). Concurrently, mining processing plants also generate a significant amount of waste rock and tailings.

Paste backfilling is a relatively new tailings management technique, which utilizes tailing in the form of a paste as the backfill material, also known as paste backfill, to fill-up stopes and improve general underground stability. Paste backfill stabilized with cement binder is commonly known as cemented paste backfill (CPB). The CPB has been used in many underground mining operations due to its technical, environmental, and economic strong points (Li and Yang 2015; Jaouhar et al., 2018). The CPB is a flowable material that is made from dewatered tailing, cement binder, and water. It can become a self-supporting material after a few days to provide adjacent support within stopes (Helinski et al., 2007; Ghirian and Fall 2015). The widely used mix proportion of CPB uses cement

binder approximately 3%–7% by dry weight and tailings approximately 70%–85% by total weight (Landriault 1995; Orejarena and Fall 2011). The CPB with 2.5%–7% water to cement ratio has better flowability without clogging the pipeline (Ramlochan et al., 2004).

After gaining enough shear strength, the weight of the backfill is transferred to the stope bottom and sidewalls due to a phenomenon, known as arching (Fahey et al., 2009). When arching occurs in a filled stope, the vertical stress at the bottom of the fill is less than the fill's weight due to stress transfer to the stope sidewalls (Janssen 1895; Marston 1930; Terzaghi 1943). Arching is primarily associated with the frictional and/or cohesive interaction between the backfill and the stope sidewalls (Belem and Benzaazoua 2008; Moradi and Abbasnejad 2015).

The stability of CPB structures is a function of many factors, such as the mechanical properties of the CPB as well as the interfacial properties between the CPB and the sidewalls. Therefore, the understanding on the interfacial shear strength parameter of the CPB stope sidewall is important (Nasir and Fall 2008; Koupouli et al., 2016). In common design practice, the interfacial friction angle of CPB is often ignored as the shear failure is not likely to occur at CPB rock interface due to the high surface roughness of the unevenly blasted wall (Pierce 2001).

In-stope monitoring of CPB deposition at different mine sites shows an anomalous stress increase during rest periods, which was speculated due to the increase in temperature (Thompson et al., 2012; Hasan et al., 2014; Doherty et al., 2015). The rest period in this paper refers to the period after the backfilling stops either temporarily (i.e., between plug pour and subsequent backfilling) or permanently (i.e., after the final backfilling). The presence of additional heat causes the CPB to expand and, therefore, increases the exerted pressure (Mitchell et al., 1982). The available *in situ* data show that the temperature typically increases up to 50°C (Grabinsky and Thompson 2009; Thompson et al., 2012; Hasan et al., 2014). The change in shearing temperature constitutes to the final shear parameter of the material (Karademir 2011). Lee et al. (2016) showed the significance of the shear parameter on the reduction of earth pressure in stress transfer. As a consequence of the temperature increase, the strength parameter obtained from tests at a constant temperature may not be adequate to explain the stress distribution within the backfill.

A recent laboratory model experiment has shown that the temperature increase within the backfill can potentially cause an increase in total stress (Hasan et al., 2018; Ting et al., 2020). The paste backfill expands as shown by the volumetric strain observed from the unrestrained top of the backfill during the temperature increase. Such evident has proved that the temperature increase directly affects the total stress parameter of the paste backfill through the volumetric expansion. On the other hand, an alternative explanation for total stress increase was associated with creep behavior of the surrounding rock mass, which was proven through numerical investigation and a few backfill tests (Qi and Fourie 2019). These two explanations are independent in nature; therefore, the anomaly might be caused by either one or both at the same time.

Figure 1 illustrates the importance of the paste backfill mechanism within stope wall when there is a thermal expansion due to the temperature increase. As the backfill is deposited within a stope, the vertical stress is transferred to the sidewalls due to arching; exothermic reaction from the cement hydration and other sources of heat contribute to the expansion. Thus, arching is intensified. To date, there have been no explanations on how this temperature increase affects the Mohr–Coulomb's effective strength parameters of the paste backfill.

Mohr–Coulomb's effective strength parameters are expressed a linear relationship between the shear stress, τ, kPa (y-axis), and normal effective stress, σ', kPa (y-axis) as follows:

$$\tau = c' + \sigma' tan\varphi' \quad (1)$$

where c' is the intercept of the linear model (equation) to y-axis and the ϕ' is the effective friction angle. The c' is appropriately known as apparent cohesion, in which the value can be originated from the true cohesion (in cohesive or cemented materials) or merely as a result of statistical curve fitting. Experimental evidences showed that Mohr–Coulomb linear relationship can produce a statistical apparent cohesion in cohesionless granular material, which is contributed from the dilatancy, particle angularity, and interlocking (Alshibli et al., 2000).

The objective of this paper is to extend the understanding whether the Mohr–Coulomb's effective strength parameters are affected by the temperature increase by presenting the experimental results on the paste backfill in the forms of the apparent cohesion and the internal and interfacial friction behaviors under different shearing temperature conditions. The results were obtained from a series of modified direct shear tests, which will improve the understanding regarding the stress parameters within the backfill when the increase in temperature is expected.

MATERIALS AND METHODS

The CPB is reproduced in the laboratory by mixing fine silica flour, binder, and water. The properties of these three materials are determined and controlled to ensure the reproducibility and repeatability of the results. For comparison purposes, the uncemented paste backfill (UCPB) is also investigated along with the CPB.

Silica flour is selected as tailing replacement material. It is a finely ground crystalline silica manufactured by SILVERBOND® Pasir Gudang, Johor, Malaysia. It contains high purity of SiO_2 quartz and free of sulfide minerals as shown in **Table 1**. Note that the presence of sulfide is undesirable because sulfide oxidizes into sulfate and affects the shear strength of CPB. The silica flour is inert, is neutral in pH, comes with good uniformity, and shall not degrade at high temperature (<110°C).

The use of silica flour as tailing replacement has been widely adopted by researchers (Fall et al., 2010; Wu et al., 2016) due to its similarity of particle size toward the average of nine Canadian mine tailings (Nasir and Fall 2008; Fall et al., 2010; Abdul-Hussain and Fall, 2012; Ghirian and Fall, 2015). Its mixture with water can be categorized as paste fill because it contains particles at least 15% cumulative passing of 20 μm (Potvin et al., 2005). **Figure 2** shows the particle size distribution of the silica flour. The particle's mean diameter, d, is 25 μm, and the

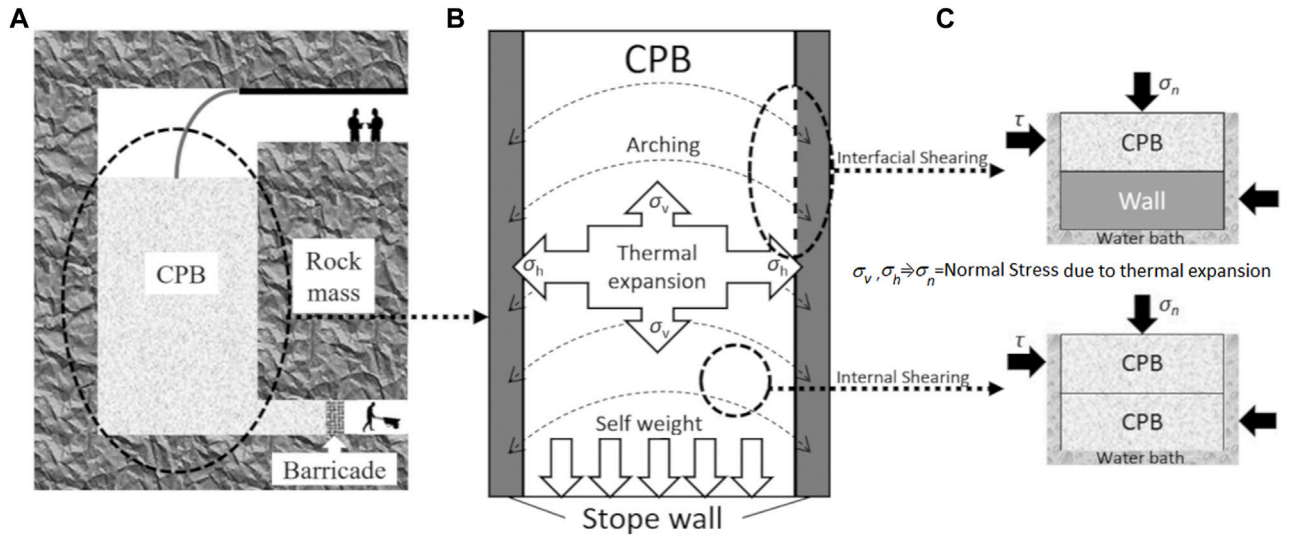

FIGURE 1 | Illustration of paste backfill mechanism. **(A)** Deposition of CPB into stope, **(B)** stress mechanism of CPB, and **(C)** simulated mechanism in laboratory test.

TABLE 1 | Chemical elements and physical properties of the silica flour.

Chemical elements		Physical properties		
Element's name	**Percent weight (%)**	**Properties**	**Unit**	**Value**
Al	0.33	G_s	—	2.67
Ca	0.01	D_{10}	μm	8.2
Si	99.38	D_{30}	μm	17
Fe	0.01	D_{50}	μm	25
Na	0.01	D_{60}	μm	30
S	0.00	D_{90}	μm	56
K	0.02	C_u	—	3.66
Mg	0.01	C_c	—	1.17
Ti	0.04	—	—	—

coefficient of uniformity, *Cu*, is 3.66. The physical properties of the silica flour are summarized in **Table 1**.

Ordinary Portland cement (OPC) is used as the binder for CPB. It is obtained from a local company cement producer Cahya Mata Sarawak (CMS), whose quality of cement conforms with the standard requirement specified in Malaysian Standard MS EN 94 197-1, which is equivalent to ASTM C150.

Tap water is used for mixing, which is neutral in pH, free from chemical residual, low total dissolved solids, and no salinity as stated in the quality control standards. The water pH, the total dissolved solids, and the salinity are 6.84, 74.3 ppm, and 0.0627 ppt, respectively. These data are obtained from water quality tests using PCSTestr35 EUTECH Instruments.

MODIFIED DIRECT SHEAR TESTS

Apparatus

ELE International digital direct shear apparatus is used as the main component. A temperature controlling system is incorporated in the direct shear apparatus, which consists of a digital temperature controller, two heating elements, and a thermocouple. For the interfacial shear test, the mold is modified such that only the upper half (top) is filled with paste sample whereas the lower half (bottom) is replaced with an aluminum plate to simulate the stope sidewalls. The aluminum plate measures 60 mm wide, 60 mm long, and 5 mm thick. Note that it has the same cross-sectional area as the inner side of the mold. The sample and the aluminum surface were precisely positioned at the shearing plane. Aluminum material is used because it has an elastic modulus of about 70 GPa, which is in the range of the elastic modulus of the rock mass (20–100 GPa) in mine stopes (Hoek and Diederichs 2006; Belem and Benzaazoua 2008). For every test, a new aluminum plate obtained from the same material is used to ensure similar surface roughness.

The direct shear test is performed conforming to ASTM (2011). During the test, the shear box is filled with water to keep the sample fully saturated throughout shearing. Water heating elements are immersed in the shear box to generate heat. The temperature is controlled and monitored using a temperature controller and thermocouples. Such incorporation of temperature controlling system as shown in **Figure 3A** does not cause disturbance toward the shearing process. Normal stress is applied accordingly, and the sample is sheared under drained condition at the rate of 1 mm/min until 15% shear strain is achieved. The shearing rate is selected on the basis of the longest time required for UCPB or CPB samples to achieve 90% consolidation (t_{90}), which is measured at about 0.5 min (ASTM, 2011). The total elapsed time to failure is 5.8 min, and the horizontal displacement at failure is about 6 mm. Thus, the maximum displacement rate suitable for these experiments is 1.0 mm/min. During testing, the pore water is freely to dissipate (drain-out) from the top and bottom of the mold. A photograph of the setup is shown in **Figure 3B**.

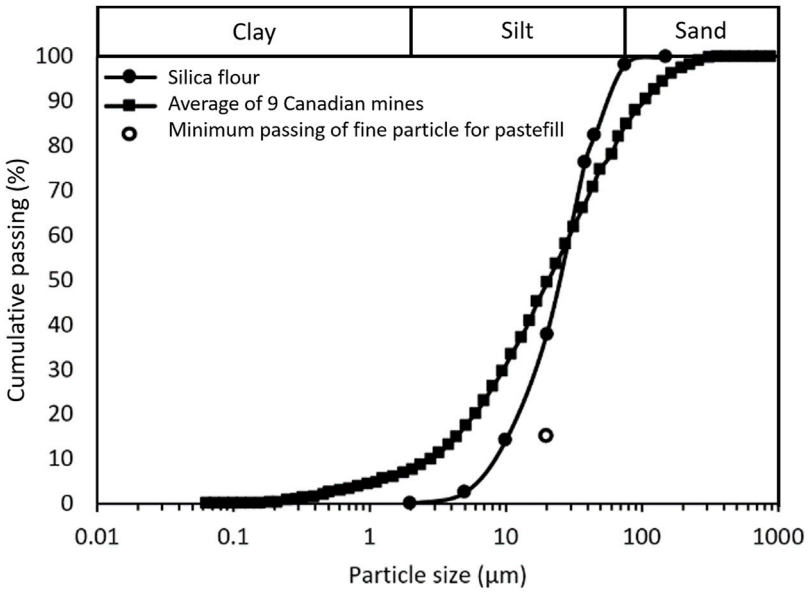

FIGURE 2 | Particle size distribution of silica flour.

Sample Preparation and Tests

Fresh silica flour that consists of less than 0.2% bulk water content (from the bag) is used for the preparation of all samples. A series of slump tests and UCS tests are performed to acquire the most suitable mix design for both UCPB and CPB, which are illustrated in **Figure 4**. Unconfined compressive strength (UCS) of CPB is usually between 200 and 5,000 kPa, but the common target strength in practice is 1,000 kPa at 28 days or 300 kPa at 3 days (Sheshpari 2015). Ghirian and Fall (2016) and Wu et al. (2016) also showed similar findings, where at 3 days of curing, the UCS should be approximately 300 kPa. From **Figure 4A**, 5% of the binder is chosen to obtain the UCS at approximately 300 kPa after 3 days of curing. The amount of OPC (binder) used is decided by the percentage of solid dry mass, B_w, as given in **Eq. 1**.

$$\boldsymbol{B_w\%} = \frac{\boldsymbol{W_B}}{\boldsymbol{W_{dry-s}}} \times 100\% \tag{2}$$

where W_B is the weight of binder and $W_{dry\text{-}S}$ is the dry weight of solid.

Figure 4B shows the relationship between three variables, solid content, yield stress, and normalized slump height (z/H) for samples with 5% cement binder content. Note that z is the slump and H is the height of the slump cylinder. A range of normalized slump height (z/H) versus yield stress estimation is also shown in **Figure 4B**, which is adopted from Pashias et al. (1996). Yield stress below 200 Pa is recommended for a clog-free flow within the pipeline (Cooke 2008). Therefore, 72% solid content with 115 Pa of yield stress is chosen.

Table 2 lists the number of specimens and tests conducted. Mix composition of 72% solid content and 28% water content are used for UCPB and CPB sample specimens. The cement binder content for UCPB and CPB are 0% and 5%, respectively, for all tests. The water–cement ratio for CPB is 7.7. UCPB and CPB specimen's mixture properties are summarized in **Table 2**. Three levels of temperature are selected, 25°C, 50°C, and 70°C. The lowest temperature represents the normal ambient temperature when paste is poured into the stope. The middle temperature represents the typical temperature increase based on available literature data, whereas the highest temperature is chosen to look at further effect at the higher temperature level. Two types of shearing conditions are applied to UCPB and CPB specimens, namely, internal (INT) and interfacial (IFC) tests. The interfacial tests for CPB are further divided into two types, namely, precast (PC) and cast *in situ* (CIS). Unlike CIS, the PC specimen is prepared in an external mold prior to testing, which does not possess the cementation bonding between CPB and its shearing surface. The paste is mixed with water in a flour mixer until it becomes homogenous. The time of mixing is approximately 5 min, which is within dissolution stage of hydration process. The PC specimen is prepared by pouring the mix into a 60 mm–by–60 mm mold (the same size as the direct shear mold), whereas CIS CPB specimen is casted directly in the direct shear box mold. **Figure 5** shows specimens before testing. The CPB specimen is cured under high humidity for 2 days and cured under saturated condition for the remaining 1 day. The binder content and curing time are maintained for every test as the internal and interfacial shear behavior is significantly affected but does not apply to CPB specimens that are prepared using PC.

RESULTS AND DISCUSSIONS

The expansion of UCPB and CPB specimens is evident from the vertical displacement from dial gauge measurement as shown in

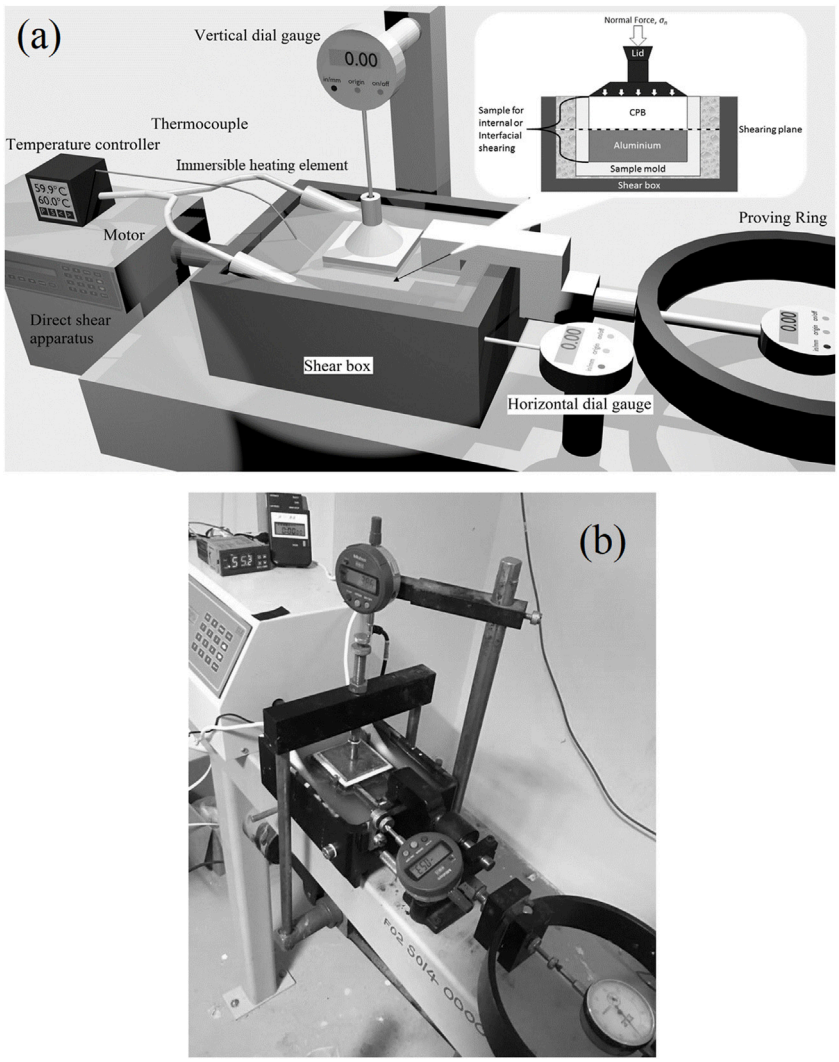

FIGURE 3 | The apparatus. **(A)** Illustration of the setup. **(B)** The photograph.

Figure 6. As the temperature increases, both types of specimen expand vertically until the temperature becomes constant. The CPB specimen maintains its vertical displacement, whereas the UCPB specimen shows a slight decrease after the peak is reached. It is thought due to that particles in UCPB specimens can freely rearrange and reconsolidate during the temperature increase, whereas the cementation in CPB prevents such rearrangement. As a result, the vertical displacement between CPB and UCPB appears to be quite significant. It is also shown in **Figure 6** that the time to reach a constant temperature is approximately 1,100 s. For the estimation based on simple calculation using thermal conductivity formula, the time needed to heat the specimen from 24°C to 70°C is only about 88.6 s. The time difference between actual and calculated might be due to the heat dissipation to the box mold, box carriage, and the surrounding air.

The stress–strain curves for UCPB and CPB are shown in **Figure 7** and **Figure 8**, respectively. In general, the stress increases as the strain increases until peak stress is reached after which the stress becomes constant. Peak stresses are mostly shown for CPB samples, where the stress slightly diminishes afterward and becomes constant at residual.

Internal and Interfacial Shear Stress of UCPB at Different Temperature

Figures 7A–C show the stress–strain behavior of the INT UCPB, whereas **Figures 7D–F** show the interfacial stress–strain behavior between UCPB and aluminum plate (IFC UCPB) at different temperature conditions. The initial density of the UCPB samples is 1,750 kg/m^3. On average, the peak stress of IFC UCPB is lower than peak stress of INT UCPB by an average of 32.25%.

Upon reaching the desired temperature, non-cohesive material such as UCPB is able to reconsolidate to balance out the change in volume caused by thermal expansion. After reconsolidation, the material behaves slightly over-consolidated. Therefore, small differences in peak residual strength are observed at 50°C and 70°C.

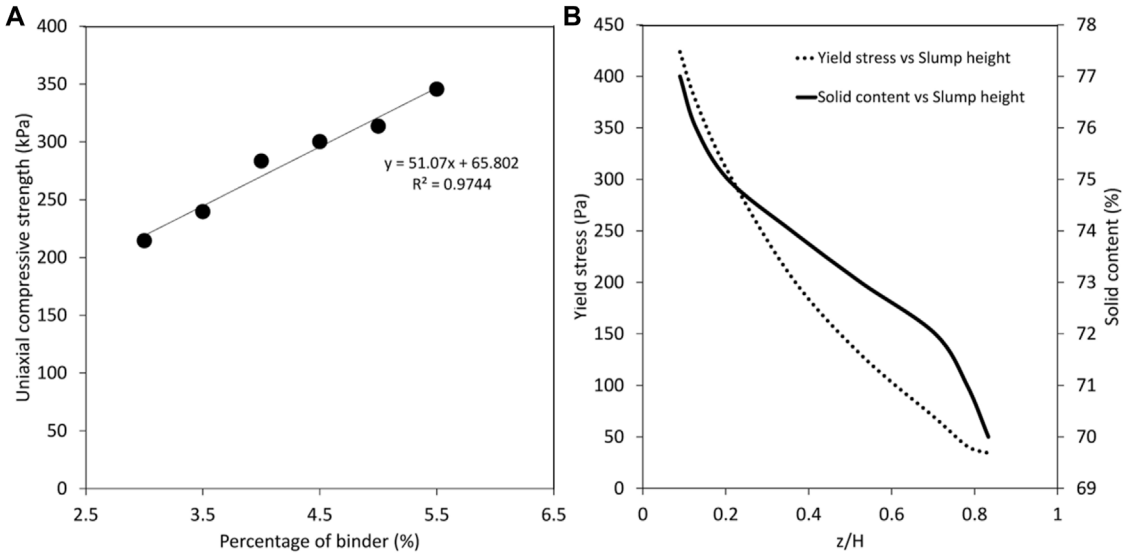

FIGURE 4 | Slump and strength tests results. **(A)** UCS versus percent binder. **(B)** Yield stress versus solid content and normalized slump height for samples with 5% cement binder content.

TABLE 2 | List of test and specimen mixture properties.

Specimen*	Shearing condition	Shearing temperature (°C)		
UCPB*	Internal	25	50	70
	Interfacial	25	50	70
CPB*	Internal	25	50	70
	CIS interfacial	25	50	70
	PC interfacial	25	50	70

Mixture Properties	*Specimen	
	UCPB	CPB
Binder content, Bw (%)	0	5
Solid mass content, Cw (%)	72	72
Water content (out of total), wT (%)	28	28
Water content (out of solid), wS (%)	38.9	38.9
Water to cement ratio, w/c	—	7.7
Slump height, S (mm)	21	17
UCS (kPa) 3 days	48	314
Estimated yield stress (Pa)	70	115

Overall, **Figure 7** shows that the shear stress for internal shearing is higher than stress for interfacial shearing. This is expected because the shear plane for interfacial shearing takes place between paste-and-smooth aluminum plate as compared to particle-and-particle in internal shearing. For INT UCPB, there is a total gain of stress by 16.36% from 25°C to 50°C and by 10.40% from 50°C to 70°C that is with an average gain of 0.156 kPa/°C. As for the interfacial shearing, there is a total gain of stress by 18.52% from 25°C to 50°C and by 11.38% from 50°C to 70°C that is with an average gain of 0.098 kPa/°C.

Internal and Interfacial Shear Stress of CPB at Different Temperature

Figures 8A–C show the shear stress–strain behavior of INT CPB at different temperature conditions, whereas **Figures 8D–I** show the interfacial shear stress strain behavior of CPB and aluminum plate (IFC CPB) using different casting methods, namely, CIS (8d to 8f) and PC (8g–8i) specimen's preparation. The peak stress is

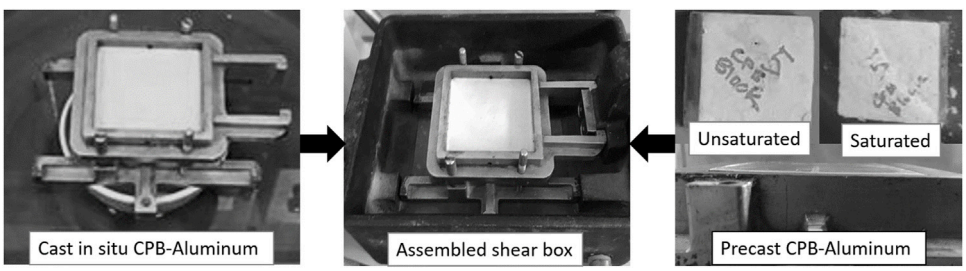

FIGURE 5 | Preparation of CPB specimens.

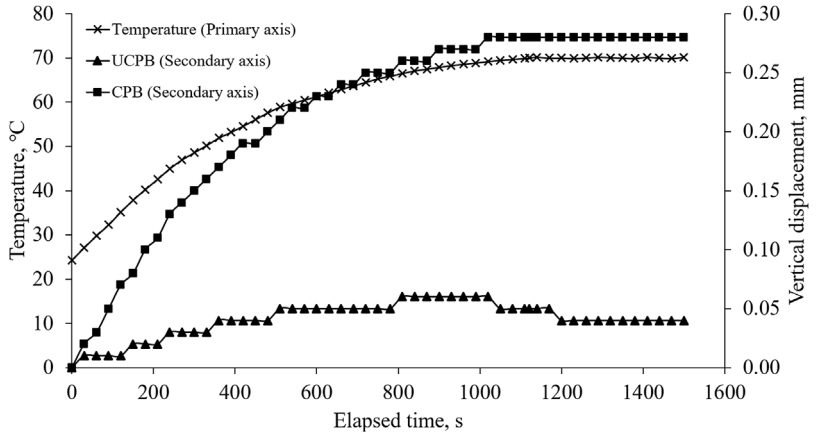

FIGURE 6 | Change in vertical displacement with temperature.

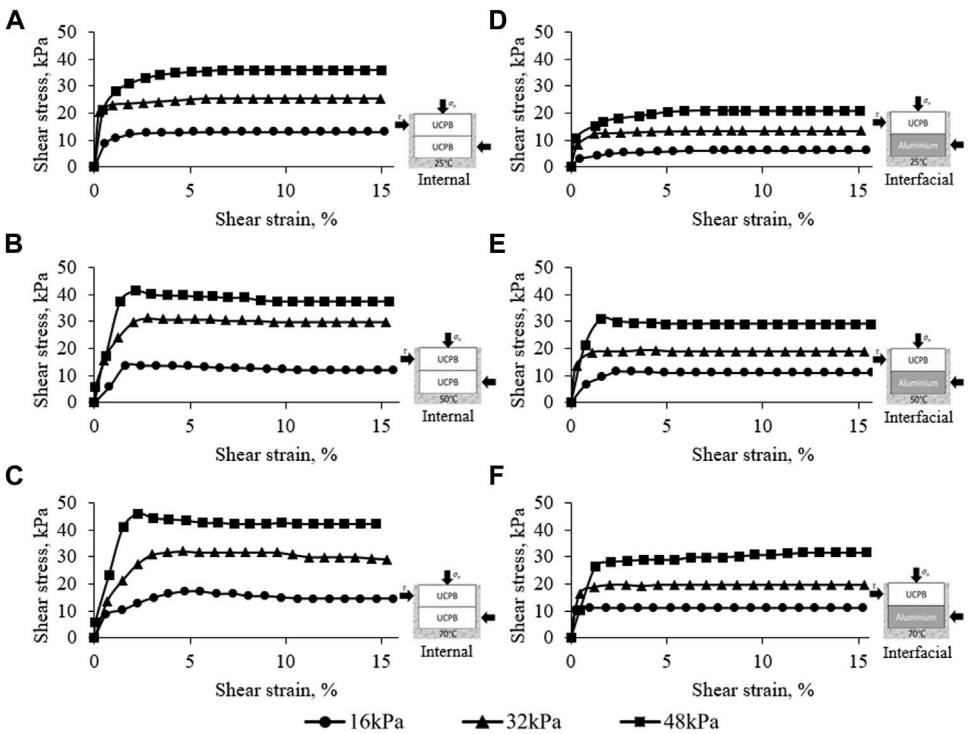

FIGURE 7 | Shear stress–strain of UCPB under different shearing conditions. **(A)** INT UCPB at 25°C, **(B)** INT UCPB at 50°C, **(C)** INT UCPB at 70°C, **(D)** IFC UCPB at °C, **(E)** IFC UCPB at 50°C, and **(F)** IFC UCPB at 70°C.

observed at the region less than 3% shear strain for both internal and interfacial shearing. It is observed during this experiment that there is a cement bonding seen in between CIS CPB and the surface of the aluminum. The interfacial shear stress of CIS IFC CPB is lower than the shear stress INT CPB by an average of 36.26%. During post-interfacial shear test, the sample is inspected and found that every sample had nearly perfect failure occurring precisely on the shearing plane although some small irregularities are observed.

After the peak stress is reached, the stress remains or reduces to the residual state after 3% shear strain. INT CPB possesses the highest shear strength, then followed by CIS IFC CPB, and finally PC IFC CPB as the weakest. For INT CPB, there is a total gain of stress by 36.96% from 25°C to 50°C and by 27.26% from 50°C to 70°C that is with an average gain of 0.583 kPa/°C. As for IFC CPB, there is a total gain of stress by 17.38% from 25°C to 50°C and by 11.40% from 50°C to 70°C that is with an average gain of 0.176 kPa/°C. **Figures 8G–I** (CIS CPB) show similar

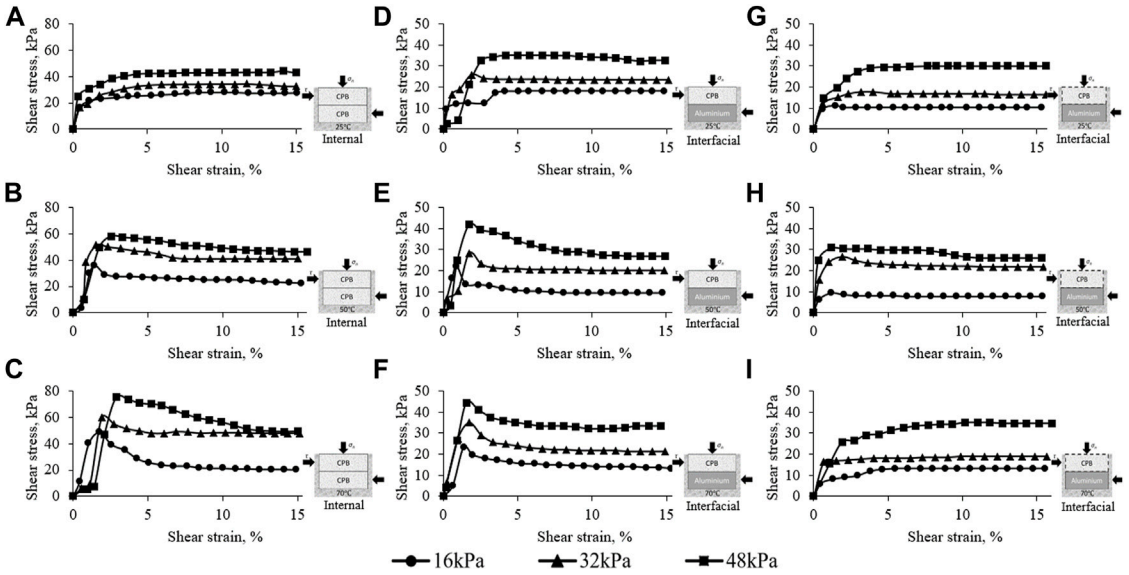

FIGURE 8 | Shear stress–strain of CPB under different shearing conditions. **(A)** INT CPB at 25°C, **(B)** INT CPB at 50°C, **(C)** INT CPB at 70°C, **(D)** CIS IFC CPB at 25°C, **(E)** CIS IFC CPB at 50°C, **(F)** CIS IFC CPB at 70°C, **(G)** PC IFC CPB at 25°C, **(H)** PC IFC CPB at 50°C, and **(I)** PC IFC.

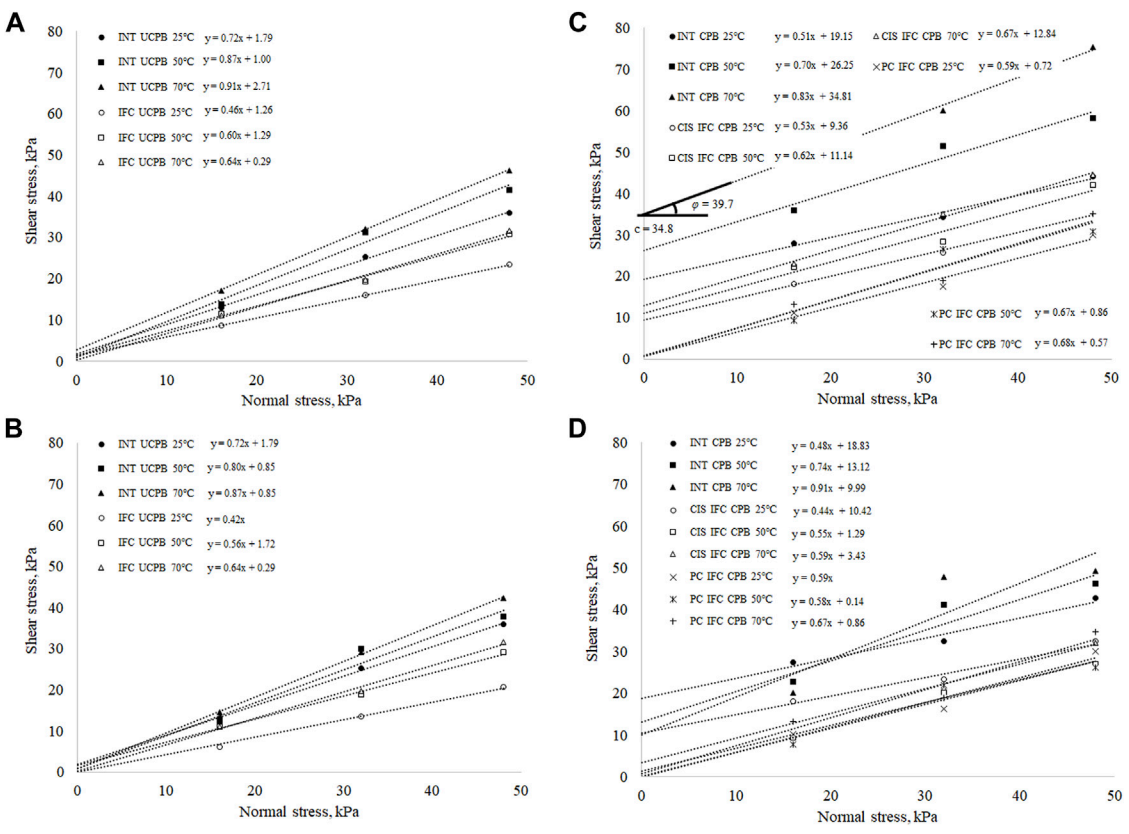

FIGURE 9 | Mohr–Coulomb envelope on **(A)** peak stress of UCPB, **(B)** residual stress of UCPB, **(C)** peak stress of CPB, and **(D)** residual stress of CPB under different shearing conditions.

TABLE 3 | Test samples apparent cohesion and friction angle under each shearing condition.

Material	UCPB						CPB								
Shearing condition	INT			IFC			INT			CIS IFC			PC IFC		
Temperature, °C	25	50	70	25	50	70	25	50	70	25	50	70	25	50	70
Peak Friction Angle, °	35.8	41.0	42.3	24.7	31.0	32.6	27.0	35.0	39.7	27.9	31.8	33.8	30.5	33.8	34.2
Residual Friction Angle, °	35.8	38.7	41.0	22.8	29.2	32.6	25.6	36.5	42.3	23.7	28.8	30.5	30.5	30.1	33.8
Peak Apparent Cohesion	1.8	1.0	2.7	1.3	1.3	0.3	19.2	26.3	34.8	9.4	11.1	12.8	0.7	0.9	0.6
Residual Apparent Cohesion	1.8	0.9	0.9	0.0	1.7	0.3	18.8	13.1	10.0	10.4	1.3	3.4	0.0	0.1	0.9

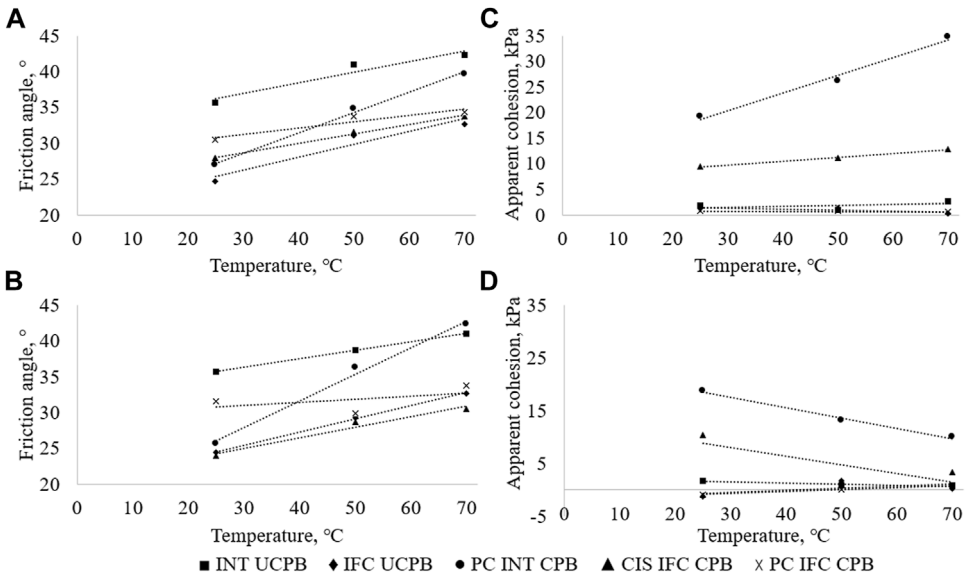

FIGURE 10 | Effects of temperature on **(A)** peak friction angle, **(B)** residual friction angle, **(C)** peak apparent cohesion and **(D)** residual apparent cohesion for every sample.

stress–strain behavior as **Figures 8D–F** (PC CPB). They show that CIS CPB possesses higher shear stress by an average of 12.46%.

Apparent Cohesion and Friction Angle Comparison at Different Temperature Conditions

Overall, CPB specimens possess higher shear stress than UCPB samples at higher temperatures. The difference is clearly contributed from the cohesivity of the CPB due to cement bonding that gives additional strength to the shearing. INT CPB shows stress with an average of 85.95% higher than INT UCPB, whereas the same increment applies for IFC CPB by an average of 69.25% in comparison to IFC UCPB. The effect of temperature on INT CPB and CIS IFC CPB tests shows higher shear strength increment, whereas it only shows slight inconsistent increment on INT UCPB, IFC UCPB, and PC IFC CPB tests. The peak residual stress is more significant for CPB in comparison to UCPB.

Figure 9 shows the Mohr–Coulomb envelope of UCPB and CPB under different shearing conditions, and **Table 3** lists values of the apparent cohesion and friction angle obtained from **Figure 9**. These envelopes are produced by fitting a linear regression line for each dataset. Every shear failure envelope obeys the Mohr–Coulomb failure criterion where the increase in stress is linear to the normal stress induced. **Figure 10** shows the Mohr–Coulomb effective strength parameters at different temperature conditions.

It is expected that the apparent cohesion is negligible (or zero) for cases other than INT CPB and CIS IFC CPB. Minor apparent cohesion in the range of 0.1–2.7 kPa is obtained as results from curve fitting. It is noticeable from the UCPB Mohr–Coulomb envelope that the minor apparent cohesion created in INT UCPB shearing, in general, is higher than IFC UCPB. PC CPB at 3 days found to be slightly dissolved by the water during saturation. The dislodgement of CPB particles causes the surface of CPB to be slightly adhesive when the specimen was removed from water. However, because the rate of the displacement was low enough, the small value of apparent cohesion (i.e., less than 1 kPa) in PC

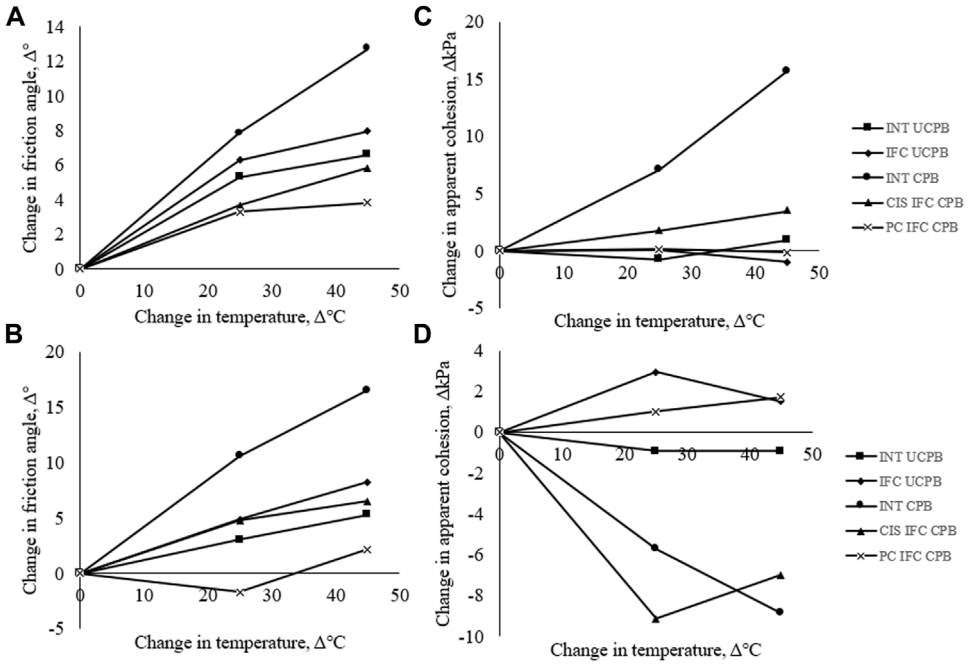

FIGURE 11 | Effect of change in temperature on the change of **(A)** peak friction angle, **(B)** residual friction angle, **(C)** peak apparent cohesion, and **(D)** residual apparent cohesion for every sample.

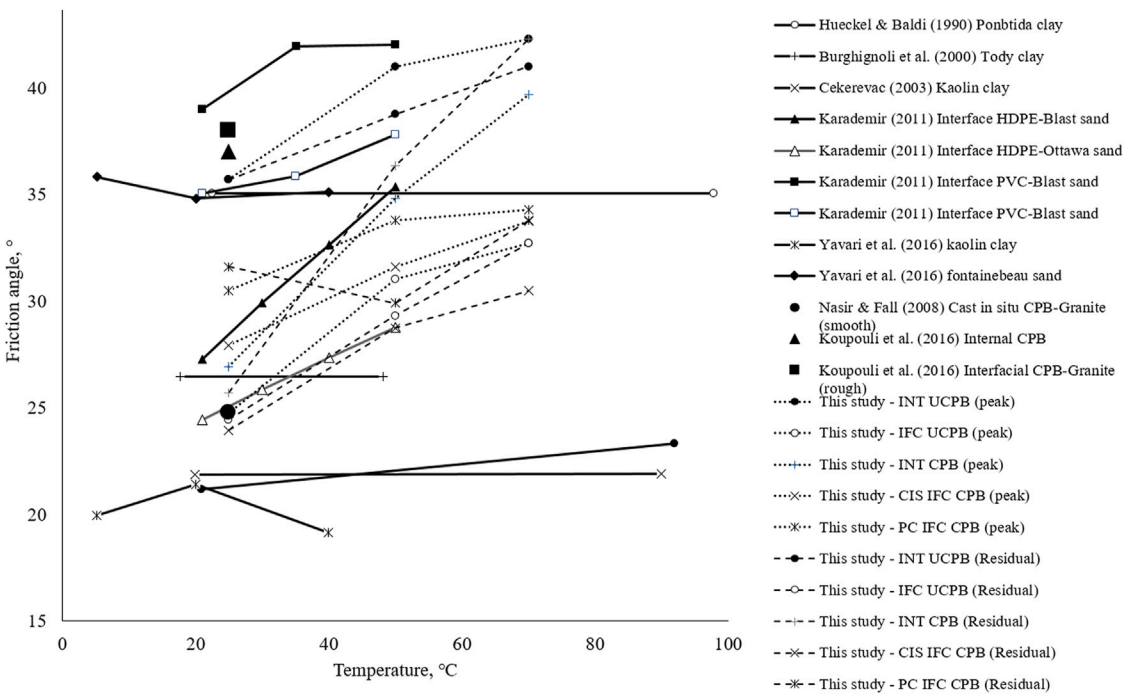

FIGURE 12 | Summary of findings from stated researchers on different material, shearing plane, and temperature.

UCPB might also be originated from curve fitting. The apparent cohesion obtained from INT CPB shearing is greater than CIS IFC CPB by 104.6% at 25°C, 135.7% at 50°C, and 171.1% at 70°C. **Figure 10C** shows that higher temperature has a positive effect on the peak apparent cohesion value of the CIS IFC CPB sample and a greater influence on the INT CPB sample. However, **Figure 10D**

shows that the residual apparent cohesion for CIS IFC CPB decreases as the temperature increases. This could be due to the effect of difference in thermal expansion between the plate and CPB on compromising hydration bond, which is reflected in residual apparent cohesion. For INT CPB, there is a total gain of apparent cohesion by 37.06% from 25°C to 50°C and by 32.61% from 50°C to 70°C that is with an average gain of 0.356 kPa/°C. As for IFC CPB, there is a total gain of stress by 18.99% from 25°C to 50°C and by 15.29% from 50°C to 70°C that is with an average gain of 0.078 kPa/°C.

The friction angle generally increases with respect to the increase of shearing temperature, but the increment of friction angle varies according to the material and shearing condition. Unlike apparent cohesion values, the angle of friction of PC IFC CPB is found to be higher than that of CIS IFC CPB for both peak and residual, which means that interfacial area in PC IFC is rougher than CIS IFC. The interfacial roughness condition from two materials (CPB and plate) just introduced before the test contributes to a higher interfacial friction angle compared to the interface created in CIS IFC (although previously bonded). The friction angles in IFC UCPB are slightly closer to the CIS IFC CPB compared to PC IFC CPB. The effect of adhesion bonding during CIS only increases the apparent cohesion but not the friction angle. The friction angle of IFC UCPB is significantly lower by an average of 25.64% due to the smooth surface of aluminum platforms in comparison to friction angle of INT CPB. The friction angle of PC IFC CPB is higher than that of IFC UCPB by an average of 11.38% as the surface roughness of CPB aluminum is higher than that of UCPB aluminum.

Although INT CPB acquires the greatest gain in friction angle at higher temperatures (0.23°/°C), UCPB or non-coesive sample generally possesses a greater friction angle although the gain (0.07–0.14°/°C) due to temperature is less significant as shown in **Figure 10**. Cohesive material (i.e., INT CPB and CIS IFC CPB) possesses lower frictional angle because of the higher initial stress needed to overcome cementation bond. Thus, it shows less stress gain from the variation of normal stress applied and reduces the friction angle of the material upon obeying the linear law of Mohr–Coulomb envelope. On the basis of **Figure 11**, the effects of change in temperature on the change of friction angle and apparent cohesion can be clearly seen.

Some of the findings on thermal shearing using different materials, shearing plane, and temperature range are used to be compared with the findings from this study (**Figure 12**). Different types of sand and clay had been used to investigate the effect of temperature on its shear behavior, but none had performed such testing on CPB. The clay is slightly affected by the change in temperature, but the effect on the changes in friction angle is inconsistent as reported by Hueckel and Baldi (1990), Burghignoli et al. (2000), and Cekerevac (2003). The effect of temperature on interfacial shearing is discussed by Karademir (2011) by varying the surface plane with high-density polyethylene and polyvinyl chloride with Blast sand and Ottawa sand. The finding shows a clear increment of friction angle with the increase in shearing temperature for every variation. Such findings discussed above are comparable to INT UCPB and IFC UCPB. The interfacial friction angle at the backfill aluminum is lower than internal friction angle of the backfill itself with an average factor of 0.69 at room temperature in comparison to 0.67, which is commonly used.

Nasir and Fall (2008) showed the interfacial friction angle and adhesion of CIS CPB to be 24.78° and 27.06 kPa, respectively, with no shearing temperature stated, and smooth limestone rock was used (dry, binder = 4.5%, w/c = 7.6, and cured at 3 days). The adhesion is higher than our results as the surface roughness of aluminum is smoother than the rock that is claimed to be smooth. Koupouli et al. (2016) showed that the internal and interfacial friction angle along with adhesion of CPB and in between PC CPB and smooth granite 266 rock were 37° and 15 kPa and 38° and 8 kPa, respectively (shearing temperature not stated), that is 102.7% higher for friction angle and 46.7% lower for apparent cohesion.

CONCLUSION

The paper presents the experimental results on the shear strength behavior of effective internal and interfacial friction between UCPB and CPB with 5% binder content, observed at the temperature of 25°C, 50°C to 70°C under five different shearing conditions and three effective stress levels (16, 32, and 48 kPa). Comparisons between the findings with related published data are reported. A thorough analysis is made on each dataset obtained; then, the following conclusions can be drawn:

- The shear failure envelopes both internal and interfacial tests at all temperature fit Mohr–Coulomb failure criterion.
- The effective internal and interfacial friction angle (ϕƏ) values increase with temperature.
- The temperature does not significantly affect the apparent cohesion.
- The interfacial shear parameters for both CIS and PC IFC CPB aluminum are comparable with the previous finding on interfacial shear behavior of CIS and PC CPB rock (assumed to be at room temperature of 25°C).

This study shows the significance of accurate design parameters such as shear strength, apparent cohesion, and friction angle at different temperature conditions for realistic and safer stress distribution estimation on mine backfill design.

DATA AVAILABILITY STATEMENT

The raw data supporting the conclusion of this article will be made available by the authors, without undue reservation.

AUTHOR CONTRIBUTIONS

AH is the lead investigator. WT is the student of the lead investigator who conducts the experiment under the guidance of the lead investigator.

FUNDING

This research is financially supported by Fundamental Research Grant Scheme (no. FRGS/TK01 (01)/1301/2015 (18)) by the Ministry of Higher Education Malaysia.

ACKNOWLEDGMENTS

The authors would also like to acknowledge the technical support and facilities provided by the Department of Civil Engineering, University of Malaysia Sarawak.

REFERENCES

Abdul-Hussain, N., and Fall, M. (2012). Thermo-hydro-mechanical Behaviour of Sodium Silicate-Cemented Paste Tailings in Column Experiments. *Tunnelling Underground Space Tech.* 29, 85–93. doi:10.1016/j.tust.2012.01.004

Adajar, M. Q., and Pabilona, W. K. (2018). Soil-structure Interface Behavior of Cemented-Paste Backfill Material Mixed with Mining Waste. *Int. J. GEOMATE* 14 (44), 102–108. doi:10.21660/2018.44.7109

Alshibli, K. A., Sture, S., and Costes, N. C. (2000). Constitutive and Stability Behavior of Soils in Microgravity Environment. *AIP Conf. Proc.* 504, 246–252. doi:10.1063/1.1302489

ASTM (2011). *D3080 Standard Test Method for Direct Shear Test of Soils under Consolidated Drained Conditions*. West Conshohocken. PA: ASTM International.

Bai, E., Guo, W., Tan, Y., and Yang, D. (2018). The Analysis and Application of Granular Backfill Material to Reduce Surface Subsidence in China's Northwest Coal Mining Area. *PLoS ONE* 13 (7), e0201112. doi:10.1371/journal.pone.0201112

Belem, T., and Benzaazoua, M. (2008). Design and Application of Underground Mine Paste Backfill Technology. *Geotech Geol. Eng.* 26 (2), 147–174. doi:10.1007/s10706-007-9154-3

Burghignoli, A., Desideri, A., and Miliziano, S. (2000). A Laboratory Study on the Thermomechanical Behaviour of Clayey Soils. *Can. Geotech. J.* 37 (4), 764–780. doi:10.1139/t00-010

Cekerevac, C. (2003). Thermal Effects on the Mechanical Behaviour of Saturated Clays: an Experimental and Constitutive Study. Ph.D Dissertation. Lausanne(Switzerland): EPFL.

Cooke, R. (2008). "Pipeline Design for Paste and Thickened Tailings Systems," in Proceedings of the 12th International Conference of Tailings and Mine Waste '08, Vail, Colorado, USA, October 19-22, 2008, 95–100. doi:10.1201/9780203882306.ch9

Doherty, J. P., Hasan, A., Suazo, G. H., and Fourie, A. (2015). Investigation of Some Controllable Factors that Impact the Stress State in Cemented Paste Backfill. *Can. Geotech. J.* 52 (12), 1901–1912. doi:10.1139/cgj-2014-0321

Fahey, M., Helinski, M., and Fourie, A. (2009). Some Aspects of the Mechanics of Arching in Backfilled Stopes. *Can. Geotech. J.* 46, 1322–1336. doi:10.1139/t09-063

Fall, M., Célestin, J., Pokharel, M., and Touré, M. (2010). A Contribution to Understanding the Effects of Curing Temperature on the Mechanical Properties of Mine Cemented Tailings Backfill. *Eng. Geology.* 114 (3-4), 397–413. doi:10.1016/j.enggeo.2010.05.016

Ghirian, A., and Fall, M. (2015). Coupled Behavior of Cemented Paste Backfill at Early Ages. *Geotech Geol. Eng.* 33 (5), 1141–1166. doi:10.1007/s10706-015-9892-6

Ghirian, A., and Fall, M. (2016). Strength Evolution and Deformation Behaviour of Cemented Paste Backfill at Early Ages: Effect of Curing Stress, Filling Strategy and Drainage. *Int. J. Mining Sci. Tech.* 26 (5), 809–817. doi:10.1016/j.ijmst.2016.05.039

Grabinsky, M. W., and Thompson, B. D. (2009). Thermally Induced Stresses in Cemented Paste Backfill. *Geotechnical News* 27 (3), 36–40.

Hasan, A., Fourie, A., Doherty, J. P., and Suazo, G. H. (2014). "*In Situ* measurements of Cemented Paste Backfilling in an Operating Stope at Lanfranchi Mine," in Proceedings of the 11th International Symposium on Mining with Backfill, Perth, Western Australia, Australia, May 20-22, 2014 (Australian Centre for Geomechanics), 327–336. doi:10.36487/acg_rep/1404_26_hasan

Hasan, A., Ting, W. K., Sahdi, F., Taib, S. N. L., Sutan, N. M., Aziz, B. A., et al. (2018). Temperature Change and the Total Stress Anomaly in Paste Backfill. *Int. J. GEOMATE* 14 (44), 90–95. doi:10.21660/2018.44.7121

Helinski, M., Fahey, M., and Fourie, A. (2007). Numerical Modeling of Cemented Mine Backfill Deposition. *J. Geotech. Geoenviron. Eng.* 133 (10), 1308–1319. doi:10.1061/(asce)1090-0241(2007)133:10(1308)

Hoek, E., and Diederichs, M. S. (2006). Empirical Estimation of Rock Mass Modulus. *Int. J. Rock Mech. Mining Sci.* 43, 203–215. doi:10.1016/j.ijrmms.2005.06.005

Hueckel, T., and Baldi, G. (1990). Thermoplasticity of Saturated Clays: Experimental Constitutive Study. *J. Geotechnical Eng.* 116 (12), 1778–1796. doi:10.1061/(asce)0733-9410(1990)116:12(1778)

Janssen, H. (1895). Versuche Uber Getreidedruck in Silozellen. *Z. des Vereines deutscher Ingenieure* 39, 1045–1049.

Jaouhar, E. M., Li, L., and Aubertin, M. (2018). An Analytical Solution for Estimating the Stresses in Vertical Backfilled Stopes Based on a Circular Arc Distribution. *Geomech. Eng.* 15 (3), 889–898. doi:10.12989/gae.2018.15.3.889

Karademir, T. (2011). Elevated Temperature Effects on Interface Shear Behavior. Ph.D Dissertation. Georgia(US): Georgia Institute of Technology.

Koupouli, N. J. F., Belem, T., Rivard, P., and Effenguet, H. (2016). Direct Shear Tests on Cemented Paste Backfill-Rock wall and Cemented Paste Backfill-Backfill Interfaces. *J. Rock Mech. Geotechnical Eng.* 8 (4), 472–479. doi:10.1016/j.jrmge.2016.02.001

Landriault, D. A. (1995). "Paste Backfill Mix Design for Canadian Underground Hard Rock Mining," in Proc. Of the 97th Annual General Meeting of the CIM Rock Mechanics and Strata Control Session, Halifax: Nova Scotia, May 14–18.

Lee, I.-M., Kim, D.-H., Kim, K.-Y., and Lee, S.-W. (2016). Earth Pressure on a Vertical Shaft Considering the Arching Effect in C-Φsoil. *Geomech. Eng.* 11 (6), 879–896. doi:10.12989/gae.2016.11.6.879

Li, L., and Yang, P. (2015). A Numerical Evaluation of Continuous Backfilling in Cemented Paste Backfilled Stope through an Application of Wick Drains. *Int. J. Mining Sci. Tech.* 25 (6), 897–904. doi:10.1016/j.ijmst.2015.09.004

Marston, A. (1930). *The Theory of External Loads on Closed Conduits in the Light of Latest Experiments. Bulletin No. 96.* Ames, Iowa: Iowa Engineering Experiment Station, 1–36.

Mitchell, R. J., Olsen, R. S., and Smith, J. D. (1982). Model Studies on Cemented Tailings Used in Mine Backfill. *Can. Geotech. J.* 19 (1), 14–28. doi:10.1139/t82-002

Moradi, G., and Abbasnejad, A. (2015). Experimental and Numerical Investigation of Arching Effect in Sand Using Modified Mohr Coulomb. *Geomech. Eng.* 8 (6), 829–844. doi:10.12989/gae.2015.8.6.829

Nasir, O., and Fall, M. (2008). Shear Behaviour of Cemented Pastefill-Rock Interfaces. *Eng. Geology.* 101 (3-4), 146–153. doi:10.1016/j.enggeo.2008.04.010

Orejarena, L., and Fall, M. (2011). Artificial Neural Network Based Modeling of the Coupled Effect of Sulphate and Temperature on the Strength of Cemented Paste Backfill. *Can. J. Civ. Eng.* 38 (1), 100–109. doi:10.1139/l10-109

Pashias, N., Boger, D. V., Summers, J., and Glenister, D. J. (1996). A Fifty Cent Rheometer for Yield Stress Measurement. *J. Rheology* 40 (6), 1179–1189. doi:10.1122/1.550780

Pierce, M. E. (2001). "Stability Analysis of Paste Backfill Exposures at Brunswick Mine," in Proceedings of 2nd international FLAC Symposium, Lyon, France, October 29-31, 2001, 147–156.

Potvin, Y., Thomas, E., and Fourie, A. (2005). *Handbook on Mine Fill*. Crawley: Australian Centre for Geomechanics.

Qi, C., and Fourie, A. (2019). Numerical Investigation of the Stress Distribution in Backfilled Stopes Considering Creep Behaviour of Rock Mass. *Rock Mech. Rock Eng.* 52, 3353–3371. doi:10.1007/s00603-019-01781-0

Ramlochan, T., Grabinsky, M., and Hooton, R. (2004). "Microstructural and Chemical Investigations of Cemented Paste Backfills," in Proceedings of the Eleventh Tailings and Mine Waste Conference, Vail, Colorado, USA, October 10-13, 2004, 293–304. doi:10.1201/9780203021637.ch35

Rankine, R. M., and Sivakugan, N. (2007). Geotechnical Properties of Cemented Paste Backfill from Cannington Mine, Australia. *Geotech Geol. Eng.* 25 (4), 383–393. doi:10.1007/s10706-006-9104-5

Sheshpari, M. (2015). A Review of Underground Mine Backfilling Methods with Emphasis on Cemented Paste Backfill. *Electron. J. Geotechnical Eng.* 20 (13), 5183–5208.

Terzaghi, K. (1943). *Arching in Ideal Soil: Theoretical Soil Mechanics*. New York: J. Wiley and Sons, Inc.

Thompson, B. D., Bawden, W. F., and Grabinsky, M. W. (2012). *In Situ* measurements of Cemented Paste Backfill at the Cayeli Mine. *Can. Geotech. J.* 49 (7), 755–772. doi:10.1139/t2012-040

Ting, W. K., Hasan, A., Sahdi, F., Linda Taib, S. N., Sutan, N. M., Aziz, B. A., et al. (2020). A Narrow Wall System to Capture Temperature Stress-Strain Behavior in Paste Backfill. *Geotech. Test. J.* 43 (2), 20170383. doi:10.1520/GTJ20170383

Wu, A., Wang, Y., Zhou, B., and Shen, J. (2016). Effect of Initial Backfill Temperature on the Deformation Behavior of Early Age Cemented Paste Backfill that Contains Sodium Silicate. *Adv. Mater. Sci. Eng.* 2016, 1–10. doi:10.1155/2016/8481090

Xuan, D., Xu, J., and Zhu, W. (2013). Backfill Mining Practice in China Coal Mines. *J. Mines Met. Fuels* 61 (7–8), 225–234.

Yilmaz, E., Kesimal, A., Ercikdi, B., and Alp, I. (2003). "Determination of the Optimum Cement Content for Paste Backfill Samples," in 18th International Mining Congress and Exhibition of IMCET 2003, Antalya, Turkey, June 10-13, 2003, 119–125.

Conflict of Interest: The authors declare that the research was conducted in the absence of any commercial or financial relationships that could be construed as a potential conflict of interest.

Publisher's Note: All claims expressed in this article are solely those of the authors and do not necessarily represent those of their affiliated organizations or those of the publisher, the editors, and the reviewers. Any product that may be evaluated in this article, or claim that may be made by its manufacturer, is not guaranteed or endorsed by the publisher.

frontiers in Materials

ORIGINAL RESEARCH
published: 14 March 2022
doi: 10.3389/fmats.2022.858517

Experimental Study on Sulfate Wetting–Drying Cycle of Metal Tailings Powder Concrete

Ruidong Wu[1,2], *Min Zou*[1,2], *Juanhong Liu*[1,2]*, *Guangtian Zhang*[1,2,3] *and Yueyue Zhang*[1,2]

[1]College of Civil and Resource Engineering, University of Science and Technology Beijing, Beijing, China, [2]Beijing Key Laboratory of Urban Underground Space Engineering, University of Science and Technology Beijing, Beijing, China, [3]Hebei Academy of Building Research, Shijiazhuang, China

In order to absorb a large amount of metal tailings powder and alleviate the shortage of mineral admixture in concrete, metal tailings powder can form a compound admixture with slag powder to prepare concrete. The sulfate wetting–drying cycle test of concrete with different contents of metal tailings powder was carried out to study the action law of metal tailings powder on the sulfate corrosion resistance of concrete. Scanning electron microscope, XRD, and nuclear magnetic resonance microscopic tests were used to reveal the deterioration mechanism of metal tailings powder concrete eroded by sulfate. The results show that proper addition of metal tailings powder can increase the sulfate corrosion resistance of C50 concrete. When the ratio of metal tailings powder to slag powder is 3:7 and 5:5, the sulfate corrosion resistance grade can reach KS180. There is a strong linear relationship between the relative ultrasonic velocity factor and relative compressive strength factor. The sulfate failure mechanism of metal tailings powder concrete is mainly the internal formation of corrosion products ettringite and gypsum. The introduction of metal tailings powder can reduce the alkalinity of concrete and improve the pore structure, thus improving the sulfate corrosion resistance of concrete.

Keywords: metal tailings, sulfate, wetting–drying cycle, micro powder, durability

OPEN ACCESS

Edited by:
Erol Yilmaz,
Recep Tayyip Erdoğan University, Turkey

Reviewed by:
Baoxu Yan,
Xi'an University of Science and Technology, China
Chen Qiusong,
Central South University, China

***Correspondence:**
Juanhong Liu
liujuanhong66@126.com

Specialty section:
This article was submitted to Structural Materials, a section of the journal Frontiers in Materials

Received: *20 January 2022*
Accepted: *31 January 2022*
Published: *14 March 2022*

Citation:
Wu R, Zou M, Liu J, Zhang G and Zhang Y (2022) Experimental Study on Sulfate Wetting–Drying Cycle of Metal Tailings Powder Concrete. Front. Mater. 9:858517. doi: 10.3389/fmats.2022.858517

INTRODUCTION

With the continuous development of economy and society, the mining volume of metal ore increases year by year. A large amount of tailings will be produced in the process of metal ore beneficiation. Most of the tailings will be stacked in the tailings pond after centralized discharge (Lvu et al., 2018; Huang et al., 2021; Zhao et al., 2021). Different from nonmetallic ores, there are many tailings produced by mineral processing of nonferrous ores, and the mining and stripping quality ratio of nonferrous ores is mostly between 1:2 and 1:14 (Yang and Guo, 2018).

According to statistics, there are about 70 billion tons of tailings stockpile in China (Yao et al., 2021), and the utilization rate of tailings is relatively low, resulting in the increase of mine solid waste stockpile year by year. A large number of tailings are accumulated in the tailings pond, which not only occupies a large amount of land and pollutes the surface environment but is also one of the major hazard sources, which seriously threatens the surrounding environment and safety. At present, tailings are mainly used for mine backfilling (Liu et al., 2017; Qi and Fourie, 2019; Wu et al., 2014), soil reclamation, preparation of building materials (Ullah et al., 2021), and preparation of new functional materials such as molecular sieve (Zhang et al., 2019; Yang et al., 2021). With the continuous development of beneficiation technology, tailings have become finer and finer. The stock

TABLE 1 | Property indexes of reference cement.

Fineness, mm	Water requirement of normal consistency, %	Setting time, min		Compressive strength, MPa		Flexural strength, MPa		Stability
		Initial	Final	3d	28d	3d	28d	
0.5	27.2	155	215	28.3	53.2	5.5	10.3	Qualified

of fine-grained tailings below 75 μm accumulates rapidly (Wu et al., 2020). Fine-grained tailings will cause a series of problems such as filling rheology and high cost (Zhang et al., 2021; Chen et al., 2022). The reuse of fine-grained tailings is difficult, and the utilization rate is very low (Wu et al., 2018), resulting in the comprehensive utilization rate of tailings being far lower than the new output of tailings; in particular, the industrialized utilization of fine-grained tailings needs to be solved urgently.

Continuous investment in infrastructure increases concrete consumption. High-quality mineral admixtures such as fly ash and slag powder are indispensable components of modern high-performance concrete. There is a shortage of high-quality mineral admixtures in some areas. Thermal power generation is gradually replaced, and the content of fly ash is bound to decline year by year. Therefore, it is imperative to find new admixtures for preparing concrete. The fine particles of metal tailings mainly take SiO_2 and Al_2O_3 as the main chemical components. The fine powder of metal tailings can be used as concrete admixture, which can not only alleviate the shortage of high-quality concrete admixture but also absorb a large number of fine-grained tailings. Han et al. (2017, 2019) believed that the hydration reaction of metal tailings powder in cement-based materials is slow. Wu et al. (2021) found that a small part of iron tailings powder can undergo hydration reaction after a long period. Hou et al. (2019) and Liu et al. (2019) found that the strength of metal tailings powder concrete increases with the increase of fineness. Lu et al. (2021) considered that the curing method has a great impact on the iron tailings micro powder concrete. Song et al. (2017), Song et al. (2019), and Song and Chen (2020) found that tailings powder can replace fly ash to prepare concrete. Research on the composite admixture of metal tailings mainly focuses on the mechanical properties and hydration process (Li et al., 2021; Zhang et al., 2021), and there are few studies on the impact of metal tailings powder on the durability of concrete, especially the research on the sulfate wetting–drying cycle of metal tailings powder concrete. The durability of concrete determines the service time of concrete. In order to realize the resource utilization of metal tailings powder in concrete, the influence law and action mechanism of tailings on the durability of concrete have to be studied. In this paper, the effect of metal tailings powder on the sulfate wetting–drying cyclic corrosion resistance of concrete is studied. The deterioration mechanism of metal tailings powder concrete in sulfate is revealed through micro analysis such as scanning electron microscope (SEM) and X-ray diffraction (XRD), which lays a theoretical foundation for the large-scale application of metal tailings powder concrete in a sulfate environment.

EXPERIMENTAL PROCEDURES

Raw Material

In order to avoid the influence of admixtures in cement on the test, P.I.42.5 pure Portland cement is adopted, and its properties are shown in **Table 1**. The mineral composition of cement is C_3S (59.6%), C_2S (19.5%), C_3A (7.2%), and C_4AF (8.3%).

The micro powder of metal tailings comes from a copper zinc mine in Fujian, China. It is fine-grained tailings screened by drying (45 μm sieve residue is 6.45%). The main component of tailings is SiO_2, as well as some chemical components such as iron, aluminum, copper, and zinc. An S95-grade slag is selected as slag powder, and its main components are SiO_2, CaO, Al_2O_3, etc. See **Tables 2**, **3** for specific technical indexes and the chemical composition of metal tailings powder and slag powder.

The coarse and fine aggregates used in the experiment are natural aggregates, and the indexes meet the national standards, as shown in **Table 4**.

Polycarboxylic acid superplasticizer is used as the admixture, with a solid content of about 20%.

Tap water is used for concrete mixing, and the chemical composition in tap water contains very little chloride ion, which will not affect the corrosion test.

Concrete Mix Proportion

In order to explore the action law of metal tailings powder on the sulfate resistance of concrete, the compound admixture of metal tailings powder and slag powder is adopted. The proportion of metal tailings powder in the compound admixture is 0%, 30%, 50%, 70%, and 100%. Two kinds of common concrete, C30 and C50, are prepared. Based on the consideration of low carbon and environmental protection, a low cement clinker and low water binder ratio system are adopted. The cement in C30 concrete is only 30% of the cementitious material, and the basic water binder ratio is 0.40. The cement in C50 concrete is 40% of the cementitious material, and the basic water binder ratio is 0.29. Because it is a low cement clinker system, through trial mixing, the basic water binder ratio is slightly lower than that of ordinary concrete. The water binder ratio of concrete decreases with the increase of the content of nonactive admixture, metal tailings powder, so as to ensure that the strength can meet the design grade. The specific proportion is shown in **Table 5**.

Experimental Procedures

Place the test piece (100 mm × 100 mm × 100 mm) standard curing for 26 days, take it out of the standard curing room, put it into the drying oven, and dry it at (80 ± 5)°C for 48 h. Take it out after drying, cool it to room temperature, and put the test block into a sulfate wetting–drying cycle test chamber. Prepare 5%

TABLE 2 | Technical indexes of metal tailings powder and slag powder.

	Density, g·cm^{-3}	Specific surface area, m^2·kg^{-1}	45 μm sieve residue, %	Water requirement ratio, %
Metal tailings	2.82	450	6.45	90
Slag	2.80	485	6.20	96.2

TABLE 3 | Main chemical components of metal tailings powder (%).

Chemical composition	SiO_2	CaO	Fe_2O_3	Al_2O_3	MgO	CuO	ZnO
Metal tailings	67.55	4.23	9.86	8.69	1.24	0.31	0.21
Slag	52.12	38.11	0.43	8.18	1.03	-	-

TABLE 4 | Technical indexes of coarse and aggregate.

	Apparent density, kg·m^{-3}	Bulk density, kg·m^{-3}	Porosity, %	Mud content, %	Crushing index, %	Needle and flake content, %	Fineness modulus
Coarse	2,743	1,569	42.8	1.0	5.2	5.5	-
Fine	2,595	1,534	39.0	1.6	-	-	2.7

TABLE 5 | Mix proportion of metal tailings powder concrete (kg/m^{-3}).

	Cement	Metal tailings powder	Slag powder	Sand	Stone	Water	W/B	PC
C30-0	113	0	264	840	1,018	151	0.40	3.4
C30-30	113	79	185			147	0.39	
C30-50	113	132	132			143	0.38	
C30-70	113	185	79			140	0.37	
C30-100	113	264	0			136	0.36	
C50-0	191	0	287	725	1,071	139	0.29	6.7
C50-30	191	86	201			134	0.28	
C50-50	191	144	144			129	0.27	
C50-70	191	201	86			124	0.26	
C50-100	191	287	0			119	0.25	

Na_2SO_4 solution as corrosion solution, and replace the sulfate solution every other month. The wetting–drying cycle is 24 h, including soaking for 16 h, drying for 6 h at a drying temperature of 80°C, and cooling for 2 h. The sulfate wetting–drying cycle experiment equipment is a NELD-LSC automatic sulfate wetting–drying cycle test machine. The concrete quality, ultrasonic velocity, and compressive strength of concrete were tested every 30 wetting–drying cycles. When the compressive strength of the concrete decreased to 75% before the test, it was regarded as sulfate erosion failure, and the test was stopped.

RESULTS AND DISCUSSION

Test Index Results of Concrete Sulfate Wetting–Drying Cycle

The sulfate wetting–drying cycle experiment of concrete with different mix proportions was carried out to compare the concrete quality, ultrasonic velocity, and compressive strength after different wetting–drying cycles, so as to study the influence of different metal tailings powder content on the sulfate corrosion resistance.

The relative compressive strength factor P is defined and calculated as follows:

$$P = \frac{P_i - P_0}{P_0} \times 100\% \quad (1)$$

P is the relative intensity factor; P_0 is the compressive strength of the test piece before sulfate wetting–drying cycle, MPa. P_i is the compressive strength of the test piece after the ith cycle sulfate wetting–drying, MPa. The compressive strength of each group is tested after different sulfate wetting–drying cycles, as shown in **Figure 1**. The relative compressive strength factor is calculated, and the results are shown in **Table 6**.

In practice, testing the compressive strength needs to consume a large number of test blocks and cannot reflect

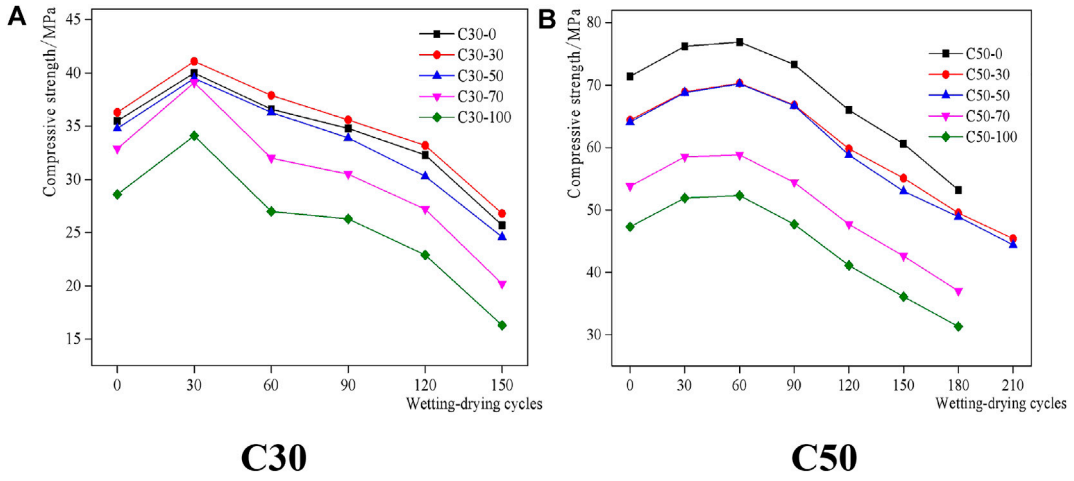

FIGURE 1 | Compressive strength of concrete after different wetting–drying cycles.

TABLE 6 | Relative compressive strength factor of concrete after sulfate wetting–drying cycles.

	30c	60c	90c	120c	150c	180c	210c
C30-0	12.6	3.1	−2.1	−8.9	**−27.7**		
C30-30	13.1	4.5	−1.8	−8.5	**−26.1**		
C30-50	13.5	4.2	−2.4	−12.8	**−29.3**		
C30-70	18.8	−2.7	−7.3	−17.2	**−38.5**		
C30-100	19.2	−5.6	−8.2	−19.9	**−43.1**		
C50-0	6.7	7.8	2.6	−7.6	−15.1	**−25.5**	
C50-30	7.1	9.1	3.8	−7.1	-14.5	−23.1	**−29.5**
C50-50	7.3	9.5	4.1	−8.2	-17.3	−23.6	**−30.8**
C50-70	8.8	9.3	1.2	−11.3	−20.8	**−31.2**	
C50-100	9.7	10.5	0.9	−13.2	−23.6	**−33.9**	

The bold value means that the sulfate failure condition is reached.

TABLE 7 | Relative mass factor of concrete after sulfate wetting–drying cycles.

	30c	60c	90c	120c	150c	180c	210c
C30-0	5.12	11.23	3.67	−2.22	**−6.20**		
C30-30	6.34	13.72	4.15	−2.83	**−5.72**		
C30-50	9.43	16.31	7.88	−1.43	**−3.13**		
C30-70	10.76	17.87	3.31	−4.49	**−10.28**		
C30-100	14.31	19.12	2.25	−6.66	**−13.12**		
C50-0	2.55	6.74	3.33	1.18	−0.67	**−2.03**	
C50-30	2.72	6.90	3.26	1.21	−0.55	−2.61	**−4.05**
C50-50	3.75	7.58	4.39	2.25	1.11	0.07	**−1.17**
C50-70	4.84	9.05	3.55	0.42	−1.84	**−5.67**	
C50-100	5.88	10.71	3.81	0.15	−3.71	**−8.92**	

The bold value means that the sulfate failure condition is reached.

the sulfate corrosion process of concrete in structural service. Therefore, some nondestructive testing indicators such as quality and ultrasonic velocity should be developed. The relative quality factor M is defined and calculated as follows:

$$M = \frac{m_i - m_0}{m_0} \times 100\% \quad (2)$$

TABLE 8 | Relative ultrasonic velocity factor of concrete after sulfate wetting–drying cycles.

	30c	60c	90c	120c	150c	180c	210c
C30-0	5.21	1.36	−0.88	−3.72	**−11.83**		
C30-30	5.52	1.90	−0.75	−3.58	**−10.88**		
C30-50	5.81	2.25	−1.02	−5.51	**−12.34**		
C30-70	8.13	−1.10	−3.08	−7.25	**−16.12**		
C30-100	8.45	−3.65	−3.56	−8.43	**−18.13**		
C50-0	2.76	3.25	1.21	−3.29	−6.29	**−10.76**	
C50-30	2.91	3.84	1.59	−3.06	−5.99	−9.63	**−12.29**
C50-50	3.08	4.08	1.75	−3.51	−7.33	−9.83	**−13.01**
C50-70	3.71	3.93	0.55	−4.78	−8.81	**−13.12**	
C50-100	4.15	4.46	0.38	−5.61	−9.95	**−14.28**	

The bold value means that the sulfate failure condition is reached.

M is the relative quality factor, M_0 is the mass of the test piece before the sulfate wetting–drying cycle, g. M_i is the mass of the test piece after the ith sulfate wetting–drying cycle, g. Test the mass of each group concrete after different sulfate wetting-drying cycles, and calculate the relative quality factor. The results are shown in **Table 7**.

The relative ultrasonic velocity factor V is defined, and the calculation formula is as follows:

$$V = \frac{V_i - V_0}{V_0} \times 100\% \quad (3)$$

V is the relative wave velocity factor, V_0 is the ultrasonic velocity of the test piece before the sulfate wetting–drying cycle, m/s; V_i is the ultrasonic velocity of the test piece after the ith sulfate wetting–drying cycle, m/s. Test the ultrasonic velocity of each group concrete after different sulfate wetting–drying cycles, and calculate the relative ultrasonic velocity factor. The results are shown in **Table 8**.

The relative quality factor, relative ultrasonic velocity factor, and relative compressive strength factor of concrete specimens first increase and then decrease with the increase of sulfate dry

FIGURE 2 | Picture of concrete specimen damaged by sulfate wetting–drying cycles.

and wet corrosion cycles. At the initial stage of corrosion, sodium sulfate solution continuously enters the concrete block through the pores. These sodium sulfate react with calcium hydroxide in the concrete to generate ettringite, gypsum, and other erosion products. In addition, the sodium sulfate solution continuously crystallizes inside, and these substances fill the small pores in the concrete. Therefore, the quality of the block has increased compared with that before corrosion, the interior is more dense, the ultrasonic velocity increases, and the compressive strength continues to improve. With the continuous advancement of the sulfate corrosion process, more and more ettringite, gypsum, and sodium sulfate crystals continue to accumulate in the concrete. Compared with the original hydration products, the expansion rate of these products increases, resulting in the continuous increase of internal volume, and micro cracks slowly occur in the concrete block. These micro cracks continue to expand and extend, resulting in the peeling off of the skin around the block, as shown in **Figure 2**. The relative quality factor, relative ultrasonic velocity factor, and relative compressive strength factor of concrete are reduced. When the expansion stress produced by erosion products is greater than the internal tensile strength of concrete, the micro cracks develop to the degree of penetration, and the concrete is corroded.

According to the standard, when the compressive strength decreases to 75% of the initial strength before corrosion, it is regarded as sulfate corrosion failure. The sulfate corrosion resistance grade of C30-0 to C30-100 groups is KS120. The sulfate resistance grade of C50-0, C50-70, and C50-100 groups is KS150, while the sulfate resistance grade of concrete with 30% and 50% of metal tailings powder accounting for mineral admixtures is KS180, which shows that the appropriate amount of metal tailings powder can improve the sulfate resistance of concrete, which is obvious in the C50 concrete. Taking C30-30 and C50-30 groups, in which the content of metal tailings powder accounts for 30% of mineral admixtures, as an example, the mass, ultrasonic velocity, and compressive strength are the smallest, and the sulfate corrosion resistance is relatively strong.

Relationship Between Three Corrosion Deterioration Factors

As the indicator of sulfate corrosion in the national standard is compressive strength, but in the actual test process, the compressive strength test requires a large number of concrete blocks, it is difficult to test the accurate compressive strength in the actual application of a typical environment. Nondestructive corrosion factors such as ultrasonic velocity are an important supplement to the study of metal tailings powder concrete sulfate resistance. The three corrosion indexes of relative quality factor, relative ultrasonic velocity factor, and relative compressive strength factor have been defined earlier, and the relative relationship of the three corrosion factors has been established. See **Figure 3** to study the internal relationship and mutual characterization law of the three corrosion factors.

It can be seen from the above figure that the correspondence between the relative quality factor, the relative ultrasonic velocity factor, and the relative compressive strength factor is not obvious, so the change of the quality cannot reflect the change of the compressive strength after a certain number of wetting–drying cycles. The change of quality slightly lags behind the change of ultrasonic wave velocity and compressive strength. This is because the expansion, falling off, and filling are carried out together, and fine falling-off particles are locked in the concrete block, resulting in a small increase in the quality of concrete specimen when the ultrasonic velocity and compressive strength are reduced. However, there is a strong correlation between relative ultrasonic velocity factor and relative compressive strength factor, showing a linear relationship, and the correlation reliability is as high as 0.999. Ultrasonic nondestructive testing can be used to characterize the change of compressive strength, and the corresponding relationship is as follows.

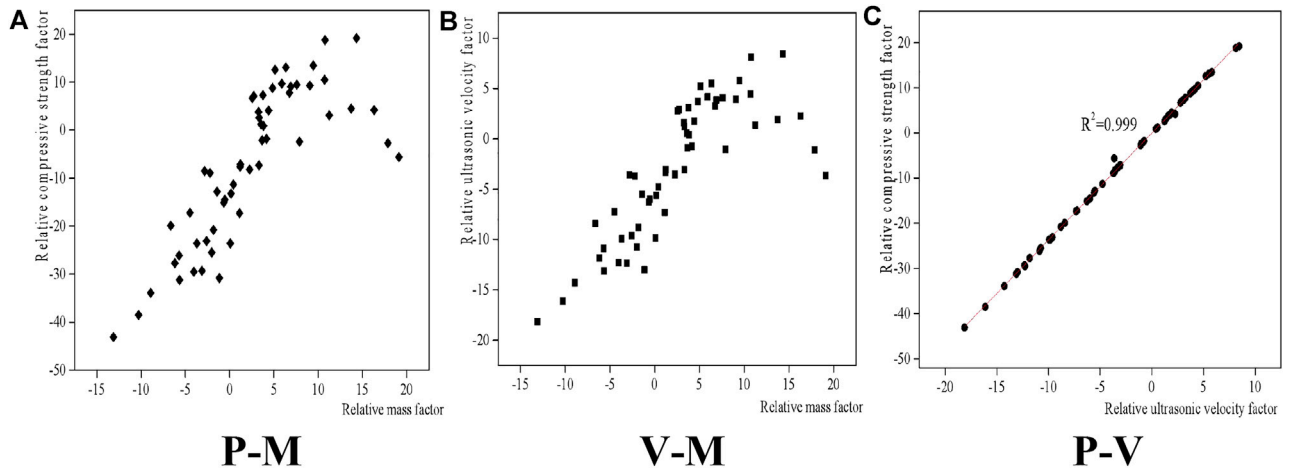

FIGURE 3 | Corresponding relationship of three corrosion factors.

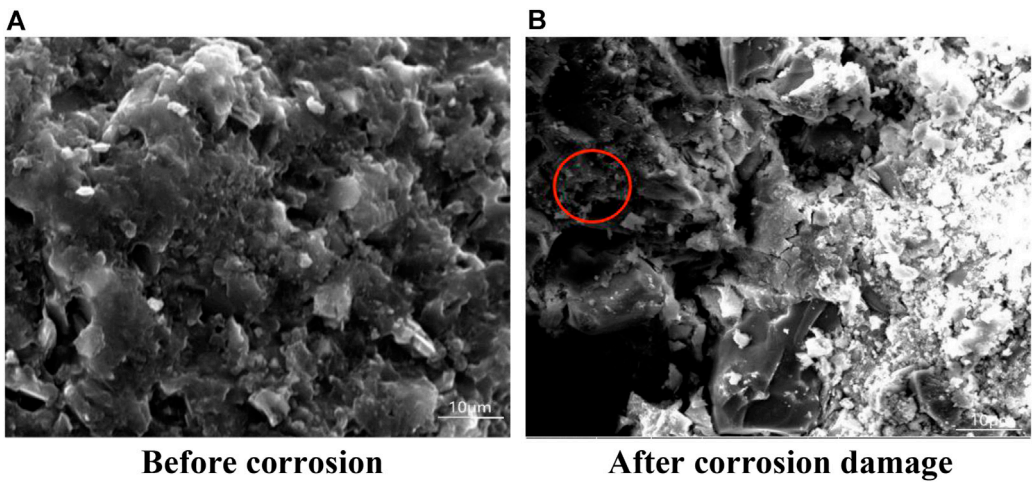

FIGURE 4 | SEM images of C50-0 concrete before and after sulfate corrosion.

$$P = 2.365V - 0.0274$$

With the above formula, the concrete compressive strength can be converted by ultrasonic velocity, so as to understand the corrosion degree of concrete subjected to sulfate wetting–drying cycles.

Sulfate Corrosion Deterioration Mechanism of Metal Tailings Powder Concrete

In order to explore the corrosion deterioration mechanism of metal tailings powder concrete after sulfate wetting–drying cycle, the C50-0 group with single slag powder and C50-50 group with strong sulfate corrosion resistance are selected to study the micro morphology and products of concrete before corrosion and after corrosion damage by SEM and XRD. **Figures 4** and **5** shows the SEM image of concrete before and after corrosion. The image is of ×5,000 magnification.

Compared with the micro morphology of the concrete before and after corrosion, the internal structure of the concrete before corrosion is very dense. After sulfate wetting–drying cycle damage, there are many flake gypsum and some needle rod ettringite in the concrete. The volume of these corrosion products expands, the expansion stress is greater than the tensile stress in the concrete, and cracks appear in the concrete, resulting in the damage of the micro morphology. The macroscopic performance is that the compressive strength of concrete decreases to 75% of the initial strength.

Figure 6 is the XRD spectrum of concrete before and after the sulfate wetting–drying cycle corrosion damage. From the spectrum, excluding the influence of silica, there is an obvious $Ca(OH)_2$ diffraction peak before corrosion. But after corrosion

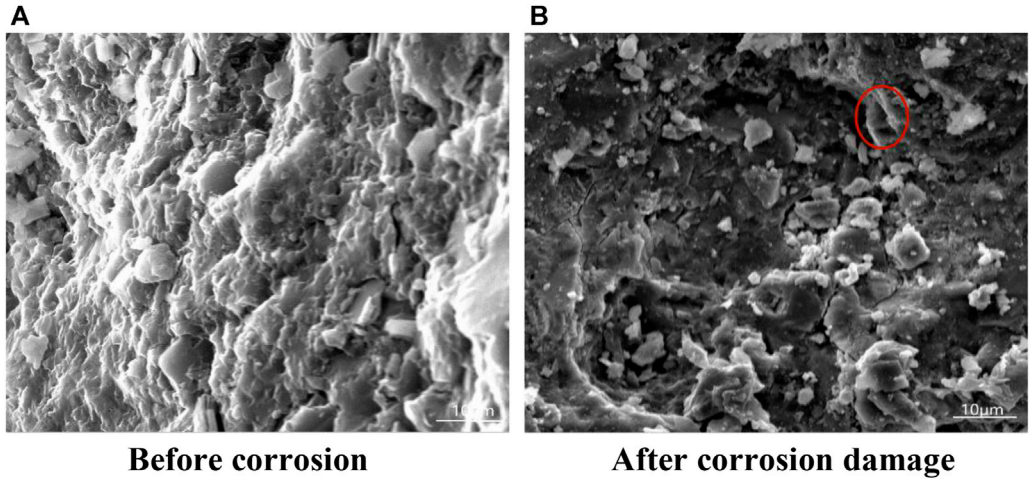

FIGURE 5 | SEM images of C50-50 concrete before and after sulfate corrosion.

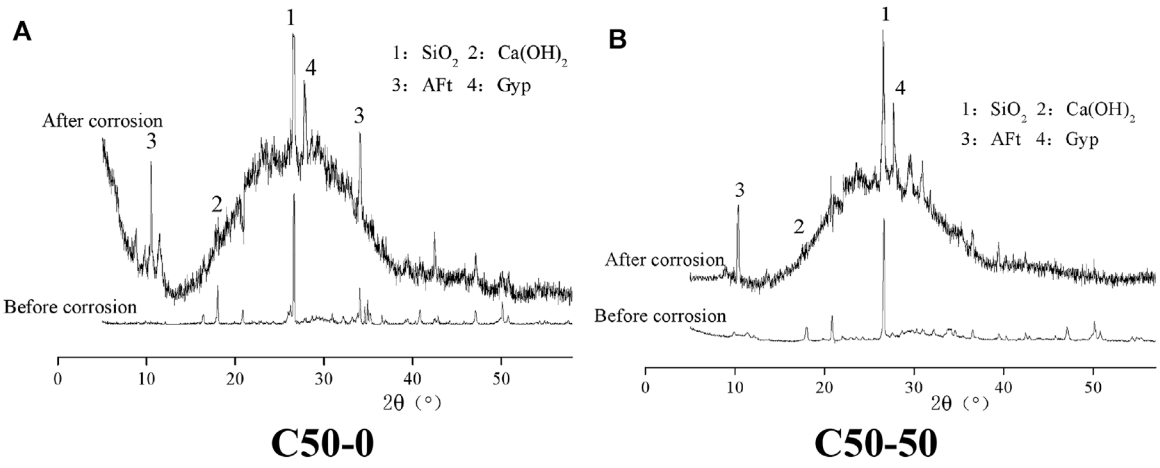

FIGURE 6 | XRD spectrum of concrete before and after sulfate corrosion failure.

damage, the $Ca(OH)_2$ diffraction peak no longer exists. There are obvious ettringite and gypsum diffraction peaks after corrosion, which indicates that the sulfate corrosion of concrete is mainly due to the sodium sulfate solution entering the concrete and reacting with the internal $Ca(OH)_2$. The production reaction formula of ettringite is as follows:

$$Na_2SO_4 \cdot 10H_2O + Ca(OH)_2 \rightarrow CaSO_4 \cdot 2H_2O + 2NaOH + 8H_2O$$

$$3(CaSO_4 \cdot 2H_2O) + 4CaO \cdot Al_2O_3 \cdot 12H_2O + 14H_2O \rightarrow 3CaO \cdot Al_2O_3 \cdot 3CaSO_4 \cdot 32H_2O + Ca(OH)_2$$

Gypsum formation reaction is as follows:

$$Ca(OH)_2 + Na_2SO_4 \rightarrow Ca^{2+} + SO_4^{2-} + Na^+ + OH^-$$

$$Ca^{2+} + SO_4^{2-} + H_2O \rightarrow CaSO_4 \cdot 2H_2O$$

Proper addition of metal tailings powder can increase the sulfate corrosion resistance of concrete. Combined with the analysis of SEM and XRD test results, the $Ca(OH)_2$ diffraction peak intensity of concrete with metal tailings powder accounting for 50% of mineral admixture before corrosion is significantly lower than that of the C50-0 group with slag powder alone. XRD analysis after corrosion shows that the diffraction peak intensity of ettringite and gypsum in the C50-50 group is significantly lower than that in the C50-0 group, which shows that the addition of metal tailings powder can effectively reduce the generation of sulfate corrosion products, so as to improve the ability of concrete to resist sulfate corrosion.

Nuclear magnetic resonance (NMR) is used to test the porosity of the two kinds of concrete, and the harmless holes (below 0.02 μm), less harmful holes (0.02–0.1 μm), harmful holes (0.1–0.2 μm), and multi harmful holes (above 0.2 μm) are

TABLE 9 | Porosity of concrete (%).

	Total porosity	Below 0.02 μm	0.02-0.1 μm	0.1-0.2 μm	Above 0.2 μm
C50-0	7.12	6.64	0.21	0.11	0.16
C50-50	7.59	6.83	0.58	0.09	0.09

calculated, as shown in **Table 9**. It can be found that the addition of metal tailings powder will increase the number of less harmful holes and harmless holes in concrete. The introduction of these holes can effectively reduce the stress formed by the expansion of sulfate corrosion products and improve the ability of concrete to resist sulfate corrosion.

The results show that an appropriate amount of inactive metal tailings powder can reduce the content of $Ca(OH)_2$ in concrete, so as to reduce the formation of ettringite, gypsum, and other corrosion products. At the same time, the metal tailings powder will optimize the pore structure and reduce the expansion stress of corrosion products.

CONCLUSION

(1) The sulfate resistance of C30 concrete has no strong correlation with the metal tailings powder content, and the sulfate resistance grade is KS120. Proper addition of metal tailings powder can increase the sulfate resistance of C50 concrete, which can reach more than KS150. When the content of metal tailings powder and slag powder is 3:7 and 5:5, the sulfate resistance of C50 concrete is the strongest, up to KS180.

(2) There is a linear relationship between relative ultrasonic velocity factor and relative compressive strength factor. Nondestructive ultrasonic testing can be used to reflect the compressive strength of concrete after a certain number of wetting–drying and cycles.

(3) By analyzing the microscopic test results of concrete such as SEM, XRD, and NMR, the sulfate damage mechanism of metal tailings powder concrete is mainly the internal generation of corrosion products ettringite and gypsum. The introduction of metal tailings powder can reduce the concrete alkalinity and improve the pore structure, so as to improve the sulfate corrosion resistance of concrete.

DATA AVAILABILITY STATEMENT

The original contributions presented in the study are included in the article/Supplementary Material, further inquiries can be directed to the corresponding author.

AUTHOR CONTRIBUTIONS

JL and RW conceived and designed the experiments; RW, MZ, GZ, and YZ performed the experiments; RW and JL wrote the paper. All authors read and approved the manuscript.

FUNDING

This research was financially supported by the National Natural Science Foundation of China (51834001) and Fundamental Research Funds for the Central Universities (FRF-BD-20-01B).

REFERENCES

Chen, Q., Tao, Y., Zhang, Q., and Qi, C. (2022). The Rheological, Mechanical and Heavy Metal Leaching Properties of Cemented Paste Backfill under the Influence of Anionic Polyacrylamide. *Chemosphere* 286, 131630. doi:10.1016/j.chemosphere.2021.131630

Han, F., Li, L., Song, S., and Liu, J. (2017). Early-age Hydration Characteristics of Composite Binder Containing Iron Tailing Powder. *Powder Technol.* 315, 322–331. doi:10.1016/j.powtec.2017.04.022

Han, F., Song, S., Liu, J., and Huang, S. (2019). Properties of Steam-Cured Precast concrete Containing Iron Tailing Powder. *Powder Technol.* 345, 292–299. doi:10.1016/j.powtec.2019.01.007

Hou, Y. F., Liu, J. T., Zhao, S. R., and Peng, X. D. (2019). Effect Mechaniam of Iron Tailing Powder on Cement Mortar Properties. *Joural Basic Sci. Eng.* 27 (05), 1149–1157. doi:10.16058/j.issn.1005-0930.2019.05.018

Huang, T. M., Li, S. C., Li, X. H., Zhang, P. J., Yang, H. B., Ruan, L., et al. (2021). Study on Resource Utilization Technology of Nonferrous Metals Tungsten and lead-zinc Tailings. *Chin. J. Nonferrous Met.* 31 (4), 1057–1073. doi:10.11817/j.ysxb.1004.0609.2021-39637

Li, N., Lv, S. W., Wang, W., Guo, J., Jiang, P., and Liu, Y. (2021). Experimental Investigations on the Mechanical Behavior of Iron Tailings Powder with Compound Admixture of Cement and Nano-clay. *Construction Building Mater.* 254, 119259. doi:10.1016/j.conbuildmat.2020.119259

Liu, J.-h., Zhou, Y.-c., Wu, A.-x., and Wang, H.-j. (2019). Reconstruction of Broken Si-O-Si Bonds in Iron Ore Tailings (IOTs) in concrete. *Int. J. Miner Metall. Mater.* 26 (10), 1329–1336. doi:10.1007/s12613-019-1811-z

Liu, J. H., Wu, R. D., Wu, A. X., and Wang, S. Y. (2017). Bleeding Characteristics and Improving Mechanism of Self-Flowing Tailings Filling Slurry with Low Concentration. *Minerals* 7 (8), 1–7. doi:10.3390/min7080131

Lu, D., Zhong, J., Yan, B., Gong, J., He, Z., Zhang, G., et al. (2021). Effects of Curing Conditions on the MECHANICAL and Microstructural Properties of Ultra-high-performance Concrete (UHPC) Incorporating Iron Tailing Powder. *Materials* 14 (1), 215. doi:10.3390/ma14010215

Lvu, X. D., Liu, Z. A., Zhu, Z. G., and Li, B. X. (2018). Study of the Progress of Tailings Comprehensive Utilization of Raw Materials in Cement and concrete. *Mater. Rep.* 32 (S2), 452–456.

Qi, C., and Fourie, A. (2019). Cemented Paste Backfill for mineral Tailings Management: Review and Future Perspectives. *Minerals Eng.* 144, 106025. doi:10.1016/j.mineng.2019.106025

Ruidong, W., Yu, S., Juanhong, L., Linian, C., Guangtian, Z., and Yueyue, Z. (2021). Effect of Iron Tailings and Slag Powders on Workability and Mechanical Properties of concrete. *Front. Mater.* 8, 723119. doi:10.3389/fmats.2021.723119

Song, S. M., and Chen, H. Y. (2020). Influence of Iron Tailings Powder on Performance of Low Clinker Cementitious Material concrete. *Bull. Chin. Ceram. Soc.* 39 (08), 2557–2566. doi:10.16552/j.cnki.issn1001-1625.2020.08.026

Song, S. M., and Liu, X. D. (2017). Lnfluence of Iron Ore Tailings Powder on the Performance of High Fluidity concrete. *Concrete* 11, 77–80. doi:10.3969/j.issn.1002-3550.2017.11.018

Song, S. M., Zhang, L. Y., and Li, Z. Y. (2019). Effect of Iron Tailings Micropowder on Late-Property of Cement concrete. *Concrete* 01, 128–131. doi:10.3969/j.issn.1002-3550.2019.01.031

Ullah, S., Yang, C., Cao, L., Wang, P., Chai, Q., Li, Y., et al. (2021). Material Design and Performance Improvement of Conductive Asphalt concrete Incorporating Carbon Fiber and Iron Tailings. *Construction Building Mater.* 303, 124446. doi:10.1016/j.conbuildmat.2021.124446

Wu, D., Cai, S.-j., and Huang, G. (2014). Coupled Effect of Cement Hydration and Temperature on Rheological Properties of Fresh Cemented Tailings Backfill Slurry. *Trans. Nonferrous Met. Soc. China* 24 (9), 2954–2963. doi:10.1016/S1003-6326(14)63431-2

Wu, R., and Liu, J. (2018). Experimental Study on the concrete with Compound Admixture of Iron Tailings and Slag Powder under Low Cement Clinker System. *Adv. Mater. Sci. Eng.* 2018, 1–7. doi:10.1155/2018/9816923

Wu, R., Liu, J., Zhang, G., Zhang, Y., and An, S. (2020). Research on Carbonation Characteristics and Frost Resistance of Iron Tailings Powder concrete under Low-Cement Clinker System. *Adv. Mater. Sci. Eng.* 2020, 1–11. doi:10.1155/2020/9192757

Yang, H. M., and Guo, J. L. (2018). *Tailings and Waste Rock Comprehensive Utilization technology[M]*. Beijing: Chemical Industry Press, 187–217. doi:10.1016/b978-0-12-803581-8.10303-0

Yang, J., Xu, L.-h., Wu, H.-q., and Jin, J. (2021). Preparation and Properties of Porous Ceramics from Spodumene Flotation Tailings by Low-Temperature Sintering. *Trans. Nonferrous Met. Soc. China.* 31 (9), 2797–2811. doi:10.1016/S1003-6326(21)65694-7

Yao, H. H., Cai, L. B., Liu, W., Qin, W. Q., Jiao, F., and Yang, C. R. (2021). Current Status and Development of Comprehensive Utilization of Waste Rock in Metal Mines in China. *Chin. J. Nonferrous Met.* 31 (6), 1649–1660. doi:10.11817/j.ysxb.1004.0609.2021-35986

Zhang, N., Tang, B., and Liu, X. (2021). Cementitious Activity of Iron Ore Tailing and its Utilization in Cementitious Materials, Bricks and concrete. *Construction Building Mater.* 288, 123022. doi:10.1016/j.conbuildmat.2021.123022

Zhang, P. J., Huang, T. M., He, H. J., Wei, X. X., Zhao, M. M., Ruan, L., et al. (2019). Hydrothermal Synthesis of ZSM-5 Using Tin Ore Tailing as Raw Material. *Chin. J. Nonferrous Met.* 29 (08), 1790–1800. doi:10.19476/j.ysxb.1004.0609.2019.08.24

Zhang, Q.-l., Li, Y.-t., Chen, Q.-s., Liu, Y.-k., Feng, Y., and Wang, D.-l. (2021). Effects of Temperatures and pH Values on Rheological Properties of Cemented Paste Backfill. *J. Cent. South. Univ.* 28 (6), 1707–1723. doi:10.1007/s11771-021-4728-4

Zhao, Y., Zhao, G. Y., Pei, D. F., Wu, P., Qiu, J., and Li, Y. (2021). Analysis on Connotation, Characteristics and Type of green Mining Mode for Underground Metal Mines. *Chin. J. Nonferrous Met.* doi:10.11817/j.ysxb.1004.0609.2021-40152

Conflict of Interest: The authors declare that the research was conducted in the absence of any commercial or financial relationships that could be construed as a potential conflict of interest.

Publisher's Note: All claims expressed in this article are solely those of the authors and do not necessarily represent those of their affiliated organizations, or those of the publisher, the editors and the reviewers. Any product that may be evaluated in this article, or claim that may be made by its manufacturer, is not guaranteed or endorsed by the publisher.

frontiers in Materials

ORIGINAL RESEARCH
published: 15 March 2022
doi: 10.3389/fmats.2022.864264

Experimental Study on Direct Tensile Properties of Cemented Paste Backfill

Lijie Guo[1,2], *Xiaopeng Peng*[1,2]*, *Yue Zhao*[1,2], *Guangsheng Liu*[1,2], *Guoxing Tang*[1,2] and *Andrew Pan*[3]

[1]Beijing General Research Institute of Mining and Metallurgy, Beijing, China, [2]National Center for International Joint Research on Green Metal Mining, Beijing, China, [3]Department of Civil and Mineral Engineering, University of Toronto, Toronto, ON, Canada

Cemented paste backfill (CPB) has been increasingly utilized in mines for efficient mineral obtaining and regional ground support. To guarantee the work performance, the mechanical properties of CPB have long been a topic of study among researchers. But the research progress on the tensile strength of CPB is limited, mainly because of the lack of an appropriate test method due to the low tensile strength of CPB. Therefore, instead of the conventional splitting indirect tensile strength test method, a new direct tension test method, which utilizes the specifically designed compression to tension load converter (CTLC) and dog-bone-shaped specimen, has been applied to study the direct tensile properties of CPB. In this study, the direct tensile strength (DTS) of 47 CPB mix designs were measured using CTLC, and the unconfined compressive strength (UCS) of the corresponding mix design was also tested. The experimental results showed that the increase in the binder content, solid mass content, and curing period led to higher CPB direct tensile strength, and the DTS of CPB was most sensitive to the binder content. Furthermore, the influence of the slurry mass solid content on the tensile strength of CPB was not linear. The influence of the binder content became increasingly notable with the increase in the solid content, especially if the binder content exceeded 75%. The effect of the curing period was found to be rather marginal due to the decreasing amount of unhydrated cementitious materials left with the increase of the curing period. Overall, the DTS generated using dog-bone specimens and the CTLC apparatus are valid for better mine backfill designs. Finally, a linear correlative between UCS and DTS with a formula in the form of σDT (DTS) = 0.171 σc (UCS) was obtained, and the correlation was sufficient for further calculation of DTS using measured UCS.

Keywords: tensile strength, direct tension, cemented backfill, tailings, dog-bone specimen

OPEN ACCESS

Edited by:
Erol Yilmaz,
Recep Tayyip Erdoğan University, Turkey

Reviewed by:
Eren Komurlu,
Giresun University, Turkey
Baoxu Yan,
Xi'an University of Science and Technology, China

***Correspondence:**
Xiaopeng Peng
pengxiaopeng@bgrimm.com

Specialty section:
This article was submitted to Structural Materials, a section of the journal Frontiers in Materials

Received: *28 January 2022*
Accepted: *11 February 2022*
Published: *15 March 2022*

Citation:
Guo L, Peng X, Zhao Y, Liu G, Tang G and Pan A (2022) Experimental Study on Direct Tensile Properties of Cemented Paste Backfill. Front. Mater. 9:864264. doi: 10.3389/fmats.2022.864264

1 INTRODUCTION

Mining with backfill, which utilizes solid mine wastes to manage and backfill mined-out stopes, has become a well-accepted method for efficient mineral obtaining and regional ground support (Grice, 1998; Belem and Benzaazoua, 2004; Jahanbakhshzadeh et al., 2017). The cemented paste backfill (CPB), a kind of the backfill method, has been increasingly utilized in mines across the world (Benzaazoua et al., 2008; Thompson et al., 2012). CPB is a composite backfill material usually consisting of mine tailings, water, and a hydraulic binder (Belem et al., 2000); ingredients will be first homogeneously mixed in a backfill plant; and the prepared slurries/paste will then be transported by pipelines and placed in underground stopes to backfill the voids. After days of binder hydration, the

cemented backfill body can acquire adequate strength and provide a stable platform for mining the next stage (le Roux, et al., 2005; Rankine and Sivakugan, 2007). To guarantee the work performance, the mechanical properties of CPB have long been a study focus and application concerns by researchers and engineers, and many significant achievements have been worked out to better understand its properties, including the strength acquisition mechanism (Nasir and Fall, 2010) and failure features under uniaxial (Yilmaz et al., 2014) or triaxial compression (Klein and Simon, 2006; Fall et al., 2007). However, in terms of the tensile strength, due to the lack of an appropriate test method, the research progress has been limited. Although the tensile strength may only account for 20–30% of compressive strength (Komurlu et al., 2007; Fall et al., 2010), in many cases, such as in cut and fill mining or the large exposure of primary CPB during the ore mining of a secondary stope, the tensile strength is the key factor resulting in the failure of a cemented body (Yu, 1992). Indeed, it is necessary to precisely measure and analyze the tensile strength of CPB.

At present, the tensile strength test of CPB commonly takes the standards and methods of concrete or rocks as references (Huang et al., 2011; Chen et al., 2019; Zhou et al., 2021). Currently, the methods can be divided into three categories, namely, the direct tension test, splitting tensile test, and bending/flexural test (Raphael, 1984; Zheng et al., 2001; Erzar and Forquin, 2010). First, the direct tension test will have both ends of the specimen clamped firmly, and then axial tension will be produced by the loading instrument to damage it. The highest recorded stress value is the direct tensile strength (DTS). Hoek et al. (Hoek, 1964) proposed a dog-bone-shaped sample for the DTS test of rocks, as the extended parts of a sample ends can be conveniently clamped by designed wedge gadgets so that direct tension can be effectively applied. Another well-accepted way to clamp the sample is to glue the ends with the pressure arm of a press machine, which has been recommended as a standard DTS test method of a rock by ISRM in 1978 (Bieniawski and Hawkes, 1978), and many studies have been conducted by using this test (Rots and De Borst, 1989; Bolzan and Huber, 1993; Kim and Reda Taha, 2014). There are other direct test methods by changing the shapes of a specimen (Van Mier and Van Vliet, 2002), such as the dumbbell shape (Klanphumeesri., 2002) or "8" shape (Tamrakar et al., 2005). But the common problem of them is that the assembly of samples has to be properly centered; otherwise, the load on the specimen will be higher than the allowed tension value and results in a larger DTS (Cattaneo and Rosati, 1999; Nguyen et al., 2017; Alhussainy et al., 2019).

By contrast, the splitting and the bending tests are both indirect methods. For the splitting test, the "Brazilian test" is recommended and widely used as the standard method for calculating the indirect tensile strength (ITS) of concrete and rock (Carneiro, 1943; Fairhurst, 1964; Rocco et al., 1999). This method was developed separately by Caneiro (Cattaneo and Rosati, 1999) and Akazawa (Akazawa, 1943) in 1943. During the test, a cylindrical sample was placed horizontally in the press chamber, and the load was applied on the sample gradually until a vertical crack formed at the center of its cross section and finally penetrates the sample (Fairhurst, 1964). Then, based on the method theory, the applied force on the sample can be converted into ITS. However, some studies pointed out that the contact surfaces of the sample and press machine in this test are usually very narrow, making the tensile crack eccentric and leading to the overestimation of the real tensile strength (Lin and Wood, 2003; Fahimifar and Malekpour, 2012; Yong., 2005). For the bending test, a cubic sample was used, and after fixing the top and bottom, a concentrated load will be applied on the center part until the test piece bends and finally breaks. Then the highest applied force can be converted to the ITS (British Standard Institution, 1983; ASTM, 2012). This is also a convenient test method, but the conversion theory regarding the bending strength to ITS is based on many restricted assumptions, for example, the cross-sectional area of the test piece is assumed to be unchanged during the test, or the mechanical parameters of the sample such as Young's modulus are all assumed to be unchanged (Wright and Garwood, 1952; Rüsch, 1960; Zweben et al., 1979). Therefore, studies have argued that the ITS obtained by this method would be bigger than the real tensile strength (Rüsch, 1960; Arezoumandi et al., 2015).

In terms of the tensile strength test of CPB, the splitting test is the most commonly used method (Yilmaz et al., 2009; Deng et al., 2017; Zhang and Zhang, 2020; Libos and Cui, 2021; Li et al., 2022). But many research studies assume that the crack failure begins when the tensile stress reaches a maximum point, and the splitting test is more suitable for brittle materials because they will not turn into plastic deformation before the tensile fracture occurs (Yu et al., 1997; Coviello et al., 2005; Lu et al., 2007; Li and Wong, 2013). Thus, as CPB is a kind of a relatively soft material (softer than rocks), the tensile strength of it may not be appropriately tested by using the splitting test. Moreover, for the bending test, as CPB usually has a larger porosity and smaller Young's modulus than rocks and concrete, the cross-sectional area of the specimen will change sharply during the test, which, as explained above, cannot properly match the theoretically assumption.

Therefore, in the present study, the dog-bone-shaped CPB specimens were prepared so that direct tensile tests could be carried out. To optimize the sample clamping by avoiding stress concentration (Sedlacek and Halden, 1962), a compression to tension load converter (CTLC) was utilized (Pan and Grabinsky, 2021). The aim of this article was to verify and further use a new direct tensile strength test method to measure and empirically analyze the direct tensile properties of CPB.

2 DIRECT TENSILE TEST PROCEDURE

2.1 Specimen-Curing Mold

To obtain dog-bone-shaped CPB specimens, a special mold has been designed for casting and curing of fresh CPB, which is shown in **Figure 1A**. It can be found that the mold consists of a baseplate, two enclosure plates, and two-sided baffles. The components are all made from polylactic acid (PLA), which is a kind of waterproof and biodegradable material. Also, all components were separate and could be assembled by bolts. After assembling, some waterproof agents, such as silicone grease, need to be applied on the baseplate to

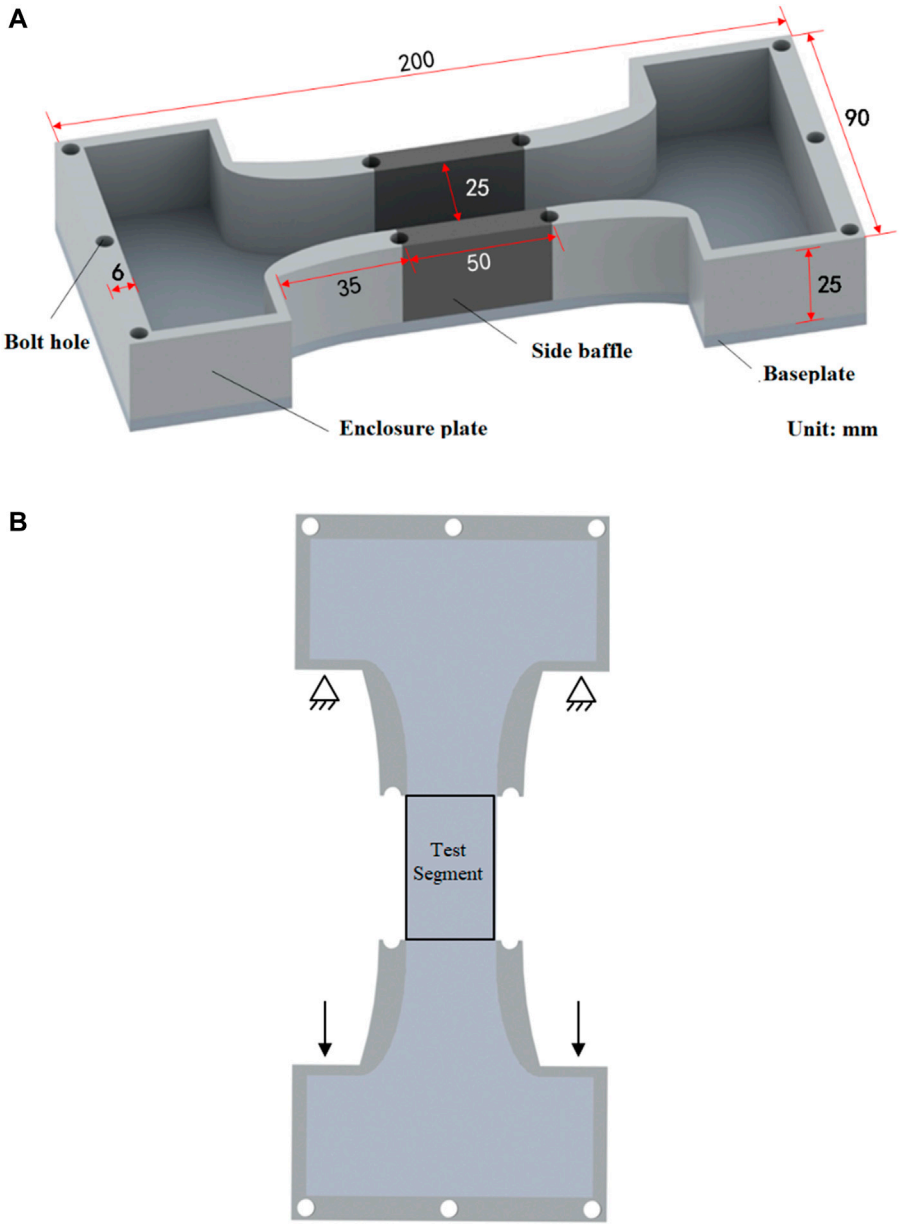

FIGURE 1 | Design and dimensions of the curing mold: **(A)** dimensions of different parts of the mold and **(B)** the usage of the mold.

increase the sealability of the mold, and then the fresh CPB can be cast into it. Thereafter, we used plastic films to cover the surface of the mold to prevent the evaporation of fresh CPB and put the mold into a curing room with steady temperature and humidity for designed days. After curing, only the baseplate and two-sided baffles need to be removed, and the left parts of the mold will be put with the cured CPB test piece together into the CTLC for next testing (see **Figure 1B**).

2.2 Compression to Tension Load Converter

As aforementioned, during the DTS test of the dog-bone sample, the extended head and foot parts will be clamped firmly before testing. As the tensile strength of CPB is much lower than concrete or a rock, the pre-stress caused by clamping may lead to extra pressure on the sample, which will affect the test results. Therefore, a CTLC needs to be used (see **Figure 2**).

As shown in **Figure 2A**, this apparatus was assembled by using two brackets with the same dimensions, of which the length, width, and height are 158, 116, and 176.7 mm, respectively. Also, each bracket consists of a fixing plate, a loading plate, and four screw rods (diameter 10 mm). There was a clamping groove on a fixing plate, which can carry the extended parts of the specimen. The cured CPB samples need to be firstly installed into the two fixing plates. Thereafter, the screw rods are used to connect the loading plate.

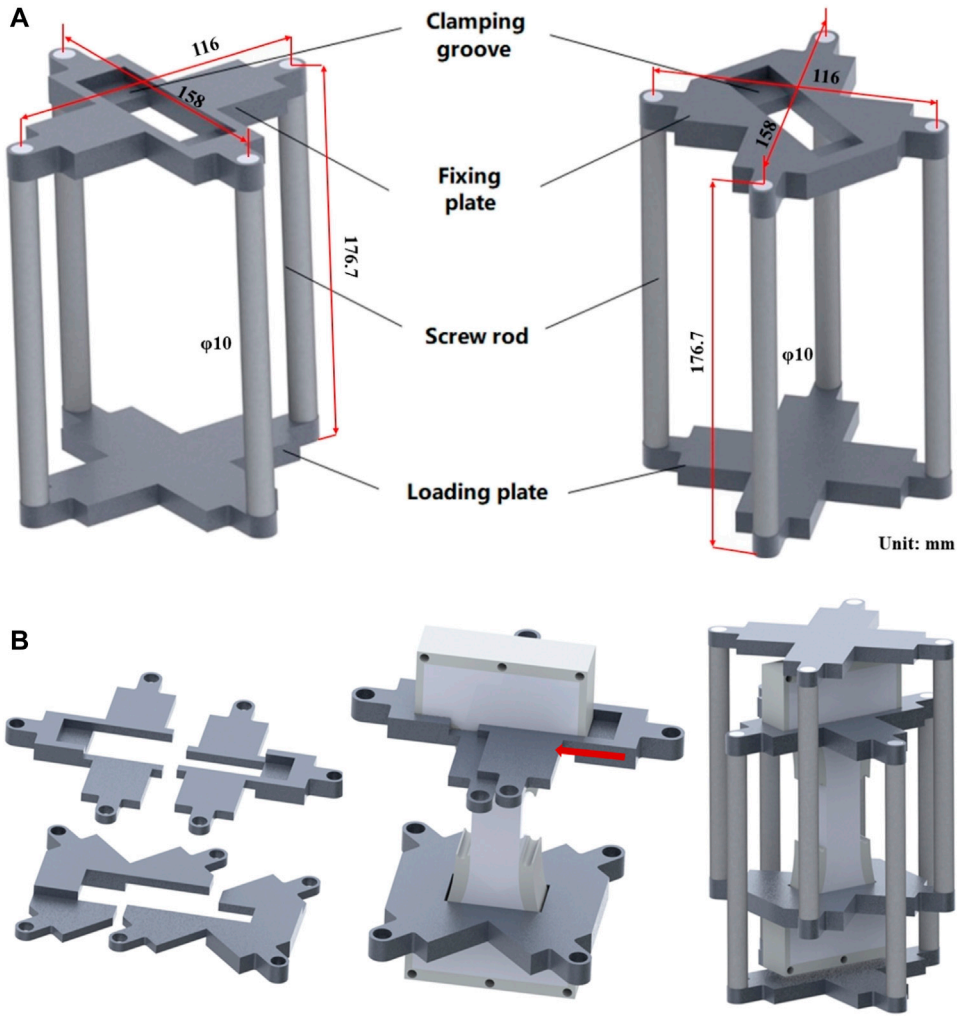

FIGURE 2 | Compression to tension load converter: **(A)** different parts of the apparatus and **(B)** the assembly of the apparatus.

As the two brackets were separated in order not to be hinged, the specimen will hang down and be clamped by weight and then centered. The assembly process is shown in **Figure 2B**. In the test, this apparatus could be placed into any uniaxial loading press, and by applying pressure on the loading plate, the relative movement of the brackets could convert the compressive stress to direct tensile stress on the testing sample. Also, as the apparatus was made from an aluminum alloy, its weight was limited and would not apply much prestress on the sample, affecting the accuracy of the test.

3 MATERIALS AND TEST METHODS

3.1 Test Raw Materials

The processed tailings used in this study were sourced from the Jinchanghe gold mine, Yunnan province, China. About 500 kg of wet tailings was obtained at the processing plant of the Jinchanghe gold mine and dried by the oven in the lab for cemented paste backfill (CPB) sample preparation.

Ordinary Portland cement (OPC 42.5) sourced from a local manufacturer was used as the cementitious binder for backfill sample preparation. Tap water was used for sample preparations.

Following sampling, the physical and chemical characterizations of the tailings were determined. **Figure 3** illustrates the particle size distribution (PSD) of the used tailings determined by using a Malvern Mastersizer 2000 (Malvern Instruments Ltd., Malvern, United Kingdom). As shown in **Figure 3**, the tailings consisted of 75.51% fine particles less than 74 μm and 57.75% of fine fractions less than 38 μm which are suitable for cement paste backfill slurry preparation (Yılmaz et al., 2014; Zhao et al., 2020).

The chemical characterizations of the tailing material are shown in **Table 1**. The chemical composition of tailings mainly consisted of silicon dioxide (SiO_2), ferric oxide (Fe_2O_3), and calcium oxide (CaO), with mass fractions of 34.96%, 25.28%, and 21.81%, respectively.

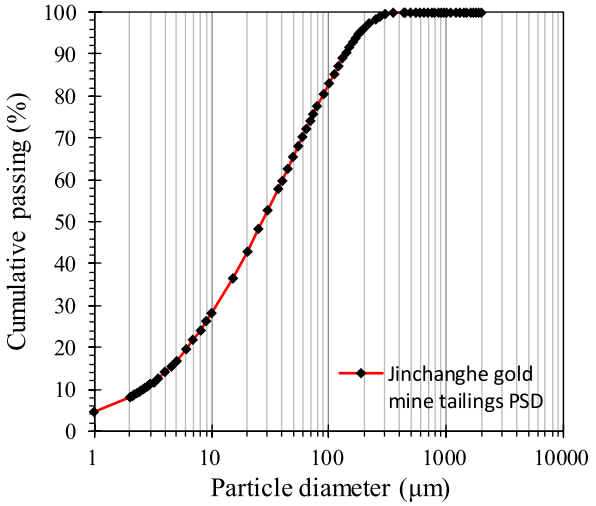

FIGURE 3 | Particle size distribution of tailings sourced from the Jinchanghe gold mine.

3.2 Test Methods

3.2.1 Mix Design and Sample Preparation

In our study, a total of 48 mix designs were examined, as shown in **Table 2**. The following naming system was used to represent specific mix designs:

$$S_xB_yT_z, \tag{1}$$

where S_x is x% of the solid mass content, B_y is y% of the binder (cement) content, and T_z is z days of the curing period.

The solid mass content and binder content is defined as follows:

$$S_c = \frac{m_B + m_T}{m_B + m_T + m_W}, \tag{2}$$

$$B_c = \frac{m_B}{m_B + m_T}, \tag{3}$$

where S_c is the solid mass content of the CPB slurry, B_c is the binder content, m_B is the mass of the binder, m_T is the mass of dry tailings, and m_W is the mass of the mixing water.

A bakery mixer was used for CPB slurry preparation in this study. An appropriate number of tailings and binder were initially weighed and mixed in the dry form for 5 min according to the mix design shown in **Table 2**. Tap water was then added to achieve the designed solid mass content of CPB slurry and wet mixed for at least 5 min to obtain homogenized paste slurry. The resultant slurries were poured into I-shaped rectangular molds (as discussed in **Section 2.1**) and cylindrical molds (50 mm diameter, 100 mm length) to form rectangular dog-bone specimens and cylindrical specimens for the direct tensile (DT) and unconfined compression (UC) tests. During the pouring of paste-like slurries, the molds were filled with one-third length increments each time. After filling each layer, a small metal rod was used to tamp the mold approximately 25 times to remove entrapped air. The prepared CPB samples were then sealed and

TABLE 1 | Chemical composition of tailings used.

Chemical composition (Wt.%)	CaO	SiO_2	Al_2O_3	MgO	Fe_2O_3	P_2O_5	K_2O	Na_2O	SO_3	other
Tailings	21.81	34.96	1.78	2.47	25.28	0.05	0.37	0.24	0.50	12.53

TABLE 2 | Mix designs and their properties.

Mix designs	Solid content (wt.%)	Binder content (wt.%)	Curing period (days)
$S_{68}B_{9.1}T_{7,14,28}$	68	9.1	7,14,28
$S_{68}B_{11.1}T_{7,14,28}$	68	11.1	7,14,28
$S_{68}B_{14.3}T_{7,14,28}$	68	14.3	7,14,28
$S_{68}B_{20}T_{7,14,28}$	68	20	7,14,28
$S_{70}B_{9.1}T_{7,14,28}$	70	9.1	7,14,28
$S_{70}B_{11.1}T_{7,14,28}$	70	11.1	7,14,28
$S_{70}B_{14.3}T_{7,14,28}$	70	14.3	7,14,28
$S_{70}B_{20}T_{7,14,28}$	70	20	7,14,28
$S_{72}B_{9.1}T_{7,14,28}$	72	9.1	7,14,28
$S_{72}B_{11.1}T_{7,14,28}$	72	11.1	7,14,28
$S_{72}B_{14.3}T_{7,14,28}$	72	14.3	7,14,28
$S_{72}B_{20}T_{7,14,28}$	72	20	7,14,28
$S_{75}B_{9.1}T_{7,14,28}$	75	9.1	7,14,28
$S_{75}B_{11.1}T_{7,14,28}$	75	11.1	7,14,28
$S_{75}B_{14.3}T_{7,14,28}$	75	14.3	7,14,28
$S_{75}B_{20}T_{7,14,28}$	75	20	7,14,28

cured at a constant temperature in a humidity chamber maintained at 90% relative humidity and a temperature of 20 ± 0.5°C to premeasured curing periods.

3.2.2 Unconfined Compressive Test

Unconfined compression (UC) tests were conducted using cylindrical specimens at designed curing periods (7, 14, and 28 days) with a computer-controlled loading machine (HM-5030, Humboldt Mfg. Co., Elgin, IL, United States), as shown in **Figure 4**, in accordance with ASTM C39–18 (ASTM C39/C39M-18, 2018). The axial loading rate was fixed at 1mm/min, and the strains and corresponding stresses were recorded during the unconfined compressive test until the failure of the CPB sample. For the accuracy of test results, five cylindrical samples were prepared, and tests were conducted in triplicate for each mix at various curing periods. The average value was considered for further analyses.

3.2.3 Direct Tensile Test

Direct tensile (DT) tests were conducted using rectangular dog-bone specimens at designed curing periods (7, 14, and 28 days) with the same computer-controlled loading machine (HM-5030, Humboldt Mfg. Co., Elgin, IL, United States) as the UC test. A compression to tension load converter (CTLC), as shown in **Figure 5** and illustrated in **Section 2.2**, was used to convert the axial load provided by the loading machine to a tensile load. The loading rate of the machine was fixed at 0.2 mm/s, and the strains and corresponding stresses were recorded during the unconfined compressive test until the failure of dog-bone-shaped specimens. Considering the weight of CTLC and dog-bone-shaped specimens, the direct tensile strength of each sample was calculated as follows:

$$\sigma_{DT} = \frac{F + \frac{1}{2}(m_s + m_z)g}{S}, \tag{4}$$

where σ_{DT} is the measured direct tensile strength, F is the peak load achieved, m_s is the mass of the tested specimen, m_z is the mass of CTLC apparatus, g is the acceleration of gravity, and S is the cross-sectional area of failure plan.

For the accuracy of test results, five dog-bone-shaped specimens were prepared, and tests were conducted in triplicates for each mix at various curing periods. The average value was considered for further analyses.

4 RESULTS AND DISCUSSION

4.1 Failure Pattern of Direct Tensile Tests

In this study, the authors successfully measured the direct tensile strength of CPB rectangular dog-bone specimens of 47

FIGURE 4 | Unconfined compressive test of the cylindrical CPB specimen.

FIGURE 5 | Direct tensile test of the dog-bone CPB specimen.

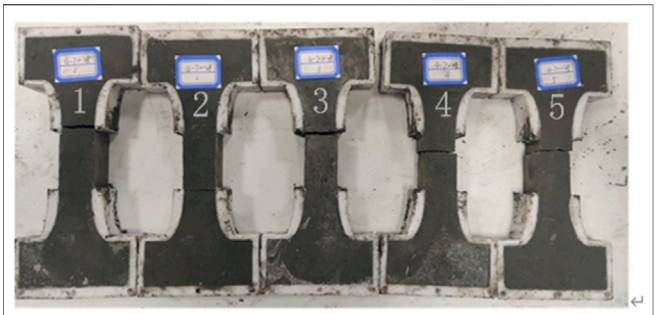

FIGURE 6 | Failure pattern of the sample $S_{70}B_{20}T_{28}$.

mix designs. For the sample S68B9.1T7, the tensile strength was too low, and the sample could easily break under the gravity of the CTLC apparatus during installation; hence, the tensile strength could not be obtained.

Figure 6 illustrates the failure pattern of the five samples for the mix S70B20T28; the observed fracture surface is a flat and typically straight fracture line perpendicular to the direction of the tensile force. Among the five specimens of S70B20T28, samples 3, 4, and 5 failed at the center of dog-bone specimens, as Pan et al. (Pan, A. N., & Grabinsky, M. W., 2021) reported, where the smallest cross-section is at or near the midsection of the failure zone of all the specimens. However, samples 1 and 2 failed at the grip of the dog-bone sample. It might have been caused by the partial separation of the head plate and sample, which led to a reposition of both ends of the dog-bone sample and brought non-uniform tensile stress across the specimen. During our empirical study, all samples that failed such as this were not included for further analyses. The average value of three successful tests will be used as the direct tensile strength of each mix design.

4.2 Direct Tensile Test Results

Figure 7 illustrates the variations of the direct tensile strength (DTS, σDT) against the binder content with different solid mass contents at various curing periods. Overall, the increase in the binder content, solid mass content, and curing period led to a higher cemented paste backfill tensile strength.

For instance, the sample S70B9.1T7, exhibited a direct tensile strength (σDT) of 115.45 kPa, while the inclusion of Bc = 11.1%, 14.3%, and 20%, at the same 7-day curing condition, resulted in σDT of 159.94, 219.57 and 408.66 kPa, respectively. For the same binder content of 11.1% and curing period of seven days, the tensile strength was 146.32, 159.94, 174.64, and 229.65 kPa for samples

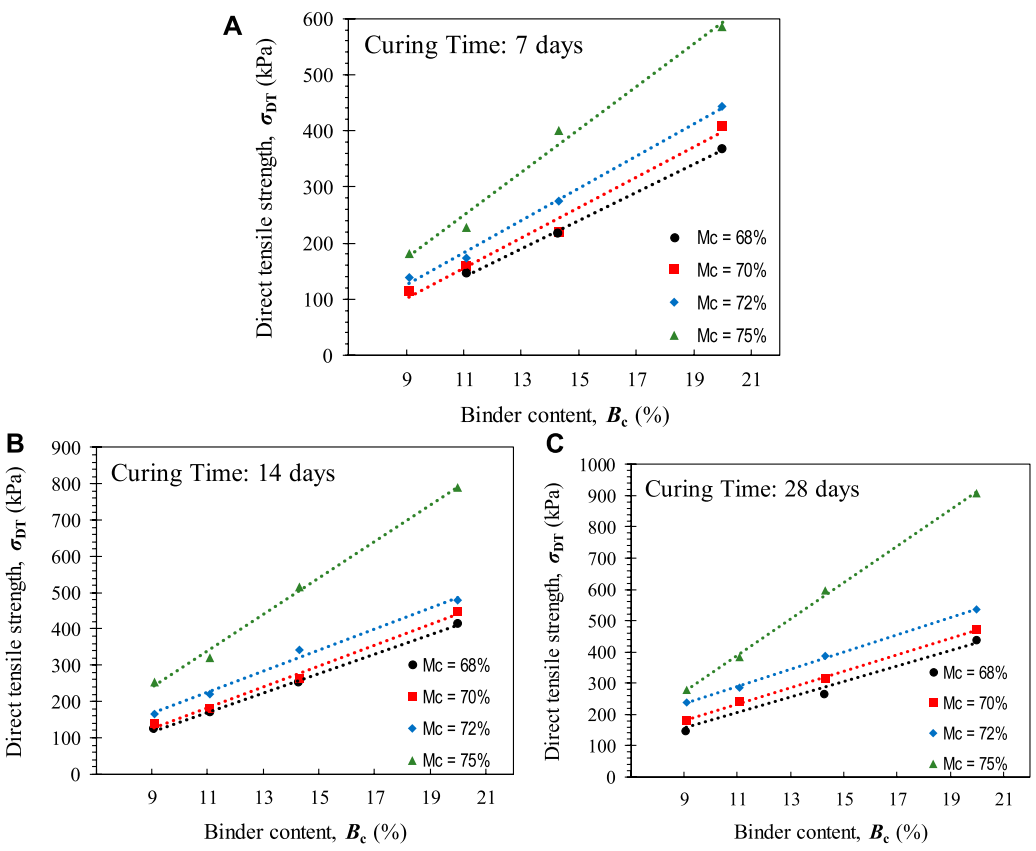

FIGURE 7 | Variations of direct tensile strength σDT against the binder content with different solid mass contents for samples cured for **(A)** 7 days, **(B)** 14 days, and **(C)** 28 days.

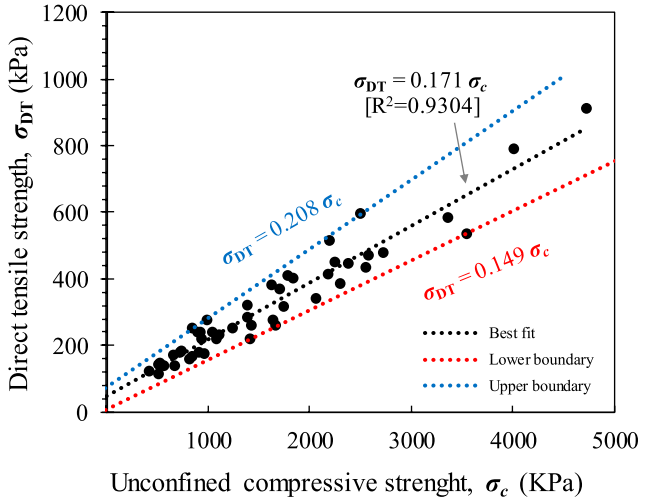

FIGURE 8 | Variations of direct tensile strength σDT against unconfined compressive strength σc for all CPB mix designs.

S68B11.1T7, S70B11.1T7, S72B11.1T7, and S75B11.1T7, respectively. Similarly, for any given binder content and solid mass content, the increase of the curing period promoted an increase of CPB tensile strength at a smaller step. For instance, the tensile strength for the sample S68B20T7 resulted in 408.66 kPa, and the tensile strength increased with values of 448.69 and 470.44 kPa for the same mix proportion curried at 14 and 28 days.

With the analysis of tensile strength results, even the increase in the binder content, solid mass content, and curing period promoted the resultant sample tensile strength. The tensile strength sensitivity to these three influencing factors was different. The CPB tensile strength was most sensitive for the binder content, as the tensile strength increased from 115.45 to 408.66 kPa, with a change of 9.1% binder content to 20% binder content, at the same 7-day curing period and 70% solid mass content. As shown in **Figure 6**, the increment rate of tensile strength dramatically increased while the solid mass content increased to 75%. Hence, the influence of the solid mass content of the slurry was not linear. The influence of Bc became increasingly notable with the increase in the solid content, especially for Bc after 75%. In a similar but adverse manner, with the same solid content and binder content, the increment of tensile strength was more pronounced for the 7–14-day curing period than the 14–28-day curing period. Moreover, the effect of the curing period was found to be rather marginal due to the decreasing amount of un-hydrated cementitious materials left with the increase in the curing period.

4.3 Direct Tensile Strength and Unconfined Compressive Strength

This study measured the unconfined compressive strength (UCS) of all 48 different mix designs using prepared CPB cylindrical samples. Uniaxial compressive strength (UCS) is one of the significant and common characteristics used to define the mechanical performance of CPB. For cement paste backfill, the tensile strength is difficult and expensive to measure; hence, tensile strength is often calculated based on UCS results (Nazir, et al., 2013). **Figure 8** illustrates the direct tensile strength, σDT, variations against un-confined compressive strength, σc, for all CPB mix designs. **Figure 8** is generated based on the successfully measured direct tensile strength of CPB rectangular dog-bone specimens of 47 different mix designs and the corresponding UCS value measures. As the direct tensile strength of the sample, S68B9.1T7 was too low, and the sample easily broke under the gravity of the CTLC apparatus during installation. Hence, the experimental data of mix design S68B9.1T7 was not included in **Figure 8**. A linear correlation was found between σc and σDT. The variations of σDT lied within the $0.149\ \sigma c < \sigma DT < 0.208\ \sigma c$ domains (σDT and σc in kPa). In this case, a linear correlative formula in the form of $\sigma DT = 0.171\ \sigma c$ (R2 = 0.9304) was obtained. Deng et al. (2017) measured the UCS and splitting tensile strength of CPB samples by varying solid contents, binder content, and curing period. Their results indicated that the splitting tensile strength was about 10%–20% of UCS. Pan and Grabinsky et al. (2021) measured the direct tensile strength and UCS of CPB samples with different binder contents, and the direct tensile strength was about 16%–25% of CPB UCS. Hence, the direct tensile strength measured using dog-bone specimens and CTLC apparatus is correct, and the correlation is sufficient for further calculation of direct tensile strength using measured UCS. This linear correlation between σDT and σc is based on a large amount of experimental data, which can be used as an experience formula to guide engineers on the relationship between the direct tensile and unconfined compressive strength. However, the σDT and σc experience conversion formula still got its limitations. It is not applicable when the strength is deficient.

5 CONCLUSION

This study presents an experimental study on the direct tensile strength measurement of the CPB dog-bone sample. A compression to tension load converter (CTLC) was used to transmit compression to tensile load on dog-bone samples to achieve direct tensile measurement using a standard loading machine. In this study, the direct tensile strength and unconfined compressive strength were successfully measured for a total of 47 CPB mix designs, and the following conclusions can be drawn:

First, by using dog-bone specimens and CTLC apparatus, the direct tensile strength of CPB could be measured effectively. This method is the first proven scientifically valid measurement method for tensile strength of CPB, which can provide a reliable means for obtaining the tensile mechanical parameters of mine backfill.

Second, the increase in the binder content, solid mass content, and curing period leads to higher cemented paste

backfill tensile strength. The tensile strength sensitivity to these three influencing factors differs, and the CPB tensile strength is most sensitive to the binder content.

Third, the influence of slurries' mass solid content on CPB tensile strength is not linear. The influence of binder content becomes increasingly notable with the increase of solid content, especially for binder content after 75%.

Fourth, the effect of the curing period was found to be rather marginal due to the decreasing amount of un-hydrated cementitious materials left with the increase of the curing period.

Fifth, a linear correlative experience conversion formula between UCS and DTS in the form of $\sigma DT = 0.171\ \sigma c$ ($R2 = 0.9304$) is first obtained. The correlation is sufficient for further calculation of DTS using measured UCS.

Finally, the σDT and σc experience conversion formulas still have their limitations; it is not applicable when the strength is deficient. The applicability of σDT and σc experience conversion formula on CPB samples prepared by various binders and aggregates should also be further developed.

DATA AVAILABILITY STATEMENT

The original contributions presented in the study are included in the article/Supplementary Material, further inquiries can be directed to the corresponding author.

AUTHOR CONTRIBUTIONS

LG and GT contributed significantly to the design of the study. LG, XP, and YZ developed the math analysis model and wrote the first draft of the manuscript. LG and GT provided constructive discussions and contributed to manuscript revision. GL and AP made important revisions to the manuscript. All authors agree to be accountable for the content of this work.

FUNDING

This research was supported by the National Key R&D Program of China (No. 2021YFC2900600).

REFERENCES

Akazawa, T. (1943). New Test Method for Evaluating Internal Stress Due to Compression of concrete (The Splitting Tension Test)(part 1). *J. Jpn. Soc. Civ Eng.* 29, 777

Alhussainy, F., Hasan, H. A., Sheikh, M. N., and Hadi, M. N. (2019). A New Method for Direct Tensile Testing of concrete. *J. Test. Eval.* 47 (2), 704–718. doi:10.1520/jte20170067

American Society for Testing and Materials (Astm) (2012). *Standard Test Method for Flexural Strength of Soil-Cement Using Simple Beam with Third-point Loading' West Conshohocken*. West Conshohocken, Pennsylvania: ASTM International.

Arezoumandi, M., Smith, A., Volz, J. S., and Khayat, K. H. (2015). An Experimental Study on Flexural Strength of Reinforced concrete Beams with 100% Recycled concrete Aggregate. *Eng. Structures* 88, 154. doi:10.1016/j.engstruct.2015.01.043

ASTM C39 C39M-18 (2018). *Standard Test Method for Compressive Strength of Cylindrical Concrete Specimens*. West Conshohocken, PA: ASTM International.

Belem, T., and Benzaazoua, M. (2004). An Overview on the Use of Paste Backfill Technology as a Ground Support Method in Cut-And-Fill Mines. In *Proceedings of the 5th Int. Symp. On Ground Support in Mining and Underground Construction. Villaescusa & Potvin* (eds.), pp. 637

Belem, T., Benzaazoua, M., and Bussière, B. (2000). "Mechanical Behaviour of Cemented Paste Backfill," in *Proc. Of 53rd Canadian Geotechnical Conference* (Montreal, 373–380.

Benzaazoua, M., Bussière, B., Demers, I., Aubertin, M., Fried, É., and Blier, A. (2008). Integrated Mine Tailings Management by Combining Environmental Desulphurization and Cemented Paste Backfill: Application to Mine Doyon, Quebec, Canada. *Minerals Eng.* 21 (4), 330–340. doi:10.1016/j.mineng.2007.11.012

Bieniawski, Z. T., and Hawkes, I. (1978). Suggested Methods for Determining Tensile Strength of Rock Materials. *Int. J. Rock Mech. Mining Sci.* 15 (3), 99–103. doi:10.1016/0148-9062(78)90956-7

Bolzan, P. E., and Huber, G. A. (1993). *Direct Tension Test Experiments (No. SHRP-A-641)*. Washington, DC: Strategic Highway Research ProgramNational Research Council.

British Standard Institution(Bs) (1983). *-118 Method for Determination of Flexural Strength'*. London: BSI

Carneiro, F. L. L. B. (1943). A New Method to Determine the Tensile Strength of concrete. *Proc. 5th Meet. Braz. Assoc. Tech. Rules* 3 (16), 126

Cattaneo, S., and Rosati, G. (1999). Effect of Different Boundary Conditions in Direct Tensile Tests: Experimental Results. *Mag. Concrete Res.* 51 (5), 365–374. doi:10.1680/macr.1999.51.5.365

Chen, X., Shi, X., Zhou, J., and Yu, Z. (2019). Influence of Polypropylene Fiber Reinforcement on Tensile Behavior and Failure Mode of Tailings Cemented Paste Backfill. *IEEE Access* 7, 69015–69026. doi:10.1109/access.2019.2919480

Coviello, A., Lagioia, R., and Nova, R. (2005). On the Measurement of the Tensile Strength of Soft Rocks. *Rock Mech. Rock Engng.* 38 (4), 251–273. doi:10.1007/s00603-005-0054-7

Deng, X., Zhang, J., Klein, B., Zhou, N., and Dewit, B. (2017). Experimental Characterization of the Influence of Solid Components on the Rheological and Mechanical Properties of Cemented Paste Backfill. *Int. J. Mineral Process.* 168, 116–125. doi:10.1016/j.minpro.2017.09.019

Erzar, B., and Forquin, P. (2010). An Experimental Method to Determine the Tensile Strength of concrete at High Rates of Strain. *Exp. Mech.* 50 (7), 941–955. doi:10.1007/s11340-009-9284-z

Fahimifar, A., and Malekpour, M. (2012). Experimental and Numerical Analysis of Indirect and Direct Tensile Strength Using Fracture Mechanics Concepts. *Bull. Eng. Geol. Environ.* 71 (2), 269–283. doi:10.1007/s10064-011-0402-7

Fairhurst, C. (1964). On the Validity of the 'Brazilian' Test for Brittle Materials. *Int. J. Rock Mech. Mining Sci. Geomechanics Abstr.* 1 (4), 535–546. doi:10.1016/0148-9062(64)90060-9

Fall, M., Belem, T., Samb, S., and Benzaazoua, M. (2007). Experimental Characterization of the Stress-Strain Behaviour of Cemented Paste Backfill in Compression. *J. Mater. Sci.* 42 (11), 3914–3922. doi:10.1007/s10853-006-0403-2

Fall, M., Célestin, J. C., Pokharel, M., and Touré, M. (2010). A Contribution to Understanding the Effects of Curing Temperature on the Mechanical Properties of Mine Cemented Tailings Backfill. *Eng. Geology.* 114 (3-4), 397–413. doi:10.1016/j.enggeo.2010.05.016

Grice, T. (1998). *Underground Mining with Backfill*. Brisbane, Nov: 2nd Annual Summit on Mine Tailings Disposal Systems, 24–25.

Hoek, E. (1964). Fracture of Anisotropic Rock. *J. South. Afr. Inst. Mining Metall.* 64 (10), 501

Huang, S., Xia, K., and Qiao, L. (2011). Dynamic Tests of Cemented Paste Backfill: Effects of Strain Rate, Curing Time, and Cement Content on Compressive Strength. *J. Mater. Sci.* 46 (15), 5165–5170. doi:10.1007/s10853-011-5449-0

Jahanbakhshzadeh, A., Aubertin, M., and Li, L. (2017). A New Analytical Solution for the Stress State in Inclined Backfilled Mine Stopes. *Geotech Geol. Eng.* 35 (3), 1151–1167. doi:10.1007/s10706-017-0171-6

Kim, J. J., and Reda Taha, M. (2014). Experimental and Numerical Evaluation of Direct Tension Test for Cylindrical concrete Specimens. *Adv. Civil Eng.* doi:10.1155/2014/156926

Klanphumeesri, S. (2002). *Direct Tension Testing of Rock Specimens, Master's Thesis*. Nakhon Ratchasima, Thailand: Suranaree University of Technology.

Klein, K., and Simon, D. (2006). Effect of Specimen Composition on the Strength Development in Cemented Paste Backfill. *Can. Geotech. J.* 43 (3), 310–324. doi:10.1139/t06-005

Komurlu, E., Kesimal, A., and Demir, S. (2016). Experimental and Numerical Analyses on Determination of Indirect (Splitting) Tensile Strength of Cemented Paste Backfill Materials under Different Loading Apparatus. *Geomech. Eng.* 10 (6), 775–791. doi:10.12989/gae.2016.10.6.775

le Roux, K., Bawden, W. F., and Grabinsky, M. F. (2005). Field Properties of Cemented Paste Backfill at the Golden Giant Mine. *Mining Techn.* 114 (2), 65–80. doi:10.1179/037178405x44557

Li, D., and Wong, L. N. Y. (2013). The Brazilian Disc Test for Rock Mechanics Applications: Review and New Insights. *Rock Mech. Rock Eng.* 46 (2), 269–287. doi:10.1007/s00603-012-0257-7

Li, Z., Shi, X., and Chen, X. (2022). Effect of Rice Straw on Tensile Properties of Tailings Cemented Paste Backfill. *Appl. Sci.* 12 (1), 526. doi:10.3390/app12010526

Libos, I. L. S., and Cui, L. (2021). Time- and Temperature-Dependence of Compressive and Tensile Behaviors of Polypropylene Fiber-Reinforced Cemented Paste Backfill. *Front. Struct. Civ. Eng.* 15 (4), 1025–1037. doi:10.1007/s11709-021-0741-9

Lin, Z., and Wood, L. (2003). Concrete Uniaxial Tensile Strength and cylinder Splitting Test. *J. Struct. Eng.* 129 (5), 692–698. doi:10.1061/(asce)0733-9445(2003)129:5(692)

Lu, N., Wu, B., and Tan, C. P. (2007). Tensile Strength Characteristics of Unsaturated Sands. *J. Geotech. Geoenviron. Eng.* 133 (2), 144–154. doi:10.1061/(asce)1090-0241(2007)133:2(144)

Nasir, O., and Fall, M. (2010). Coupling Binder Hydration, Temperature and Compressive Strength Development of Underground Cemented Paste Backfill at Early Ages. *Tunnelling Underground Space Techn.* 25 (1), 9–20. doi:10.1016/j.tust.2009.07.008

Nazir, R., Momeni, E., Armaghani, D. J., and Amin, M. M. (2013). Correlation between Unconfined Compressive Strength and Indirect Tensile Strength of limestone Rock Samples. *Electron. J. Geotech Eng.* 18 (1), 1737

Nguyen, D. H., Dao, V. T. N., and Lura, P. (2017). Tensile Properties of concrete at Very Early Ages. *Construction Building Mater.* 134, 563–573. doi:10.1016/j.conbuildmat.2016.12.169

Pan, A. N., and Grabinsky, M. W. (2021). Tensile Strength of Cemented Paste Backfill. *Geotechnical Test. J.* 44 (6), 1–13. doi:10.1520/gtj20200206

Rankine, R. M., and Sivakugan, N. (2007). Geotechnical Properties of Cemented Paste Backfill from Cannington Mine, Australia. *Geotech Geol. Eng.* 25 (4), 383–393. doi:10.1007/s10706-006-9104-5

Raphael, J. M. (1984). Tensile Strength of concrete. *J. Proc.* 81 (2), 158

Rocco, C., Guinea, G. V., Planas, J., and Elices, M. (1999). Size Effect and Boundary Conditions in the Brazilian Test: Experimental Verification. *Mat. Struct.* 32 (3), 210–217. doi:10.1007/bf02481517

Rots, J. G., and De Borst, R. (1989). Analysis of concrete Fracture in "Direct" Tension. *Int. J. Sol. Structures* 25 (12), 1381–1394. doi:10.1016/0020-7683(89)90107-8

Rüsch, H. (1960). Researches toward a General Flexural Theory for Structural concrete. *J. Am. Concrete Inst.* 57 (1), 1–28.

Sedlacek, R., and Halden, F. A. (1962). Method for Tensile Testing of Brittle Materials. *Rev. Scientific Instr.* 33 (3), 298–300. doi:10.1063/1.1717827

Tamrakar, S. B., Toyosawa, Y., and Itoh, K. (20052004). *Tensile Strength of Soil Measured Using Newly Developed Tensile Strength Apparatus*. Kiyose, Japan: Research Reports of National Institute of Industrial Safety

Thompson, B. D., Bawden, W. F., and Grabinsky, M. W. (2012). *In Situ* measurements of Cemented Paste Backfill at the Cayeli Mine. *Can. Geotech. J.* 49 (7), 755–772. doi:10.1139/t2012-040

Van Mier, J. G. M., and Van Vliet, M. R. A. (2002). Uniaxial Tension Test for the Determination of Fracture Parameters of concrete: State of the Art. *Eng. Fracture Mech.* 69 (2), 235–247. doi:10.1016/s0013-7944(01)00087-x

Wright, P. J. F., and Garwood, F. (1952). The Effect of the Method of Test on the Flexural Strength of concrete. *Mag. Concrete Res.* 4 (11), 67–76. doi:10.1680/macr.1952.4.11.67

Yilmaz, E., Benzaazoua, M., Belem, T., and Bussière, B. (2009). Effect of Curing under Pressure on Compressive Strength Development of Cemented Paste Backfill. *Minerals Eng.* 22 (9-10), 772–785. doi:10.1016/j.mineng.2009.02.002

Yılmaz, T., Ercikdi, B., Karaman, K., and Külekçi, G. (2014). Assessment of Strength Properties of Cemented Paste Backfill by Ultrasonic Pulse Velocity Test. *Ultrasonics* 54 (5), 1386–1394. doi:10.1016/j.ultras.2014.02.012

Yong, Y. U. (2005). Questioning the Validity of the Brazilian Test for Determining Tensile Strength of Rocks. *Chin. J. Rock Mech. Eng.* 24 (7), 1150

Yu, T. R. (1992). "Mechanisms of Fill Failure and Fill Strength Requirements," in *Proceedings of 6th Canadian Rock Mechanics Symposium*, 1–6.

Yu, Y., Jianxun, Z., and Jichun, Z. (1997). A Modified Brazilian Disk Tension Test. *Int. J. Rock Mech. Mining Sci.* 46 (2), 421

Zhang, X., and Zhang, S. (2020). Experimental Investigation on Mechanical Properties of *In Situ* Cemented Paste Backfill Containing Coal Gangue and Fly Ash. *Adv. Civil Eng.* 2020, 1–12. doi:10.1155/2020/7964267

Zhao, Y., Taheri, A., Karakus, M., Chen, Z., and Deng, A. (2020). Effects of Water Content, Water Type and Temperature on the Rheological Behaviour of Slag-Cement and Fly Ash-Cement Paste Backfill. *Int. J. Mining Sci. Techn.* 30 (3), 271–278. doi:10.1016/j.ijmst.2020.03.003

Zheng, W., Kwan, A. K. H., and Lee, P. K. K. (2001). Direct Tension Test of concrete. *Mater. J.* 98 (1), 63–71.

Zhou, Y., Yan, Y., Zhao, K., Yu, X., Song, Y., Wang, J., et al. (2021). Study of the Effect of Loading Modes on the Acoustic Emission Fractal and Damage Characteristics of Cemented Paste Backfill. *Construction Building Mater.* 277, 122311. doi:10.1016/j.conbuildmat.2021.122311

Zweben, C., Smith, W. S., and Wardle, M. W. (1979). "Test Methods for Fiber Tensile Strength, Composite Flexural Modulus, and Properties of Fabric-Reinforced Laminates," in *Composite Materials: Testing and Design (Fifth Conference)* (West Conshohocken, Pennsylvania: ASTM International).

Conflict of Interest: The authors declare that the research was conducted in the absence of any commercial or financial relationships that could be construed as a potential conflict of interest.

Advantages of publishing in Frontiers

OPEN ACCESS
Articles are free to read for greatest visibility and readership

FAST PUBLICATION
Around 90 days from submission to decision

HIGH QUALITY PEER-REVIEW
Rigorous, collaborative, and constructive peer-review

TRANSPARENT PEER-REVIEW
Editors and reviewers acknowledged by name on published articles

Frontiers
Avenue du Tribunal-Fédéral 34
1005 Lausanne | Switzerland

Visit us: www.frontiersin.org
Contact us: frontiersin.org/about/contact

REPRODUCIBILITY OF RESEARCH
Support open data and methods to enhance research reproducibility

DIGITAL PUBLISHING
Articles designed for optimal readership across devices

FOLLOW US
@frontiersin

IMPACT METRICS
Advanced article metrics track visibility across digital media

EXTENSIVE PROMOTION
Marketing and promotion of impactful research

LOOP RESEARCH NETWORK
Our network increases your article's readership